DEPARTMENT OF PHYSICS
UNIVERSITY OF JYVÄSKYLÄ
RESEARCH REPORT NO. 1/2015

Laser developments and high resolution resonance ionization spectroscopy of actinide elements

by
Volker Sonnenschein

Academic Dissertation
for the Degree of
Doctor of Philosophy

To be presented, by permission of the
Faculty of Mathematics and Natural Sciences
of the University of Jyväskylä,
for public examination in Auditorium YAA303 of the
University of Jyväskylä on January 8th, 2015
at 12 o'clock noon

Jyväskylä, Finland
December 2014

ABSTRACT

Sonnenschein, Volker
Laser developments and high resolution resonance ionization spectroscopy of actinide elements
Jyväskylä: University of Jyväskylä, 2014, 176 p.
Department of Physics Research Report
ISSN 0075-465X; **1/2015**)
ISBN 978-951-39-6049-0 (paper version)
ISBN 978-951-39-6050-6 (electronic version)
Diss.

Laser development of pulsed Ti:sapphire laser systems has been carried out at the IGISOL facility in the University of Jyväskylä, Finland. To further the applications of Ti:sapphire technology in the domain of resonance laser ionization, several new laser resonator designs have been implemented. Studies for the development of ionization schemes have been simplified by use of a grating-based cavity. For increased spectroscopic resolution a dual-etalon as well as an injection-locked Ti:sapphire laser have been built and characterized. Increased output power of higher harmonics has been achieved with the technique of intra-cavity frequency doubling. Extension to a new frequency domain has been realized using difference frequency mixing.

These new developments have been successfully applied in experimental studies at the University of Mainz (Germany), the LISOL facility (Belgium) as well as at IGISOL (Finland). High resolution resonance ionization spectroscopy has been used to study the ground state hyperfine structure of ^{229}Th in an ongoing effort to identify a highly sought after nuclear isomer. Further high resolution work has been carried out on ^{227}Ac as well as several isotopes of plutonium. Systematic studies of the hyperfine structure of natural copper have been employed to determine the accuracy of future in-source laser spectroscopy applications at IGISOL.

Keywords: Resonance ionization, laser, Ti:sapphire, hyperfine structure

Author

Volker Sonnenschein
Department of Physics
University of Jyväskylä
Finland

Supervisor

Dr. Iain Moore
Department of Physics
University of Jyväskylä
Finland

Reviewers

Prof. Gerda Neyens
KU Leuven
Nuclear and Radiation Physics Section
Celestijnenlaan 200d - box 2418
3001 Leuven, Belgium

and

Dr. Paul Campbell
The School of Physics and Astronomy
University of Manchester
Oxford Road
Manchester
M13 9PL, UK

Opponent

Prof. Jon Billowes
The School of Physics and Astronomy
University of Manchester
Oxford Road
Manchester
M13 9PL, UK

PREFACE

This work has been carried out at the Accelerator Laboratory of the Department of Physics, University of Jyväskylä, Finland from 2009 to 2014. Financial support from the Graduate School for Particle and Nuclear Physics (GRASPANP), the Doctoral Programme in Particle and Nuclear Physics (PANU) and the University of Jyväskylä is greatly appreciated.

ACKNOWLEDGEMENTS

I am grateful to Prof. Juha Äystö for taking me into the group as well as for the continued support from his successor Prof. Ari Jokinen. I want to thank the whole IGISOL group for a great working experience and support during the on- and off-line laser runs.

Special mention goes to the people of the IGISOL-laser subunit. My supervisor Dr. Iain Moore for his ever-present guidance and contagious motivation. Mikael Reponen for his introduction to the local nightlife and the shared wasted hours tweaking laser systems under the green sun. Thomas Kessler is acknowledged for his introduction to the laser systems, Ilkka Pohjalainen for his contributions to the data acquisition system and Annika Voss for her recent support on laser spectroscopy.

I am indebted to all our collaborators for allowing me to take part in several interesting experiments. Thanks go to Rafael Ferrer and Yuri Kudryavtsev at the LISOL facility, Tetsuo Sonoda and Michiharu Wada at RIKEN, Hideki Tomita from Nagoya and Nathalie Lecesne at GANIL. I also want to express my gratitude to my german supervisor Prof. Klaus Wendt and his group, as many of these opportunities and further experiments at Mainz were set in motion through their efforts. Thanks go to his current and former group members for their contributions, discussions as well as some wicked kicker games. Great thanks go to Sebastian Raeder, without whom the experiments in Mainz likely would not have been that successful.

Furthermore, i am grateful to the local staff of the mechanical and electrical workshop, who have brought my designs and ideas into reality and helped greatly during the move to IGISOL 4. I also want to thank the secretaries for their kind support and for not getting fed up with all my equipment orders and other administrative needs.

Cheers to Sebastian Rothe for the late night brainstorming sessions on laser construction and cheers as well to my conspirators for galactic domination Tommi and Tobias - ‘‘For the swarm!’’.

Ich bedanke mich bei meiner Familie und meinen Großeltern für die langjährige Unterstützung und Interesse an meinem Fortschritt und Wohlergehen. Danke auch an meine Frau für die willkommene Abwechslung von der Arbeitsroutine ‘‘完了! 牛逼了！’’.

LIST OF INCLUDED ARTICLES

This thesis is based on the six publications listed below. The author had a major contribution to experiment, analysis and writing of articles I and IV and is the main author for publications II, III, V and VI. The author has been involved in several international experiments. These include laser spectroscopic studies on thorium, actinium and plutonium at the University of Mainz, first laser ionization tests with the new Ti:sapphire laser system in GANIL, the comparison of a dye and Ti:sapphire laser system at LISOL (Article I), first tests of in-jet laser ionization of niobium with Ti:sapphire lasers at the PALIS prototype system at RIKEN and involvement in the setting up of an injection-locked Ti:sapphire laser at the University of Nagoya. Furthermore, the author has won the 2013 LA^3NET prize, in part due to the contribution to these experiments.

Article I: *Performance of a high repetition pulse rate laser system for in-gas-jet laser ionization studies with the leuven laser ion source @ LISOL.*
R. Ferrer, V. T. Sonnenschein, B. Bastin, S. Franchoo, M. Huyse, Yu. Kudryavtsev, T. Kron, N. Lecesne, I.D. Moore, B. Osmond, D. Pauwels, D. Radulov, S. Raeder, L. Rens, M. Reponen, J. Roßnagel, H. Savajols, T. Sonoda, J.C. Thomas, P. Van den Bergh, P. Van Duppen, K. Wendt, and S. Zemlyanoy.
NIM B **291**, 29 – 37, 2012.

Article II: *Intracavity Frequency Doubling and Difference Frequency Mixing for Pulsed ns Ti:sapphire Laser Systems at On-line Radioactive Ion Beam Facilities*
V. Sonnenschein, I. D. Moore, I. Pohjalainen, M. Reponen, S. Rothe and K. Wendt.
Accepted for publication (JPS Conf. Proc., 2014).

Article III: *Characterization of a dual-etalon Ti:sapphire laser via resonance ionization spectroscopy of stable copper isotopes.*
V. Sonnenschein, I. D. Moore, H. Khan, I. Pohjalainen and M. Reponen.
Hyperfine Interactions **227**, 113-123, 2014.

Article IV: *Resonance ionization spectroscopy of thorium isotopes - towards a laser spectroscopic identification of the low-lying 7.6 eV isomer of ^{229}Th.*
S. Raeder, V. Sonnenschein, T. Gottwald, I. D. Moore, M. Reponen, S. Rothe, N. Trautmann, and K. Wendt.
J. Phys. B **44**, 165005, 2011.

Article V: *The search for the existence of ^{229m}Th at IGISOL.*
V. Sonnenschein, I.D. Moore, S. Raeder, A. Hakimi, A. Popov, and K. Wendt.
Eur. Phys. J. A. **48**, 52, 2012.

Article VI: *Determination of the ground-state hyperfine structure in neutral ^{229}Th.*
V. Sonnenschein, S. Raeder, A. Hakimi, I. D. Moore and K.Wendt
J. Phys. B **45**, 165005, 2012.

LIST OF FIGURES

LIST OF TABLES

CONTENTS

1 INTRODUCTION

In recent years laser ion sources (LIS) have continued to gain traction at radioactive ion beam (RIB) facilities, not only for their competitive ionization efficiency but also for their highly selective nature [1]. The multi-step resonant excitation and ionization with tunable laser systems uses the ''fingerprint'' of electronic levels in the atom to provide element selective and in some cases even isotopic or isomeric selective ionization. The purity of the resulting ion beams is advantageous for many subsequent experiments. At the ISOLDE facility at CERN the laser ion source RILIS is now employed for more than 50% of the beam time [2].

An overview of the currently existing and planned LIS at RIB facilities around the world is shown in Fig. 1. With the exception of the LISOL facility in Belgium and the FURIOS ion source at the IGISOL facility in Finland, which use a buffer gas-filled stopping cell, the remaining existing LIS are based on a hot-cavity source.

The main benefit of hot-cavity sources is the use of thick targets resulting in high production rates of exotic isotopes. Drawbacks to this method are the relatively long release time through a diffusion and effusion process for some elements as well as losses through chemical reactions. This limits experimental studies of short-lived isotopes as well as refractory or reactive elements.

The complementary approach, called IGISOL (Ion Guide Isotope Separation On-Line), uses a thin target, stopping the recoil products directly in a low pressure (50-500 mbar) noble gas filled chamber. Release of the products happens through supersonic expansion of the gas at a nozzle exit. Using ultra-pure helium prevents losses through chemical reactions and with a small stopping cell fast release of the order of a few ms can be achieved. A recent review of three decades of gas cell development in Jyväskylä may be found in [3].

A third approach will be implemented in the near future at RIKEN with the PALIS (Parasitic Laser Ion Source) [4] facility. Pre-separated high energy (>100 MeV/u) ions from an in-flight fragment separator will be stopped using a degrader and a high pressure (>1 bar) gas cell. From there the isotopes will be laser ionized and extracted via gas flow and a radiofrequency (RF) sextupole ion guide (SPIG). The gas cell is positioned so as not to disturb the main beam for

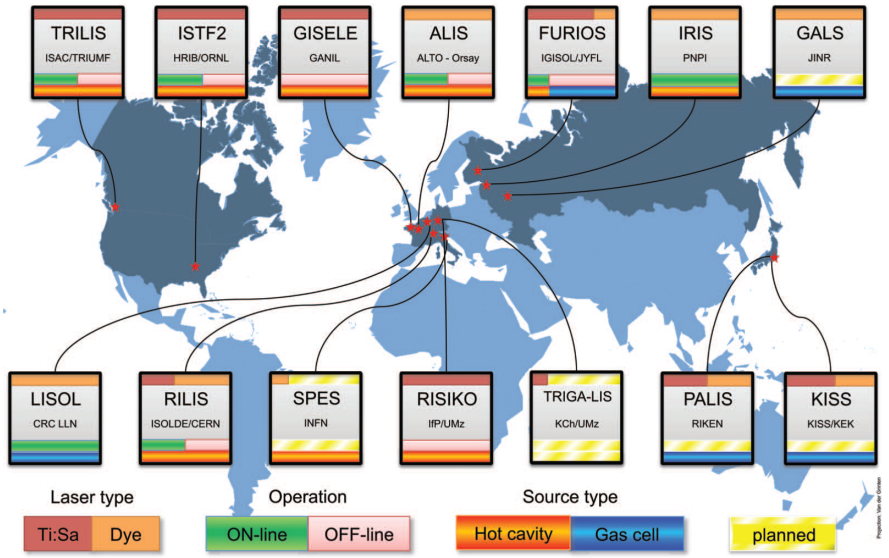

FIGURE 1 International facilities for on- and offline studies of exotic isotopes using laser ion sources. Figure taken from [2], based on an updated version of Sebastian Rothe's original figure at the 2012 DPG meeting.

other experiments. This ''parasitic'' arrangement will allow for experiments at RIKEN during a large portion of the total beamtime.

Laser ionization in combination with the IGISOL approach has been pioneered at the LISOL facility, (Louvain-la-Neuve, Belgium). Re-neutralisation of laser ions by the plasma in the gas cell created by the primary cyclotron beam proved to be a major hindrance for the success of this approach. This was finally solved by the development of a new dual-chamber gas cell design [5], which was also employed in Article I [6].

In-source laser spectroscopy can be performed both in gas cell and hot cavity sources. With the high efficiency of this process first low-resolution estimates of isotopic shifts and hyperfine structure of the element of interest can be obtained, limited by the Doppler broadening or pressure broadening of the atomic transition.

A further increase in selectivity is possible with the LIST (Laser Ion Source and Trap) method [7], which has been successfully applied at ISOL [8], LISOL [9] and IGISOL [10] facilities. Background ions are deflected with a repeller electrode. Subsequent laser ionization in a RF multipole guiding structure yields ultra-pure beams with high beam quality. This higher selectivity however comes at the cost of efficiency. The spread of the atomic beam before reaching the laser interaction region leaves only a small percentage of the population accessible to the LIST. Additionally, the high velocity of the atoms reduces the interaction time with the laser, so that even at laser pulse repetition rates of 10 kHz the atoms may only ''see" a single laser pulse. This is a dramatic change compared to in-source laser ionization, whereby atoms may interact with a large number of pulses due to confinement in the hot cavity or the slow gas flow.

Development of laser ionization in the supersonic gas jet is an ongoing focus at IGISOL-type facilities. The divergence of the expanding gas jet can be influenced

by nozzle design as well as adjustment of the background pressure [11,12]. A well-collimated jet may reduce the aforementioned efficiency losses. Furthermore, the supersonic expansion is accompanied by a reduced gas temperature and density, providing ideal conditions for higher resolution laser spectroscopy.

The increased interest in in-source spectroscopy and in higher resolution in-gas jet spectroscopy also requires the design of laser systems more suitable for the needs of these methods. A reduction in laser linewidth, while still providing the high power levels required for saturation of the atomic transitions is required. Further increases in laser power may allow for a larger laser interaction region in the LIST approach thus improving the efficiency.

As seen in Fig. 1 the field of laser ionization at RIB facilities is an international endeavour with many competing institutes. This competition has however not hindered collaborative efforts. IGLIS-NET, for example, is an international network for exchange of information related to In-Gas Laser Ionization and Spectroscopy [13]. In a broader context of laser-based applications at accelerators LA^{3}NET is an EU funded training program for young researchers and regular topical workshops and international conferences are held [14]. Article I, as shown in the following section, further highlights the more direct impact of these collaborations with an experiment involving the personnel and material contributions from several of the aforementioned institutes. The article also motivates some of the developments discussed in this thesis, such as the narrowband Ti:sa laser for in-source spectroscopy and the injection-locked Ti:sa for high-resolution spectroscopy in the gas jet.

The rest of the thesis is organized as follows. Chapter 2 contains the theoretical background needed for the topics covered in this thesis. The foundations of laser spectroscopy, light propagation in optical media, the non-linear processes for higher harmonic generation, the rate equations governing the dynamics of the laser as well as the frequency selective elements of the laser resonator are all presented. Chapter 3 provides an overview about the laser system at the IGISOL facility and includes Article II, detailing the implementation of intra-cavity second harmonic generation and difference frequency mixing, the latter providing access to a frequency domain previously accessible primarily to dye laser systems.

The experimental results are presented in chapters 4-7. Chapter 4 discusses the setup of a grating-based Ti:sapphire laser and its application to a search for a laser ionization scheme of samarium. The development of a dual-etalon Ti:sapphire laser with reduced linewidth optimized for in-source spectroscopy is discussed in chapter 5 along with Article III. Furthermore the chapter provides a thorough explanation of the new Fabry-Pérot Interferometer system for more accurate wavelength calibration. Chapter 6 focuses on the high resolution injection-locked Ti:sapphire laser as well as showcasing its performance on the elements copper, actinium and plutonium. Chapter 7 is dedicated to the search for the elusive isomer of the isotope ^{229}Th, covered in articles IV-VI, after which a short summary of the thesis results and outlook for future experiments is given.

1.1 Article I

Article I, published in *Nuclear Instruments and Methods in Physics Research Section B* volume 291 (2012), pages 29-37, highlights the collaborative nature of the in gas-cell laser ionization community. An experiment was performed at LISOL to compare the performance of the medium repetition-rate dye laser system with the high repetition-rate Ti:sapphire system presented in this thesis. The comparison was made for cobalt (off-line) and copper (off-line and on-line) and a first on-line demonstration of in gas-jet ionization of ^{59}Cu was accomplished. The article is shown in the following 9 pages (print version only).

2 THEORY

2.1 Laser spectroscopy

The theoretical background of the interaction between light and the atomic system is well established. This section will provide only the basic information necessary to understand the experimental studies highlighted in this work. Further information may be found in textbooks, for example in [15, 16].

2.1.1 Atomic structure

The electronic states in atoms can be described in an orbital model. The orbital wave functions describe the probability distribution of the electron positions and are eigenstates of the atomic Hamiltonian, with the states defined by their respective quantum numbers n, l, m_l and m_s. The principal quantum number n is a positive integer, the angular momentum quantum number l can assume values from $l = 0, 1, \ldots n-1$ and the magnetic quantum number from $m_l = -l, -l+1, \ldots, l-1, l$. Furthermore the spin of the electron $s = 1/2$ can assume values $m_s = \pm 1/2$. The spin-orbit interaction between the angular momentum $\vec{l}$ and the electron spin $\vec{s}$ leads to a coupling to the total angular momentum $\vec{j} = \vec{l} + \vec{s}$ with values $j = |l - s| \ldots l + s - 1, l + s$.

For multi-electron systems two different possibilities exist for coupling. The first is the so-called L-S or Russell-Saunders coupling. Here the spins $\vec{s_i}$ of the electrons couple to a total spin $\vec{S}$ and the angular momenta $\vec{l}$ to $\vec{L}$, which then couple to $\vec{J} = \vec{L} + \vec{S}$. The coupled states are then referred to using the atomic term symbol

$$^{2S+1}L_J. \tag{1}$$

The angular momentum L is often designated with letters using the relation $L = (0, 1, 2, 3) \longleftrightarrow L = (S, P, D, F)$. For heavy elements the spin-orbit interaction increases and the so-called j-j coupling is preferred. In j-j coupling first the spins $\vec{s_i}$ and angular momenta $\vec{l_i}$ of each electron couple to $\vec{j_i} = \vec{l_i} + \vec{s_i}$, which then couple to

the total spin $\vec{J} = \sum_i \vec{j_i}$. In most cases an intermediate between L-S and j-j coupling is required for an accurate description.

Conservation of angular momentum and symmetry considerations lead to the selection rules, which restrict the possible optical electric dipole transitions between two states. In general $\Delta l = \pm 1$ and $\Delta m_l = 0, \pm 1$ and $\Delta J = 0, \pm 1$ have to hold, except $J = 0 \rightarrow 0$, which is not allowed. Further for L-S coupling $\Delta L = 0, \pm 1$ and $\Delta S = 0$. This does not mean that all optical transitions have to obey these rules, but electric dipole forbidden transitions are generally several orders of magnitude weaker (or commuted by multi-photon transitions).

Without further interactions a state with total angular momentum J consists of $2J + 1$ energy degenerate sublevels with quantum numbers $m_j = -J, -J + 1, \ldots J - 1, J$. An atomic ensemble at a temperature T follows the Boltzmann distribution, so that the population of an excited state can be estimated using

$$N_j = N_0 \cdot \frac{g_j}{g_0} \cdot e^{-\frac{E_j}{k_b T}}. \tag{2}$$

N_0 and N_j are the populations of the ground state and the excited state j, while g_0 and g_j are their respective degrees of degeneracy. E_j is the energy level of state j and k_b is the Boltzmann constant. If n states contribute to the distribution the probability p_j to be in the excited state can be found by normalizing:

$$p_j = \frac{N_j}{\sum_{i=0}^{n} N_i} = \frac{g_j \cdot e^{-\frac{E_j}{k_b T}}}{\sum\limits_{i=0}^{n} g_i \cdot e^{-\frac{E_j}{k_b T}}}. \tag{3}$$

For high temperatures the atomic ground state may thus not be the state with the largest population, if an excited state has a higher degree of degeneracy.

2.1.2 Light-atom interaction

The interaction of the light field with the electronic states can be described through the interaction Hamiltonian

$$H_{\text{int}} = -\mathbf{d} \cdot \mathbf{E}. \tag{4}$$

Models describing this interaction for a two-level system are, for example, the Jaynes Cummings model [17] (also known as the dressed atom model) or the Optical Bloch Equations [18] (OBE). In resonance ionization spectroscopy one has to consider the interaction of the light fields with multiple atomic levels. A thorough description of the multi-step laser ionization process may be found in [19]. For simplicity the discussion here is limited to a simple two-level atom interacting with one laser as described by the OBE. The results for such a system can often be applied at least qualitatively to the more general case.

Assuming an atom with two states $|1\rangle$ and $|2\rangle$ with resonance frequency $\omega_{21} = (E_2 - E_1)/\hbar$ and a laser frequency ω_L with detuning $\delta = \omega - \omega_{21}$ the

excited state population ρ_{22} in steady state conditions is given as

$$\rho_{22} = \frac{S_0/2}{1 + S_0 + 4\delta^2/\gamma^2} \tag{5}$$

$$= \frac{S_0}{2(S_0+1)} \cdot \frac{1}{1 + 4\delta^2/\gamma'^2}. \tag{6}$$

Here γ is the spontaneous decay rate of state $|2\rangle$ and $S_0 = I/I_{\text{sat}}$ is the resonant saturation parameter. I_{sat} is the saturation intensity

$$I_{\text{sat}} = \frac{\pi hc}{3\lambda^3\tau}, \tag{7}$$

where λ is the laser wavelength and τ the excited state lifetime. The profile of ρ_{22} is a Lorentzian function with full width at half maximum (FWHM) of

$$\gamma' = \gamma \cdot \sqrt{1 + S_0}, \tag{8}$$

which depends on the intensity of the laser. This effect is known as saturation broadening.

2.1.3 Line broadening effects

In addition to the aforementioned saturation broadening, the observed transition linewidth can be affected by Doppler- and pressure broadening effects as well as by the linewidth of the laser.

Movement of the atom causes a velocity dependent frequency shift, in the non-relativistic approximation given by

$$f' = f_0(1 \pm \frac{v}{c}), \tag{9}$$

with the positive sign in the case when the emitter moves towards the observer and the negative sign in the reversed situation. The thermal motion described by the Maxwell-Boltzmann distribution thus causes a spread of the frequencies observed by the atoms. The probability distribution for the frequencies is

$$P(f)df = \sqrt{\frac{mc^2}{2\pi\, k_b T f_0^2}} \cdot \exp\Big(-\frac{mc^2(f-f_0)^2}{2\, k_b T f_0^2}\Big)\, df. \tag{10}$$

This is a Gaussian profile with standard deviation

$$\sigma_D = f_0\sqrt{\frac{k_b T}{mc^2}} \tag{11}$$

or full width at half maximum

$$\Delta_{\text{FWHM}} = f_0\sqrt{\frac{8\, k_b T \ln 2}{mc^2}}. \tag{12}$$

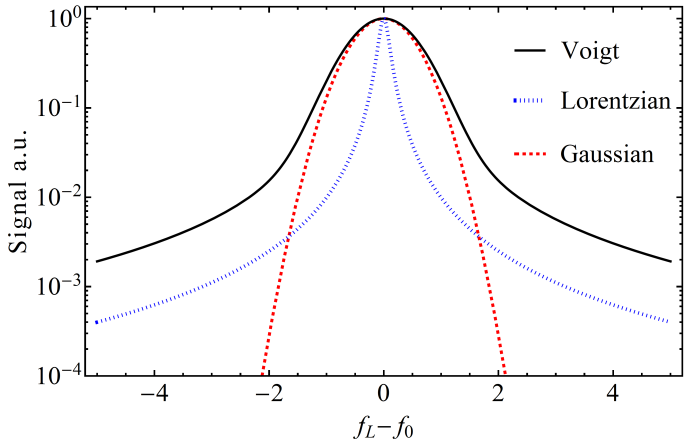

FIGURE 2 Comparison of Lorentzian, Gaussian and Voigt profiles. The widths of Gaussian and Lorentzian were assumed at a ratio of 10:1. Note the logarithmic scale.

To get the shape of the transition line profile the convolution of the saturated Lorentzian curve of Eq. 5 and the Gaussian profile of Eq. 10 has to be performed

$$V_{\text{atom}}(f) = \int L(f - f')G(f')df'. \tag{13}$$

The convolution of a Lorentzian and a Gaussian is known as the Voigt profile which has to be evaluated numerically. The FWHM of the Voigt profile can be approximated by [20]

$$\Delta f_V = 0.5346\,\Delta f_L \sqrt{0.2166\Delta f_L^2 + \Delta f_G^2}, \tag{14}$$

where Δf_L and Δf_G are the Lorentzian and Gaussian FWHM, respectively. A comparison of the Voigt profile with Gaussian and Lorentzian is shown in Fig. 2. The shape of the Voigt is close to the Gaussian profile in the central region, but the tails of the peak follow the Lorentzian shape.

The frequency spectrum of pulsed laser systems can often be approximated by a Gaussian. For two Gaussians with widths Δ_1 and Δ_2 the convolution is again a Gaussian with width

$$\Delta = \sqrt{\Delta_1^2 + \Delta_2^2}. \tag{15}$$

A further contribution to the linewidth, especially important for laser spectroscopy in a gas cell is the pressure broadening. Collisions of the atoms with the buffer gas can be either elastic or inelastic. Inelastic collisions lead to a depopulation of the excited state. This mainly occurs whenever resonant energy transfer is possible between the excited state of the atom and states of the collision partner and is as such critically dependent on the electronic configurations. Elastic scattering, also called ''phase-perturbing collision'' may cause both a broadening as well as a shift of the transition frequency. The broadening γ_p as well as the shift Δ_p are related

to the scattering cross sections σ

$$\gamma_p = 2n_{\text{gas}}\langle(\sigma_{b,el} + \sigma_{b,inel})v\rangle \tag{16}$$
$$\Delta_p = n_{\text{gas}}\langle(\sigma_{s,el})v\rangle. \tag{17}$$

The cross sections are averaged over the relative velocity v between the two atoms. Noticeable is the direct proportionality to the gas density n_{gas}. For helium gas at 300 K typical values are $\gamma_p \sim \Delta_p \sim$10 MHz/mbar [16].

2.1.4 Hyperfine structure

Thus far the impact of the atomic nucleus has been ignored. The interaction between the magnetic dipole and electric quadrupole moment of the nucleus with the electron leads to a further splitting of the levels. The nuclear spin $\vec{I}$ couples to the angular momentum $\vec{J}$ to produce the new quantum number F with $\vec{F} = \vec{I} + \vec{J}$. The energy shifts of the states are given by

$$\Delta E_{\text{hfs}} = \frac{A \cdot C}{2} + \frac{B}{4}\frac{3/2C(C+1) - 2I(I+1)J(J+1)}{I(2I-1)J(2J-1)} \tag{18}$$

with the so-called Casimir factor

$$C = F(F+1) - J(J+1) - I(I+1). \tag{19}$$

The hyperfine parameters may be written as follows:

$$A = \frac{\mu_I B_e(0)}{IJ} \tag{20}$$
$$B = eQ_s\langle\frac{\partial^2 V}{\partial z^2}\rangle. \tag{21}$$

The magnetic hyperfine coupling constant A describes the interaction between the magnetic dipole moment of the nucleus μ_I and the magnetic field at the centre of the nucleus $B_e(0)$ created by the electron. The second term B, the electric quadrupole coupling constant, accounts for the interaction between the electric quadrupole moment and the electric field gradient. For $I \leq 1/2$ or $J \leq 1/2$ the second term in Eq. 18 vanishes.

The intensity distribution of the hyperfine components for a transition from J to J' can be given using the 6-j symbol as [21]

$$S_{FF'} = S(F \to F') = \frac{(2F+1)(2F'+1)}{2I+1}\begin{Bmatrix} J' & F' & I \\ F & J & 1 \end{Bmatrix}^2 \tag{22}$$

with the combined intensity normalized to 1

$$\sum_{F,F'} S_{FF'} = 1. \tag{23}$$

2.1.5 Isotope Shift

The change of the transition frequency or the centre of gravity of a hyperfine structure from one isotope with mass number A to another with A' is called the isotope shift. This frequency shift can be separated into a mass related term, the mass shift, and a term related to the charge distribution, the field shift

$$\delta\nu_{\mathrm{IS}}^{AA'} = \delta\nu_{\mathrm{MS}}^{AA'} + \delta\nu_{\mathrm{FS}}^{AA'}. \tag{24}$$

The mass shift may be further sub-divided into the normal mass shift (NMS) and the specific mass shift (SMS)

$$\delta\nu_{\mathrm{MS}}^{AA'} = \delta\nu_{\mathrm{NMS}}^{AA'} + \delta\nu_{\mathrm{SMS}}^{AA'}. \tag{25}$$

Both the NMS and the SMS are related to the change in reduced mass of the system

$$\delta\nu_{\mathrm{NMS}}^{AA'} = \frac{A'-A}{A'A} \cdot m_e\nu \tag{26}$$

$$\delta\nu_{\mathrm{SMS}}^{AA'} = \frac{A'-A}{A'A} K_{\mathrm{SMS}}, \tag{27}$$

where m_e is the electron mass, ν is the transition frequency for an infinitely heavy nucleus and K_{SMS} is a term related to electron correlations. The NMS can be accurately calculated, the SMS however becomes difficult to compute for elements heavier than Li.

The field shift (also knows as the volume effect) can be given as

$$\delta\nu_{\mathrm{FS}}^{AA'} = \frac{Ze^2}{6\epsilon_0 h} \cdot \Delta|\Psi(0)|^2 \cdot \lambda^{AA'}, \tag{28}$$

$$= F \cdot \lambda^{AA'}. \tag{29}$$

The field shift factor F scales with the atomic or electron number Z and $\Delta|\Psi(0)|^2$, the change in electron density at the nucleus caused by the atomic transition. The nuclear parameter $\lambda^{AA'}$ is a power series of the mean-square charge radius and is known as the Seltzer moment [22]

$$\lambda^{AA'} = \delta\langle r^2\rangle^{AA'} + \frac{C_2}{C_1}\delta\langle r^4\rangle^{AA'} + \frac{C_3}{C_1}\delta\langle r^6\rangle^{AA'} + \ldots \tag{30}$$

$$\approx K(A)\delta\langle r^2\rangle^{AA'}, \tag{31}$$

where the factors C_2/C_1, C_3/C_1,... describe the contribution from the higher order radial moment. A compilation of the parameters C_i is found for example in [22,23] and the correction factor K in [24]. The factor is close to unity for most elements but is important in the heavier elements as discussed at the end of chapter 6. The

full expression for the isotope shift can then be given as

$$\delta\nu_{\mathrm{IS}}^{AA'} = \frac{A'-A}{A'A}(K_{\mathrm{SMS}} + m_e\nu) + F\lambda^{AA'} \tag{32}$$

$$= M\frac{A'-A}{A'A} + F \cdot K(A) \cdot \delta\langle r^2\rangle^{AA'} \ . \tag{33}$$

The isotope-independent factors M and F may be calculated for light nuclei, but for heavy nuclei only approximate numerical simulations are possible and information may be available only for a few optical transitions. It is however possible to relate the atomic factors for one transition to another using the King plot method [25]. The isotope shift equation may be multiplied by a modification factor

$$\mu = \frac{AA'}{A'-A} \tag{34}$$

resulting in the equations for two transitions i and j

$$\mu\,\delta\nu_i^{AA'} = M_i + F_i \cdot K(A) \cdot \mu\,\delta\langle r^2\rangle^{AA'} \tag{35}$$

$$\mu\,\delta\nu_j^{AA'} = M_j + F_j \cdot K(A) \cdot \mu\,\delta\langle r^2\rangle^{AA'}, \tag{36}$$

from which the factor $K(A) \cdot \mu\,\delta\langle r^2\rangle^{AA'}$ can be eliminated resulting in the equation for a straight line

$$\mu\,\delta\nu_j^{AA'} = \frac{F_j}{F_i} \cdot \mu\,\delta\nu_i^{AA'} + (M_j - \frac{F_j}{F_i}M_i) \tag{37}$$

with slope F_j/F_i and intercept $M_j - M_iF_j/F_i$. An additional factor for a standard reference pair of isotopes

$$\xi = \mu \cdot \frac{A'_{\mathrm{ref}} - A_{\mathrm{ref}}}{A'_{\mathrm{ref}}A_{\mathrm{ref}}} \tag{38}$$

can be included for presentation purposes.

2.2 Light propagation in optical systems

The calculation of beam propagation through an optical system is an important tool. It can help in choosing the right combination of lenses for collimation of a laser beam over a long distance to a target area, or to estimate the light intensity at the minimal focus diameter in order to avoid reaching the damage threshold of an optical coating. Another useful application is the calculation of resonator modes and optimization of laser mode-matching.

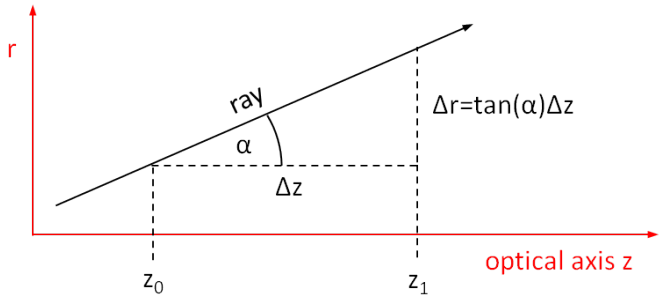

FIGURE 3 Propagation of a ray of light along the optical axis in free space.

2.2.1 Matrix formalism for ray optics

In ray optics or geometric optics the propagation of light is simplified by assuming that the light propagates in straight lines perpendicular to the wavefront. This assumption is valid as long as the dimensions of the physical system are much larger than the wavelength of light. Effects such as interference or diffraction however can not be described with this approach. For simplicity we assume that the axis of the optical system lies in the z-direction. A ray can then be defined by the ray vector $\binom{r(z)}{\alpha(z)}$ composed out of the distance to the optical axis of the system $r(z)$ and its angle $\frac{dr}{dz} = r'(z) = \alpha(z)$.

In the simple case of free space propagation as shown in Fig. 3 the angle of the ray does not change and the relations between the ray parameters after a distance Δz are

$$r(z_1) = r(z_0) + \tan(\alpha)\Delta z \approx r(z_0) + \alpha\Delta z \tag{39}$$

$$\alpha(z_0) = \alpha(z_1). \tag{40}$$

The approximation assumes that the angles with respect to the optical axis are small, which is also known as the ''paraxial approximation''. In this case the propagation can also be written in matrix form,

$$\begin{pmatrix} r(z_1) \\ \alpha(z_1) \end{pmatrix} = \begin{pmatrix} 1 & \Delta z \\ 0 & 1 \end{pmatrix} \cdot \begin{pmatrix} r(z_0) \\ \alpha(z_0) \end{pmatrix} = \begin{pmatrix} r(z_0) + \alpha\Delta z \\ \alpha(z_0) \end{pmatrix}. \tag{41}$$

This matrix and similar matrices describing other optical elements are often called the ray-transfer matrix or simply the ABCD matrix. A more complicated example, though one that can be used to describe many possible configurations, is the incidence of a beam at an arbitrary angle and refraction at the curved intersection between two media with refractive indices n_1 and n_2. This example can be used to calculate the matrix for a Brewster-cut surface or the transmission of a pump beam through a curved mirror at a non-normal angle of incidence. The situation is visualized in Fig. 4. A central ray (dashed black line) has an angle θ_1 with respect to the surface normal of the curved surface. The propagation of this central ray defines the optical axis of the system. This implies a change of the direction of the optical axis at the intersection. We are now interested in a second ray offset

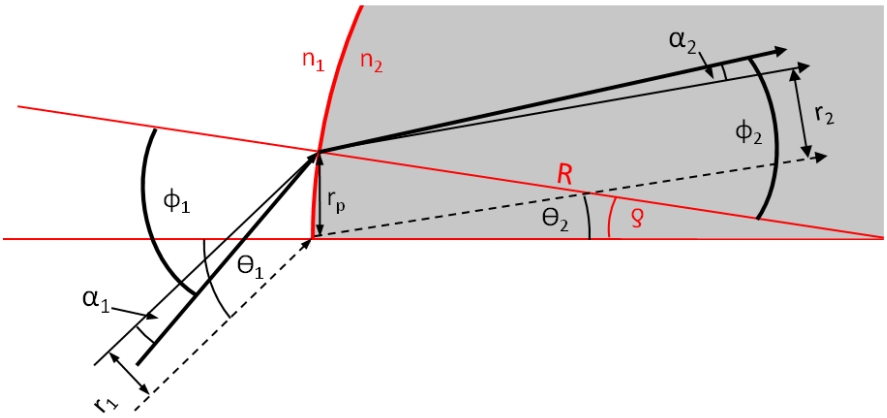

FIGURE 4 Refraction of a ray at a curved surface between two dielectric media with indices n_1 and n_2 and radius of curvature R.

by r_1 and incident at a slightly different angle $\theta_1 + \alpha_1$ and want to describe the properties of this ray after refraction with respect to the changed optical axis. The surface of the intersection has a curvature of radius R with $r_1 \ll$ R.

The refraction at the surface can be described by Snell's Law so for the central ray

$$n_1 \sin(\theta_1) = n_2 \sin(\theta_2). \tag{42}$$

For the second ray the projection on the surface directly yields the relation between r_1 and r_2 immediately after crossing the surface

$$r_p = \frac{r_1}{\cos(\theta_1)} = \frac{r_2}{\cos(\theta_2)} \tag{43}$$

$$r_2 = \frac{\cos(\theta_2)}{\cos(\theta_1)} \cdot r_1 = \frac{\cos(\arcsin(\frac{n_1}{n_2}\sin(\theta_1))}{\cos(\theta_1)} \cdot r_1\,. \tag{44}$$

For the angle relation the change of the surface normal due to the curvature as well as the different starting angle have to be taken into account. With the angle of incidence given by $\phi_1 = \theta_1 + \alpha_1 + \rho$ and the refracted angle by $\phi_2 = \theta_2 + \alpha_2 + \rho$ Snell's law can be applied again

$$n_1 \sin(\phi_1) = n_2 \sin(\phi_2) \tag{45}$$

$$n_1 \sin(\theta_1 + \alpha_1 + \rho) = n_2 \sin(\theta_2 + \alpha_2 + \rho). \tag{46}$$

Using the addition theorem $\sin(a + b) = \sin(a)\cos(b) + \cos(a)\sin(b)$ and the approximation for small angles $\sin(\alpha, \rho) \approx \alpha, \rho$ and $\cos(\alpha, \rho) \approx 1$ gives

$$n_1(\sin(\theta_1) + \cos(\theta_1)(\alpha_1 + \rho)) = n_2(\sin(\theta_2) + \cos(\theta_2)(\alpha_2 + \rho)). \tag{47}$$

After inserting Eq. 42 into 47 and using $\rho \approx r_p/R = r_1/(R\cos(\theta_1))$ the relation

for the angle α_2 can be extracted:

$$\alpha_2 = \frac{n_1 \cos(\theta_1)}{n_2 \cos(\theta_2)} \cdot \alpha_1 + \frac{n_1 \cos(\theta_1) - n_2 \cos(\theta_2)}{n_2 \, R \cos(\theta_1) \cos(\theta_2)} \cdot r_1. \tag{48}$$

The resulting matrix equation is then given by

$$\begin{pmatrix} r_2 \\ \alpha_2 \end{pmatrix} = \begin{pmatrix} \frac{\cos(\theta_2)}{\cos(\theta_1)} & 0 \\ \frac{n_1 \cos(\theta_1) - n_2 \cos(\theta_2)}{n_2 R \cos(\theta_1) \cos(\theta_2)} & \frac{n_1 \cos(\theta_1)}{n_2 \cos(\theta_2)} \end{pmatrix} \cdot \begin{pmatrix} r_1 \\ \alpha_1 \end{pmatrix}. \tag{49}$$

Using the matrix formalism the propagation of a ray through a complex optical system can be simply calculated by performing matrix multiplication. A collection of often used matrices is given in Tab. 1. For the elements that are not normal to the optical axis of the system it is important to distinguish between the ''tangential'' and ''sagittal'' planes. The tangential plane also referred to as the ''plane of incidence'', or ''meridional'' plane is spanned by the incoming ray and the surface normal of the optical element. The sagittal plane is orthogonal to the tangential plane. For a ray in the tangential plane a lens will appear perspectively shortened leading to an effective shorter focal length. This is also noticeable in the examples given in Table 1, where for the tangential plane matrices the radius R is multiplied by a factor $\cos(\theta)$, which is missing for the sagittal plane.

Formulations of the matrices can be found in many optics books, for example in [26] or [27], however one has to be careful as to the used conventions. In [26] the ray vector is defined differently, using $n(z) \cdot \alpha(z)$ instead of $\alpha(z)$, so that the local refractive index is included in the second component of the vector, which changes the definition of the matrices as well. Furthermore the definition of the sign of the radius of curvature is opposite compared to that given in the example here.

2.2.2 Gaussian beams

To more accurately describe the evolving shape of a laser beam, ray optics are insufficient. In ray optics the focal spot could become infinitesimally small giving rise to unphysical singularities. These can be eliminated using wave optics. In free space the wave equation for the electric field is given by

$$\nabla^2 \vec{E} - \frac{1}{c^2} \frac{\partial^2}{\partial t^2} \vec{E} = 0. \tag{50}$$

Laser beams are highly directional and have in most cases only slowly varying properties along the direction of propagation. For simplicity we choose a wave with a single frequency ω and wave vector $k = 2\pi/\lambda$ propagating along the z-axis so that the solution will be of the form

$$\vec{E}(r,t) = \vec{E}(\vec{r}) \cdot \exp[(i(kz - \omega t))]. \tag{51}$$

TABLE 1 ABCD matrices or ray transfer matrices for often used optical elements.

Description	**Matrix**
Propagation over distance d in medium with refractive index n	$\begin{pmatrix} 1 & d \\ 0 & 1 \end{pmatrix}$
Thin lens with focal length f - normal incidence	$\begin{pmatrix} 1 & 0 \\ -\frac{1}{f} & 1 \end{pmatrix}$
Refraction at a curved surface with radius R, going from refractive index n_1 to n_2 with angle of incidence θ_1 - tangential plane	$\begin{pmatrix} \frac{\cos(\theta_2)}{\cos(\theta_1)} & 0 \\ \frac{n_1\cos(\theta_1)-n_2\cos(\theta_2)}{n_2 R\cos(\theta_1)\cos(\theta_2)} & \frac{n_1\cos(\theta_1)}{n_2\cos(\theta_2)} \end{pmatrix}$
Refraction at a curved surface with radius R, going from refractive index n_1 to n_2 with angle of incidence θ_1 - sagittal plane	$\begin{pmatrix} 1 & 0 \\ \frac{n_1\cos(\theta_1)-n_2\cos(\theta_2)}{n_2 R} & \frac{n_1}{n_2} \end{pmatrix}$
Reflection at a curved surface with radius R with angle of incidence θ - tangential plane	$\begin{pmatrix} 1 & 0 \\ \frac{-2}{R\cos(\theta)} & 1 \end{pmatrix}$
Reflection at a curved surface with radius R with angle of incidence θ - sagittal plane	$\begin{pmatrix} 1 & 0 \\ \frac{-2\cos(\theta)}{R} & 1 \end{pmatrix}$

The ''fast'' fluctuations are described by a plane wave in the z direction and a ''slowly'' varying term $E(r)$ that describes changes in diameter and amplitude. Inserting Eq. 51 into 50 yields

$$(\frac{\partial^2}{\partial x^2}+\frac{\partial^2}{\partial y^2}+\frac{\partial^2}{\partial z^2}+2ik\frac{\partial}{\partial z})\vec{E}(r)=0. \tag{52}$$

We now assume that the field varies only gradually along the z-axis

$$\left|\frac{\partial^2 E(r)}{\partial z^2}\right| \ll \left|2k\frac{\partial E(r)}{\partial z}\right| . \tag{53}$$

This is the wave optics equivalent of the already discussed paraxial approximation, which is valid as long as the beam travels almost parallel along the beam axis. Applying this approximation leads to the paraxial wave equation:

$$(\frac{\partial^2}{\partial x^2}+\frac{\partial^2}{\partial y^2}+2ik\frac{\partial}{\partial z})\vec{E}(x,y,z)=0. \tag{54}$$

The cartesian solutions to this differential equation, applicable to laser systems without cylindrical symmetry, can be given using the Hermite polynomials

$$\begin{aligned}\vec{E}(x,y,z)=\sum_{m,n} c_{nm}\vec{E}_0\frac{\omega_0}{\omega(z)}H_m[\frac{\sqrt{2}x}{\omega(z)}]H_n[\frac{\sqrt{2}y}{\omega(z)}]\\ \cdot\exp[\frac{-x^2+y^2}{\omega^2(z)}]\exp[-i(m+n+1)\psi(z)+i\frac{k(x^2+y^2)}{2R(z)}],\end{aligned} \tag{55}$$

with m and n positive integers, H_m the m$^{\text{th}}$ order Hermite Polynomial and the other parameters defined as

$$z_R=\frac{k\omega_0}{2} \tag{56}$$

$$\omega(z)=\omega_0\sqrt{1+z^2/z_R^2} \tag{57}$$

$$R(z)=z+\frac{z_R^2}{z}=\frac{kz_R}{2z}\omega^2(z) \tag{58}$$

$$\psi(z)=\arctan(\frac{z}{z_R}) \tag{59}$$

with z_R called the Rayleigh range, $\omega(z)$ the beam waist, $R(z)$ the radius of curvature of the wavefronts and $\psi(z)$ the Gouy phase. At the coordinate $z=0$ lies the focal spot of the beam, the waist reaches its minimum value ω_0 while the radius of curvature diverges. A visualization of the behaviour of these parameters can be found in Fig. 5. At the Rayleigh range the waist increases to $\sqrt{2}$ times its minimum value, the radius of curvature diverges at the focal spot and the Gouy phase has a transition from $-\pi/2$ to $\pi/2$ with a zero-crossing at the focus.

The information about the beam properties can be encoded into a single

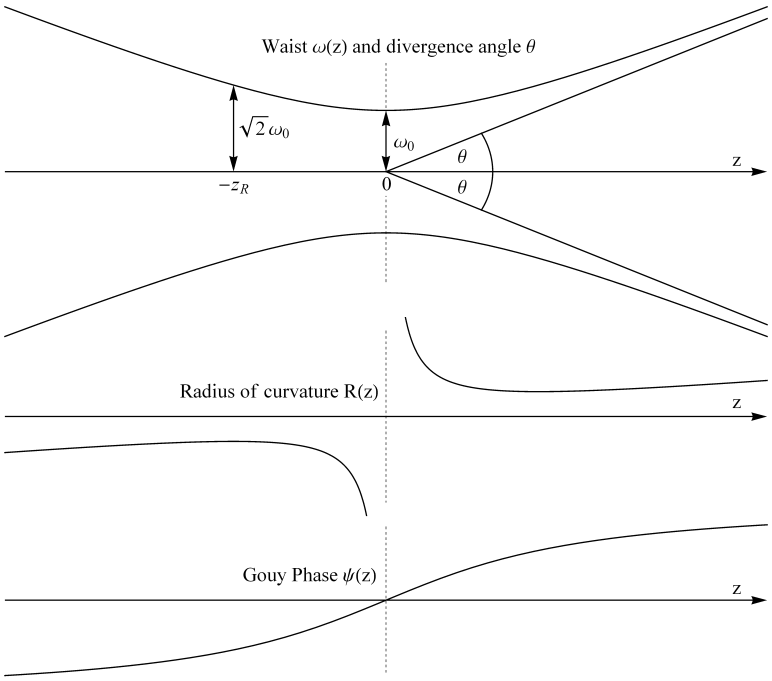

FIGURE 5 Propagation of a Gaussian beam close to the focal spot, showing the mode waist $\omega(z)$, the divergence angle θ as well as the Gouy phase $\psi(z)$.

variable called the complex beam parameter q, where

$$q(z) = z + iz_R \tag{60}$$

$$\frac{1}{q(z)} = \frac{1}{z + iz_R} = \frac{z}{z^2 + z_R^2} - \frac{iz_R}{z^2 + z_R^2} = \frac{1}{R(z)} - i\frac{\lambda}{\pi\omega^2(z)}. \tag{61}$$

For $m = n = 0$ we get

$$\vec{E}(x, y, z) = \vec{E}_0 \sqrt{\frac{2}{\pi}} \frac{q(0)}{\omega_0 q(z)} \exp(-ik\frac{x^2 + y^2}{2q(z)}) \tag{62}$$

which is also called the zero order transversal electromagnetic wave or TEM_{00} wave. This wave is often the most important one in laser systems as it has the lowest divergence and smallest possible focal spot diameter. The divergence is often given by the opening angle θ which is defined as

$$\theta = \lim_{z \to \infty} \arctan(\frac{\omega(z)}{R(z)}) \approx \frac{\lambda}{\pi\omega_0} \tag{63}$$

only depending on the wavelength and the minimum waist diameter. To describe the propagation of higher order modes a new parameter M^2, the so-called ‘‘beam

quality factor'', is introduced,

$$\theta = M^2 \frac{\lambda}{\pi \omega_0}. \tag{64}$$

For a pure Hermite-Gaussian beam of order m, n the M^2 factor is $2m+1$ in the x- and $2n+1$ in the y-direction, however in the general case the beam can be a mixture of multiple modes and the M^2 factor has to be experimentally measured. In high power laser systems a large M^2 can be useful, as the larger waist diameter reduces the maximum intensity on optical elements.

2.2.3 Matrix formalism for Gaussian beams

An interesting feature of Gaussian beams is the possibility to apply the same matrices developed for ray optics to the complex beam parameter q in order to calculate the beam properties as it passes through optical elements. The application of a ray transfer matrix $M = \begin{pmatrix} A & B \\ C & D \end{pmatrix}$ to the beam parameter is performed in the following way:

$$q_{\text{out}} = M \circ q_{\text{in}} = \frac{A \cdot q_{\text{in}} + B}{C \cdot q_{\text{in}} + D}. \tag{65}$$

A derivation of this result can be found in chapter 20 of [26]. It can be easily demonstrated that the successive application of matrices in this way is again equivalent to matrix multiplication, so that

$$M_2 \circ (M_1 \circ q) = (M_2 \cdot M_1) \circ q. \tag{66}$$

2.2.4 Resonator design

If the matrices for all elements in an optical resonator are known, the round-trip matrix M_R can be calculated. The condition for a stable cavity is that the beam parameter is reproduced after a full round trip,

$$q_{\text{in}} \stackrel{!}{=} q_{\text{out}} = M_R \circ q_{\text{in}}. \tag{67}$$

The exclamation mark above the equal sign is inserted to emphasize that this is true only for a stable resonator. This leads to the following quadratic equation for the beam parameter:

$$\frac{1}{q_{\text{in}}} = \frac{2C}{A - D \pm \sqrt{4BC + (D-A)^2}}. \tag{68}$$

As the beam parameter is assumed to be a true complex number with a negative imaginary part, the root in the above equation has to be imaginary and the positive sign has to be chosen resulting in

$$4BC + (D-A)^2 < 0. \tag{69}$$

Combining this with a further property of the round-trip matrix M_R

$$\det(M_R) = \begin{vmatrix} A & B \\ C & D \end{vmatrix}_{\text{round-trip}} = AD - BC = 1 \tag{70}$$

yields the stability condition

$$(A + D)^2 < 4. \tag{71}$$

With this the beam parameter q_{in} is defined and the properties of the mode can be calculated along the whole length of the cavity using Eq. 65.

It should be noted that the stability condition is not necessarily a requirement for laser resonators. For high power laser system often unstable resonators are preferable as they can lead to a magnification of the resonator mode for each round-trip, reducing the probability of mirror coating damage. An overview of such unstable resonators can be found for example in [28], but will not be discussed in this work.

Throughout this thesis the ABCD matrix formalism for Gaussian beams has been applied. Examples for this are the cavity-mode diameter calculations made for the grating-based Ti:sa and injection-locked Ti:sa described in Chapters 4 and 6, as well as for the mode-matching to the semi-hemispheric FPI discussed in Chapter 5.

2.3 Wave Propagation in optical media

The Maxwell equations in a medium are given by

$$\vec{\nabla} \cdot \vec{D} = \vec{\nabla} \cdot (\epsilon_0 \vec{E} + \vec{P}) = \rho \tag{72}$$

$$\vec{\nabla} \cdot \vec{B} = 0 \tag{73}$$

$$\vec{\nabla} \times \vec{E} = -\frac{\partial \vec{B}}{\partial t} \tag{74}$$

$$\vec{\nabla} \times \vec{H} = \vec{J} + \frac{\partial \vec{D}}{\partial t}, \tag{75}$$

with the relations for the fields

$$\vec{D} = \epsilon_0 \vec{E} + \vec{P} \tag{76}$$

$$\vec{H} = \mu_0 \vec{B} + \vec{M} \tag{77}$$

using the polarization $\vec{P}$ and magnetization $\vec{M}$. For an optically transparent medium we can assume that there are no currents and free charges, so that $\vec{J} = 0$ and $\rho = 0$. Furthermore we assume a non-magnetic medium $\vec{M} = 0$.

2.3.1 Fresnel equations

An electromagnetic field crossing from one optical medium to another obeys the following boundary conditions, with $\vec{n}$ the normal vector of the surface

$$\vec{n} \times (\vec{E_2} - \vec{E_1}) = 0 \tag{78}$$
$$\vec{n} \cdot (\vec{D_2} - \vec{D_1}) = 0 \tag{79}$$
$$\vec{n} \cdot (\vec{B_2} - \vec{B_1}) = 0 \tag{80}$$
$$\vec{n} \times (\vec{H_2} - \vec{H_1}) = 0. \tag{81}$$

This means that the tangential components of $\vec{E}$ and $\vec{H}$ as well as the normal components of $\vec{D}$ and $\vec{B}$ are continuous at the surface. From these boundary conditions the reflection and transmission properties of the medium may be determined. An electric field may be written as a superposition of states parallel (p-polarized) or perpendicular (s-polarized, from the german word ''senkrecht'') to the plane of incidence, with the plane of incidence spanned by the vector $\vec{n}$ and the wave vector $\vec{k}$. The electric field amplitude reflection coefficients r_p, r_s and transmission coefficients t_p, t_s for these p-polarized and s-polarized field components are given by the Fresnel equations:

$$r_p = \frac{\tan(\theta_i - \theta_o)}{\tan(\theta_i + \theta_o)} \tag{82}$$
$$r_s = \frac{\sin(\theta_i - \theta_o)}{\sin(\theta_i + \theta_o)} \tag{83}$$
$$t_p = \frac{2\sin(\theta_o)\cos(\theta_i)}{\sin(\theta_i + \theta_o)\cos(\theta_i - \theta_o)} \tag{84}$$
$$t_s = \frac{2\sin(\theta_o)\cos(\theta_i)}{\sin(\theta_i + \theta_o)}. \tag{85}$$

Here θ_i is the angle of incidence with respect to the surface normal and θ_o the angle of the refracted wave in the medium, which may be related using Snell's law, Eq. 42. The reflectivity R and transmission T for the intensity of the radiation is

$$R_{p,s} = r_{p,s}^2 \tag{86}$$
$$T_{s,p} = \frac{\tan\theta_i}{\tan\theta_o} t_{s,p}^2. \tag{87}$$

For $\theta_i + \theta_o = \pi/2$, Eq. 82 and thus R_p reaches zero, this is the case for Brewster's angle

$$\theta_B = \arctan\left(\frac{n_2}{n_1}\right). \tag{88}$$

Optical elements at Brewster's angle are often used in low gain laser systems, where even small losses have to be avoided. An example for this is the birefringent filter used for frequency selection discussed in Section 2.5.2.

2.3.2 Wave propagation in crystals and nonlinear interactions

Many atomic transition lines are in the UV or visible wavelength range and can not be directly excited by the fundamental laser light. It is therefore necessary to expand the wavelength range by frequency conversion processes. In a vacuum, electromagnetic waves do not interact with each other (below the Schwinger limit [29]), however in a nonlinear medium such interactions can occur given sufficiently high intensities. The theory for these interactions is given in the following.

Nonlinear wave equation Using the curl operator on the third Maxwell equation, Eq. 72, and combining it with the time derivative of the fourth equation yields

$$\vec{\nabla} \times \vec{\nabla} \times \vec{E} = \frac{1}{c^2} \frac{\partial^2 (\vec{E} + \vec{P}/\epsilon_0)}{\partial t^2} . \tag{89}$$

The polarization vector P in a medium can generally be described as

$$\vec{P} = \epsilon_0 \chi(\vec{E}) \cdot \vec{E} = \epsilon_0 \cdot (\chi^{(1)} \cdot E + \chi^{(2)} : EE + \chi^{(3)} : EEE + \dots) \tag{90}$$

where $\chi^{(i)}$ are the i^{th} order susceptibilities of the medium represented by a tensor of (i+1) order. In crystals or other anisotropic media the polarization $\vec{P}$ thus does not generally point in the direction of the electric field $\vec{E}$. For the transparent, non-magnetic media discussed here the first order susceptibility tensor is symmetric and can be diagonalized. In the new coordinate system defined by the principal axes ($i = x, y, z$) of the medium the polarization is then

$$P_i = \epsilon_0 \chi_{ii}^{(1)} E_i. \tag{91}$$

The refractive indices along the principal axes of the medium are related to the susceptibility as well

$$n_{ii} = \sqrt{1 + \chi_{ii}^{(1)}}. \tag{92}$$

Using the vector relation

$$\vec{\nabla} \times \vec{\nabla} \times \vec{V} = \vec{\nabla}(\vec{\nabla} \cdot \vec{V}) - \vec{\nabla}^2 \vec{V} \tag{93}$$

for Eq. 89 and replacing the first order susceptibility using Eq. 92 results in the optical nonlinear wave equation

$$\vec{\nabla}(\vec{\nabla} \cdot \vec{E}) - \vec{\nabla}^2 \vec{E} + \frac{n^2}{c^2} \frac{\partial^2}{\partial t^2} \vec{E}^2 = -\frac{1}{\epsilon_0 c^2} \frac{\partial^2}{\partial t^2} \vec{P}_{\text{NL}} \tag{94}$$

with the nonlinear part of the polarization described by $\vec{P}_{\text{NL}}$. The first term of the equation is often omitted using $\vec{\nabla} \cdot \vec{E} \approx 0$. This true for the so-called slowly-varying envelope approximation (SVEA).

Coupled wave equations For two electric fields $\vec{E}_1$ and $\vec{E}_2$ with frequencies ω_1 and ω_2 the second order polarization will lead to the generation of electromagnetic waves with frequencies $2\omega_1$, $2\omega_2$, $\omega_1+\omega_2$, $\omega_2-\omega_1$ and $\omega_2-\omega_2=\omega_1-\omega_1=0$. The first two terms reflect the so-called ''frequency doubling'' or second harmonic generation (SHG) process, the third term is known as sum-frequency generation (SFG), the fourth is difference frequency mixing (DFG) and the fifth is known as optical rectification.

Usually the interest is only in one of these terms. For the case of sum frequency generation the wave is generated at a third frequency $\omega_3=\omega_1+\omega_2$. Assuming plane waves travelling in the z-direction the fields may be written as (j=1,2,3)

$$E_j(z) = A_j(z)\cdot e^{i(k_j z - w_j t)} \tag{95}$$

with $k_j = n_j\omega_j/c$. The evolution of the amplitudes A_j can then be described by the coupled wave equations

$$\frac{dA_1}{dz} = iB_1 A_3 A_2^* e^{-i\Delta k z} \tag{96}$$

$$\frac{dA_2}{dz} = iB_2 A_3 A_1^* e^{-i\Delta k z} \tag{97}$$

$$\frac{dA_3}{dz} = iB_3 A_1 A_2 e^{i\Delta k z} \tag{98}$$

using $B_j = \omega_j\, d_{\text{eff}}/n_j c$ with the effective nonlinearity $d_{\text{eff}} = \frac{1}{2}\chi_{\text{eff}}$ which depends on the involved polarizations of the waves and the symmetry class of the crystal medium. The phase mismatch between the three waves is

$$\Delta_k = k_1 + k_2 - k_3. \tag{99}$$

Small signal solutions For small conversion between the waves, $A_1(z)$ and $A_2(z)$ can be assumed constant. With the starting condition $A_3(z=0)=0$, Eq. 98 can be directly integrated over the crystal length L yielding

$$A_3(z) = iB_3 A_1 A_2 \cdot \text{sinc}\Big(\frac{\Delta kL}{2}\Big) e^{\frac{i\Delta kL}{2}}. \tag{100}$$

For the intensity of the wave ($I = \epsilon_0 nc/2\cdot|E|^2$)

$$I_3 = \frac{2\pi^2 L^2 d_{\text{eff}}^2}{n_1 n_2 n_3 \lambda_3^2 \epsilon_0 c} I_1 I_2 \cdot \text{sinc}^2\Big(\frac{\Delta kL}{2}\Big). \tag{101}$$

The intensity has a quadratic dependence on the length of the crystal and the nonlinear coefficient and is directly proportional to the intensities I_1, I_2 of the input waves. The sinc function $\text{sinc}(x) = \sin(x)/x$ drops off very quickly for increasing phase mismatch Δk and crystal length L. As such it is important to keep this mismatch very small so that $\Delta k \to 0$.

For frequency doubling $\omega_2 = 2\omega_1$, $\Delta_k = 2k_1 - k_2$ the intensity is

$$I_2 = \frac{8\pi^2 L^2 d_{\text{eff}}^2}{n_1^2 n_2 \lambda_1^2 \epsilon_0 c} I_1^2 \cdot \text{sinc}^2\Big(\frac{\Delta k L}{2}\Big). \tag{102}$$

Notable here is the quadratic dependence on the laser intensity. Analytical solutions for the cases with higher conversion are not discussed here. These cases as well as solutions for the interaction of Gaussian beams can be found for example in [30]. Furthermore a discussion of SHG and DFG in a resonator may be found in [31, 32]. A versatile tool to simulate the frequency conversion process is the freeware software SNLO [33], used in Article II of this thesis.

Birefringent phasematching The dispersion properties of the refractive index $dn(\lambda)/d\lambda < 0$ make it in principle impossible to fulfill the condition $\Delta k = 0$. However, as seen in Eq. 92 the refractive index is generally dependent on the polarization direction of the electromagnetic wave, so that it is possible to fulfill the condition for waves with different polarization states. Crystals with these properties are classified as biaxial, when $n_{xx} \neq n_{yy} \neq n_{zz}$, and uni-axial, when $n_{xx} = n_{yy} \neq n_{zz}$.

The discussion here is concerned only with negative uniaxial crystals such as BBO (β-Barium-Borate). These crystals have a so-called extraordinary (e) refractive index $n_{zz} = n_e$ for light polarized along the crystal optical axis and ordinary (o) refractive index $n_{xx} = n_{yy} = n_o$ for light polarized in the other two directions. The ''negative'' indicates that $n_e < n_o$.

The extraordinary index depends on the angle θ between the wave vector $\vec{k}$ and the optical axis of the crystal

$$n_e(\theta) = \frac{n_e n_o}{\sqrt{n_e^2 \sin^2(\theta) + n_o^2 \cos^2(\theta)}}. \tag{103}$$

The dispersion relation for the refractive index can be approximated using the Sellmeier equation

$$n_{e,o}^2(\lambda) = A + \frac{B}{\lambda^2 + C} + D\lambda^2. \tag{104}$$

For BBO the parameters A-D are given in Table 2. Phasematching now requires the right choice of polarizations and angle θ. For BBO, Type I and Type II phasematching are possible. With $\omega_3 > \omega_2, \omega_1$ Type 1 phasematching requires that waves 1 and 2 have ordinary and wave 3 extraordinary polarization. For Type II phasematching only one of either ω_2 or ω_1 have ordinary polarization.

With Type I and Type II we have the conditions

$$n_o(\omega_1)\omega_1 + n_o(\omega_2)\omega_2 = n_e(\omega_3, \theta)\omega_3 \tag{105}$$

$$n_o(\omega_1)\omega_1 + n_e(\omega_2, \theta)\omega_2 = n_e(\omega_3, \theta)\omega_3. \tag{106}$$

Parameter	A	B	C	D
n_o	2.7359	0.01878	-0.01822	-0.01354
n_e	2.3753	0.01224	-0.01667	-0.01516

TABLE 2 Sellmeier equation parameters for BBO with values given assuming the wavelength λ in units of µm.

For SHG with $\omega_2 = 2\omega_1 = 2\omega$ the relations for Type I and II simplify to

$$n_o(\omega) = n_e(2\omega, \theta) \tag{107}$$

$$n_o(\omega) + n_e(\omega, \theta) = 2\, n_e(2\omega, \theta). \tag{108}$$

For Type I SHG phasematching the situation is visualized on the left panel of Fig. 6. The crystal cut angle $(90° - \theta)$ required for Type I phasematching depending on the fundamental wavelength is shown in the right panel of Fig 6.

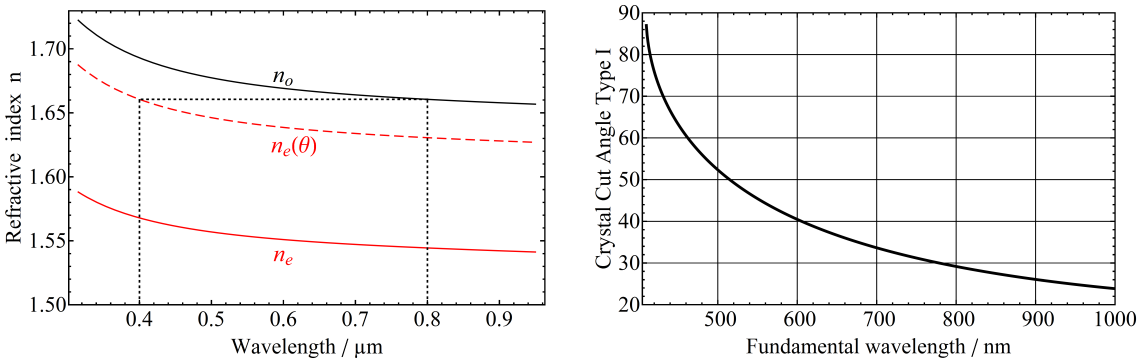

FIGURE 6 Phasematching angles for SHG using a BBO crystal. Left Panel: dispersion of the refractive indices in BBO calculated using the Sellmeier equation, illustrating the condition for phasematching. Right Panel: crystal cut angles required for Type I SHG phasematching in BBO.

2.4 Ti:sapphire laser theory

This section will describe the theory behind the Ti:sapphire laser systems covering the gain medium, the dynamics of the pulsed laser output as well as the equations for the frequency-selective elements.

2.4.1 Ti:sapphire medium

The core of the Ti:sapphire (Ti:sa) laser is a Ti^{3+} doped Al_2O_3 sapphire crystal. Ti:sa is a four-level laser medium with a maximum cross-section for absorption around 500 nm and an emission band from 670 to 1100 nm. The pumping and lasing transitions are shown in Fig 7. The gain cross-section peaks around 790 nm as shown in the left panel of Fig. 8 at a value of $3.0 - 3.9 \cdot 10^{-19}$ cm^2 [34--36] and

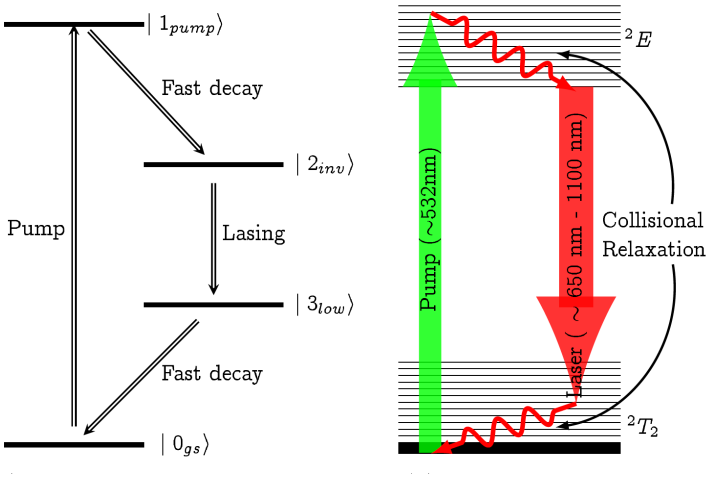

FIGURE 7 Level structure of the Ti:sa gain medium. The pump laser excites the electron from the ground state into the vibrational band ^2E. The electrons quickly relax into the lowest level of the band, from which the lasing transition into the lower $^2T_2$ band occurs, further quickly relaxing into the ground level. Figure taken from [37].

is strongest for p-polarized light. The doping density is usually chosen so that 90-95% of pump light is absorbed when passing through the crystal. For a crystal of length l=20 mm this is equivalent to an absorption coefficient of $\alpha_{532} = 1.5\,\mathrm{cm}^{-1}$ with the intensity of the pump beam through the crystal approximately following the Lambert-Beer law

$$I(z) = I_0 \cdot e^{-\alpha \cdot z}. \tag{109}$$

For high pump intensities the depopulation of the ground state has to be considered, reducing the effective absorption.

A wide residual absorption band, shown in the right panel of Fig. 8, at the laser wavelength exists, which is attributed to the formation of Ti^{3+}-Ti^{4+} pairs [38]. The strength of this absorption is usually given as the figure of merit value (FOM) defined as the ratio of absorption at the pump wavelength and the lasing wavelength, FOM=$\alpha_{532}/\alpha_{800}$ assuming a Nd:YAG pump laser operating at 532 nm. With the progress of crystal growing and annealing techniques the FOM can presently reach above values of 1000 [39], however most commercially available crystals are still far below this value and in the range of 100-300, with the crystals used in this thesis having a FOM value of ≈ 150.

The lifetime of the upper lasing level $|2_{\mathrm{inv}}\rangle$ at room temperature is 3.2 µs, with a slight increase to 3.9 µs at lower temperatures. Above room temperature the lifetime decreases relatively fast, so that cooling is required for good performance. Further benefits of cooling are improvements in thermal properties such as heat capacitance and heat conductivity. High average pumping powers can cause significant thermal lensing effects in the gain medium, reducing beam quality and output power. A detailed simulation of thermal lensing in a Brewster-cut Ti:sa crystal can be found in [41]. Compensation of this effect can partially be done by optimizing the cavity design, however the average output power of Ti:sa lasers is limited to about 5-10 W. Cryogenic cooling weakens this thermal lensing,

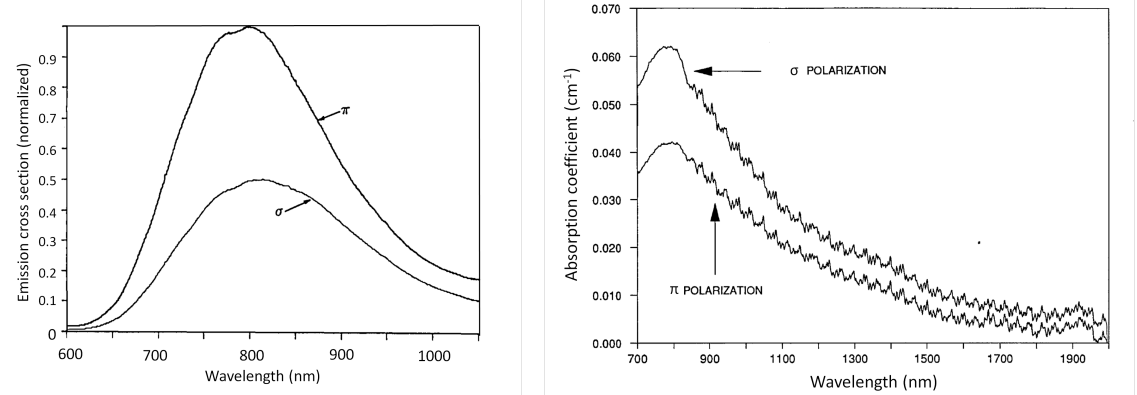

FIGURE 8 Emission and absorption bands of the Ti:sapphire medium. Left panel: stimulated emission cross section for both s-polarized and p-polarized light [35]. Right panel: residual infrared absorption band [40]. Maximal absorption is close to the gain maximum at 800 nm.

reducing thermal distortion by a factor 200. This permits a dramatic increase in maximal output power [42, 43] and is included in next generation petawatt laser systems [44].

2.4.2 Rate equations

The rate equations of the laser describe the temporal evolution of the photon number in the laser cavity. While Ti:sapphire is a four-level laser medium, the relaxation of the pump level $|1_{\text{pump}}\rangle$ into the upper laser level $|2_{\text{inv}}\rangle$ and the decay of the lower laser level $|3_{\text{low}}\rangle$ to the ground state $|0_{\text{gs}}\rangle$ happen in very short time scales compared to the laser pulse dynamics, namely on the ns scale. The distribution of the Ti^{3+} ions is thus sufficiently described by the inversion $N_2 = N(|2_{\text{inv}}\rangle) - N(|3_{\text{low}}\rangle) \approx N(|2_{\text{inv}}\rangle)$, with $N(i)$ denoting the population of the state i. The model used here, taken from [45], is given by the following differential equations:

$$\frac{dN_{\gamma,i}}{dt} = \frac{c\sigma_e(\lambda_i)}{LA} N_2(N_{\gamma_i} + 1) - \frac{N_{\gamma,i}}{\tau_i} \tag{110}$$

$$\frac{dN_2}{dt} = -\frac{N_2}{\tau_d} - \sum_i \frac{c\sigma_e(\lambda_i)}{LA} N_2 N_{\gamma,i} + f_p(t) \cdot N_2(0) \tag{111}$$

$$\tau_i^{-1} = -\frac{c}{2L}\ln(1-T) - \frac{c}{2L}\ln(1-D(\lambda_i)) - \frac{c}{2L}\ln(1-D_{PC}(t))\,. \tag{112}$$

Here $N_{\gamma,i}$ is the photon number of laser mode i. The photon number increases through the gain, given by the first term on the right hand side of Eq. 110. The gain term consists of the speed of light c, the stimulated emission cross section $\sigma_{e,i}$ depending on the wavelength λ_i, the cavity length L and the effective area A as well as the inversion N_2 and the photon number $N_{\gamma,i}$ itself. The additional ''+1'' term can only be truly explained in a quantum field theory framework, as it is related to the spontaneous emission process, which can be described as the interaction of the vacuum mode with the inversion. Effectively the spontaneous

emission acts as if an additional photon was in each mode of the resonator.

This additional term is not required in the description of the inversion population as given by Eq. 111 as it is included through the decay time τ_d, which covers the decay into all possible (resonator and free-space) modes. The inversion loses population through the stimulated emission process of the sum of all modes.

Generation of the inversion is described through a function $f_p(t)$, which follows the time profile of the pump pulse and is normalized to one,

$$\int_{-\infty}^{\infty} f_p(t)\, dt = 1 \tag{113}$$

and an effective starting inversion $N_2(0)$. Both the effective area as well as the effective inversion depend on the overlap of the pump beam with the TEM_{00} resonator mode. They are derived in [45] and can be given as

$$A = \frac{\pi X}{2Y} \tag{114}$$

$$N_2(0) = \frac{X^2}{Y} \tag{115}$$

with the parameters X and Y defined as

$$X = \int_0^{L_c} \int_{-\infty}^{\infty} \int_{-\infty}^{\infty} \frac{n_2(x,y,z)}{\omega_x(z)\omega_y(z)} \exp\Big(- \frac{2x^2}{\omega_x^2(z)} - \frac{2y^2}{\omega_y^2(z)} \Big) dx\, dy\, dz \tag{116}$$

$$Y = \int_0^{L_c} \int_{-\infty}^{\infty} \int_{-\infty}^{\infty} \frac{n_2(x,y,z)}{\omega_x^2(z)\omega_y^2(z)} \exp\Big(- \frac{4x^2}{\omega_x^2(z)} - \frac{4y^2}{\omega_y^2(z)} \Big) dx\, dy\, dz\,. \tag{117}$$

The inversion density $n_2(x,y,z)$ can be estimated from ABCD matrix calculations for the pump mode intensity. Calculations can also be performed for the resonator mode waists ω_x, ω_y in the x and y-direction. To get a final number for $N_2(0)$ other loss terms such as reflections on optical surfaces and the incomplete absorption in the crystal need to be accounted for. Typical values for the Ti:sa laser systems are $A = 0.1\,\mathrm{mm}^2$ and $N_2(0) = 0.6 \cdot N_{\mathrm{pump}}$, with the number of photons in each pump pulse $N_\mathrm{p} = E_{\mathrm{pump}}/h \cdot \nu_\mathrm{p}$, containing the pump pulse energy and frequency E_p and ν_p, respectively.

The photon number in the cavity is reduced through a loss term with the characteristic time τ_i. This time constant, given in Eq. 112, depends on the cavity round-trip time $\tau_{\mathrm{cav}} = 2L/c$ as well as the logarithmic losses given by the transmission T of the output coupler, internal losses D_i as well as time-dependent losses $D_{PC}(t)$ when using a Pockels Cell. The output photon number N_{out} may be calculated using the losses by transmission through the output coupler as

$$\frac{dN_{\mathrm{out}}}{dt} = \frac{\sum_i N_{\gamma_i}}{\tau_{\mathrm{out}}} \tag{118}$$

$$\tau_{\mathrm{out}} = -\frac{c}{2L} \ln(1-T). \tag{119}$$

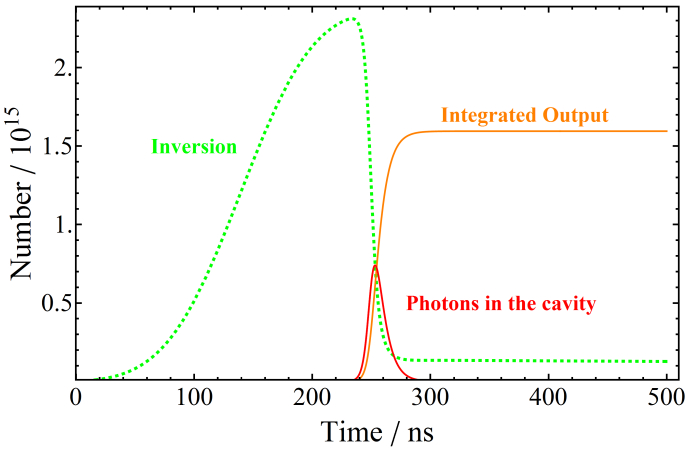

FIGURE 9 Simulation of Ti:sa pulse dynamics using rate equations. The pump pulse was assumed to have a FWHM duration of 120 ns.

An example for a simulation using these rate equations is shown in Fig. 9 at a wavelength of $\lambda = 780$ nm and with a pump energy of 1.5 mJ.

2.5 Frequency tuning

The gain bandwidth of the Ti:sa medium spans more than 150 THz. For efficient excitation of atomic transitions the laser needs to operate at the resonant frequency as well as having a linewidth similar to the spectrally broadened transition linewidth. This is achieved by the introduction of wavelength dependent losses $D(\lambda_i)$ by elements with wavelength-dependent transmission or reflection properties, such as etalons, birefringent crystals or diffraction gratings.

2.5.1 Etalon

An etalon is a frequency-selective element made out of two plane-parallel partially reflective surfaces. The propagation of light through an etalon is shown in Fig. 10. A beam of light incident on the etalon will split into multiple reflected and transmitted beams. Depending on the phase accumulated during propagation the beams will have constructive or destructive interference. Assuming a reflectivity of R_A for the entrance surface, R_B for the exit surface and no absorption losses so that $R_{A,B}+T_{A,B}= 1$ the ratio between the incident amplitude A_i and the transmitted amplitude A_0 can be written as

$$A_0 = \sqrt{T_A T_B} e^{ik_2 d/\cos(\theta_r)} \tag{120}$$

with the thickness d of the etalon and the wave vectors k in the media $k_i = n_i \omega / c$. The m^{th} order amplitudes A_m that undergo $2m$ extra internal reflections

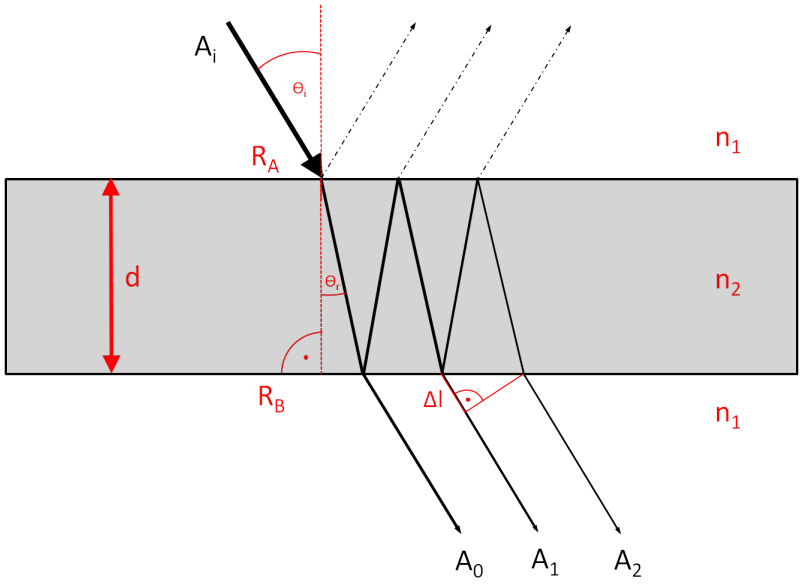

FIGURE 10 Transmission of light through an etalon. Light enters with an angle of incidence θ_i and is partially reflected or transmitted at the surfaces with reflectivities R_A and R_B. Depending on the path taken the beams accumulate a phase delay δ.

accumulate a larger phase delay δ_m which can be written as

$$\delta_m = \frac{2m\, k_2\, d}{\cos(\theta_r)} - m k_1 \Delta l. \tag{121}$$

The first term is the extra path inside the etalon, while the second term is the extra path outside, which the 0^{th} order beam has to make as the additions of the amplitudes have to be made on the wavefronts which are perpendicular to the rays;

$$\Delta l = 2d \tan(\theta_r) \sin(\theta_i). \tag{122}$$

Using Snell's law, Eq. 42, the incident angle θ_i can be expressed using θ_r so that the phase shift between successive orders can be expressed as

$$\delta = 2\, k_2\, d \cos(\theta_r). \tag{123}$$

The m^{th} order transmitted beam can be written as

$$A_m = \sqrt{T_A T_B} \cdot (R_A R_B)^{m/2} \cdot e^{im\delta} \tag{124}$$

with a common phase factor removed and assuming the incident amplitude A_i is normalized to 1. The total amplitude is the sum of all individual beam amplitudes which is then also the amplitude transmission coefficent t,

$$t = \sqrt{T_A T_B} \sum_{m=0}^{\infty} (R_A R_B)^{m/2} \cdot e^{im\delta}. \tag{125}$$

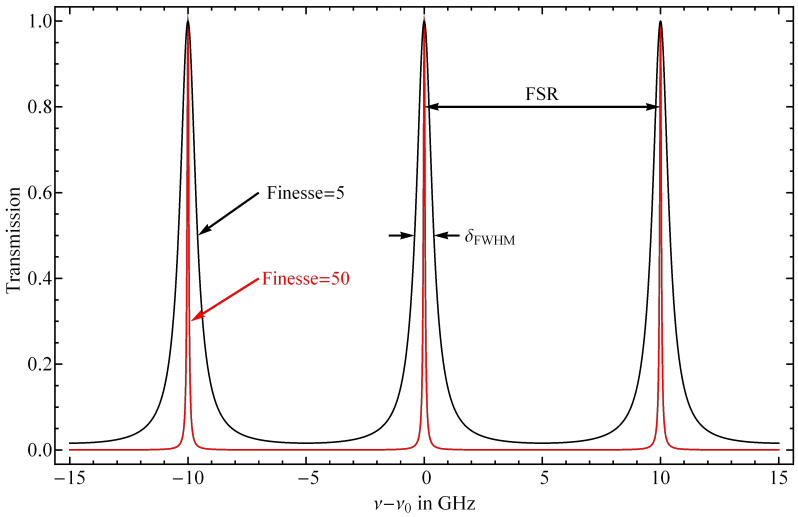

FIGURE 11 Transmission curve of an etalon with a FSR of 10 GHz. The red curve shows the case with a finesse value of $\mathcal{F} = 50$, the black curve with $\mathcal{F} = 5$.

This is a geometric series and can be expressed analytically. The transmission for the intensity T is then

$$T = tt^* = \frac{T_A T_B}{1 + R_A R_B - 2\sqrt{R_A R_B}\cos(\delta)}. \tag{126}$$

For equal reflectivities $R_A = R_B = R = 1 - T$ this formula simplifies to

$$T = \frac{(1-R)^2}{(1-R)^2 + 4R\sin^2(\delta/2)} \tag{127}$$

$$= \frac{1}{1 + \mathrm{F}\sin^2(\delta/2)}, \tag{128}$$

using $\mathrm{F} = 4R/(1-R)^2$. This function has a maximum whenever $\delta/2$ is a multiple of π. For normal incidence this happens whenever the optical path length $2nd$ is a multiple of λ. In terms of laser frequency this means a transmission maximum for every

$$\Delta f = \mathrm{FSR} = c/2nd, \tag{129}$$

which is called the free spectral range (FSR) of the etalon. The ratio between the FSR and the full width at half maximum (FWHM) of the transmission peak is the resolving power of the etalon and is called the Finesse $\mathcal{F}$.

$$\mathcal{F} = \mathrm{FSR}/\delta_{\mathrm{FWHM}} = \frac{\pi}{2\arcsin(\sqrt{(1/\mathrm{F})})} \approx \frac{\pi\sqrt{\mathrm{F}}}{2} \tag{130}$$

with the approximation working well for values of $\mathrm{R} > 0.5$. Example transmission curves for two finesse values are shown in Fig. 11, with a FSR of 10 GHz as would be the case for a glass plate of 1 cm thickness with a refractive index of $n = 1.5$.

The transmission function was calculated assuming a perfect overlap of the

individual beams. Inside a resonator the mode diameter can be quite small, so that the walk-off perpendicular to the beam propagation due to the internal reflections at angle θ_r will result in only partial overlap of the individual transmitted beams. The direct addition of all amplitudes as in Eq. 125 is then an incorrect assumption, which leads to a reduction of the maximal transmission. Furthermore the transmitted beam is no longer perfectly Gaussian, which may result in further losses along the cavity. An estimate for the double pass loss γ of an etalon can be found in [46]:

$$\gamma = \frac{2R}{(1-R)^2} \cdot \left(\frac{2d\theta}{n\omega_0}\right)^2. \tag{131}$$

As the thickness d and the reflectivity R mainly determine the free spectral range and finesse of the etalon which are set by the application requirements, and the waist size ω_0 is fixed by the used cavity, a low loss of the etalon requires a small tilt angle θ. For very small tilt angles however, in the so-called ''flash'' position, the reflections from the etalon surfaces can be coupled back to the cavity, leading to chaotic multi-cavity operation. One possibility to prevent this problem is given in [47], where the polarization of these reflections are rotated using quarter-wave plates.

In general the mirror substrates of the etalon may be curved. A prime example for this is the often used confocal Fabry-Pérot Interferometer. An overview of the theory of such resonators can be found in [48].

2.5.2 Birefringent filter

A birefringent filter makes use of the polarization-dependent phase-shift in a birefringent crystal. For the description of the transmission properties of this filter it is advantageous to use the Jones Matrix formalism [49]. An introduction to the topic can be found in [50]. In general the electromagnetic field in the resonator traveling in the z direction can be described by the complex envelopes in the x-y plane

$$A_x = a_x \cdot e^{i\phi_x} \tag{132}$$

$$A_y = a_y \cdot e^{i\phi_y}, \tag{133}$$

which can be written in a column vector called the Jones vector J given as

$$J = \begin{pmatrix} A_x \\ A_y \end{pmatrix}. \tag{134}$$

As the laser resonator has several Brewster-cut elements it is preferred to use the p- and s-polarized fields so that the relation x$\sim$p and y$\sim$s can be made.

The output of an optical element altering the polarization state can be written

as a superposition of the input fields

$$A'_{\mathrm{p}} = m_{\mathrm{pp}} A_{\mathrm{p}} + m_{\mathrm{ps}} A_{\mathrm{s}} \tag{135}$$

$$A'_{\mathrm{s}} = m_{\mathrm{sp}} A_{\mathrm{p}} + m_{\mathrm{ss}} A_{\mathrm{s}} \tag{136}$$

or in matrix form

$$J' = M_J \times J \tag{137}$$

with the Jones matrix

$$M_J = \begin{pmatrix} m_{\mathrm{pp}} & m_{\mathrm{ps}} \\ m_{\mathrm{sp}} & m_{\mathrm{ss}} \end{pmatrix}. \tag{138}$$

There are several publications discussing the Jones matrix for a birefringent filter plate. In many cases various simplifications have been made, for example using static reflection losses, neglecting reflection or ignoring the walk-off between the ordinary (o) and extraordinary (e) ray while calculating the phase difference between the polarizations. Publications [51] and [52] detail one of the most thorough approaches, including accurate reflection coefficients depending on the angle of incidence using Fresnel equations. The authors note that for materials with small birefringence, some approximations can be made, resulting in the following Jones Matrix for a birefringent plate with thickness d and angle of incidence θ_i:

$$\begin{pmatrix} \frac{1-R_p^2}{C^2+1}\left(C^2 \cdot e^{i\delta_o} + e^{i\delta_e}\right) & \frac{T_s C(1-R_p^2)}{T_p(C^2+1)}\left(e^{i\delta_o} - e^{i\delta_e}\right) \\ \frac{T_p C(1-R_s^2)}{T_s(C^2+1)}\left(e^{i\delta_o} - e^{i\delta_e}\right) & \frac{1-R_s^2}{C^2+1}\left(e^{i\delta_o} + C^2 e^{i\delta_e}\right) \end{pmatrix} \tag{139}$$

with

$$C = \frac{-\sin(\phi)}{\cos(\theta_o)\cos(\phi)}. \tag{140}$$

The factors R_s, R_p, T_s and T_p are the reflection and transmission coefficients for s and p polarized light, respectively, and can be calculated from the Fresnel equations 82-85. Inside the plate the refractive indices for the e-ray and the o-ray differ, so that the two polarizations incur a phase difference $\delta = \delta_e - \delta_o$. Furthermore, the two rays have a slightly different angle resulting in an offset at the end of the crystal. As the phase delay has to be taken with respect to the wavefronts an additional term is required,

$$\delta_o = \frac{2\pi \cdot d \cdot n_o}{\lambda \cdot \cos(\theta_o)} \tag{141}$$

$$\delta = \delta_e - \delta_o = \frac{2\pi \cdot d}{\lambda} \cdot (n_{eo}\cos(\theta_{eo}) - n_o \cos(\theta_o)). \tag{142}$$

with the refractive index and angle for the extraordinary wave given as

$$n_{eo}(\theta_i, \phi) = \sqrt{n_e^2 + \frac{n_o^2 - n_e^2}{n_o^2} \sin^2\theta_i \cos^2\phi} \tag{143}$$

$$\theta_{eo}(\theta_i, \phi) = \sin^{-1}\left(\frac{1}{n_{eo}(\theta_i, \phi)} \sin\theta_i\right). \tag{144}$$

To verify that no transcription or interpretation errors were made in the implementation of the formulae, the results from [51] were reproduced in Mathematica [53]. The left panel of Fig. 12 shows the original result from the publication and the right panel shows the calculations based on the above formulae.

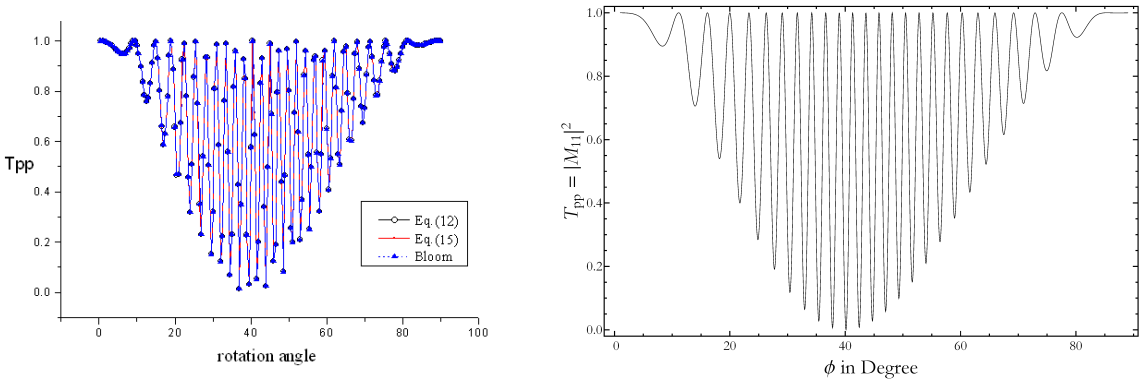

FIGURE 12 Calculations for the first Jones matrix element M_{pp} of a birefringent quartz plate. Left panel: calculations for $Tpp = |M_{pp}|^2$ according to [51]. Right panel: comparison with calculations using the described implementation of the Jones matrix in Mathematica.

In practice, an intracavity birefringent filter will make use of multiple plates with different thickness to allow for narrow transmission bands (determined by the thickest plate) while having a large separation of transmission peaks (determined by the thinnest plate). Further elements of the cavity may also have an impact on the polarization state such as Brewster surfaces or the gain medium. The roundtrip Jones matrix is then calculated through matrix multiplication. As an example, a three-plate filter with thicknesses d_1, d_2 and d_3 in a resonator with a Brewster cut Ti:sa crystal is considered, which equates to the round-trip Jones matrix

$$M_{\text{round}} = M_{\text{Brewster}} \times M_{\text{crystal}} \times M_{\text{Brewster}} \times M_{\text{BRF}}(d_1) \times M_{\text{BRF}}(d_2) \times M_{\text{BRF}}(d_3) \tag{145}$$

with the matrix for reflection at a Brewster surface given by

$$M_{\text{Brewster}} = \begin{pmatrix} \sqrt{1 - R_p(\theta_B)} & 0 \\ 0 & \sqrt{1 - R_s(\theta_B)} \end{pmatrix} \tag{146}$$

and the matrix for the crystal using the polarization-dependent cross sections,

with $\sqrt{\sigma_{e,s}/\sigma_{e,p}} \approx \sqrt{0.5}$, assumed to be

$$M_{\text{crystal}} = \begin{pmatrix} 1 & 0 \\ 0 & \sqrt{0.5} \end{pmatrix}. \tag{147}$$

In a stable resonator the polarization states will be the eigenvectors of the roundtrip matrix,

$$J'_{1,2} = M_{\text{round}} \times J_{1,2} = \lambda_{1,2} \cdot J_{1,2}\,. \tag{148}$$

The transmission coefficients $T_{1,2}$ for the eigenvectors $J_{1,2}$ are then given by the absolute square of the eigenvalues

$$T_{1,2} = \lambda_{1,2} \cdot \lambda^*_{1,2}. \tag{149}$$

For comparison the single-pass transmission curve of two filters is shown in Fig. 13, with the simulation parameters detailed in the plots. The black curve and grey curve show the transmission for the eigenvector with the largest and lowest eigenvalue, respectively. Compared with the right panel, the transmission fringes in the left panel are noticeably narrower. No difference appears in the positions of the highest maxima, which depend on the thinnest plate. The position as well as the transmission of the highest side-maxima however are different. In the left panel the second highest maxima are at T=0.91, while they are at T=0.86 in the right panel. The ratio between highest and second highest maximum is an important parameter. If the ratio is not large enough the laser can run multi-mode at two different wavelength, considering that the wavelength dependence of the gain profile also has a big impact.

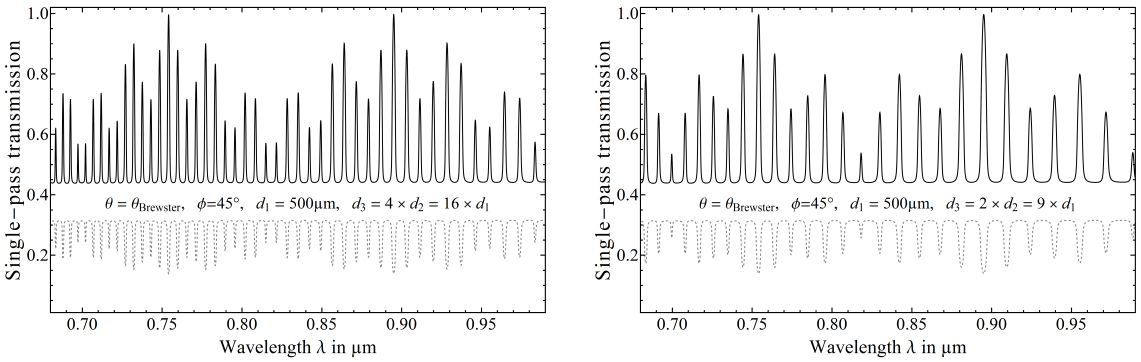

FIGURE 13 Simulated transmission curve for two birefringent filters, with specification given in the plots.

2.5.3 Grating

Diffraction gratings have periodically structured surfaces and are available in either transmissive or reflective form. The groove structure is usually made by ruling or the use of a holographic exposure method and subsequent etching. Holographic gratings usually deliver better performance as their error in periodicity

is smaller compared to the physical ruling process and they also have reduced scattering loss.

The position of intensity maxima and minima can be understood as interference of the waves coming from multiple slits. The geometry is depicted on the left panel of Fig. 14. A plane wave is incident at an angle α on the grating and diffracted at an angle θ. In the Fraunhofer approximation, the assumption is that the waves interfere at a large distance L much greater than the slit separation so that one can assume that the wave-vectors from the refracted waves are quasi-parallel. For constructive interference the optical path difference between two adjacent slits $\overline{AB}$+$\overline{BC}$ then has to be equal to an integer multiple m of the wavelength. The distance can be calculated using the angles and the slit separation $d = 1/N$, with the slit density N so that

$$\overline{AB} + \overline{BC} = d \cdot (\sin(\alpha) + \sin(\theta)) = m \cdot \lambda. \tag{150}$$

To improve efficiency (ratio of intensity at the wanted refraction order m vs. other

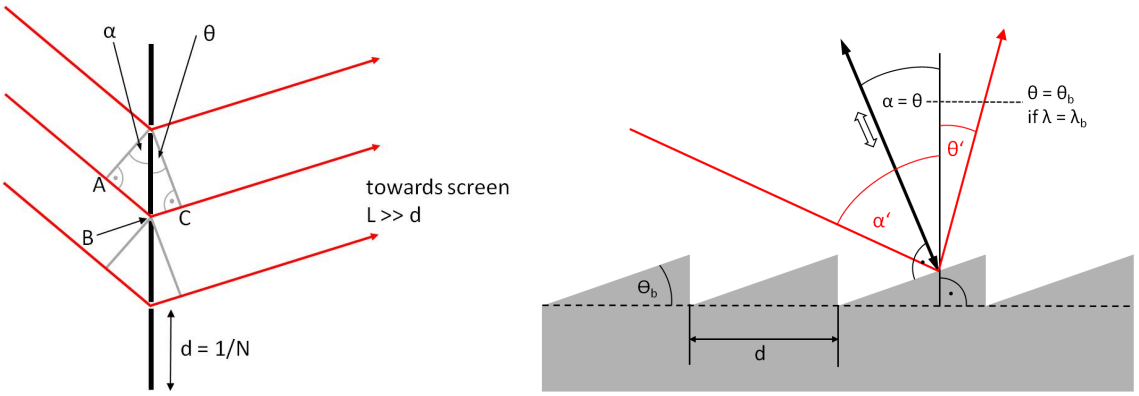

FIGURE 14 Diffraction at a grating. Left panel: interference of light diffracted at multiple slits of a transmission grating, showing the path difference $\overline{AB}$+$\overline{BC}$ between the individual rays. Right panel: diffraction at a blazed reflection grating. The angles α' and θ' indicate general diffraction, the angles $\alpha = \theta$ indicate the situation for the Littrow configuration.

orders) at a particular diffraction angle or wavelength range some gratings have their grooves made with a so-called blaze angle θ_b creating a see-saw surface profile as shown in the right panel of Fig. 14. The blaze angle is set so that the reflection from the blazed surface coincides with the angle of the targeted diffraction order. The relationship between blaze wavelength λ_b and blaze angle is given by

$$m \cdot \lambda_b = 2d \sin(\theta_b) \cdot \cos(\alpha - \theta_b). \tag{151}$$

In a standing wave resonator the so-called Littrow configuration is often used. Here the light is diffracted back into the cavity along the same direction as the incoming radiation, as depicted by the double-sided arrow in the figure, so that $\alpha = \beta$, simplifying the grating equation to

$$m \cdot \lambda = 2d \sin(\alpha). \tag{152}$$

The resolving power of a grating depends on the number of illuminated grooves N and can be given as

$$\frac{\lambda}{\delta\lambda} = m \cdot N. \tag{153}$$

3 FURIOS AT IGISOL 4

An overview of the "Fast Universal Resonant laser IOn Source" (FURIOS) can be found in the theses of M. Reponen [37] and T. Kessler [54]. Due to a number of improvements to the system an update on its elements and specifications will be given here.

The main elements of FURIOS are several tunable Ti:sapphire (Ti:sa) lasers, pumped by high power Nd:YAG lasers, laser beam transport to the target area as well as specialized gas cells optimized for the laser ionization of the produced radioactive species. In the following the specifications and operation of the laser systems are described in detail. A general change to the original design is the introduction of intra-cavity second harmonic generation (ic-SHG) as well as difference frequency generation (DFG), both described in this chapter. Further additions such as a grating-based Ti:sa laser, a dual-etalon Ti:sa as well as an injection-locked Ti:sa are discussed separately in chapters four, five and six, respectively.

3.1 Laser systems

A schematic layout of the current FURIOS laser setup is displayed in Figure 15. Optical table 1, shown on the right side of the figure, comprises the main laser system used for general purpose on-line and off-line laser ionization. The grating Ti:sa and injection-locked Ti:sa are placed on table 2, while the continuous wave (cw) Ti:sa system operates on table 3 in a separate room, supplying the input for the injection-locked Ti:sa through an optical fibre link.

3.1.1 Pump lasers

The pump laser Nd:YAG 1 (Lee Laser, LDP-200MQG) for the main system is set at 68 W output power of the second harmonic at 532 nm with a pulse repetition rate of 10 kHz. Its output power is divided using a combination of half-wave plates and polarizing beam-splitter cubes and directed to the three Ti:sa systems, yielding

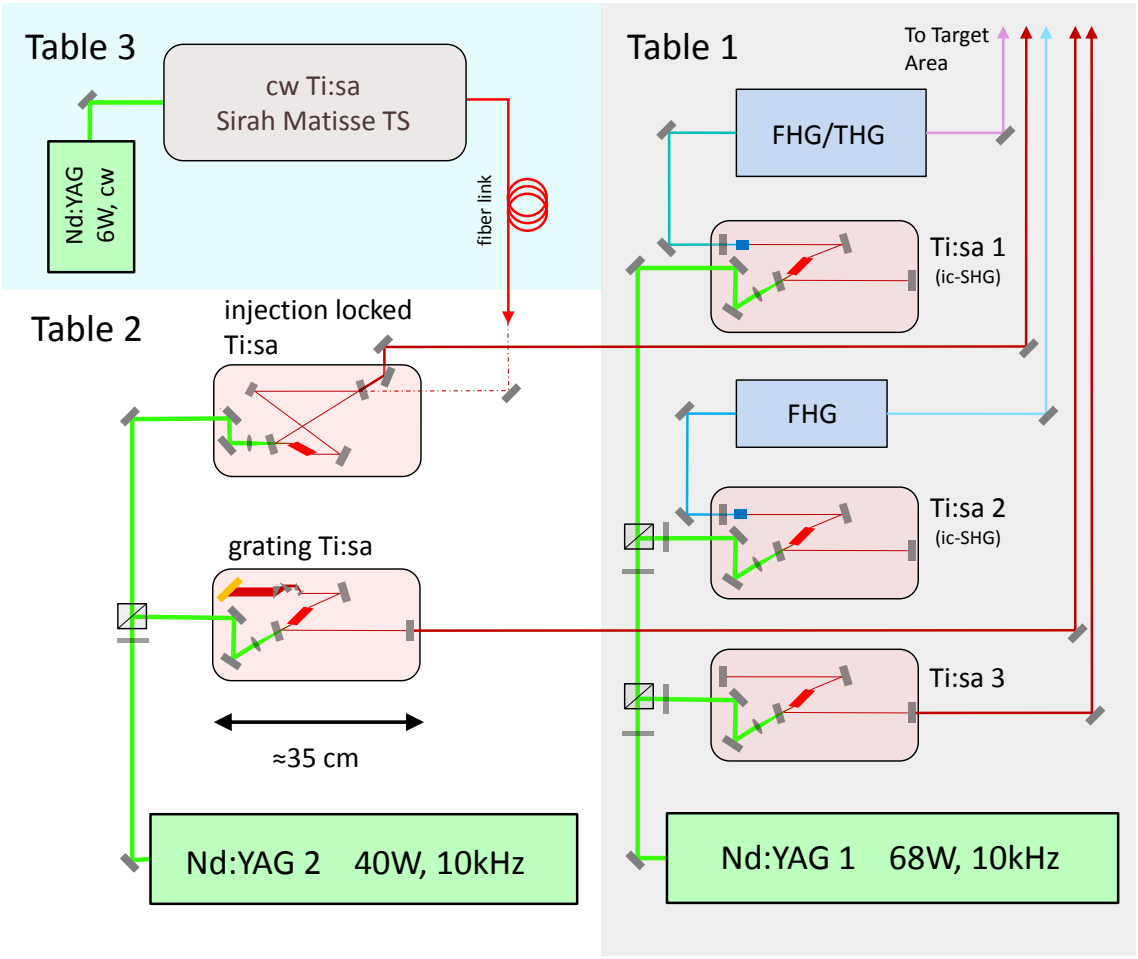

FIGURE 15 Layout of the current laser setup at FURIOS. The right side (Table 1) illustrates the general purpose laser system used for laser ionization. To the left side (Table 2) is the grating Ti:sa used for wide range scanning capabilities and ionization scheme development as well as the injection-locked Ti:sa for high resolution spectroscopy using the single-mode cw Ti:sa (Table 3) as seed for amplification.

about 20-22 W pumping power for each Ti:sa after transport losses. The power scaling of the pump laser with diode current is shown in the left panel of Fig. 16 having a nearly linear trend with a lasing threshold around 13.6 A. For the second pump laser Nd:YAG 2 (Lee Laser, LDP-200MQG, OEM model, second-hand) the specifications are nearly identical, although producing a lower maximum output power as shown on the right panel of Fig. 16. At higher diode current the output diverges from a linear trend. Realignment of the cavity may alleviate this issue. The output power is however still sufficient for the two Ti:sa systems.

An external frequency generator (Agilent 33120A) with a square-wave output provides the 10 kHz external trigger. After distributing the trigger signal to three gate and delay units the individual signals are sent to the two pump lasers as well as a Copper Vapour Laser (CVL, not shown in figure). By adjusting the delay the laser systems can be time synchronized. At this repetition rate and power level the typical pulse length of the Nd:YAG is about 120 ns long. The pump laser is running multi-mode and has a specified M^2 value of about 10-20.

The CVL provides up to 30 W of combined output power at the green (511 nm) and yellow (578 nm) lasing transitions. It was previously used as pump for a (now decommissioned) dye laser system but is now used primarily as a high power non-resonant ionization laser. Its pulse duration is about 30-40 ns, which is close to the Ti:sa pulse duration, and is thus better suited for this task than the long-pulse Nd:YAG lasers.

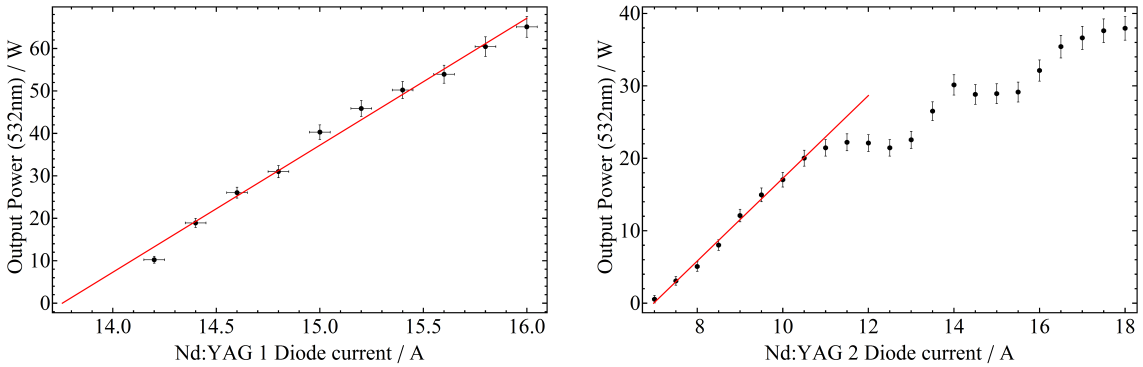

FIGURE 16 Power scaling vs diode current of pump lasers. Left panel: Power vs diode current of the main Nd:YAG 1 pump laser. The power scales nearly linear with the current. Right panel: Power vs diode current of the Nd:YAG 2 pump laser. The power scaling is only linear at currents less than 11 A.

3.1.2 Ti:sa lasers

The three ''standard'' Ti:sa lasers of the main system use the cavity design developed at the University of Mainz detailed in [45]. Modifications of this design are discussed with [55] demonstrating double-sided pumping, a new pump geometry allowing higher pump powers [56] and general optimisations of the layout for faster setup and better access for monitoring [57]. A schematic with cavity dimensions is shown in Fig. 17. The cavity is formed using a plane high reflector (HR),

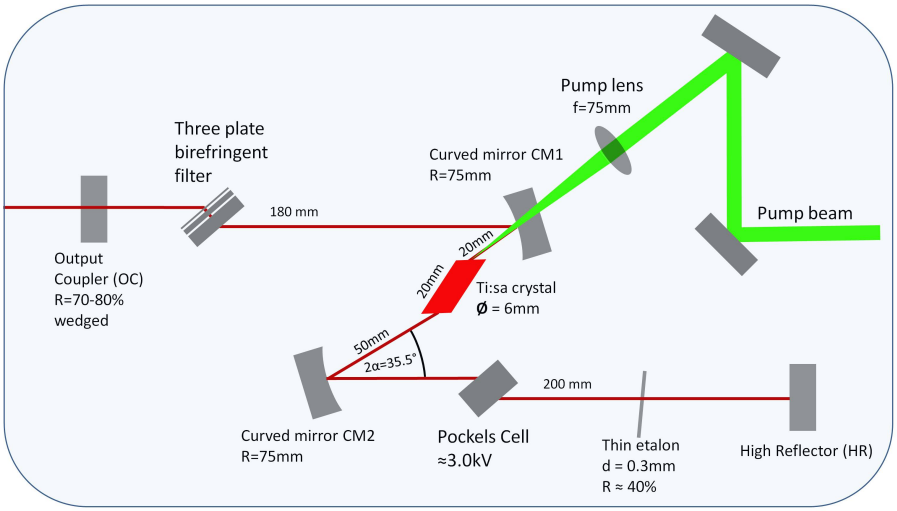

FIGURE 17 Standard Ti:sa laser cavity with dimensions and specifications.

two curved mirrors CM1 and CM2 having a dichroic coating with high reflection for the laser wavelength and an anti-reflection coating at the pump wavelength, and a wedged output coupler (OC) with 70-80% reflectivity. The pump is focused with a f=75 mm lens onto the Brewster-cut Ti:sa crystal. The focal spot of the lens with a waist of $\approx$ 200 µm is at the side of the crystal facing away from the pump source as discussed in [56].

Coarse wavelength selection is done using individual mirror sets with four standard coating choices available, covering the range from 700-950 nm, each set having a tuning range of 50-100 nm. Special mirror sets with higher reflecting output couplers can further increase the range as discussed in Article II. Finer wavelength selection is performed using a combination of a three-plate birefringent filter and a thin etalon (d = 0.3 mm, R $\approx$ 40%, FSR = 324 GHz).

Synchronization of the Ti:sa lasers is achieved using KD*P Pockels Cells. These electro-optical crystals are operated at the quarter-wave voltage of $\approx$3 kV, which due to the double-pass in the Z-shaped cavity creates a 90° rotation of the polarization axis. During the duration of the pump-pulse this high voltage is applied on the Pockels Cell increasing the losses of the cavity at Brewster surfaces, so that no lasing can occur. After a short delay time, which is adjustable for each laser individually, the HV is turned off, and the build-up of the Ti:sa laser pulse can start.

3.1.3 Laser monitoring

A small fraction of the laser light is collected either by use of a pick-off mirror or from the leakage of one of the cavity mirrors and is coupled into optical fibres. The fibres go to a home-built four-channel fibre switch, which is discussed in [37]. Inside the switchbox the inputs are split again, with a small portion sent to fast photodiodes for pulse timing monitoring, while the remaining light of one of the input channels is connected to the wavemeter (High Finesse, WS6-UV), with selection of the channel performed through a software interface.

The wavemeter has a specified accuracy of 600 MHz at the 3σ level. It was shown that the stability of the wavelength measurement depends on the choice of fibre, either multi-mode or single-mode as illustrated in the left panel of Fig.18. The measurement was performed using a stabilized HeNe laser. With single-mode fibre the wavelength measurement is stable, but with multi-mode fibre fluctuations of the order of 300 MHz occur. The multi-mode fibre measurement was also very sensitive to the coupling into the fibre as well as to touch or vibrations. Temperature affects the measurements as well as seen in the right panel of Fig. 18. The wavemeter has an in-built temperature sensor which was recorded, while the temperature of the room was varied using the air-conditioning system. Frequency shifts of up to 200 MHz/°C can be observed. This should be kept in mind whenever measurements are compared over long time periods. The air conditioning system can keep the temperature stable to about ± 0.2°C, however only as long as the laser cabin door remains closed.

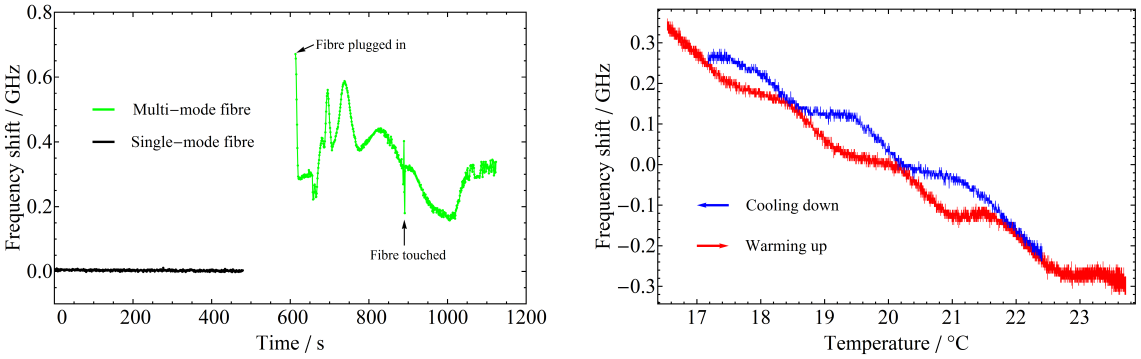

FIGURE 18 Left panel: wavemeter measurement of HeNe laser with multi- and single-mode fibres. Right panel: temperature dependence of measured HeNe wavelength with single-mode fibre.

The fibre switch uses purely multi-mode fibres. This is sufficient for the broadband Ti:sa system. For higher accuracy wavelength measurement two Fabry-Pérot Interferometers (FPI) are available. One is a self-built semi-hemispheric FPI with an adjustable free spectral range (FSR) and Finesse $\mathcal{F} \approx 70$, which is discussed in Article III in chapter 5. The second is a commercial confocal FPI (Toptica, FPI-100-0750-1) with a FSR of 1 GHz and a Finesse of 200-500 with the mirror set coated for 615-885 nm. As frequency reference a stabilized HeNe laser (Melles Griot, 25-STP-912-230) is used. The calibration of the FSR of these FPIs is discussed in chapter 5 as well.

3.1.4 Specifications of the main Ti:sa laser system

To reach the blue and UV wavelengths required for many laser ionization schemes Second, Third- and Fourth Harmonic Generation (SHG, THG and FHG) is performed using BBO crystals in an external frequency conversion unit. The design of this unit follows closely to that given in [57]. Higher conversion efficiency can be reached using intracavity-SHG, which is discussed in Article II as well as section

Wavelength range	700-960 nm
Pulse repetition rate	10 kHz
Pump power	20-22 W
Pulse duration	30-50 ns
Spectral width	4-8 GHz
Average power	3-5 W
SHG power	400-800 mW
THG power	50-100 mW
FHG power	20-50 mW
SHG range	350-470 nm
THG range	235-310 nm
FHG range	205-240 nm

TABLE 3 Specifications of the main Ti:sa laser system using the standard mirror coatings and external frequency conversion.

3.4.

The specifications of the main Ti:sa system are given in Table 3. Near the limits of the wavelength tuning range the values for output power may be significantly lower and the pulse duration higher. SHG, THG and FHG values are given for external frequency conversion only.

3.2 Atomic beam unit

The atomic beam unit (ABU), described in [54], provides a simple platform for off-line laser spectroscopy involving mainly the test and development of laser ionization schemes. A thin tube of tantalum resistively heated up to 1600 °C is used to evaporate samples of the element of interest. An atomic beam is created and collimated through a small orifice of 8 mm diameter at a distance of 12 cm from the oven exit. Compared to the description in [54] an additional electrode at a small positive potential of +80 V was installed directly behind this orifice. Using this, background signal of thermal ions coming from the hot oven could be suppressed by more than three orders of magnitude.

The collimated atomic beam interacts with the lasers sent either perpendicularly through two Brewster windows, or counter-propagating through a plane window. Laser ions created in the interaction region are guided using electrostatic ion optics toward an electron multiplier tube (EMT) operating at a voltage of -2 kV. The signal of the EMT can be read out using an amperemeter (Keithley 485). Further electronics may be used to achieve more sensitive single-ion detection along with coincidence techniques to suppress background signals [54].

3.3 Article II

Article II, recently accepted for publication at JPS Conf. Proc., covers the implementation of intra-cavity second harmonic generation (ic-SHG) for increased conversion efficiency. In addition, the first results of difference frequency generation (DFG) are shown, providing access to a wavelength region previously requiring dye laser systems. Application of DFG to laser spectroscopy is demonstrated on the D2 line of sodium. The article is presented in the following 6 pages (print version only).

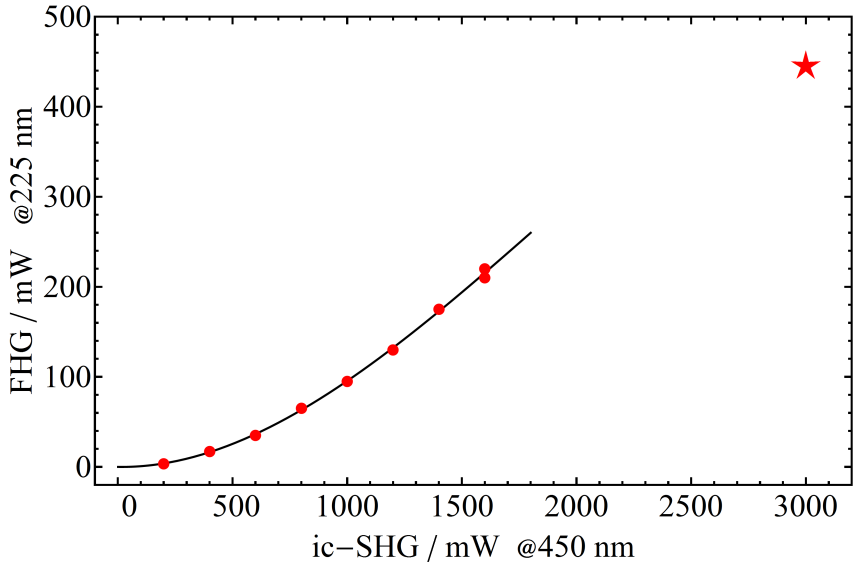

FIGURE 19 Fourth harmonic output power using ic-SHG generated 450 nm radiation. Data points in red, an expected quadratic fit curve (compare Eq. 102) in black. Measurement at 3 W of 450 nm power uses a different focusing.

3.4 Third and Fourth harmonic generation using ic-SHG output

The higher output power of the ic-SHG process also affects the generation of the third and fourth harmonic. Due to the nonlinear interaction the benefit is even more pronounced. For testing, the mirror set configuration MS3 as discussed in Article II was used. The power of the ic-SHG light at 450 nm was focused using an f=75 mm lens into a l=6 mm BBO crystal AR-coated at 455/227 nm. The output of the ic-SHG light was adjusted by varying the pump laser power. The fourth harmonic output power was measured using a photodiode-based sensor (Thorlabs, S120VC) as well as a calorimetric powermeter. The results shown in Fig. 19 are based on the photodiode sensor values. The calorimetric measurement was typically 10-15 % lower. This discrepancy may be explained by a lack of any recent calibration of the instruments.

The values below an ic-SHG power of 2 W show a good agreement with a quadratic fit. It is not fully clear whether this quadratic dependency is solely due to the nonlinear interaction (see Eq. 102) or due to pulse duration changes, caused by the pump power variation of the ic-SHG Ti:sa. Comparisons with simulations have not been made as measurement of the beam profile as well as pulse duration would be required. The last data point marked with a star at 3 W was taken with a longer focal length of 125 mm to prevent optical damage on the coating of the BBO crystal.

Third harmonic generation was so far only performed for the output of mirror set MS4a from Article II. This mirror set uses ic-SHG with a 95 % OC and thus simultaneously releases both the frequency doubled as well as the fundamental radiation. The wavelength tuning curve for this set is shown in Fig. 20. This wave-

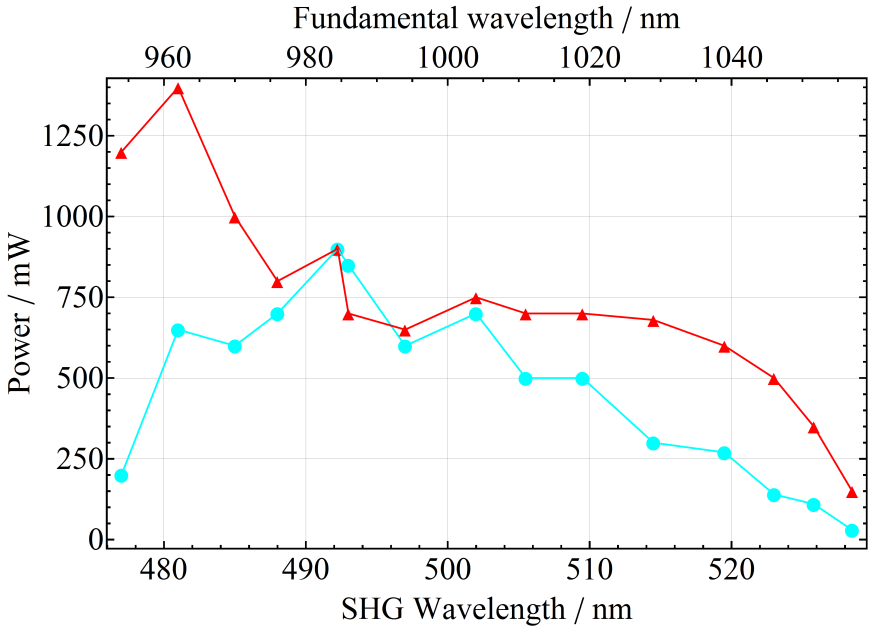

FIGURE 20 Tuning curve of mirror set MS4a for both fundamental (red triangles) and SHG (blue circles) radiation.

length region was interesting both for the laser ionization of copper and silver which have first step excitation transitions at 327.4898 nm and 328.1624 nm, respectively - equivalent to fundamental wavelengths of 982.469 nm and 984.487 nm. For these two wavelengths nearly 1 W of SHG as well as 1 W of fundamental radiation were obtained, yielding up to 160 mW in the third harmonic. Significantly higher third harmonic powers may still be expected when operating closer to the gain maximum of the Ti:sa crystal, though no suitable mirror-set was available for testing in this region.

	with ic-SHG	ext. conversion
SHG power	1500-3700 mW	400-800 mW
THG power	100-160 mW*	50-100 mW
FHG power	100-450 mW	20-50 mW
DFG power	20-60 mW	-
SHG range	340-525 nm	350-470 nm
THG range	235-340 nm	235-310 nm
FHG range	205-255 nm	205-240 nm
DFG range	550-700 nm	-

TABLE 4 Specifications of the main Ti:sa laser system using specialised coatings and ic-SHG. *Third harmonic power using ic-SHG has only been measured far off the gain peak.

3.5 Summary and applications for ic-SHG

In total up to a factor of four improvement for the second harmonic and nearly a factor of ten for the fourth harmonic has been reached by using ic-SHG. Other benefits are the very compact setup and a reduced number of collimating optics as well as a lower lasing threshold and larger tuning range of the cavities due to the replacement of the output coupler by a high reflecting mirror. A summary of the typical performance with ic-SHG is given in Table 4. with the inclusion of DFG the possible wavelengths span from 205-1050 nm, only a small wavelength region from 525-550 nm remains uncovered.

Due to the longer confinement of the fundamental light in the cavity the risk of mirror coating damage increases. This is especially the case when the conversion efficiency to the second harmonic is low. Care must be taken when changing the wavelength of the laser with the birefringent filter as this changes the phase-matching condition.

It was also noted that ic-SHG does not work well in combination with the Pockels Cell, with issues such as intensity fluctuations and extreme alignment sensitivity. Reasons for this are so far not completely clear. Since BBO is a birefringent crystal it may interact with the polarization changes induced by the Pockels Cell in a non-trivial way. An additional waveplate to compensate for polarization changes or a different cavity layout may prove of benefit here. Synchronization with other lasers is currently only possible by use of separate pump lasers, long delay lines or adjustment of pump power.

A further complication is caused by partial reflections from the coatings of the BBO crystal or the dichroic mirrors in the cavity used to separate the SHG radiation. As neither the crystal nor the dichroic mirrors are wedged they can cause spurious etalon effects, affecting both output power as well as wavelength tuning. While the anti-reflection coating of the BBO crystal seems to be sufficient in most cases, it would be helpful to obtain a set of properly coated wedged dichroic mirrors. A different option would be the design of an unidirectional ring-cavity, which could eliminate these issues.

Despite these complications, the benefits are clear. As seen in Article I, the saturation of the second step AI transition of copper in the gas cell was only sufficient due to the added power of ic-SHG. Laser ionization in a freely expanding gas jet may require very high power as well, considering that a very large area needs to be illuminated for good efficiency. There are also a few elements that are currently deemed nearly impossible for laser ionization as they require first step excitation wavelengths below the phase-matchable limit of BBO crystals (185 nm). Two-photon excitation processes may prove successful if sufficient laser intensity is available. Other elements may have interesting ionization schemes that require the use of visible light in the 500-700 nm range or above the fundamental Ti:sa range $>$1050 nm. Difference frequency mixing as discussed in Article II requires ic-SHG for improved performance.

A new program aiming at laser ionization towards doubly-charged elements,

Ion Resonance Ionization Spectroscopy (IRIS), is currently starting at the IGISOL facility [58]. Since the energy required to go beyond the second ionization potential is often significantly higher than for the first, multiple transitions in the UV wavelength range can be necessary, making the compact setup of ic-SHG more practical.

4 SAMARIUM IONIZATION SCHEME DEVELOPMENT USING A GRATING-BASED TI:SAPPHIRE LASER

4.1 Grating-based Ti:sapphire laser

For many elements there is a lack of tabulated spectroscopic data in the region of higher excited atomic states. In the case of heavier elements with complicated electronic structure the computation of energy levels to the required precision for laser excitation of $<1\,\mathrm{cm}^{-1}$ is so far deemed impossible. Using a multi-configuration Dirac-Fock method the author in [59] reproduced excited state level energies in ytterbium (Z=70) with accuracies of 700 - 1100 cm^{-1}. More recent calculations [60] using an intermediate Hamiltonian Fock-space couple-cluster (IHFSCC) approach, have been able to reduce the uncertainty to a level of 300 cm^{-1} for ytterbium and $\approx 800\,\mathrm{cm}^{-1}$ for the super-heavy element nobelium (Z=102). In nobelium no spectroscopic information is currently available, and low production rates complicate experimental determination. On the other hand, fine structure splitting energies can be reproduced with a smaller uncertainty of $\approx 30\,\mathrm{cm}^{-1}$ [61]. This is however still far from that required to build up a laser ionization scheme.

The only reliable way to obtain spectroscopic information is by direct measurement. While the standard Ti:sa lasers have a sufficiently wide tuning range, the scanning of the wavelength with an etalon and birefringent filter will inevitably lead to mode jumps and strong power dependence on the wavelength. Using a grating for wavelength selection allows for scanning over wide wavelength ranges. The development of grating-based lasers has been pursued at other facilities [56, 62, 63]. At the Oak Ridge National Laboratory a commercial device is in use [64].

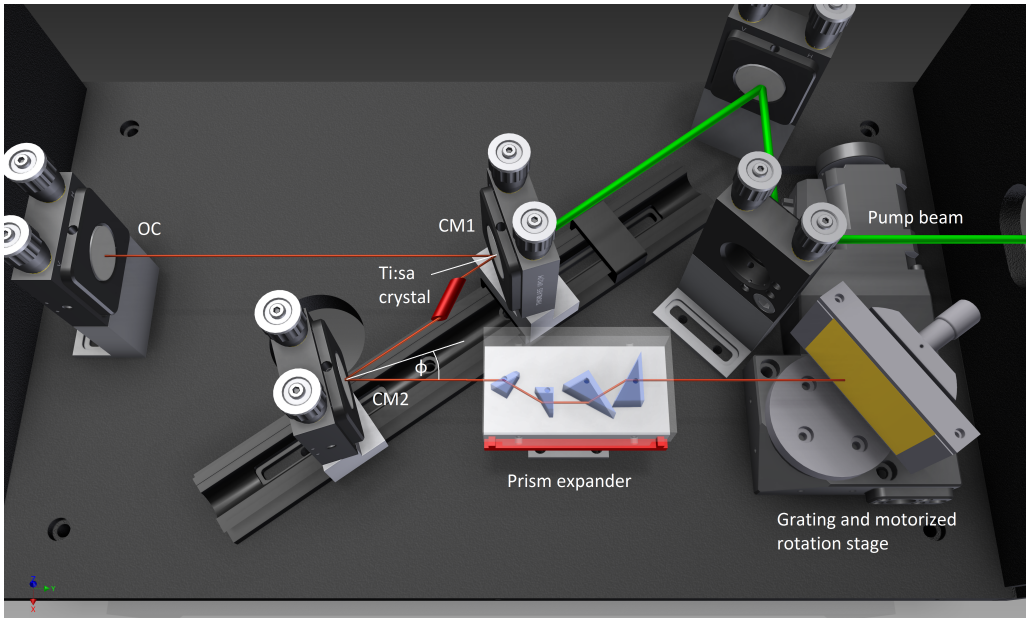

FIGURE 21 3D CAD design of the grating-based Ti:sa laser. Also indicated is the folding angle ϕ of the cavity. The water-cooled mount for the Ti:sa crystal as well as the pump lens are omitted.

4.1.1 Laser Resonator

The setup of the grating-based Ti:sa laser uses a similar resonator geometry to that of the normal Z-shaped design described in Chapter 3. The design as envisaged from a 3D CAD program (Autodesk Inventor) is shown in Fig. 21. Both the curved folding mirrors CM1 and CM2 as well as the output coupler (OC) use broadband reflective coatings from 650 nm to 1050 nm. Compared to a standard Ti:sa the end mirror of the cavity is replaced by a gold-coated diffraction grating with 1480 grooves/mm (Horiba Jobin Ivon, Part # C524 28 090/T3, Replica). The grating is used in the Littrow configuration, so that the 1^{st} order diffraction is reflected back into the cavity. As diffraction into a higher order is not possible with the high groove density of the grating, only the unused reflection at the 0^{th} order is lost. For an increased efficiency at the Ti:sa wavelength range the grating has a blaze angle optimized for 800 nm ($\approx$36° according to Eq. 151). For the central wavelength range from 750-850 nm the diffraction efficiency into the 1^{st} order is rated as >90%. As the frequency selection is accomplished using the grating, further frequency selective elements such as the birefringent filter or etalon are not required. This allows for a continuous frequency tuning of the laser by changing the incident angle of the grating according to Eq. 152. However, to achieve a desired bandwidth below $\approx$ 10 GHz a sufficient number of grooves on the grating have to be illuminated. Using Eq. 153 with $m = 1$ and $N \approx 10^4$ a bandwidth of 40 GHz can be estimated at 800 nm. For comparison the same number for the etalon is 80 GHz. The high number of round-trips in the cavity narrows the bandwidth and reduces that value to a few GHz. Additionally the grating can be sensitive to high power densities, which also suggests that the small mode diameter of the cavity should be expanded.

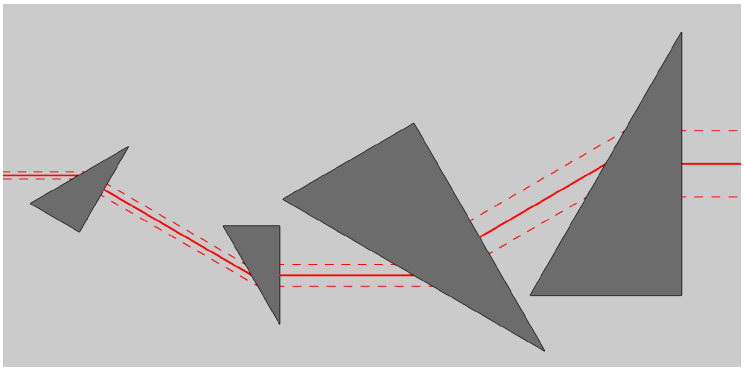

FIGURE 22 Sketch of the path of the laser beam through the four-prism beam expander showing the horizontal beam magnification due to the near Brewster angle incidence on one side of each prism. The continuous line shows the propagation of the central ray, while the dashed lines indicate the $1/e^2$ waist diameter.

For this purpose a four-prism beam expander is inserted into the cavity arm in front of the grating. The beam propagation through the expander is shown in Fig 22. Each prism is arranged so that the surface of the longest side is aligned at Brewster angle with respect to the laser mode, while the opposite surface is passed with close to zero degrees angle of incidence (AOI). This latter surface has a broadband anti-reflection (BB-AR) coating optimized for 0° AOI, with a reflectivity of R$<$ 0.8% over the entire Ti:sa emission range, minimizing the losses in the cavity. Based on the refractive index of the N-SF11 glass material ($n_{SF11} = 1.76$) of the prisms, the Brewster angle is 60.4°. This matches closely with the 30/60/90 degree cut angles of the prisms. Two small prisms with a long leg length of 12.7 mm (Thorlabs, PS871-B) and two large prisms (Altechna, custom made) with 25 mm are used. With Brewster angle incidence the expansion factor for each prism is identical to the refractive index so that the full magnification after the four prisms is close to $(n_{SF11})^4 \approx 10$. With a beam diameter of 0.6 mm before the expander a horizontal expansion to about 6 mm can be expected. The four prisms are inserted into shallow slots, which pre-set the angular alignment and are fixed with plastic screws on a rectangular metal slider which can be moved horizontally with respect to the laser beam. The expander is positioned about halfway between the curved mirror CM2 and the grating.

The grating itself is mounted on a computer-controlled stepping motor rotation stage (Micos DT-65 N). The rotation stage has a specified resolution of 0.002°. Using Eq. 152 this equals a change of 18 GHz of the laser wavelength at 800 nm. However in practice the motor motion in continuous scanning mode is by about a factor 10 more precise. This is also reflected in the unidirectional repeatability specification of 0.0002°.

4.1.2 Performance

The output power of the grating Ti:sa laser was measured as a function of the input power of the pump beam as shown in Fig. 23. The data was measured at a

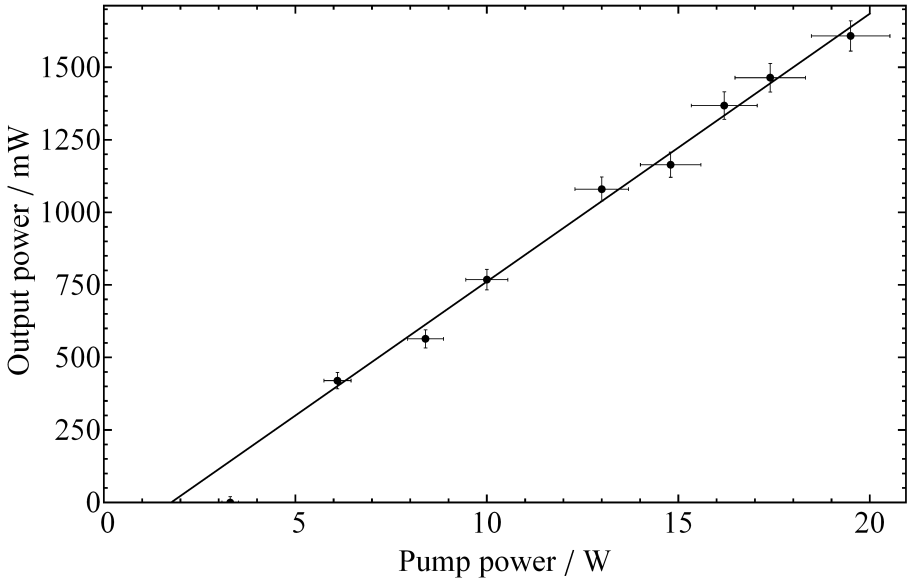

FIGURE 23 Output power vs pump power for the grating Ti:sa measured at 780 nm. The slope efficiency from the linear fit (black line) is 9.2(3)%.

wavelength of 780 nm using a broadband OC with 80% reflectivity. The threshold pump power extracted from the linear fit is 1.8(3) W. Experimentally the laser would stop lasing at pump powers below 3 W. However, this may be related to changes in the pump laser parameters which was also operating close to threshold. From the fit of the data the slope efficiency is 9.2(3)%. This is far below the typical 25-30% of the standard Ti:sa cavity, indicating relatively high internal losses of the grating Ti:sa. Furthermore, it was noticed that the output beam shape was elliptical, suggesting either multi-mode operation or bad compensation of the astigmatism introduced by the Brewster-cut Ti:sa crystal.

When constructing the grating laser, the main dimensions of the standard Z-cavity were used since the introduction of the expander was assumed from geometric optics to have little effect on the cavity stability. A new ABCD matrix calculation was performed after the first characterising tests, including the beam expansion of the four prisms. The calculation results for the first cavity design with a folding angle of $2\phi = 35.5^\circ$ are shown in Fig. 24. While the stability of the cavity is affected only slightly by the beam expansion, the results suggest that the astigmatic compensation is incomplete. Close to the output coupler the mode in the tangential plane has a $\approx$20% smaller diameter than in the sagittal plane. As seen in Fig. 25 a change of the folding angle to $2\phi = 32^\circ$ better satisfies the condition of astigmatism compensation.

After adjusting the cavity geometry for the new angles the output power as well as the beam shape did not improve significantly. In order to identify possible issues several elements were investigated or replaced. The most noticeable loss was found in the prism beam expander, having a total transmission loss of 8-10%. For the individual pairs, the small pair had a loss of about 6%, while the big pair had a loss of 3%. Considering absorption losses inside the glass as well as the specified AR reflection curve, the losses should be close to 2% per pair. Contrary

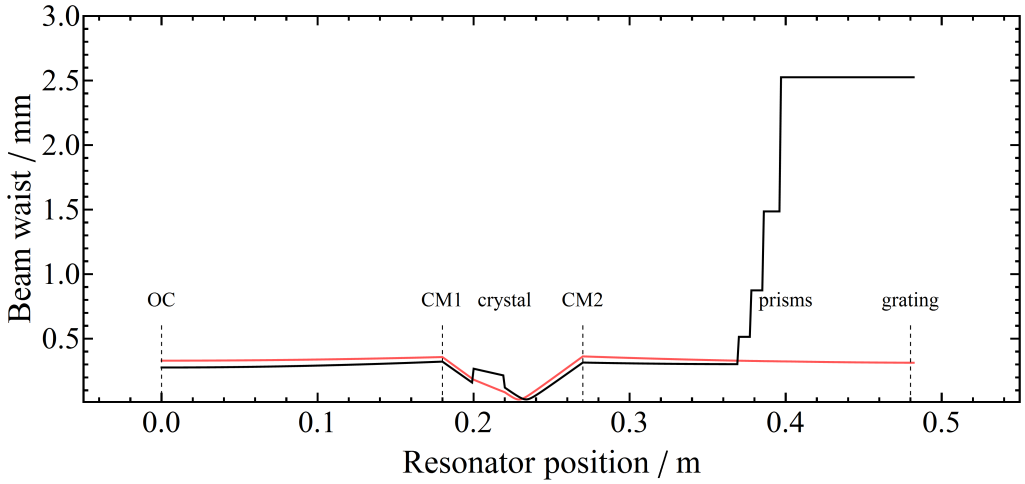

FIGURE 24 Mode waist calculation of the grating laser with the original folding angle of 2ϕ =35.5°. The results (red = sagittal plane, black = tangential plane) show a slight astigmatism, details in text.

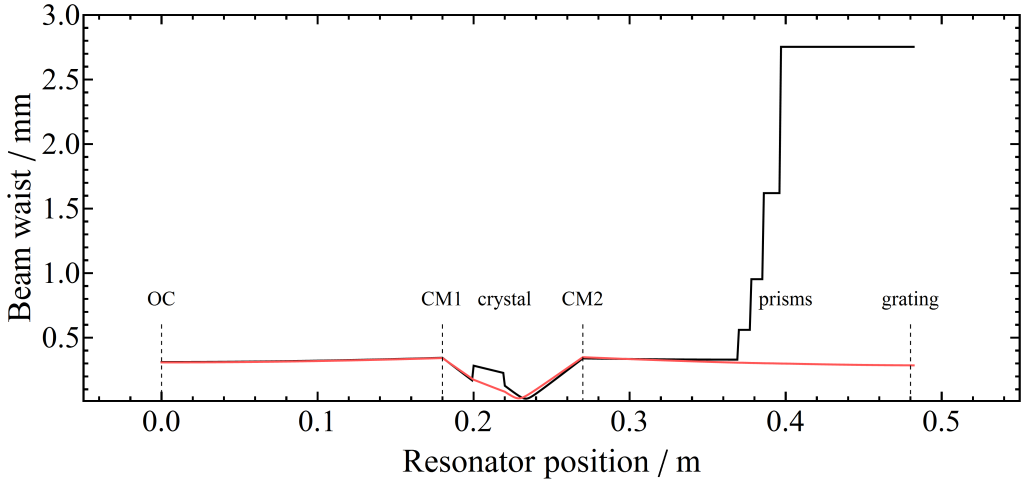

FIGURE 25 Mode waist calculation of the grating laser with the optimized folding angle of 32°. The astigmatism is compensated. Red = sagittal plane, black = tangential plane.)

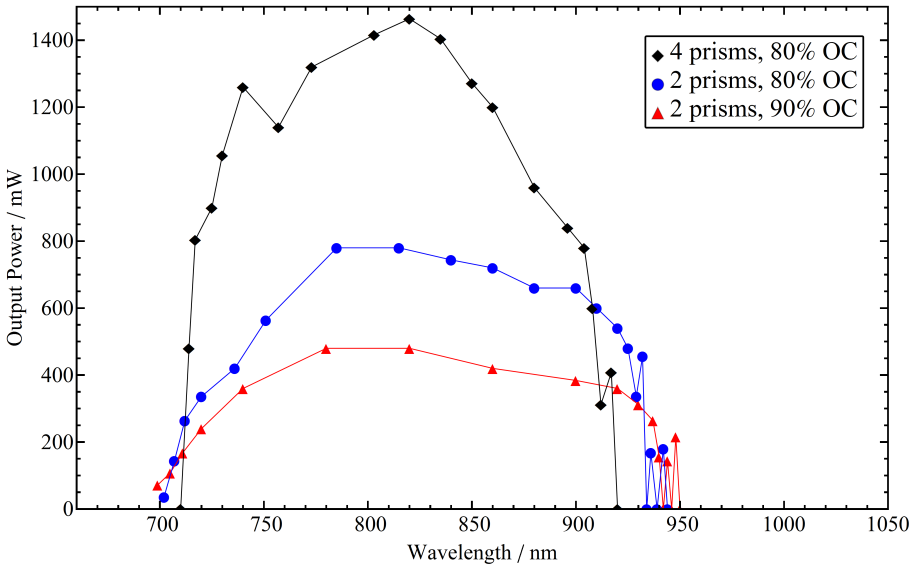

FIGURE 26 Tuning curve for the grating laser using the broadband mirror set at a pump power of 20 W. The tuning range was measured for different configurations of the prism beam expander and output coupler reflectivity.

to the previous assumption the small prism pair also had an AR coating on the leg with Brewster angle incidence and is thus not optimal for the p-polarized light in the cavity.

To see the effect of the losses of the prisms, wavelength tuning curves were taken both for the full four prism beam expander as well as using only the two larger prisms. One additional curve with two prisms and an OC with a higher reflectivity of R= 90% was obtained. The comparison of the three curves is shown in Fig. 26.

The pump power was set at 20 W. At first glance the data contradicts itself. While the power with four prisms is higher, indicating lower losses, the wavelength tuning range is narrower than with the two prisms, suggesting higher losses. This condition may be due to thermal lensing affects which were observed during measurements. For example, when tuning the grating from a position slightly above lasing threshold towards one of the limits of the wavelength range (where lasing stops), lasing action would not immediately restart when returning to the original position, but would require further movement towards the gain maximum, suggesting some dynamical instability. During lasing the inversion in the crystal is depleted relatively fast and the thermal load is low. When lasing stops, only spontaneous emission occurs, causing a higher thermal load and thus increased thermal lensing. A second possibility may be the heat load on the grating, which may expand or deform when lasing occurs. The higher output power when using four prisms therefore may be due to a compensation of the thermal lensing in the crystal, or to a wider heat distribution on the grating.

Even when using only two prisms and the 90% OC the tuning range was narrower than expected from estimates using the rate equations, which were suggesting a range of 695-1020 nm for a 80% OC. A parameter that significantly

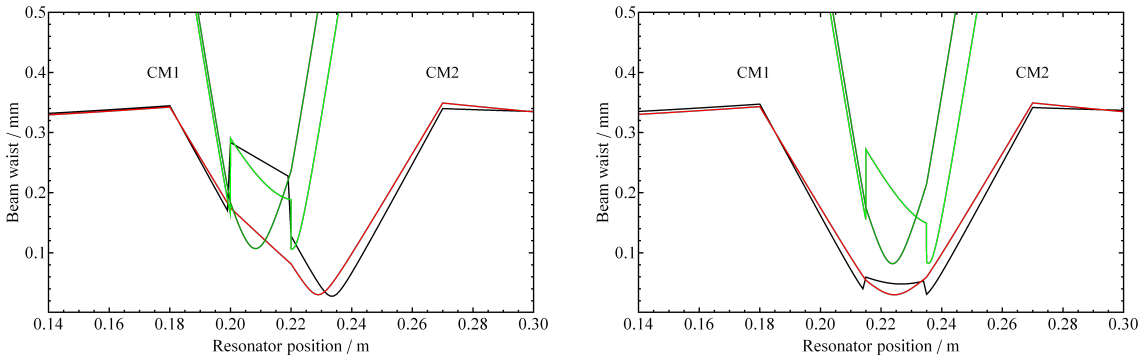

FIGURE 27 Left panel: Ti:sa mode-waist (red for sagittal, black for tangential) and pump waist (dark green for sagittal, green for tangential) with the crystal in the asymmetric position. Right panel: crystal in symmetric position between the curved mirrors.

influenced the tuning range was identified as the Ti:sa crystal positioning in between the curved mirrors. A comparison of the mode waist calculations for the two configurations is shown in Fig. 27, with the asymmetric positioning shown in the left panel and the symmetric position in the right panel. Using asymmetric positioning (normal for the Z-shaped design) the Ti:sa mode-waist in the crystal is larger. This allows for good mode-matching with the pump beam and thus a high average output power. With the crystal centred symmetrically between the folding mirrors the Ti:sa waist is smaller than the pump waist. While this leads to reduced overall output power, the gain will be higher as the Ti:sa mode is within the Gaussian intensity maximum of the pump beam and thus in an area of higher inversion density.

Using a reduced pump power of 16 W to keep below the damage threshold with the crystal centred, the wavelength tuning curves were re-measured as shown in Fig. 28. The wavelength range is considerably increased and reaches from 684-940 nm for the four prism configuration. The asymmetry of the tuning curve with the longer tail towards higher wavelengths is due to the gain profile of the Ti:sa medium shown in Fig. 8. Using only two prisms the range is expanded from 674-1010 nm and with the 90% OC from 669-1040 nm. Furthermore, the dynamic instabilities due to thermal lensing did not occur with the centred crystal position. This is likely a result of the weaker sensitivity of the smaller Ti:sa mode to lensing effects as well as the lower pump power.

The linewidth of the grating laser was measured using the WS6-UV wavemeter software. Using the four prism configuration and the Ti:sa crystal in the center position, the linewidth ranged from 2-6 GHz depending on the wavelength. With the crystal in the off-center position the linewidth often changed irregularly spanning from 2-15 GHz. For the two-prism configuration the linewidth was mostly larger than 15 GHz, regularly exceeding the maximal measurement range of the wavemeter. For comparison, in [62] a linewidth of 6.5(9) GHz and a tuning range from 690-1000 nm was reached using four different mirror sets, while the commercial system used in [64] demonstrated a range of 715-960 nm with a single mirror

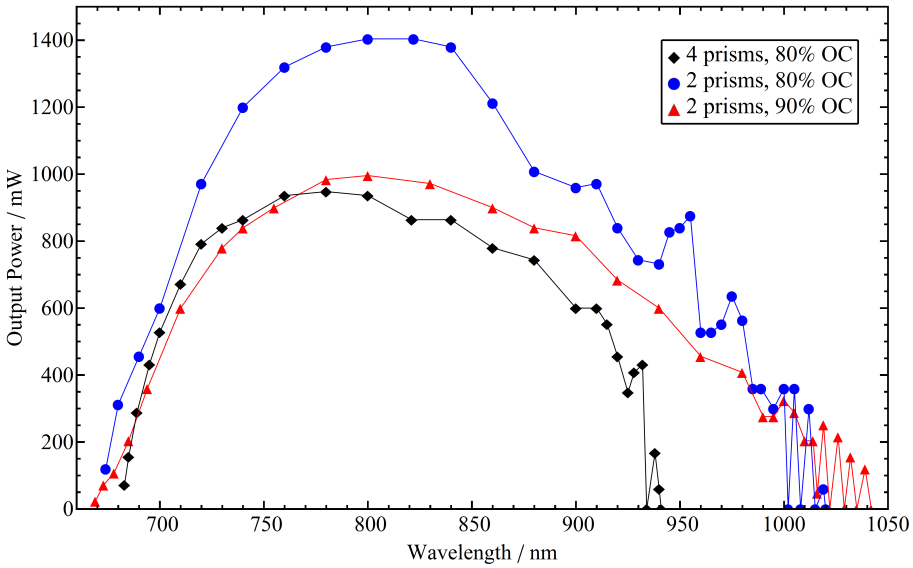

FIGURE 28 Tuning curve measured with the Ti:sa crystal centred between the curved folding mirrors and a lower pump power of 16 W. The possible wavelength range is extended and reaches from 669 nm to 1040 nm for the best case scenario. Note the higher output power of the two prism configuration.

set, but at higher output powers of up to 2.6 W.

4.2 Development of an ionization scheme for samarium

There are seven naturally occurring isotopes of samarium ($Z = 62$) from ^{144}Sm to ^{154}Sm, ranging in abundance from 3% to 27%. The isotopic chain of samarium exhibits two nuclear shape change transitions, indicated by a sudden change of the nuclear deformation parameter β. One transition is close to the stable nucleus ^{152}Sm ($N = 90$) with the other at the short-lived nucleus ^{134}Sm ($N = 72$, $T_{1/2} = 9.5$ s) [65].

High-resolution laser spectroscopic information on isotope shifts and hyperfine structure is available for all the naturally occurring isotopes on a multitude of transition lines [66, 67], for the long-lived odd nuclei ^{145,151,153}Sm [68, 69] and with slightly worse resolution for several of the neutron-deficient isotopes down to ^{138}Sm [70]. Samarium is therefore a good candidate to validate the precision of in-source measurements and sensitivity to changes in nuclear structure for any future applications without the need for on-line cyclotron beam time.

Laser excitation and ionization of samarium has been demonstrated using dye laser systems, however an efficient scheme suitable for Ti:sa lasers is so far missing. Many transitions from the atomic ground state are known [71, 72], and information about higher-lying excited states can be collected from various sources [73--77]. This data can however be considered incomplete and in most cases the transitions used are not easily available to Ti:sa lasers. As these high-lying states as well as autoionizing resonances are critical for an efficient ionization

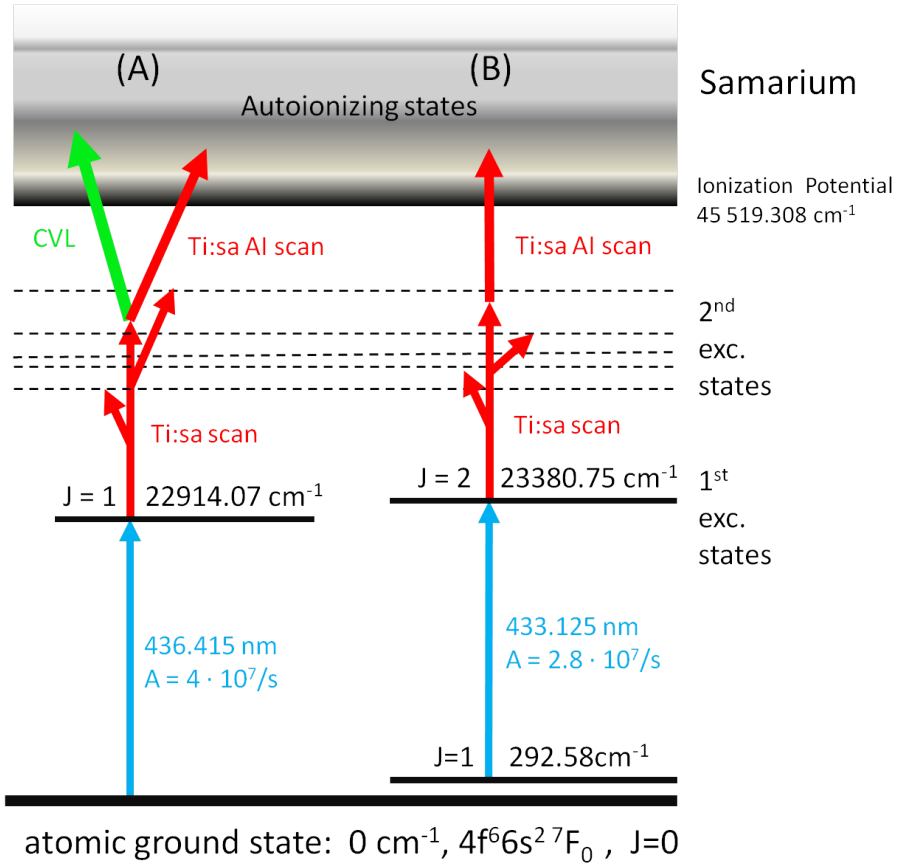

FIGURE 29 Laser excitation and ionization schemes of samarium used for the search for new high-lying excited states and autoionizing states.

process more information was gathered using the grating-based Ti:sa.

4.2.1 Experimental set-up and the search for second excited states

The search process is explained through the excitation scheme shown in Fig. 29. Two different first step transitions were used, one (A) at 436.415 nm from the ground state, the other (B) at 433.125 nm originating from a low-lying thermally populated state at 292.58 cm^{-1}. A frequency doubled broadband (single etalon) Ti:sa provided the wavelength required for these steps. The grating laser is then scanned to further excite the atom from the levels at 22914.07 cm^{-1} and 23380.75 cm^{-1}, respectively. Whenever the total photon energy matches a higher-lying excited state, an additional photon from either the grating laser or the first excitation step can photo-ionize the excited atom. Alternatively in scheme (A) a high power CVL was added, which can also provide photons for ionization. Afterwards a few select higher excited states were chosen, from which the scanning process was repeated to find new auto-ionizing (AI) states.

To provide an atomic source a small amount of samarium-oxide powder was inserted into the tantalum furnace (l=3 cm, inner ⌀=1 mm) of an atomic beam unit (ABU) (see section 3.2) and heated up to approximately 1000 °C (no accurate temperature calibration available). The laser beams were overlapped,

time synchronized and sent into the ABU perpendicular to the atomic beam. The first IP of samarium at 45519.30793(43) cm^{-1} [78,79] is below the energy that can be reached by two photons from the first step transition in both scheme (A) and (B). To minimize non-resonant background of the ion signal, the laser power for the first step was limited to a few mW. The grating Ti:sa was then scanned from about 720 nm to 900 nm. Any photo-ions created are deflected onto an electron multiplier tube (EMT) with the ion counts recorded after post-amplification of the EMT signal and time-gating for a reduction of background.

As the gain of the Ti:sa crystal changes with wavelength this affects the delay of the grating Ti:sa pulse with respect to the synchronization trigger of the two lasers. This delay had to be compensated using a Pockels Cell in the laser cavity for the first step transition, which had to be adjusted roughly every 5-10 nm.

4.2.2 Peak identification

The recorded spectrum contains many peaks that need to be identified and analysed. For this purpose an automatic peak identification procedure was written in Mathematica [53]. The non-resonantly ionized background signal appears to match well with a Poisson distribution as can be seen in the left panel of Fig. 30. When the 15 W CVL was added an additional background appeared, see right panel of Fig. 30, which showed clear super-Poissonian (wider than Poisson) counting statistics. This is likely a result of multi-photon ionization of contaminants caused by the strongly focused high power laser and the relatively large intensity fluctuations of the CVL. By using weaker focusing of the CVL this background could be minimized. The background signal can therefore be assumed to follow Poissonian statistics with a slowly varying mean λ that is affected mainly by drifts in laser power or oven temperature. This can be used to set a simple criterion:

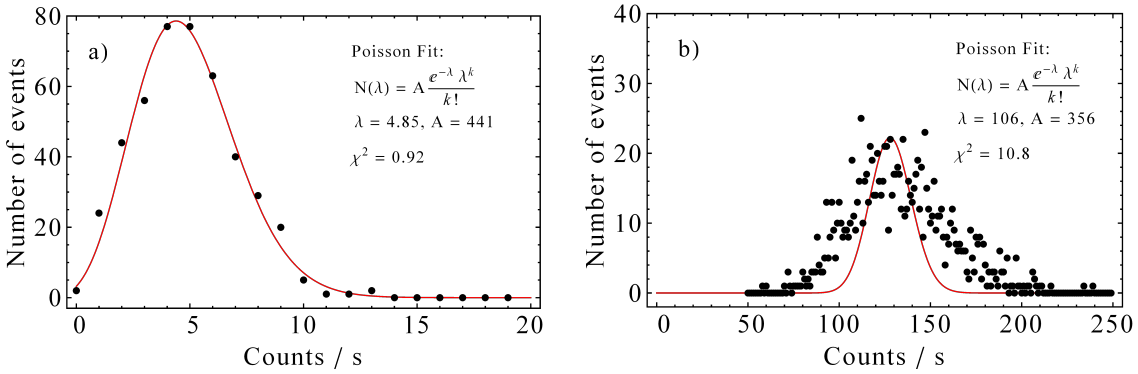

FIGURE 30 Ion count rate distribution and comparison with Poisson distribution. Left panel: the non-resonant photoionization count rate agrees well with Poisson statistics. Right panel: with a strongly focused CVL laser beam added the count rate is higher, but disagrees with the Poisson distribution.

whenever a data point deviates sufficiently from the mean background such that the probability for it being random is very small with respect to the size of the whole data set then this data point is likely to belong to a resonance peak.

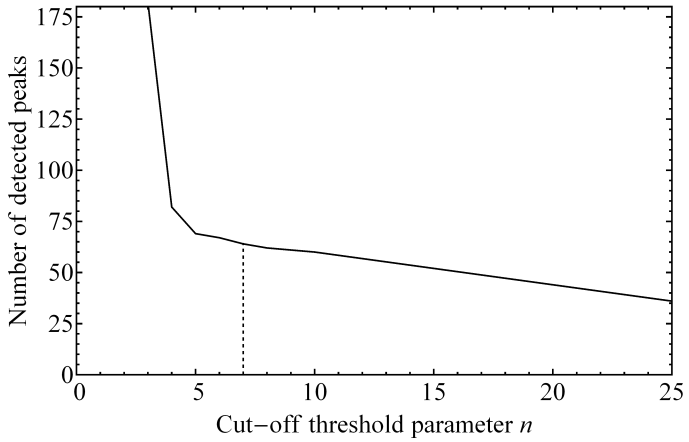

FIGURE 31 Effect of the cut-off threshold n on the number of detected peaks.

Considering a sample size of N data points and a Poisson-distributed ion signal, the probability p for a data-point to lie n standard deviations $\sigma = \sqrt{\lambda}$ above the mean λ can be given as:

$$p = 1 - \left(\mathrm{e}^{-\lambda} \cdot \sum_{k=0}^{\lambda + n \cdot \sigma} \frac{\lambda^k}{k!} \right)^N$$

with $\lambda + n \cdot \sigma$ rounded down to the nearest integer. For a typical ABU data set with close to $N = 50000$ points and a background level of five cps the threshold was set to $n = 7$ in order to reduce the chance for a false positive to below $p = 0.01$. Some of the weaker transitions might be missed with such a strict cut-off, but this is of no concern for developing an efficient RIS scheme.

From the data points exceeding this cut-off threshold the maxima are selected as starting points for the fitting procedure. As shown in Fig. 31 the number of detected maxima in a scan is critically dependent on the cut-off threshold n. For $n < 5$ the number of detections sharply rises as more and more statistical fluctuations are considered as peaks. The vertical dashed line indicates the threshold used in the evaluation. Instead of a fixed standard deviation σ this parameter is calculated directly from the data points within a small energy range of $10\,\mathrm{cm}^{-1}$; in this manner the procedure can adapt to any slow drifts of the background signal. An example showing the mean, the threshold level as well as the identified maxima for a small excerpt of the data set is shown in Fig. 32.

4.2.3 High-lying excited states

Following identification of the peak positions the spectra were fitted using a multi-peak Gaussian with a local background. The results of the scans from both first step transitions are shown in Fig. 33. The atomic levels already identified from literature are shown as dashed grey lines. For better comparability the two scans are shown on top of each other, offset by 5000 counts/s. It is noticeable that many peaks show up at identical energy levels for both the lower and the higher data

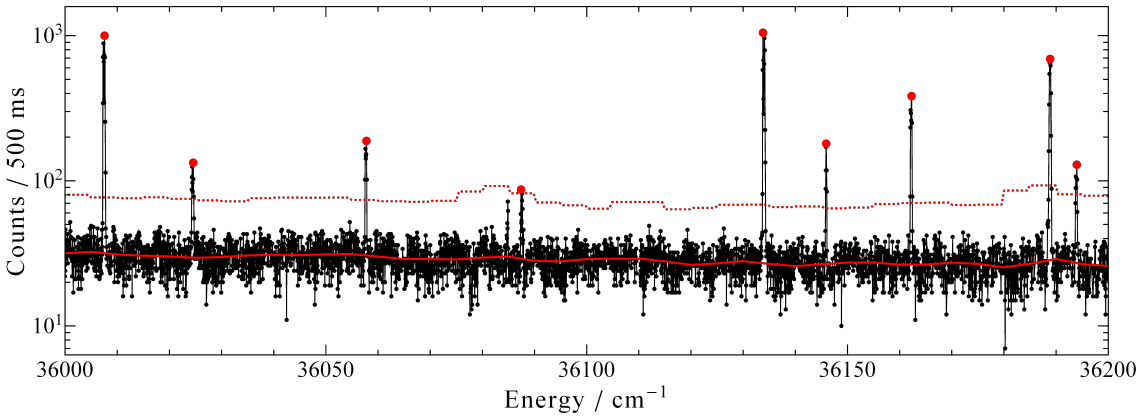

FIGURE 32 Small excerpt of a scan showing the the data (black points), the slowly varying background level (red line), the threshold level at 7σ (red, dashed line) and the identified peak positions (thick red dots).

set. This is however not always the case and the ion signal intensity of the peaks is as well often quite different. The absence or additional appearance of peaks can be explained by the different spins of the starting energy level. For scheme A which uses a $J = 1$ first excited state only higher excited states with $J = 0, 1, 2$ can be reached, while for scheme B with $J = 2$ states with $J = 1, 2, 3$ can be excited with sufficient strength.

The peak height differences are due to variations in transition strength as well as the efficiency of the ionization process, as possible auto-ionizing resonances above the IP can heavily influence the signal intensity. It is therefore not immediately clear which of the higher excited states is best suited for an ionization scheme.

4.2.4 Ionization laser comparison

The impact of a non-resonant ionization laser can be observed in Fig. 34, where a comparison is made for scheme (A), using either a second photon from the grating laser or with the addition of the CVL laser. The two scans are again separated for clarity by an offset of 10000 counts/s. For most of the peaks a significant increase of ion signal is noticeable using the CVL, in some cases by more than a factor of 20. However for a few select peaks only a minimal change in ion signal is apparent. This suggests that for those peaks the ionization process was already quite efficient considering that the power density contributed by the CVL did not affect the signal. It is therefore likely that a relatively strong AI state was accidentally encountered by a second photon from the grating laser.

A table summarizing each identified level along with information on peak intensity (normalized to 1000 for the highest peak) for the two schemes is given in Table 12 in Appendix 1. The experimentally determined energy levels were compared with a compiled list of all the literature data. The typical error of the experimentally determined values can be assumed to be $< 0.1\,\mathrm{cm}^{-1}$, which was estimated from the uncertainty of the wavemeter as well as from the comparison

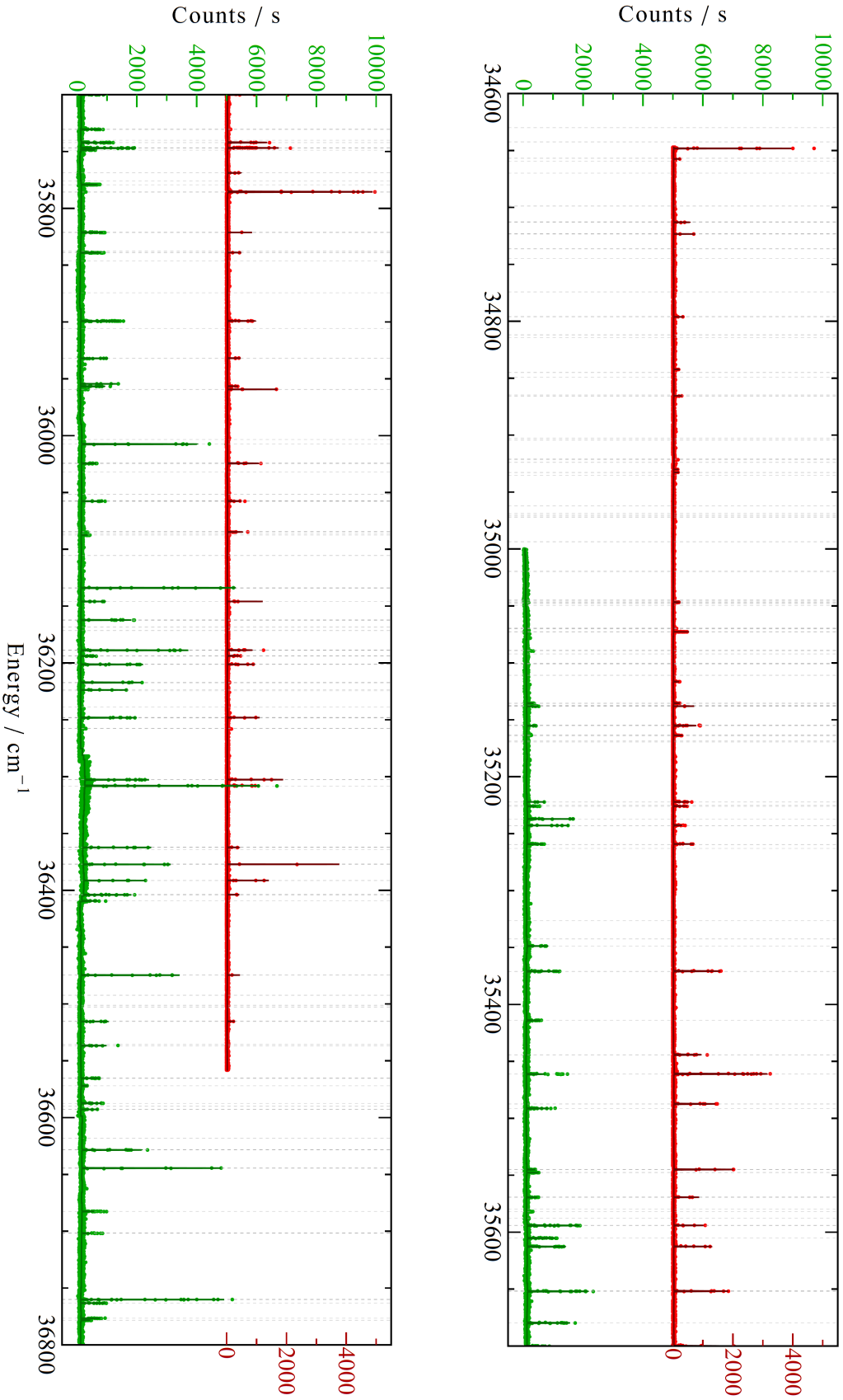

FIGURE 33 Higher-lying atomic states, excited from the lower levels at 22914 cm^{-1} (red data points and fit curve, offset by 5000 counts/s for better clarity) and 23380 cm^{-1} (green points and fit curve).

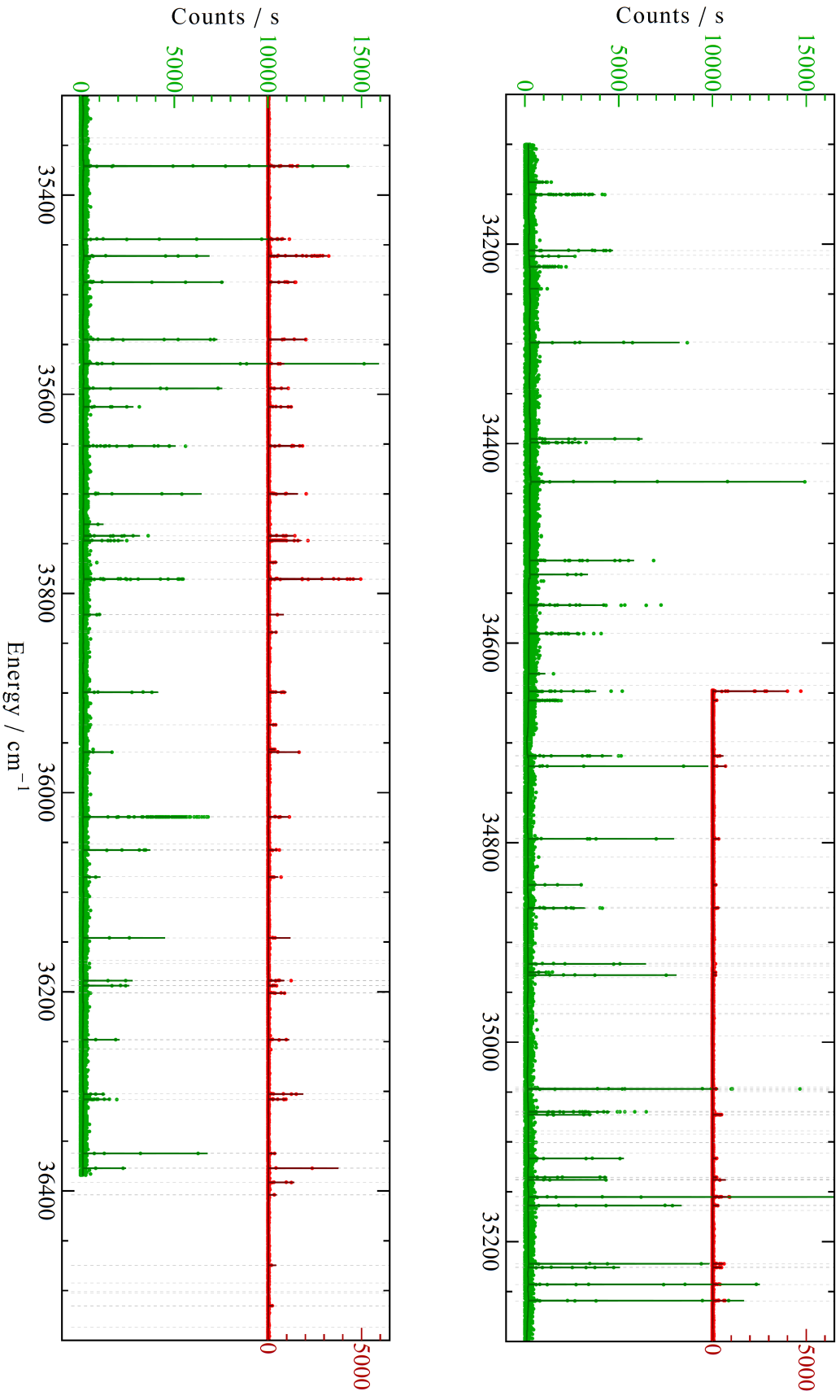

FIGURE 34 Comparison of ion signal generated from excitation from the lower level at 22914 cm^{-1} using either the 15 W CVL for the ionizing step (green points and fit curve) or only using a second IR photon from the grating laser (red points and fit curve).

between the two schemes. Whenever an agreement within 1 cm^{-1} was found, the literature value was added to the table for comparison along with its deviation from the experimental value. In most cases the agreement with literature data is good to within 0.1 cm^{-1}, though a few exceptions $> 0.5\,cm^{-1}$ exist, in particular when a comparison can only be made to the data of [74], in which an uncertainty of 0.3 cm^{-1} is stated. In total 14 new states of even parity were found. The table also lists the new J values for the states. If no new information or inconsistencies with literature was found, the literature value was taken. In a few cases however, the possible J values were narrowed down and in four cases (#51, #55, #72, #83) there is a definite disagreement with the literature assignments. The disagreement is quite obvious as the levels were excited from the J = 1 level at 22914.07 cm^{-1}, but the assigned J values were J = 3,4.

4.2.5 Auto-ionizing states

A few select second excited levels were chosen to start the search for auto-ionizing states. A second broadband Ti:sa laser was used to drive the transitions to these states. Three of the schemes use the first excited state at 22914.07 cm^{-1} and are designated A1, A2 and A3, using the second excited states at 35155.15 cm^{-1}, 34206.42 cm^{-1} and 34298.70 cm^{-1}, respectively. One additional scheme, B1, used the first excited state at 23380.75 cm^{-1} and second excited state at 36536.65 cm^{-1}. The choice of the states is mostly arbitrary. As previously noted, the ion signal intensity of the second excited states is not a reliable indicator of the actual transition strength of the second excitation step. Therefore the resulting ionization schemes are not assumed to be the most efficient ones.

The scans of the auto-ionizing states are shown in Fig. 35. The two middle scans cover the energy range just above the ionization potential at 45519 cm^{-1}, the other two scans start at a slightly higher energy scale. While many resonances with varying intensities and widths can be seen in each scan, the two intense, sharp resonances in scan A2 are particularly striking as they peak far higher than the rest.

While the automatic peak fitting routine worked well for the second excited state spectra, the auto-ionizing spectra are far more complicated as multiple peaks overlap and linewidths of the peaks strongly differ. For fitting of the AI states a more time consuming manual approach was taken. A list of some of the prominent auto-ionizing resonances is given in Table 13 in Appendix 2. The list contains the level energy, an indication marking the scheme, signal intensity (normalized to 1000 for highest signal), as well as the resonance width. Several sources give a relatively large collection of auto-ionizing states, the most recent [80] containing level energies from 46000-47000 cm^{-1} as well as an assignment of J values, [81] and [82] report on the range 45000-48000 cm^{-1} and [83] from 48800-51200 cm^{-1}. Additional information about AI states exists, with ref. [84] indicating states of even parity and ref. [85] detailing levels in the range of 60000-70000 cm^{-1}, which is far out of our measurement range. Though collectively more than 200 levels mentioned in literature lie within our measurement range only very few are

within $1\,\mathrm{cm}^{-1}$ of our identified peaks. Furthermore, some may be close just by pure coincidence due to the high level density and may not actually be a state of the same configuration. Even though the scans for A1-3 all start from a high lying J=2 state there are very few cases where peaks appear at the same energy level in two or even all three scans. Scheme B1 has no overlap in the measured energy range.

The most promising laser ionization schemes are summarized in Fig. 36. They are the ''pure'' Ti:sa schemes using the steps $0\,\mathrm{cm}^{-1} \rightarrow 22914.07\,\mathrm{cm}^{-1} \rightarrow 34206.42\,\mathrm{cm}^{-1}$ with a final step to either $46459.2\,\mathrm{cm}^{-1}$ or $45546.8\,\mathrm{cm}^{-1}$, and the ''CVL scheme'' using the transitions $0\,\mathrm{cm}^{-1} \rightarrow 22914.07\,\mathrm{cm}^{-1} \rightarrow 35155.15\,\mathrm{cm}^{-1} \rightarrow 54740\,\mathrm{cm}^{-1}$. The energy level in the CVL scheme may or may not be an actual AI state, and as the CVL is not tunable this is unknown. Both schemes delivered similar ion signal intensities, though a careful comparison with respect to focusing and saturation conditions was not made. As stated before, the CVL scheme suffered from slightly higher non-resonant background, possibly due to multi-photon ionization of contaminants with the high power CVL, as stronger focusing of the CVL considerably increased this background.

A third possibility for efficient ionization, not previously mentioned, is provided by the one-colour ''blue-blue'' scheme, which uses a single resonant transition from $292.58\,\mathrm{cm}^{-1} \rightarrow 23243.84\,\mathrm{cm}^{-1}$ and a second non-resonant or AI transition with the same wavelength towards $46195.72\,\mathrm{cm}^{-1}$. With a high laser power in the SHG of $> 500\,\mathrm{mW}$, this scheme yielded a factor of three higher ionization signal. Before using this scheme for spectroscopy the possible autoionizing structure in the continuum should be investigated. As the ionization step is using the same laser as the first step transition this unknown structure could seriously affect any measurements of isotope shifts or hyperfine structure.

4.2.6 Saturation

For all three excitation steps of the ''pure'' Ti:sa scheme with the final step to $46459.2\,\mathrm{cm}^{-1}$, saturation curves were measured and are shown in Fig. 37. The data was fitted using Eq. 5 assuming $\delta = 0$. The first two excitations steps are easily saturated at low intensity levels of $3.3(4)\,\mathrm{mW/cm^2}$ and $146(10)\,\mathrm{mW/cm^2}$, respectively. The third step, which is the AI transition, is not fully saturated even at high intensities. From the slope a saturation intensity of close to $15.1(6)\,\mathrm{W/cm^2}$ can be estimated. The errors given here are only the estimates from the fitting procedure. As the laser spot diameters were measured only by eye, the actual errors of the intensity measurement are much larger.

4.2.7 Conclusion

The grating-based Ti:sa laser is an important technical development with which new atomic states can be identified to build up efficient ionization schemes. However due to the fact that unknown higher-lying excited or auto-ionizing states influence the ion signal it is difficult to obtain an optimal scheme with the highest

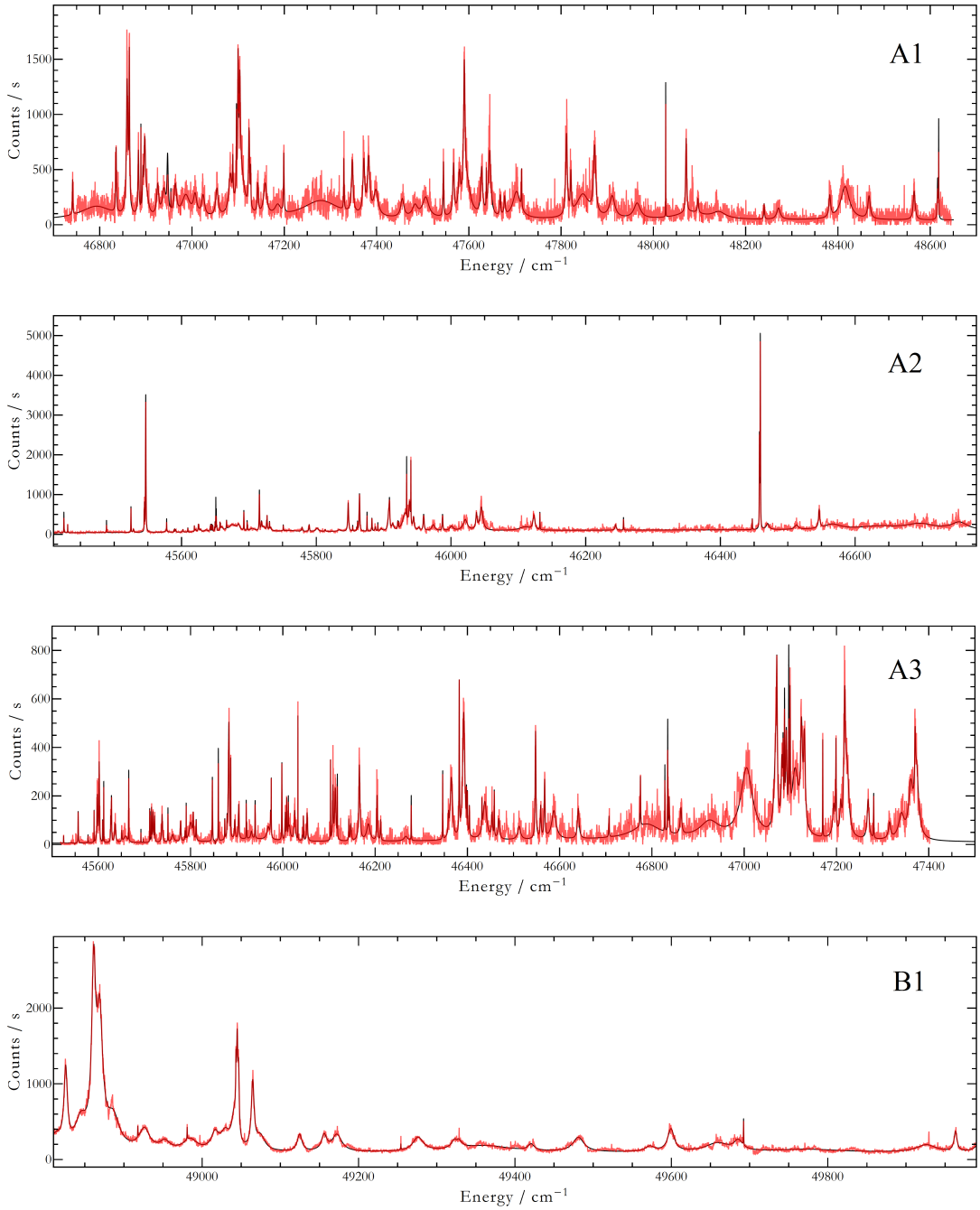

FIGURE 35 Several scans for autoionizing resonances. See text for an explanation of the designations A1-A3, B1. Fits through the data points are shown as a solid line for each scan.

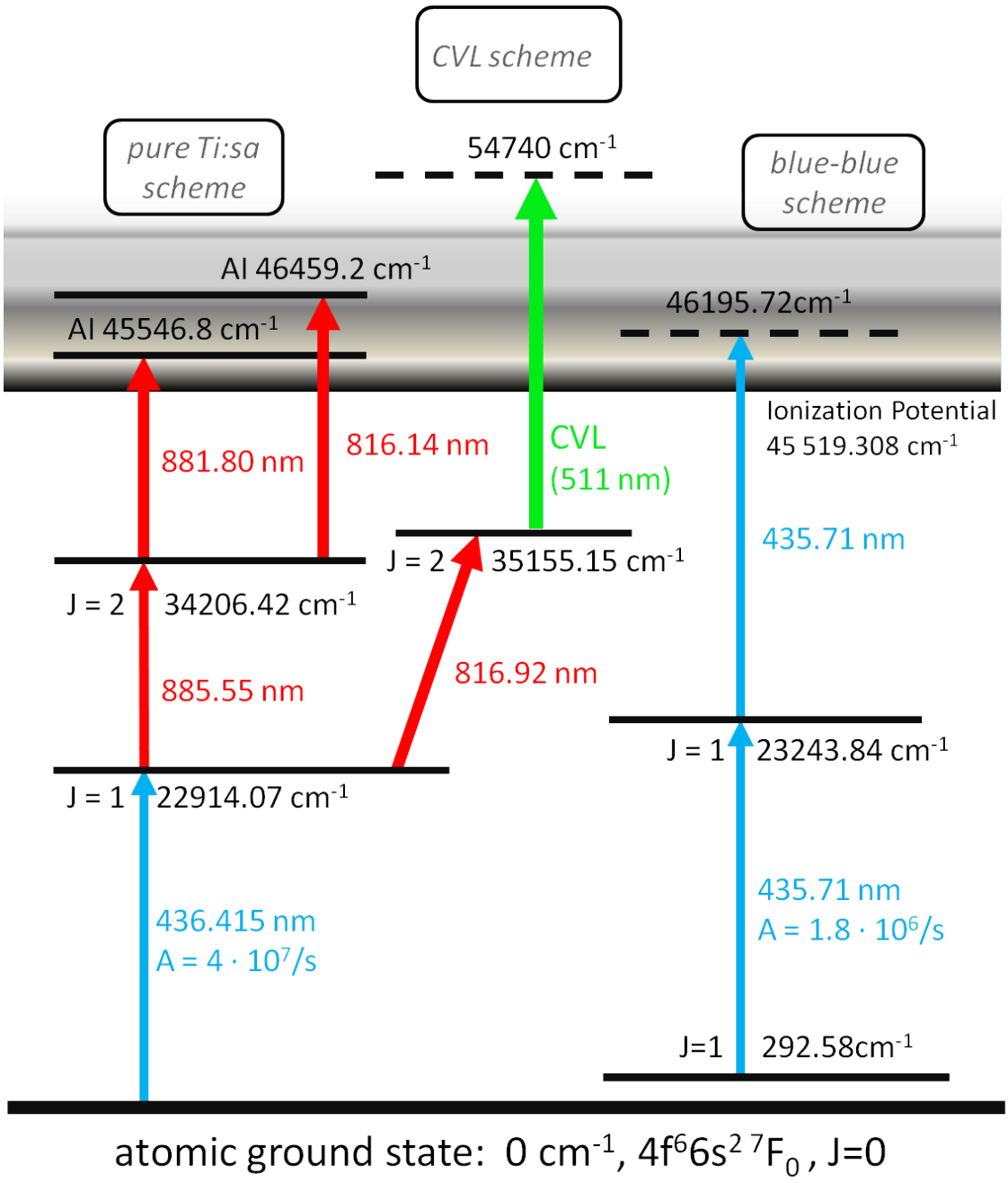

FIGURE 36 Several identified ionization schemes for samarium. The pure Ti:sa schemes use three resonant transitions and are likely candidates for further high resolution spectroscopy. The CVL scheme has similar efficiency but slightly larger non-resonant background and the blue-blue scheme provides the highest ion signal but is potentially less suitable for spectroscopy.

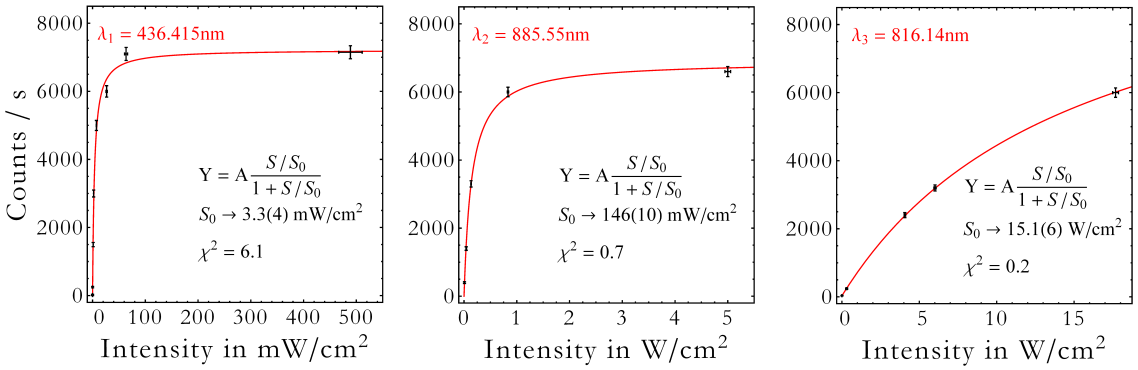

FIGURE 37 Saturation curves of excitation steps 1-3 (from left to right) of the ''pure'' Ti:sa scheme.

transition strengths. The comparison between an ionizing step provided by either a further Ti:sa laser or a high power (15 W) CVL laser shows that the efficiency of a scheme using a ''strong'' auto-ionizing step might still be weaker than a brute force non-resonant step. On the other hand, such a scheme might only be non-resonant in name as one cannot be sure that AI states might not be targeted coincidentally due to the lack of wavelength scanning capabilities of the CVL.

For future studies it would be important to have the possibility to decouple the influence of the ionization step from the evaluation of the strength of intermediate transitions. This could be done either by measuring fluorescence, or by performing multiple scans of the grating laser with varying intensity levels. The intensity dependence or saturation behaviour of the excited state transitions would be a helpful indicator to separate out the influence of the ionizing step. A different approach would be comparison with theoretical calculations. While the accuracy of theoretical calculations is often insufficient to directly identify the configuration of an identified resonance, the accuracy for level splittings might in many cases be enough to allow a comparison with experimental data. With known level configurations it is then as well possible to estimate transition amplitudes.

Studies of the isotope shifts and hyperfine structure require a laser system with a narrower linewidth as the magnitude of these perturbations in samarium is much smaller than the bandwidth of the standard Ti:sa lasers, lying in the range of several hundred MHz to a few GHz for accessible ground-state transitions [86]. Possibilities to reduce the linewidth of the Ti:sa lasers are discussed in the next two chapters.

High resolution studies also have different requirements for the choice of transitions. While the schemes developed here may provide a good signal intensity, the isotope shift of the chosen first step transition is relatively small compared to other transitions given in [86]. Furthermore the atomic ground state will have no hyperfine splitting because of its spin (J=0). Determination of the hyperfine coupling constant will therefore require either a large splitting in the upper level of the transition or the use of a thermally populated lower state. As spectroscopy during on-line runs at the IGISOL facility will be using a relatively cold source (buffer gas temperature = 300 K), ionization schemes using thermally populated

states will be weaker when compared with hot-cavity sources.

For accurate spectroscopy results in a multi-step RIS scheme the structure of the excited higher-lying states can also prove critical. To avoid misinterpretation of results it may be useful to use a simple two-step ionization scheme with the final transition to a very broad AI state, or to use a laser with a very large linewidth. This smears out most perturbing effects. To find such two-step schemes the intra-cavity frequency doubling technique should be further developed to work in combination with the grating laser. Such a widely tunable source in the blue wavelength region would be a powerful tool to simplify the search for these schemes.

5 A DUAL ETALON TI:SA LASER FOR IN-SOURCE SPECTROSCOPY AND IMPROVED WAVELENGTH CALIBRATION USING A SCANNING FPI

5.1 Motivation

For highest laser ionization efficiency in a non-spectroscopic resonance ionization scheme the spectral bandwidth of the exciting laser is usually required to be at least as wide as the splitting of the sub-levels of a transition caused by hyperfine structure. With a fundamental linewidth of approximately 5 GHz the Ti:sa lasers are well suited for this task and for special cases with very large hyperfine splittings a larger linewidth may be reached by removal of the etalon from the cavity.

If however the goal is the ionization of a specific isotope or in-source laser spectroscopy this linewidth is often too large. For a reasonable resolution while still maintaining good ionization efficiency the laser linewidth should be close to the Doppler broadened linewidth of the transition, which is typically of the order of 1-2 GHz. While a single etalon with a high finesse value could achieve this necessary linewidth reduction, a high finesse implies an increased intensity within the etalon, which can surpass the damage threshold of the coating. The solution is therefore the addition of a second thicker etalon into the laser cavity.

In the first application of such a dual-etalon Ti:sa laser to resonance ionization spectroscopy, discrepancies became apparent in comparison to high resolution data [87]. This is discussed in Article III [88], which is presented in the following section. Deviations from literature were found to correspond with the relatively high uncertainties of the wavemeter (High Finesse WS6-UV) which has a specified absolute accuracy of 600 MHz at the 3σ level. To address these discrepancies a relative wavelength measurement using a home-made scanning Fabry-Pérot Interferometer (FPI) was employed. Following publication, further calculations of the laser linewidth, an improved analysis procedure for the FPI data and a second method for the calibration of the FPI free spectral range (FSR) have been

performed and are presented in this chapter.

5.2 Article III

The article on the characterization of a dual-etalon Ti:sa laser has been published in Hyperfine Interactions, volume 227 (2014), pages 113-123. Discrepancies with high resolution literature data motivated the development of a plane-parallel Fabry-Pérot Interferometer which, when used in combination with the dual-etalon laser identified the wavemeter as the source of uncertainty. This development is presented in the following 11 pages (print version only).

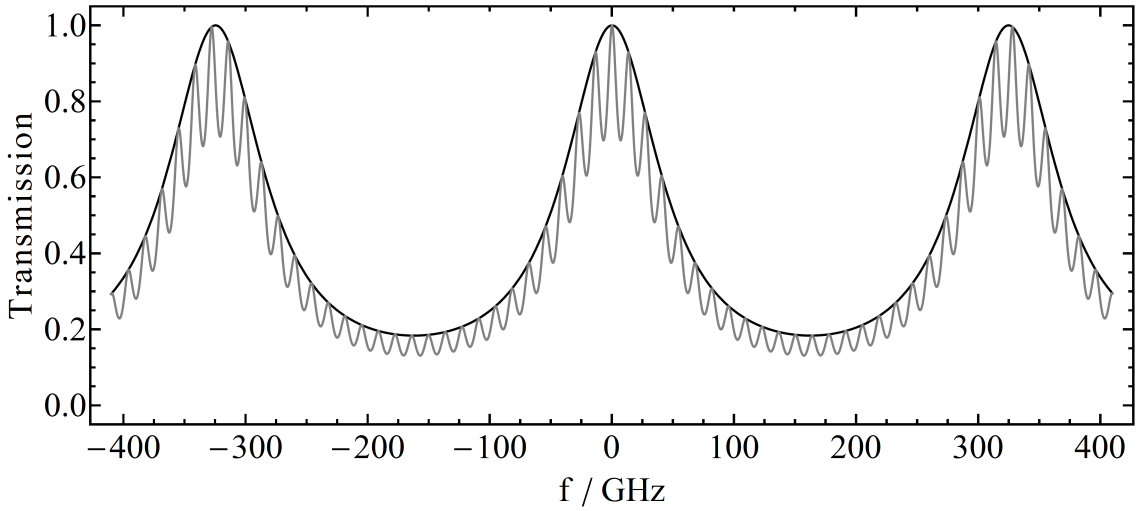

FIGURE 38 Single-pass transmission curves of the thin (0.3 mm) etalon in black and the combination of thin and thick (6 mm) etalon in grey.

5.3 Simulation of linewidth and mode structure

Estimates for the laser linewidth can be made using the number of round-trips in the cavity during pulse build-up as discussed in Article III. A more realistic approach to simulate the linewidth of the dual-etalon Ti:sa laser is the use of the rate equations 110 discussed in chapter 2. These calculations model the effective round-trip gain for each mode during pulse build-up.

The etalons introduce a wavelength-dependent loss which can be calculated using the transmission function given in Eq. 127. The transmission of the single thin etalon is shown as the black line in Fig. 38. A thickness of 0.3 mm, a single surface reflectivity R of 40 %, a refractive index n of 1.54 and a center wavelength of 800 nm were used for the calculation. The actual reflectivity will depend on the wavelength and the coating. The grey line in Fig. 38 illustrates the transmission of both the thin etalon and a second thicker etalon (the transmission functions multiply). The second etalon has a thickness of 6 mm and is made from undoped Yttrium Aluminium Garnet (YAG). The refractive index of the YAG crystal is ≈ 1.82 at 800 nm resulting in a reflectivity of 8.4 % for each surface as calculated from the Fresnel equations 82. The FSR of the thin etalon is 324 GHz and that of the thick etalon 13.6 GHz.

As long as there is no interference between the etalons, the wavelength dependent single-pass loss in the resonator is $l(\lambda) = 1 - T_{\mathrm{E1}}(\lambda) \cdot T_{\mathrm{E2}}(\lambda)$. For the Z-shaped resonator calculations the square of the transmission has to be taken, as both etalons are passed twice during each round-trip of the cavity. To keep the calculation time low only a small region around a single transmission peak of the thin etalon was taken into account as shown in Fig. 39. The other transmission peaks will have negligible impact as they are suppressed sufficiently by the birefringent filter. The multi-mode rate equations then use the loss calculated for each

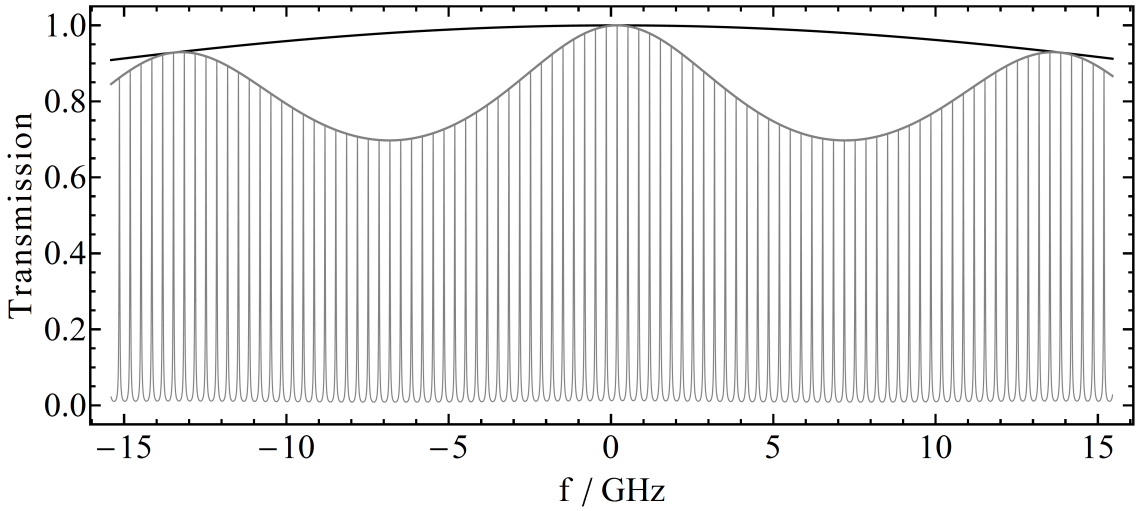

FIGURE 39 Zoomed in view of the transmission curves of the thin (black) and thick etalon (grey) as well as the mode structure of the $L = 45$ cm long Ti:sa cavity (thin grey curve).

Ti:sa mode, which are separated by one FSR of about 330 MHz, while all other parameters such as gain or output-coupler losses are kept constant.

From this input the rate equations yield the photon number of the laser for each mode for a single pump pulse. Results for the single thin etalon and the dual etalon combination are shown in Figs. 40 and 41, respectively. The calculations were performed at an average output power of 4 W and center wavelength of 800 nm. The linewidth will decrease for lower power levels as well as for wavelengths further from the gain peak.

As seen in Fig. 41 the two secondary transmission maxima within the calculation range are suppressed by nearly three orders of magnitude compared to the main peak. While this seems to be sufficient for laser spectroscopy, it may still create noticeable spurious resonances if the atomic transition is heavily saturated. Furthermore, a slight misalignment of the thick etalon with respect to the thin etalon transmission maximum will lead to an even weaker suppression of these side-modes and eventually to a mode-jump. This is the reason why a careful synchronization of the two etalon positions is required for a clean wavelength scan as demonstrated in Article III. It should however be noted that the suppression of the side-modes improves with a reduction of the laser output power. The FWHM of the simulated spectra of Figs. 40 and 41 was extracted using a Gaussian fit. The peak shape of the Gaussian agrees very well except for the tails of the peak, noticeable in the logarithmic representation.

Experimentally a relatively good agreement with the simulations for the linewidth was found. In Article III a linewidth of 0.85(10) GHz was measured at a Ti:sa wavelength of 976 nm. While this is slightly lower than the simulated value of 1.25 GHz at 800 nm shown in Fig. 41, this can be expected by the wavelength dependent gain of the Ti:sa crystal. The output power of the Ti:sa laser however was reduced more significantly as would be expected from the loss

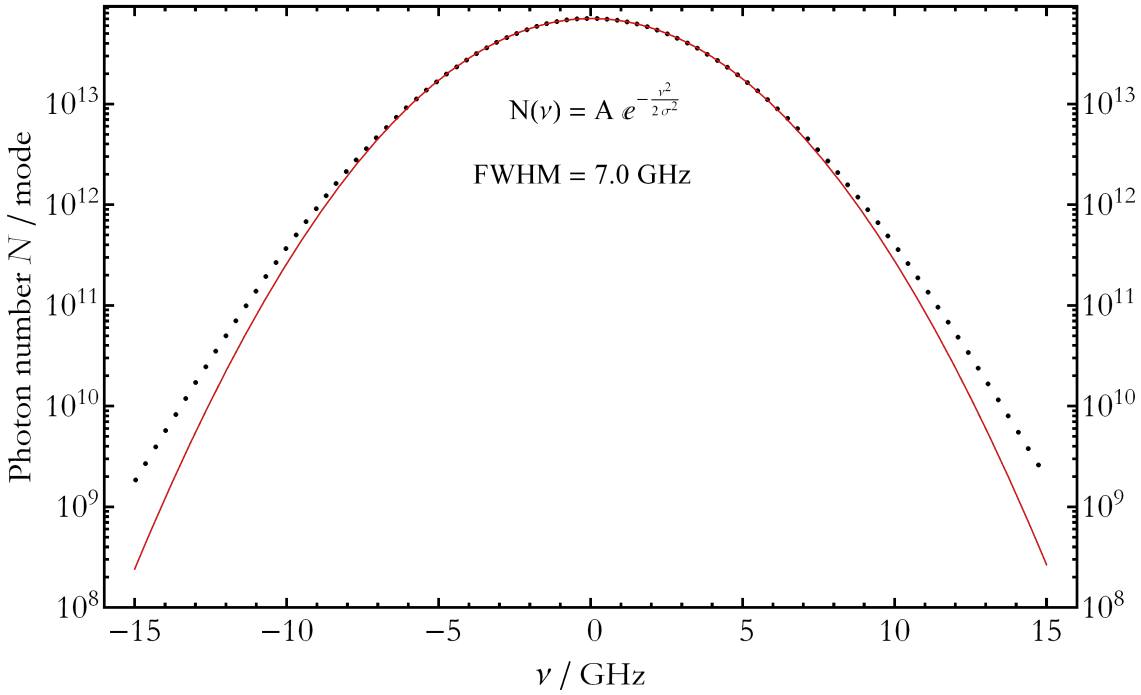

FIGURE 40 Rate equation result for the FWHM linewidth of the Ti:sa laser using the single thin etalon. Simulated photon number for each mode with data points in black and a Gaussian fit in red (note the logarithmic scale).

factor calculated from Eq. 131. Additionally with the YAG etalon inserted into the cavity, larger wavelength drifts were observed. These problems may be related to absorption of IR radiation in the YAG crystal and resulting thermal effects, such as thermal expansion or thermal lensing. Currently, new coated (R=40%) etalons made from fused silica with a thickness of 2 mm have been ordered. These etalons are expected to yield a similar linewidth to the YAG crystal, while providing good optical and thermal properties which should alleviate these issues.

5.4 Scanning FPI for wavelength calibration

Following publication of Article III a number of improvements have been made to the scanning FPI construction as well as to the data acquisition. A photograph of the current setup is shown in Fig. 42. The FPI is fixed on top of a platform mounted to a damped post (Thorlabs, DP8A/M) to minimize vibrations. The optics are aligned using a 30 mm cage system, which is placed inside an aluminium encasement.

Instead of a set of plane-parallel mirrors the FPI now uses a semi-hemispheric geometry with one flat mirror and one concave mirror with a radius of curvature of 75 mm. Both mirrors have a partial reflective coating with 97(0.5)% reflectivity in the range from 630-1050 nm and a diameter of 12.7 mm. Due to the non-confocal nature of the resonator the laser beams have to be mode-matched to the cavity

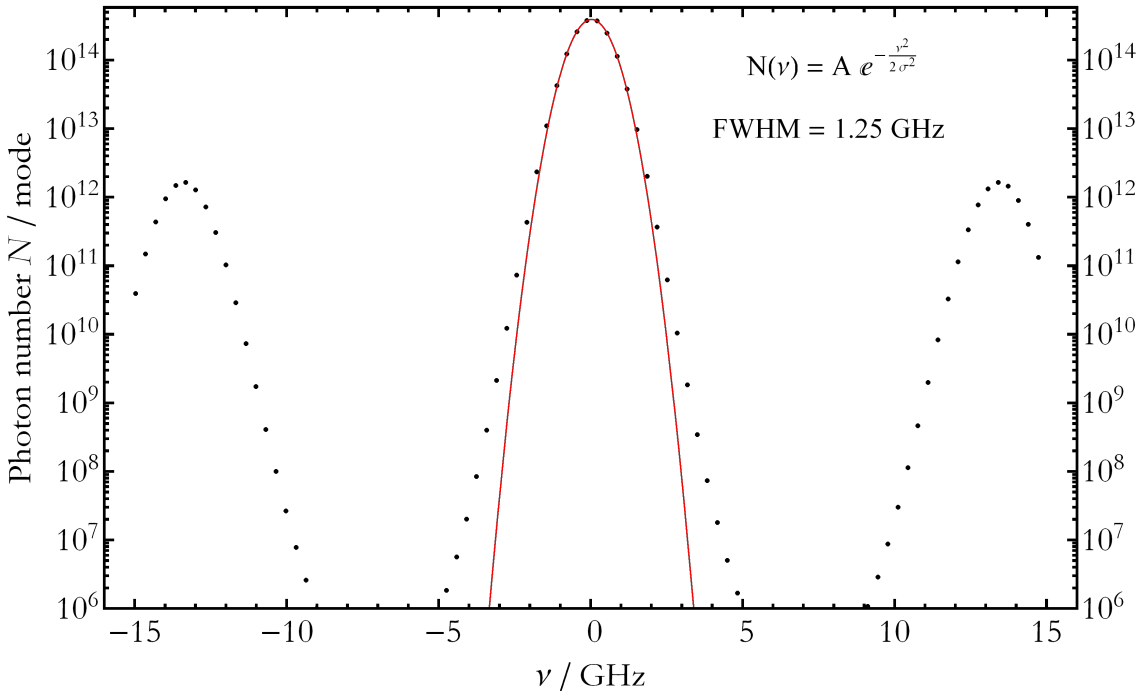

FIGURE 41 Rate equation result for the FWHM linewidth of the Ti:sa laser using the dual etalon combination. Simulated photon number for each mode with data points in black and a Gaussian fit in red (note the logarithmic scale).

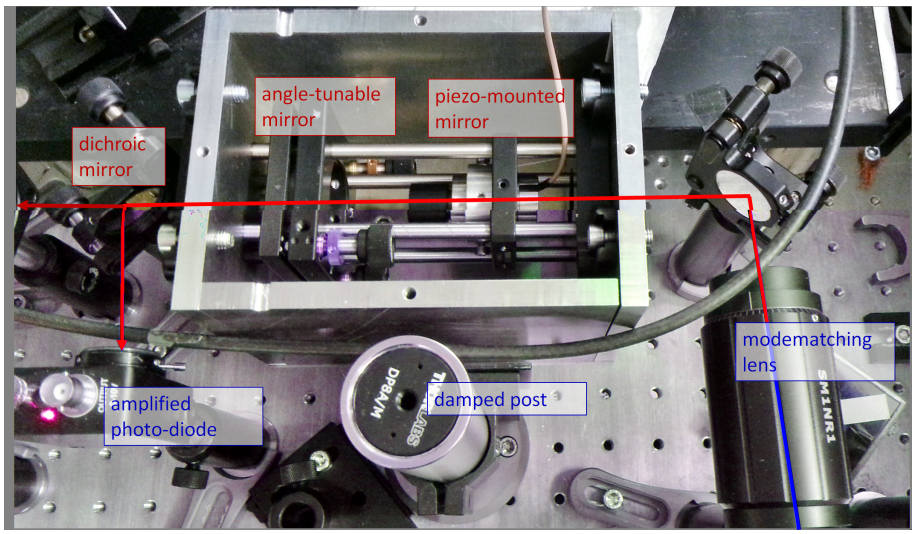

FIGURE 42 Photograph of the self-made scanning FPI system. The 0.5 mm aperture is not shown here.

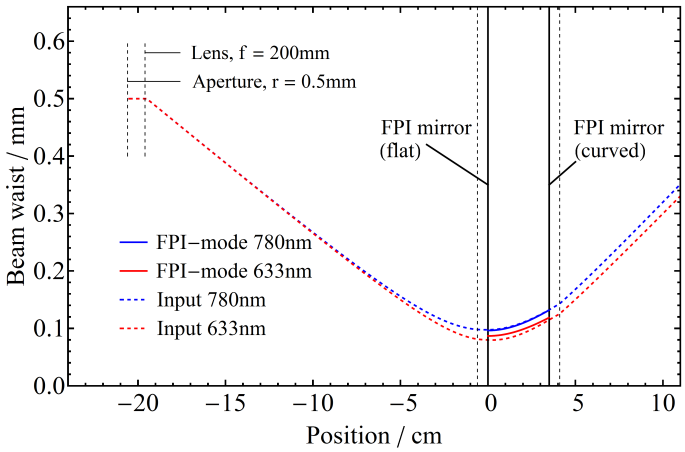

FIGURE 43 Simulation of the mode-matching to the FPI cavity. The thickness of the FPI mirror substrates is indicated by the vertical grey dashed lines.

to avoid secondary resonances from higher order Hermite-Gaussian modes. The incoming laser beams may have different waist sizes which will affect the mode-matching, and thus to prepare nearly constant initial conditions the beams first pass through an aperture of approximately 1 mm diameter before being focused into the FPI resonator. A focal length of 15-20 cm provided good results, suppressing any side-modes by a factor of 20-40 compared to the main transmission peaks.

An ABCD matrix calculation of the mode-matching is shown in Fig. 43. Here a focal length of 200 mm and a separation of 3.5 cm for the cavity mirrors was used. Due to the difference in wavelength of the Ti:sa (780 nm) and HeNe laser (633 nm) their respective mode diameters in the cavity as well as their propagation outside of the cavity differ slightly. The ratio of the resonator mode waist diameters can be estimated from the respective wavelength as $\omega_1/\omega_2 = \sqrt{\lambda_1/\lambda_2}$. The aperture creates a truncated Gaussian beam, which is not accounted for in the calculation.

No changes have been made to the ring-piezo actuator (Piezomechanik, HPSt 150/14). The piezo actuator as well as the curved mirror attached to it are fixed in a simple cage mount, while the flat mirror is placed in an angle-tunable mount. The voltage to drive the piezo actuator is supplied by a ramp generator (Toptica Miniscan 102).

To combine the beams of the HeNe laser and Ti:sa laser before the FPI and to separate them afterwards a set of cold mirrors (Thorlabs, M254C45) are used. These provide excellent transmission over the whole Ti:sa wavelength range and have good reflection in the visible. After transmission through the FPI, both HeNe laser and the Ti:sa laser are detected separately on photodetectors with variable amplification (Thorlabs, PDA36A-EC).

5.4.1 Data acquisition

The data acquisition system was upgraded from that used in Article III (National Instruments, NI USB-6009) which had a sampling rate of 48 kS/s, to a rate of

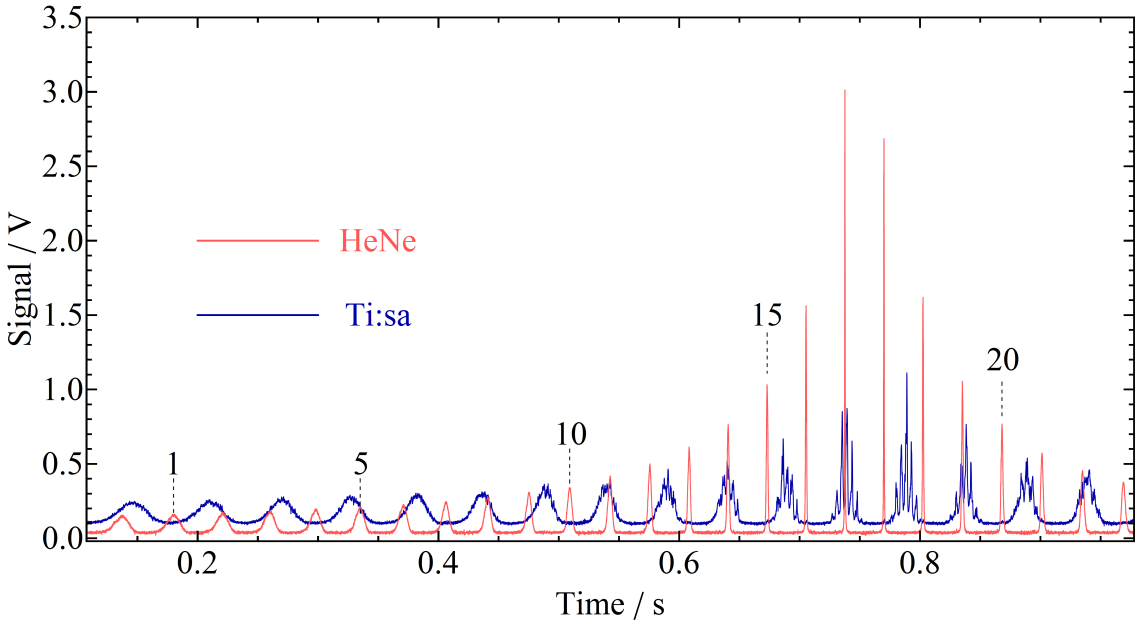

FIGURE 44 Photodiode signals of the HeNe and Ti:sa laser during a full voltage ramp of the scan generator of the FPI, using the plane-parallel mirror configuration.

250 kS/s (National Instruments, NI USB-6210). This allows for a faster scanning rate of the FPI without suffering from sampling aliasing effects on the narrow transmission peaks of the FPI.

Up to 16 analogue voltage input channels are available, however the sampling bandwidth is shared between all channels that are read out. The inputs for the channels are the two photodiode signals from the scanning FPI, the trigger signal of the ramp generator and one or more signals from an experiment such as photodiodes monitoring the laser power or the laser ion current reading from an amperemeter. For five input channels the maximal sampling frequency of each channel is thus limited to 50 kHz, in other words a time-resolution of 20 μs. The data acquisition can be triggered on the start of the voltage ramp of the scan generator. To continuously save and monitor the data of each channel a simple program was made in Labview.

5.4.2 Scanning linearity

In Article III the analysis of the FPI data was still performed without fully taking into account the non-linearity in the scanning speed of the FPI. To minimize systematic uncertainties in the analysis, the dependence of the scan linearity on parameters such as scan frequency or amplitude (maximal voltage setting of the ramp) was investigated. This was performed with the plane-parallel FPI setup.

To give an overview of these tests, Fig. 44 shows the transmission fringes from the FPI of both the HeNe laser and the dual etalon Ti:sa laser during a single full ramp of the voltage of the scan generator from 0 V to 150 V. The height as well as the resolution of the transmission peaks is not constant during the scan, suggesting that the finesse is only high in a small region. Only in this region the

individual modes of the Ti:sa spectrum are resolved. This is a result of the large sensitivity of the plane-parallel cavity configuration to any misalignments which may be introduced by the movement of the piezo actuator.

Furthermore one can notice that the separation between the peaks is not equidistant, especially at the start of the ramp. To visualize this better, the center of gravity position of each peak of the HeNe signal was calculated for a large number of scans. Due to vibrations and thermal drift the peak positions vary slightly between different scans from which standard deviation errors for the mean peak positions were calculated. After taking the difference between adjacent peaks and normalizing so that the minimal separation was set to 1, the result is shown in the left panel of Fig. 45. The peak number is taken as counted from left to right as indicated in Fig. 44. The minimal peak separation and thus fastest scan speed is around peak #15, which is also in an area where the slope or rate of change of the peak separation is minimal. This is shown in the right panel of Fig. 45. If a non-linearity below 0.5% is required only a very small section of the scan can be used. Ideally, even smaller values would be of benefit.

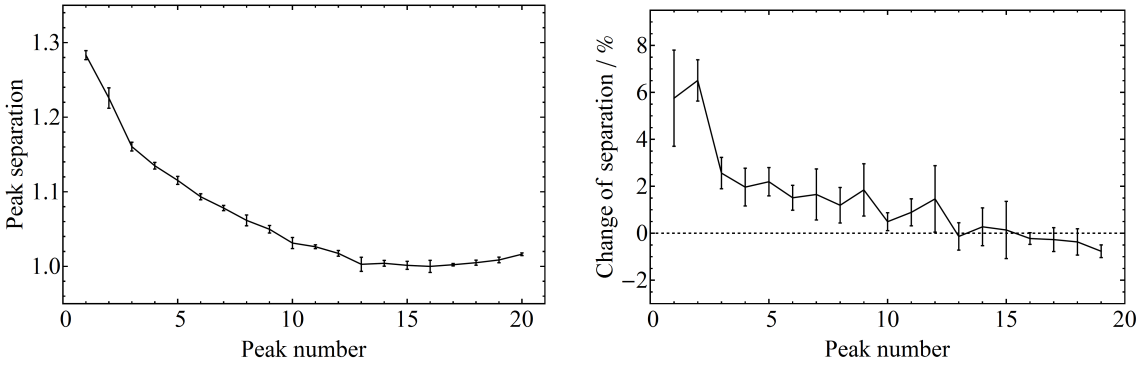

FIGURE 45 Left panel: FPI transmission peak separation vs. peak number illustrating the non-linear scan speed. Right panel: rate of change of the peak separation. This indicates that differences of more than 1% are seen from peak pair to peak pair.

Other test parameters such as frequency or voltage offset did not significantly influence the linearity of the scanning. Using a triangle wave instead of a sawtooth voltage for the ramp generator revealed hysteresis effects as the photodiode signals during upward and downward ramp were not symmetric. It is well known that piezoelectric actuators experience hysteresis and creep effects as discussed for example in [89]. To compensate for this, positioning using a closed feedback loop is frequently employed [90, 91]. Without feedback a reduction in hysteresis by a factor of up to ten may be gained by use of current control of the actuator [92].

Correction for the non-linearity can also be made during data analysis provided that the actual piezo actuator movement can be estimated. In this case reference positions can be taken from the transmission peaks of the HeNe laser. As it is running at a fixed frequency the distance between two transmission maxima is always equal to one FSR. To calibrate or linearise the scan, the position in time of the peaks is fitted against the peak FSR number with a polynomial fit. The

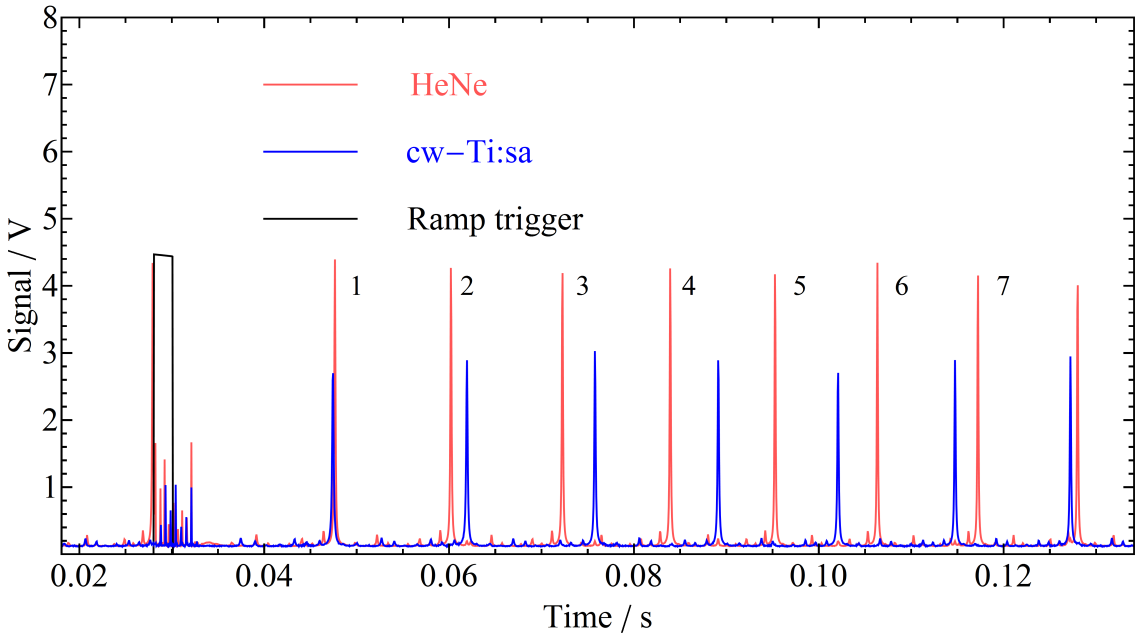

FIGURE 46 Photodiode signals of HeNe and cw Ti:sa laser during a scan of the semi-hemispherical FPI.

resulting fit can then be used to directly convert any position in time to a position in FSRs.

To test this procedure both the HeNe laser as well as a continuous wave (cw) Ti:sa were injected into the new semi-hemispheric FPI. The signals from a single ramp of the FPI can be seen in Fig. 46. Compared to the plane-parallel FPI the transmission peaks have nearly constant height and finesse. Currently the finesse is limited to a value of about 75(5), similar to the plane FPI finesse of 70 measured in Article III. This is slightly below the theoretical value of 103(+20,-12) for a specified mirror reflectivity of 97.0(5)%. This may be caused by the imperfect mode-matching, which can be observed in the scan as several side-maxima appear, though at reduced amplitude compared to the main peaks. A much higher finesse of $\mathcal{F} \approx 1500$ was reached in a previous test using a pair of high reflecting mirrors rated at R= 99.8%, however with insufficient transmission.

The timing of each of the HeNe peaks with respect to the trigger signal was identified, with the first peak set to zero for reference. The timings are then plotted against the FSR number of the peaks as seen on the left side of Fig. 47 along with a linear fit. The difference between the fit and the data points can be discerned more easily on the right side of Fig. 47, where the residuals of the fit are displayed. Residuals of fits with 2nd and 3rd degree polynomials are shown as well. While the deviation between linear fit and data points is of the order of 5% of one FSR, the 3rd degree polynomial reproduces the data accurate to 0.02%. Higher order polynomials did not significantly improve the fit.

For verification, the timing positions of the cw Ti:sa peaks were converted using the fit parameters determined from the HeNe peaks. The results have to be scaled by the ratio of the wavelengths $\lambda_{\mathrm{HeNe}}/\lambda_{\mathrm{Ti:sa}}$ to yield the FSR values of the

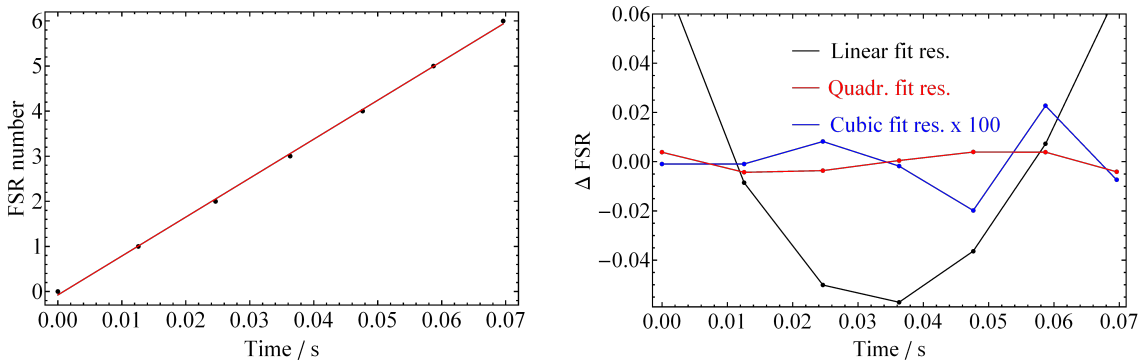

FIGURE 47 Left panel: relative timing of HeNe peaks against FSR number with the first peak position set to zero seconds. The red curve is a linear fit to the data. Right panel: residuals of linear, quadratic and cubic fits to the timing data of the HeNe peaks. The residuals of the cubic fit have been multiplied by a factor 100 for display

Ti:sa peaks. The difference between succeeding Ti:sa peaks should then be equal to one FSR. For six Ti:sa peaks the mean difference was 1.004(24) for the linear fit and 0.99963(29) for the cubic fit, with the errors for the mean calculated as $\sigma/\sqrt{N}$ with standard deviation σ and number of data points N. This suggests a remaining error for the non-linearity of $< 0.03\%$ of one FSR or $\approx$1 MHz after calibrating with a cubic fit, which is a factor 30 relative improvement compared to that in Article III. Limitations that prevent an even higher accuracy are either vibrations of the FPI cavity or the limited time resolution due to the 50 kHz sampling rate.

The tracking of the HeNe and Ti:sa peaks during a longer laser scan is performed as discussed in Article III. The algorithm programmed in Mathematica [53] used for the data evaluation is given in Appendix 3. Afterwards the set of identified peak positions is linearised with individual fits for each FPI trace using the procedure discussed above and exported for further analysis.

5.5 FSR calibration using saturated absorption spectroscopy of rubidium

Following linearisation, the main remaining uncertainty is the FSR of the FPI. The method to determine the FSR described in Article III is limited by the large uncertainty of the wavemeter. A large number of measurements would be needed to significantly improve the error of the current FSR value of 3.3279(80) GHz, which has a relative accuracy of 0.24%. A more sophisticated approach using the wavemeter is a so-called ''Nonius'' method, described in [93], in which the laser frequency is changed by multiples a of the FSR so that $\Delta\nu_{i+1} = a \cdot \Delta\nu_i$. If the distances between the frequencies are chosen properly and the number of FSR changes is known this can yield more accurate results with a smaller number of data points. Avoiding ambiguity of the results requires that the error of the wavemeter is significantly smaller than the FSR. While this is true for the FPI used

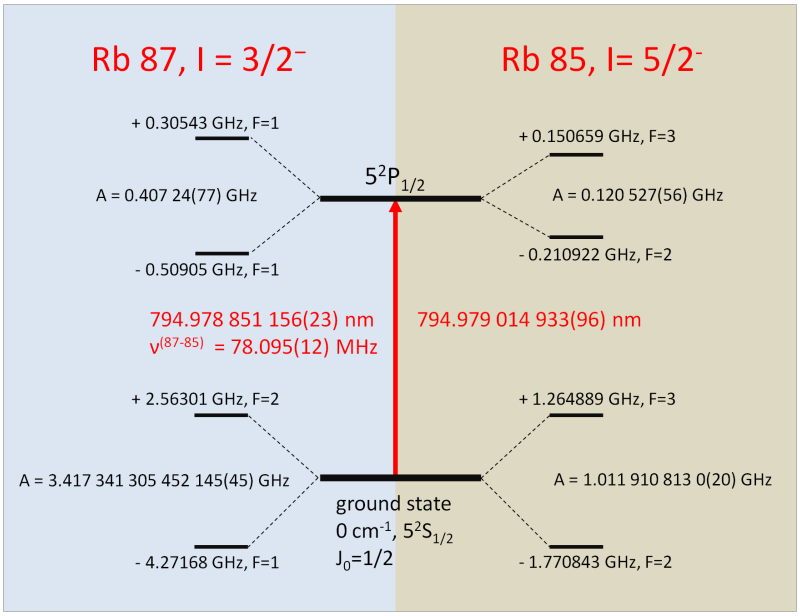

FIGURE 48 D1 line in rubidium and hyperfine splittings. Values taken from [94, 95].

for the dual-etalon Ti:sa, a different FPI with a smaller FSR of 1 GHz is used for the narrowband injection-locked Ti:sa and the cw Ti:sa discussed in chapter 6. Here this requirement is not fulfilled.

A more precise method that can be used in this case is the calibration of the FSR against a well-known hyperfine structure. So far only the commercial FPI (Toptica FPI-100-0750-1, FSR $\approx$ 1 GHz) has been calibrated in this manner, but measurements for the self-made FPI are in progress. In this work, the D1 line of Rubidium is well suited to the fundamental light of the narrow linewidth cw Ti:sa laser. Information on the $\lambda = 794.978$ nm transition for both naturally occuring isotopes ^{87}Rb (72.168%) and ^{85}Rb (27.835%) can be found in [94, 95]. The hyperfine coupling constants as well as the isotope shift are known to a very high precision shown in Fig. 48, far beyond that required for the FSR calibration.

To reach high resolution, a saturated absorption spectroscopy [96] setup was built using a rubidium-filled reference gas cell (Thorlabs, GC25075-RB). This allows for Doppler-free spectroscopy with a resolution limited only by the power-broadened natural linewidth of the transition. The setup is shown in Fig. 49. Using the fiber-coupled cw-Ti:sa output, a probe and reference beam are created by reflection from the front- and back surface of a thick (12 mm) glass plate, directed through the rubidium-filled cell towards two photodiodes (Thorlabs, FDS100). The main pump beam is expanded to a diameter of about 3 mm and overlapped counter-propagating with the probe beam by use of a D-shaped pick-off mirror (Thorlabs, BBD1-E03). The rubidium cell is tilted slightly, so that reflections of the pump beam from the cell windows do not enter the photodiodes.

The photodiode signal of the reference beam measures the normal Doppler-broadened absorption of the rubidium cell. For the probe beam the absorption is modified by the counter-propagating pump beam. Whenever probe and pump excite the same velocity class of atoms, the probe will have reduced absorption since the pump saturates the transition. For a two-level system this happens only

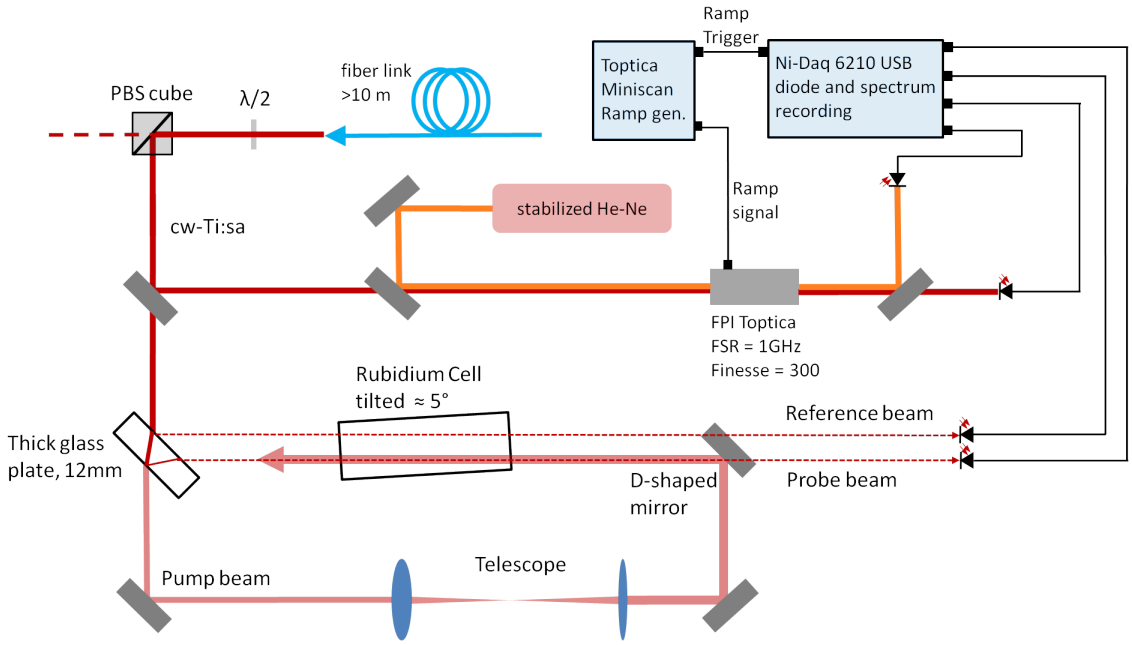

FIGURE 49 Saturation absorption spectroscopy setup for rubidium.

exactly at the transition frequency, however for a system with multiple transitions sharing a common ground state lying within a single Doppler-broadened profile, so-called ''cross-over'' resonances can occur. These lie exactly centred between the involved transitions.

The signal from the two photodiodes as well as the HeNe and Ti:sa transmission peaks of the FPI form inputs for the data acquisition system described in section 5.4.1. The difference signal $PD_{\text{probe}} - PD_{\text{ref}}$ between the two photodiodes is calculated. In this manner noise present in the laser source cancels out as both probe and reference beam experience the same fluctuations. The power of the laser was set to about 15 μW for probe and reference beam, with a beam waist of $\approx$ 0.5 mm. For the pump beam $\approx$ 40 times higher power was used. Systematic measurements of saturation and linewidth dependence on the used power have not yet been made, but the intensity can be assumed to be of the same order of magnitude as the theoretical saturation intensity (see Eq. 7) of 1.5 mW/cm^2.

The two photodiodes and their amplifiers are not perfectly balanced, so that some background fluctuations are visible in the difference signal. These fluctuations were minimized by adjustment of the steering of the probe and reference beam, but could not yet be completely eliminated. Work is currently underway to reduce possible sources of noise.

The cw-Ti:sa was scanned three times across the whole hyperfine structure while all signals were continuously recorded. The raw signal of the probe and reference beam photodiodes is shown in Fig. 50. While the reference beam signal follows the Doppler-broadened absorption profile, the probe beam shows additional narrow resonances with reduced absorption due to the influence of the counter-propagating pump beam.

From the analysis of the FPI traces the wavelength is calculated in units of the FSR, which is then plotted against the difference signal of the photodiodes

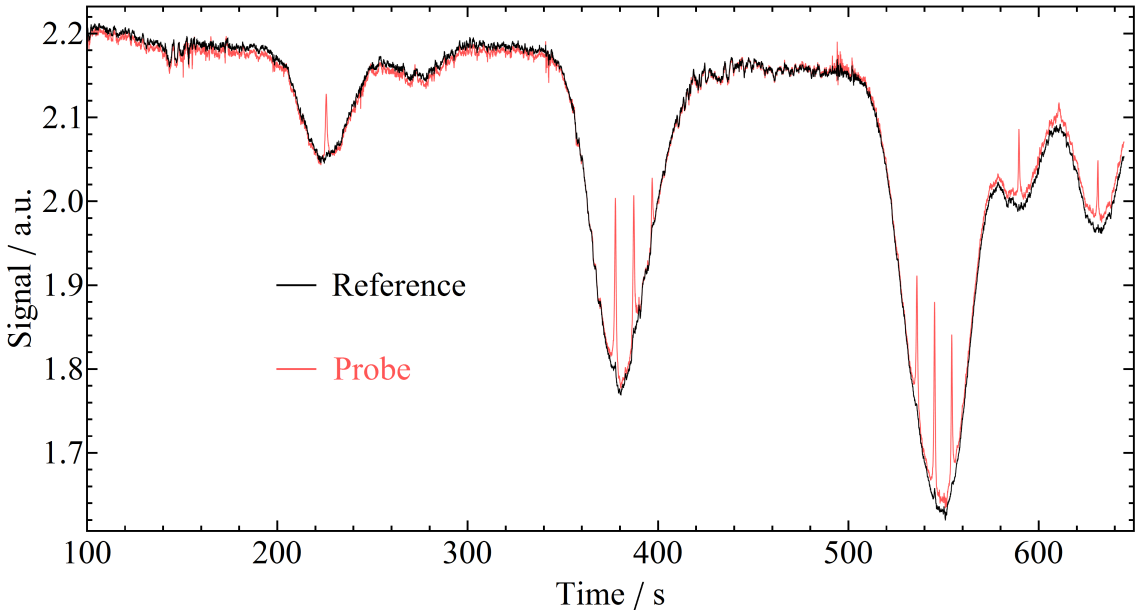

FIGURE 50 Signal of probe and reference beam during scan of the rubidium hyperfine structure.

PD_{probe}-PD_{ref}. The hyperfine structure of Rb was fitted to this dataset assuming Lorentzian peak shapes and literature values for the hyperfine constants. The fluctuations of the background were taken into account using a quadratic function. To extract the FSR of the FPI the values for the hyperfine parameters and the isotope shift in the fit function were multiplied by a single common scaling factor S. From the fitted value of S the FSR can be simply determined as FSR $= S^{-1}$.

One of the three scans is shown in Fig. 51. The frequency scale already uses the calibrated FSR value of 0.99850(15) from the fit results. The hyperfine transitions from the ground states with spin value F to upper states with F' are indicated for both isotopes. The peaks resulting from crossover resonances are indicated with "co". The observed FWHM linewidth from the fit is 14.5 MHz. Further improvements on the the relative FSR uncertainty of 0.015% may be possible if the fluctuations on the signals can be reduced, but for most of the envisaged applications the accuracy is already sufficient. Compared to the result in article III the relative error of the FSR has been reduced by a factor 15.

5.6 Summary and outlook

The dual-etalon Ti:sa laser provides an intermediate resolution improvement between the standard broadband laser and the injection-locked Ti:sa, discussed in the following chapter, or high resolution continuous wave solutions. The increased resolution highlighted the lack of an accurate wavelength determination using the commercial wavemeter, an issue which has now been addressed with the introduction of a scanning FPI. While the FPI does not provide a higher accuracy

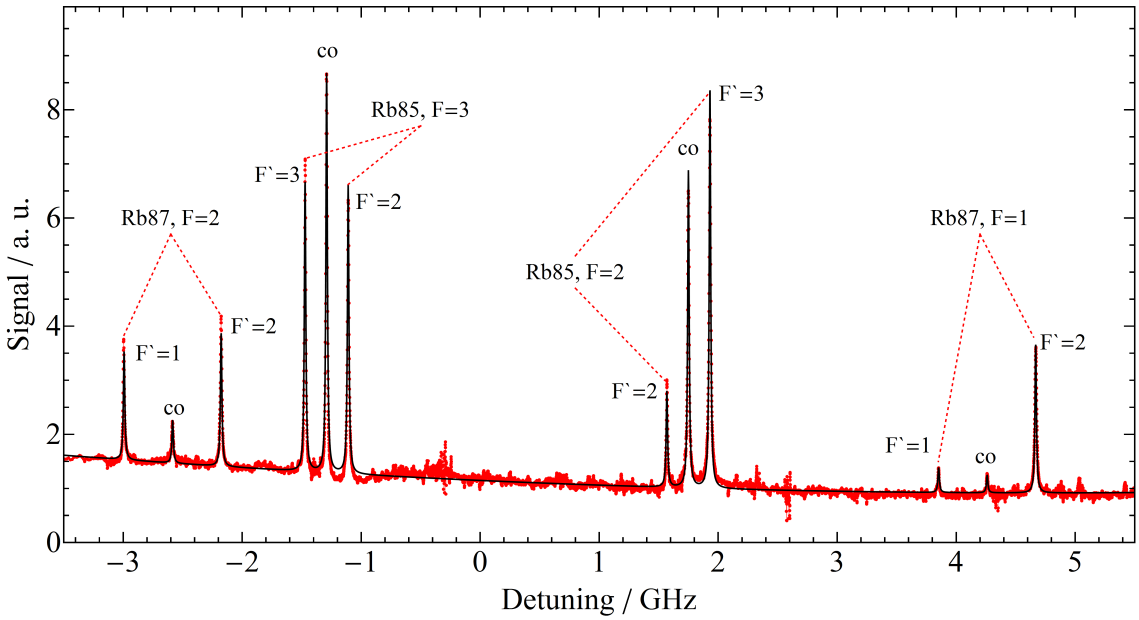

FIGURE 51 Hyperfine structure of natural rubidium measured using the saturated absorption spectroscopy setup. Measured data shown in red and fit curve used to extract the FSR value shown in black. A quadratic fit to the background was used to allow for wavelength-dependent fluctuations in the difference signal.

of absolute frequency, relative measurements can now be trusted to within a few MHz, a significant improvement from the previous system.

The saturated absorption spectroscopy setup will still be used for the FSR calibration of the self-built semi-hemispheric FPI. Furthermore, the high stability of the narrowband hyperfine transitions will be used for frequency stabilization of the cw Ti:sa laser for investigations of the long-term wavelength stability of the HeNe laser. The HeNe laser may then be used for stabilization of the cw Ti:sa to an arbitrary frequency by employing a fringe-offset stabilization routine. This is in anticipation of developing a new programme of Ti:sa-based collinear laser spectroscopy to complement the currently used dye laser system at the IGISOL facility.

6 AN INJECTION LOCKED TI:SAPPHIRE LASER FOR IN-GAS JET SPECTROSCOPY AND APPLICATIONS ON COPPER, ACTINIUM AND PLUTONIUM

Recently, the implementation of resonance ionization spectroscopy (RIS) in a cold gas jet utilizing a narrowband first step excitation has gained considerable interest [12]. Due to the cold environment this novel in-gas jet spectroscopy technique will provide high-resolution information on isotope shifts and hyperfine structure. The method will allow for the ionization of specific isotopes and isomers, or even the production of - at least partially - polarized ion beams by hyperfine level pumping. Corresponding developments are presently ongoing in a number of facilities worldwide to improve laser performance as well as experimental implementation.

At ISOL or IGISOL-type radioactive beam facilities, the existing pulsed laser systems focus mainly on an efficient production of laser ions inside the hot cavity or gas cell. The width is therefore typically of the order of several GHz in order to cover the entire Doppler ensemble. To fully demonstrate the benefits of in-jet ionization a narrow bandwidth, high power, pulsed laser source is required. While a bandwidth reduction of pulsed lasers is possible using additional intra-cavity wavelength filters, this comes with the disadvantage of reduced power levels.

A better option is the pulsed amplification of a narrow-band continuous wave (cw) laser, either by dye lasers or Ti:sa lasers. As the emission cross section of dyes is up to three orders of magnitude higher, single-pass amplification is generally sufficient, though with the drawback of regular maintenance as well as fire and health hazards accompanying dye solutions. For the lower gain Ti:sa crystal a multi-fold repeated amplification is required to reach a final output power of several kW (during the pulse) from the few mW of cw input.

This is best performed in a resonant cavity where the injected input beam (the ‘‘seed") can be amplified and recycled over a large number of round-trips. The cavity has to be kept in resonance with the frequency of the injected beam, which means that the length of the cavity has to be stabilized or locked to a multiple of the seed wavelength. The setup and performance of such an injection-locked

cavity is described in the following sections.

6.1 Experimental setup

A layout of the whole injection-locked laser system is shown in Fig. 52. It covers the cw master laser, beam transport as well as the injection-locked Ti:sa cavity used for amplification and the electronics used for its stabilization. The details of this system are described in the following.

6.1.1 Continuous wave master laser system

The input seed radiation to the injection-locked cavity is generated by a commercial continuous-wave (cw) Ti:sa laser (Sirah Matisse TS). With the currently available pump power of 6 W the cw-Ti:sa has an available wavelength range from 705-930 nm with a maximum output power of 1 W. Three different mirror sets and two birefringent filters are required to cover the whole wavelength range, however replacing one set with another and re-optimizing the output power is a relatively simple task and takes less than one hour.

For frequency stabilization the laser possesses an external fibre-coupled reference cavity. While the short term frequency stability with respect to this reference cavity is typically less than 50 kHz when locked, the external cavity is not temperature stabilized, meaning that long-term drifts can be far larger. Techniques to compensate for this drift are currently under development. Locking to a fixed frequency can be achieved by referencing to an atomic transition, for example using saturation absorption spectroscopy. Such a setup is currently under construction using a rubidium-filled quartz cell. More flexible wavelength stabilization can be done by using the fringe-offset technique [97] with the reference frequency provided by a stabilized single-mode Helium Neon laser.

6.1.2 Beam transport of master laser

A small fraction of the cw output of about 10-100 mW is separated with a $\lambda/2$ plate and a polarizing beam-splitter (PBS) cube and coupled into a fibre for transport to the main laser cabin. An optical isolator after the output of the cw system (Optics for Research, IO-5-VIR, specifications unknown) prevents feedback from the fibre tip and other surfaces to the cw-Ti:sa to maintain stable single-mode operation. As fibre for the transport, a standard single-mode fibre with FC-PC connectors and a length of 35 m was used at first, but has currently been replaced by 10 m long polarization maintaining fibres (Thorlabs PM630-HP and PM780-HP). To correctly align the incoming polarization to the slow/fast axes of the polarization maintaining fibres a second $\lambda/2$ waveplate was placed after the PBS cube. A second optical isolator (Newport Corp., ISO-05-800-BB) after the fibre is inserted to prevent both feedback from the pulsed laser system to the cw system as well

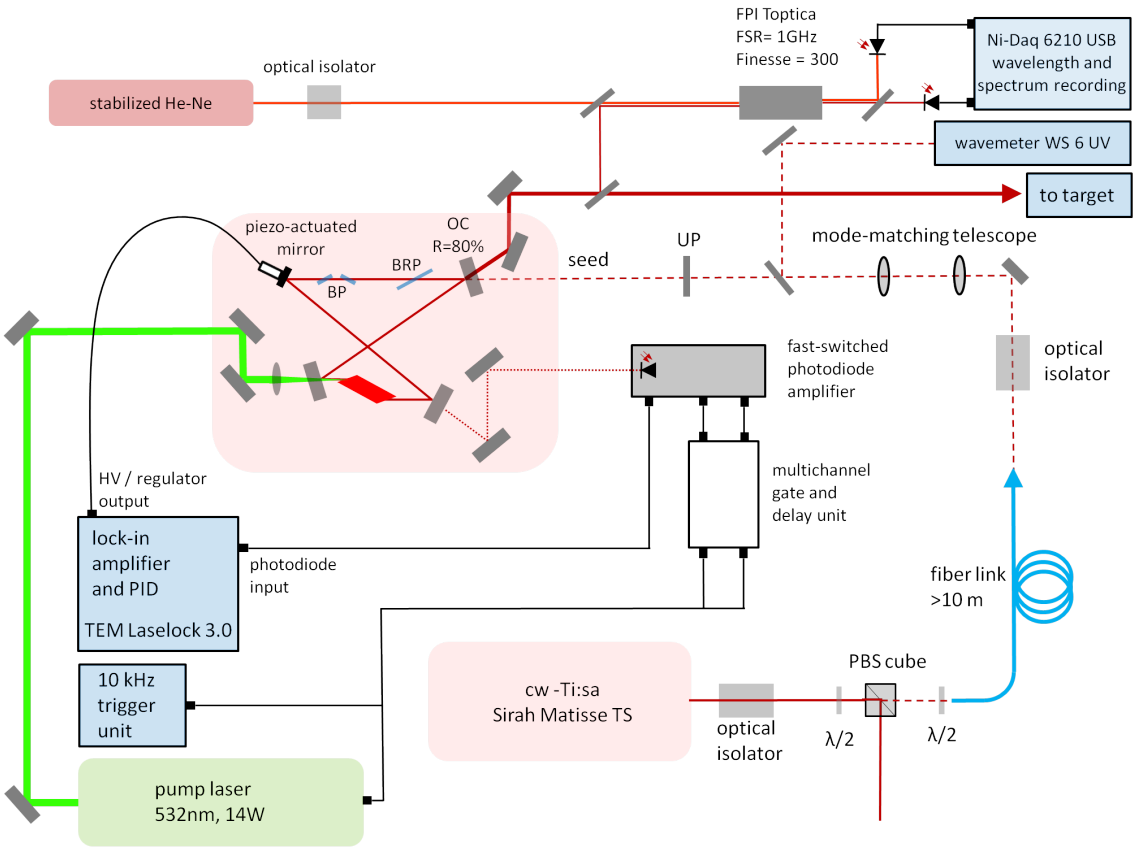

FIGURE 52 Overview of the setup of the injection-locked Ti:sa laser system; descriptions of elements in text.

as to reduce the risk of damage to the fibre. Both types of fibres allowed for a stable operation of the injection-locked cavity, however the standard single mode fibres suffered from an unstable polarization output causing short-term intensity fluctuations after the optical isolator of the order of 10-20%. The fibre-link setup is still subject to further investigations and improvements, not necessarily for the injection-locked cavity system, but for possible applications of the cw Ti:sa at the collinear laser spectroscopy station at the IGISOL facility. For this application the requirements for intensity stability will be more stringent.

For optimal injection efficiency into the slave cavity, the mode diameter of the fibre output is matched to that of the TEM_{00} mode of the cavity using an adjustable telescope on a rail system.

6.1.3 Injection-locked laser cavity

The basic geometry of the injection-locked laser cavity was adapted from the previous design discussed in [98]. The old design was constructed using a rail system with sliders. This provided good flexibility, allowing for many different positions for every mirror mount leaving many configuration possibilities for testing purposes. The new design uses mostly fixed geometry, which simplifies setup and alignment, but does not leave many possibilities for changing the cavity geometry.

The layout was constructed in a 3D CAD software (Autodesk Inventor 2012). Fig. 53 shows a cut through the cavity at the plane of the Ti:sa mode. The baseplate of the cavity is made out of stainless steel and is supported by four posts using sorbothane damping feet (Thorlabs, AV2/M) to reduce vibrations, considering the cavity sits atop an undamped table. The feet have a resonance frequency of $\approx$15 Hz, so for this lower frequency range the isolation will be relatively poor. Higher frequency vibrations which may affect locking performance should be reduced considerably.

The cavity is not completely isolated from the outside environment as several holes in the baseplate as well as in the side-walls are left open to allow for electrical and water connections as well as input and output of the laser beams. A lens with focal length $f = 75$ mm focuses the pump beam into the Ti:sa crystal. The crystal is wrapped in indium foil and placed into a copper mounting structure. The bottom part of the copper mount is water-cooled, with the top part placed on top of a peltier cooler for further reduction in temperature. The peltier (uwe electronic GmbH, UEPT-130-127-036E080E) is epoxy sealed to prevent damage from condensation and has a maximum power rating of 36 W. At low pump power levels condensation may occur on the crystal surface as well, thus an adjustable power supply for the peltier or temperature stabilization should be implemented in the future to prevent this.

The slave cavity is built using a folded bow-tie design, using the same radius of curvature for the folding mirrors and same folding angle of 17.75° as in the Z-shaped cavity. The bow-tie design is a travelling wave type resonator. Spatial hole burning, which affects standing wave cavities is not present making it easier

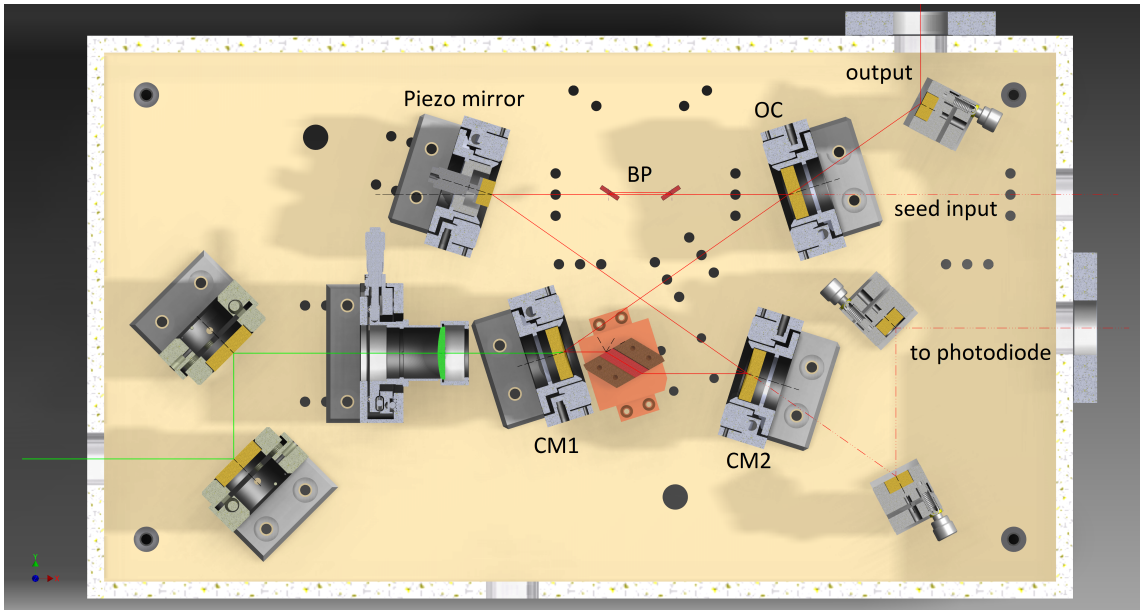

FIGURE 53 3D CAD design of the cavity.

to achieve single-mode operation. The dimensions of the cavity were set so that a single round-trip in the bow-tie has about half the length of the round-trip in the Z-shaped cavities. This should lead to comparable pulse durations and build-up times, as the gain medium is passed twice for a round-trip in the Z-shaped cavity, but only once in the bow-tie.

Two small Brewster plates (BP) have been included in the design. These were originally introduced to allow for adjustment of the cavity length by means of piezo bender actuators controlled by the locking system. By tilting the plates the effective path length for a round-trip in the cavity is changed, which would allow for an increased tuning range without the piezo actuated mirror reaching its maximum extension and the cavity having to be relocked. As will be shown in section 6.2.2, the automatic relocking of the cavity was found to be sufficiently fast. Nevertheless, the BPs may still be useful in conjunction with the birefringent filter plate (BRP) for a different purpose as will be discussed in section 6.2.6.

The waist diameter along the cavity for the given geometry was calculated in Mathematica. One slight deviation in the experimental setup is the length of the Ti:sa crystal. Previously the crystal had been re-polished, therefore it was only 18.3 mm long - 1.7 mm below the design value used for the first simulations. As the physical positions of the curved mirrors are fixed in the design, the shorter crystal means a shorter optical path length due to the lower refractive index in air. While the length change is rather minimal it still increases astigmatism and divergence angle of the laser. A comparison between calculations for the normal length crystal and re-polished crystal is shown in the left and right panel of Fig. 54, respectively.

A main goal for the system is a wide tuning range therefore, similar to the grating-based Ti:sa discussed in chapter four, all mirrors in the cavity have broadband coatings for the whole Ti:sa wavelength range from 660-1050 nm. The output coupler has a specified reflectivity of 80%. It is however possible that there

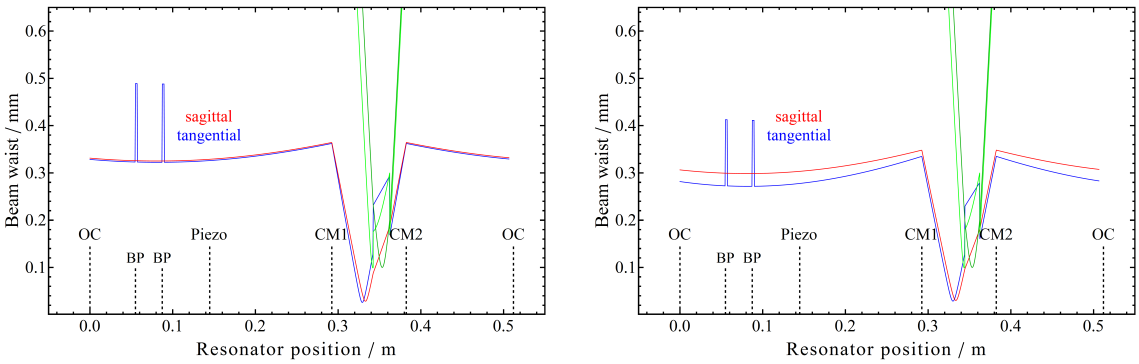

FIGURE 54 Left Panel: Ti:sa mode-waist (red and blue) along the cavity for the "design" crystal length of 20 mm. The overlap with the pump beam (green) inside the crystal is shown as well. Right Panel: same as left panel, but with re-polished crystal length of 18.3 mm.

may be significant deviations from this specification as the OC is coated for 0° AOI. The same holds true for the other cavity mirrors though it is likely that their reflectivity is still sufficiently close to 100% albeit the wavelength range may be slightly reduced. This concerns especially the long wavelength end as spectral properties of dielectric filters usually shift towards shorter wavelength with an increase in AOI [99].

If unidirectional output of the injection-locked cavity is required without using any seed, this can be achieved by a simple glass plate (UP, unidirectional plate) in front of the unwanted output direction. By reflecting a fraction (4%) of this output back into the cavity the effective gain in the other direction is increased. This leads to nearly complete unidirectional operation (>95%) without the need for more expensive solutions such as optical diodes using Faraday rotators and simultaneously keeps the losses inside the cavity at a very low level.

6.1.4 Injection-locked cavity stabilization electronics

To stabilize the cavity the dither locking technique with phase sensitive detection (Lock-in amplifier) is used [100]. To modulate and stabilize the cavity length one of the mirrors (Qioptiq Photonics GmbH, DLHS Ti:sa coating) with dimensions 12.7x5 mm is fixed to the tip of a piezo actuator (Piezomechanik GmbH, PSt 150-10-20 VS15) with a travel range of 27 μm and an unloaded resonance frequency of 30 kHz. The piezo actuator is connected to one of the two 150 V max. HV outputs of the digital stabilization system or ‘‘lock-box" (TEM Messtechnik, Laselock 3.0). The lock-box is an integrated system that provides two independent PID regulators to calculate the error ‘‘lock-in’’ signal for the feedback loop. It also includes frequency filters for the input and output signals and generates the fast modulation or dither voltage, which is applied to the piezo actuator.

The input signal originates from the photodiode amplifier positioned behind the curved mirror CM2. As the transmission of the cw light through this mirror depends on the length of the cavity, this signal is used to stabilize the cavity length to one of the transmission peaks. During and shortly after the pulse of the pump

laser however the intensity incident on the photodiode will increase dramatically, leading to saturation of the photodiode or amplifier electronics. To prevent this from happening the photodiode and amplifier are grounded during the pump pulse period using fast switches. To reduce electrical noise from the switching it is best to first ground the amplifier and then the photodiode and turn them back on in the reverse order after the high intensity in the cavity has decayed away. Using the 10 kHz trigger signal of the pump laser system as input, the time signals for the switches are set up with a multi-channel gate and delay unit. Experimentally a typical gate width of about 8 μs is used with the gate for the amplifier set slightly wider. The voltage signal of the photodiode is then only related to the cw seed, though with short drop-outs to zero while grounded. A schematic of the amplifier circuit design from the University of Mainz can be found in [54,56] with a recent version of the design shown in Appendix 4.

6.2 Characterization

6.2.1 Piezo response

The passive resonator stability was studied by monitoring the photodiode signal without stabilizing the cavity. Whenever the cavity length came close to resonance with the injected cw light strong oscillations in the photodiode output occurred as seen on the left in Fig. 55. The lowest major noise frequency component of 33.2 Hz can be obtained by analysis of the Fourier spectrum as shown on the right side of Fig. 55. The origin of the oscillations is not clear, however they lie close to twice the resonance frequency of the vibration isolating feet supporting the cavity. A comparison without the damping feet has not yet been made to confirm a possible correlation. Several sources of noise, such as vacuum pumps or power supplies were temporarily shut down to investigate their effect on the cavity stability, but no evidence for any improvement was found. The Fourier spectrum also indicated slight resonances at higher frequency with much weaker intensities. The stability of the cavity could still be improved for example by placing it on a damped optical table, however the active stabilization with the piezo actuator will compensate for most of the relatively low frequency vibrations observed.

The feedback for the regulation of the cavity length to a transmission peak can only work reliably when the response of the piezo actuator reacts predictably to the PID output in the frequency range set by the output frequency filter. The combined system of piezo actuator, mirror and mounting structure has a variety of possible mechanical resonances as there are several masses and spring forces involved. Around these resonances the feedback to the system will vary strongly in gain and in phase with respect to the driving force. The frequency filter should therefore limit the PID output to a frequency range where no resonances occur. The same holds true for the dithering frequency. External noise sources will likely have a stronger disturbing effect near natural resonance frequencies of the system

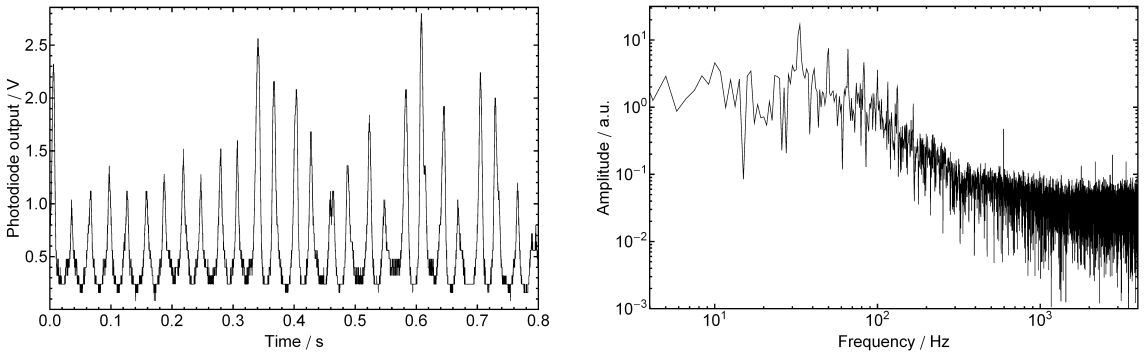

FIGURE 55 Passive resonator stability analysis. Left Panel: photodiode output voltage with the cavity drifting around a transmission peak showing strong oscillations. Right panel: Fourier spectrum of the photodiode signal using logarithmic scale, the main feature is at a frequency of 33.2 Hz.

and will therefore cause a less clear lock-in signal at these frequencies.

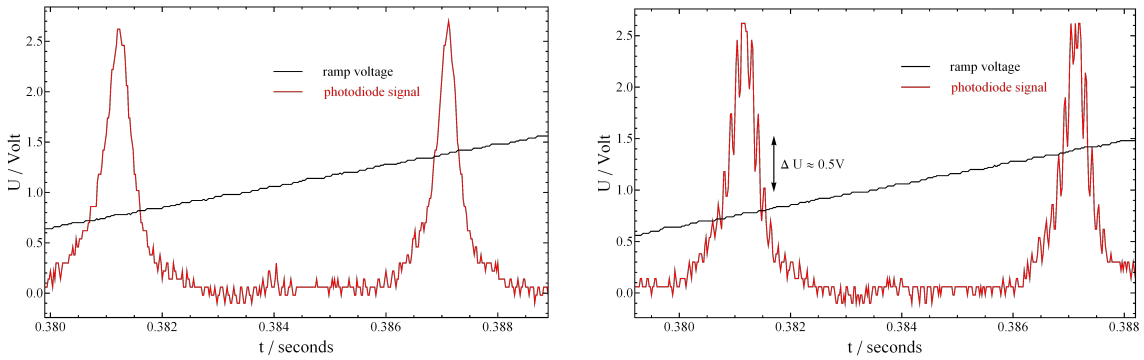

FIGURE 56 Left Panel: transmission fringes of the photodiode signal with ramp generator turned on, no dithering. Right Panel: with ramp generator and dithering turned on.

To measure the strength of the piezo actuator response as well as its phase delay to a given external force with a modulation frequency f the following procedure was performed. The ramp generator was turned on so that several transmission peaks of the injected light were visible. The maximum voltage from the photodiode was about 2.6 V as seen in the left panel of Fig. 56, the peaks following the Airy function profile. Then with a fixed dithering frequency the dither amplitude setting was adjusted. This was done so that the voltage modulation of the photodiode signal as shown on the right panel of Fig. 56 was about 0.5 V measured near half-height of the transmission peak maximum. As this was only measured by eye a relative error of about 20% for the amplitude setting can be estimated. Moreover the dither phase was adjusted for maximum lock-in signal amplitude. The adjustment for dither amplitude and phase was then repeated over a dither frequency range from 5-40 kHz. At lower frequencies noise made the measurement difficult, while higher frequencies have not yet been investigated.

The dither amplitude setting can be taken to be inversely proportional to

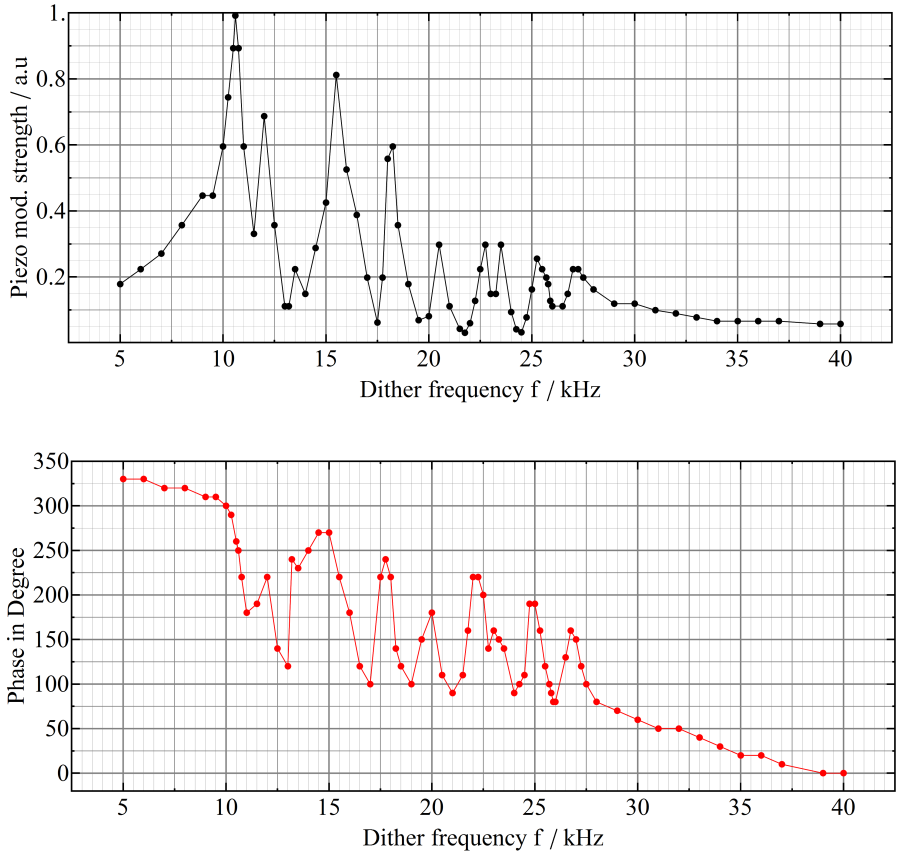

FIGURE 57 Resonances of the piezo actuator frequency response curve and phase shift required for maximal lock-in signal.

the modulation response strength of the piezo. Fig. 57 shows the acquired data for both the modulation response strength and the phase delay required for optimal lock-in signal. Between 10 kHz and 30 kHz several resonances occur which are also accompanied by a rapid change in phase, while below 10 kHz and above 30 kHz no further resonances are observed. The modulation strength in between the resonance peaks sometimes drops out relative to the low- and high-frequency tails. This is likely to be caused by ''antiresonances'', where for example a thickness eigenmode frequency of the piezo stack is excited which counteracts the length-modulation. There may be further resonances at higher frequencies than measured however these are likely to be overtones and should have lower amplitudes. While in most cases it is advantageous to use a very high dither frequency as many physical processes create so-called ''pink noise" with a power spectrum $S(f) = 1/f^{\alpha}$, with $0 < \alpha < 2$, the modulation strength drops at higher frequencies so that a value of $f \approx 40$ kHz was chosen for dithering.

6.2.2 Stabilization of the resonator

Fig. 58 shows the settings of the lock-box in the software interface. The settings for voltages are usually given in a scale from 0-100% with 100% equating to the maximum voltage of the HV amplifier which is about 150 V. After optimization

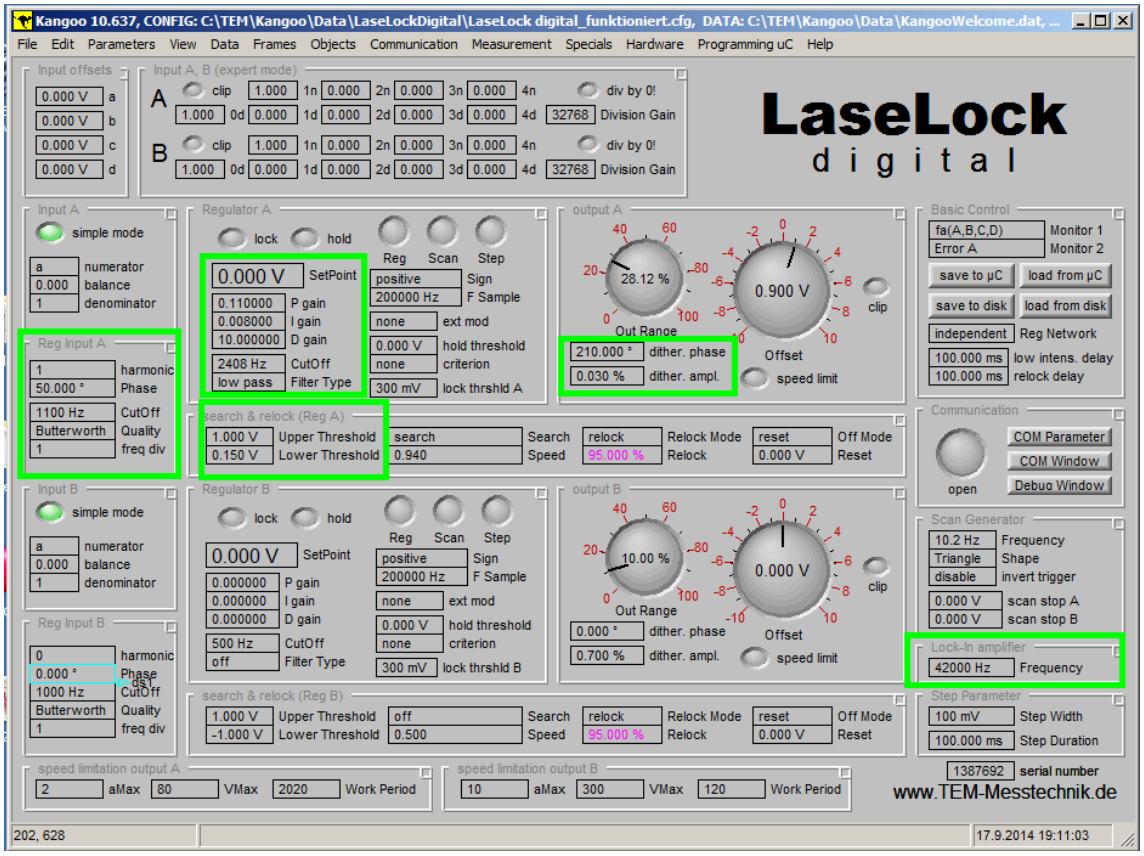

FIGURE 58 Software interface of the lock-box, showing the current settings for the PID control loop as well as parameters for the scan generator, frequency filters and search logic. Important parameters are highlighted in green. Input and regulator B are currently unused.

of the locking stability the experimentally determined settings were as follows: a dither frequency of 42 kHz was used with an amplitude of 0.03 %. The input low-pass filter is set to 1100 Hz and the output low-pass filter to 2400 Hz. The settings for the PID parameters were $P = 0.1$, $I = 0.008$ and $D = 10$. The upper threshold for the input is set at 1 V which is also the input limitation and the lower threshold is set so that it is just above any background or side-mode signal. While the input signal stays within the bounds set by these thresholds the regulation stays active. All settings can be adjusted on a touchscreen display on the lock-box itself allowing stand-alone operation.

With these settings the expected lock-in signal dependence on the transmission of the cavity can be demonstrated as seen on the left side of Fig. 59. For this measurement the dither amplitude was temporarily increased to 0.2% to get a clearer lock-in signal. For clarity the voltage scale for the lock-in signal was magnified by a factor of ten. The well-defined slope of the lock-in signal at the zero-crossing point, which occurs at the transmission maximum allows one to stabilize the cavity. A few small side-modes caused by imperfect mode-matching are visible. The effect of the 10 kHz switching on the photodiode amplifier that is required for operation is shown on the right panel of Fig. 59. Despite the now extreme fluctuations in the signal from grounding the photodiode, the lock-in

signal is affected only by a slight increase in background noise. A clearer view on the time-dependence of the signal is shown in the inset with the drop-outs having a length of about 10 μs. The drop-outs actually reach below the background level by about 500 mV. This issue is caused by the electronics and could likely be improved with a revised circuit, though it does not affect the stability.

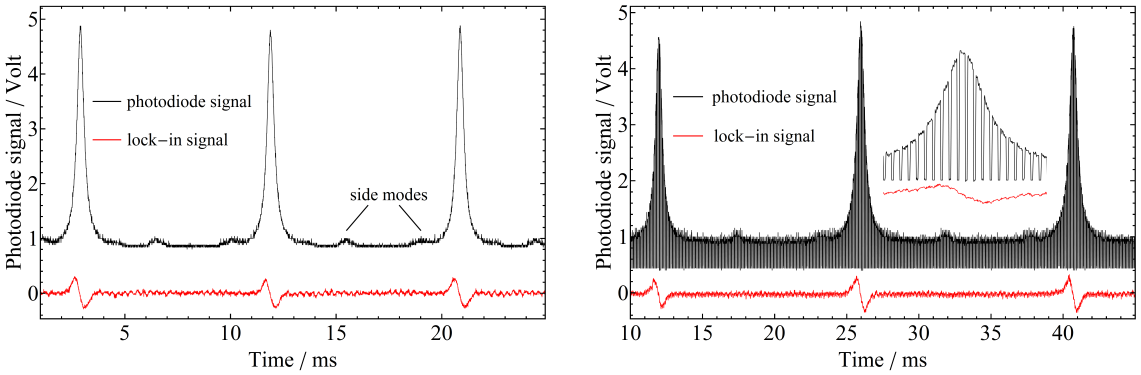

FIGURE 59 Left panel: Photo-diode and lock-in signal with the scan generator turned on. Right Panel: Same settings but with the 10 kHz trigger applied to the switches of the photo-diode amplifier. The inset shows a magnified view of a single transmission peak.

With the cavity locked the transmission stays close to the maximum level, independent on whether the 10 kHz switching is on or off, as can be seen in the comparison between the left and right panels of Fig. 60. Some signal fluctuations of about 5-10% still remain, which are related to intensity instabilities of the injected seed caused by the fibre transport. When locking to a more stable source such as the output of the stabilized HeNe laser the fluctuations were found to be less than 1%.

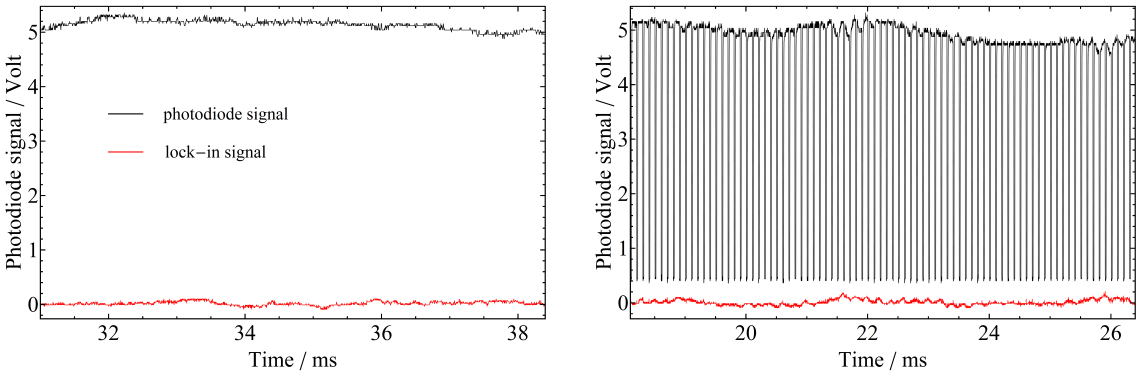

FIGURE 60 Left Panel: photodiode and lock-in signal with the cavity locked. Right panel: same settings, but with the 10 kHz trigger applied to ground the photodiode amplifier.

In summary the locking performance was found to be robust to external perturbations. Knocking on the cavity side plates or touching of the optical mounts inside the cavity may still force the cavity out of lock. With the cavity out of lock

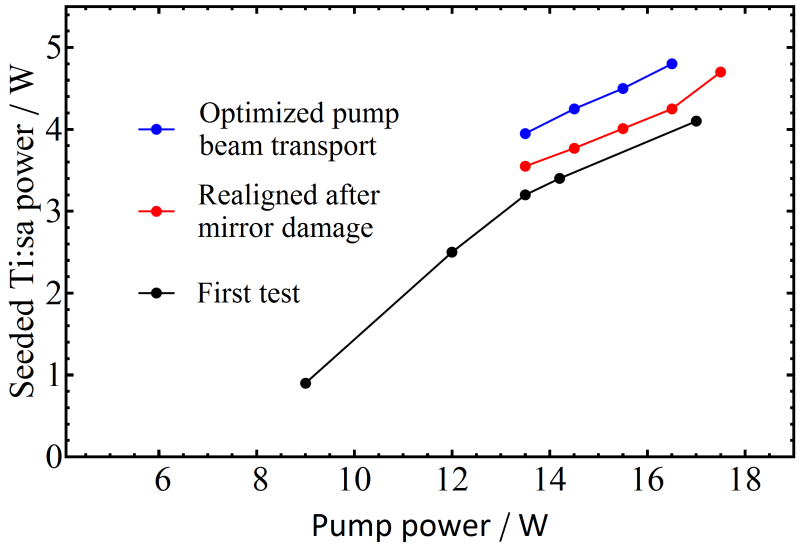

FIGURE 61 Seeded output power vs. pump power.

the search and scan routine of the lock-box initiates. Using a high search speed, the re-locking process usually takes less than 50 ms and is thus fast enough to ignore the rare "drop-outs" during spectroscopic measurements. If necessary the data taken while the lock is off could be removed using a veto signal.

6.2.3 Output power

The performance of the injection-locked laser was characterized at several pump power levels. Fig. 61 shows three power curves, which were taken separately after realignment of the cavity. It was noticed that the pump beam was cut off slightly at a waveplate; after recentering the plate a higher efficiency was reached. A maximum output power close to 5 W was achieved in all cases. The limitation here was not the available pump power, but rather the damage threshold of the cavity mirrors. A more suitable coating optimized for high average power could extend this limitation. In all measurements the cavity was locked and seeded at a wavelength of 780 nm

The slope efficiency can be estimated to be about 0.45 and the optical-to-optical conversion efficiency from green to IR is about 30% for the maximum pump power. This efficiency is slightly higher compared to that of our standard Z-shaped cavity Ti:sa lasers, as is expected considering that no frequency selective elements such as a birefringent filter or etalon are needed for operation.

6.2.4 Linewidth

The linewidth of the injection-locked Ti:sa was measured using a commercial scanning Fabry-Pérot Interferometer (Toptica FPI-100-0750-1). It features a free spectral range (FSR) of 1 GHz and for the Ti:sa wavelength of 780 nm the finesse was found to be ≈ 300, measured using the continuous wave laser radiation of the Matisse master laser. As the injection-locked system is pulsed, the FPI spectra

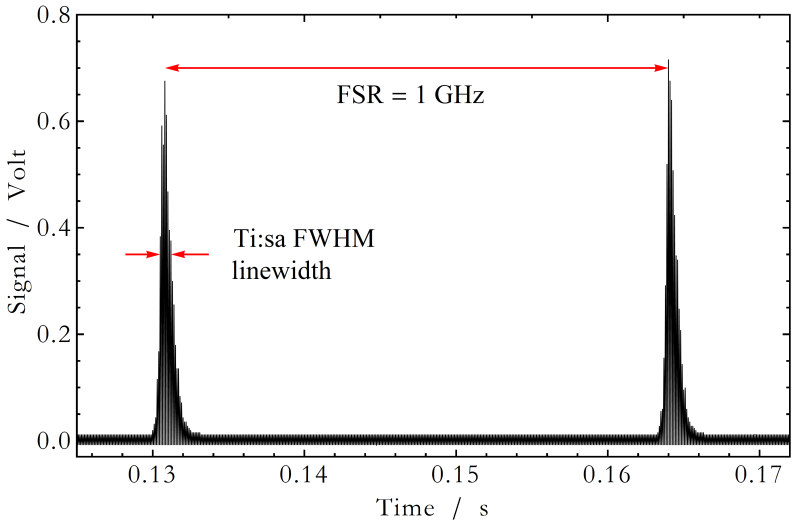

FIGURE 62 Seeded Ti:sa signal in the FPI (1 GHz FSR) showing two transmission peaks. Each transmission peak is composed of many individual shots of the 10 kHz repetition rate laser.

were taken with a slow scanning rate to allow for several individual pulses during a transmission peak of the FPI as shown in Fig. 62. Here two transmission peaks are visible, separated by the FSR of the FPI and no spectral side modes can be seen. The background level is not related to any unseeded output or fluorescence, but is just due to the limited voltage resolution of the oscilloscope at this scale.

The spectra were taken for several different output power levels, an example comparison is shown in Fig. 63 for three output power settings of 4.1 W, 3.4 W and just above the lasing threshold with a power of 0.9 W. To extract the linewidth a Gaussian fit to the peak envelope was made. The peaks show a slight asymmetry with the right flank slightly wider than the left.

The trend of the linewidth dependence on Ti:sa output power is given on the left side of Fig. 64. While a linear fit may be too simple, considering that many different parameters may influence the bandwidth, the reduced χ^2 value for the fit is close to 1. At just above lasing threshold the pulse duration of the Ti:sa can reach significantly above 100 ns. Assuming a completely Fourier-limited linewidth and a time-bandwidth product of 0.44 for a Gaussian pulse shape the expectation would be a linewidth below $\approx$ 4.4 MHz. The fit to the data crosses the y-axis at just above 10 MHz. Even considering the limited finesse of the FPI this indicates other broadening mechanisms.

As discussed in [101] the pump pulse can induce frequency chirp effects, so the linewidth data was plotted against the incoming pump power as seen on the right side of Fig. 64. Here the fit to the data has a y-axis intercept at 3.5 MHz. While not conclusive, chirp effects may indeed be one of the main factors contributing to the total linewidth. Accurate measurements of the pulse durations or using heterodyne techniques could further validate this assumption.

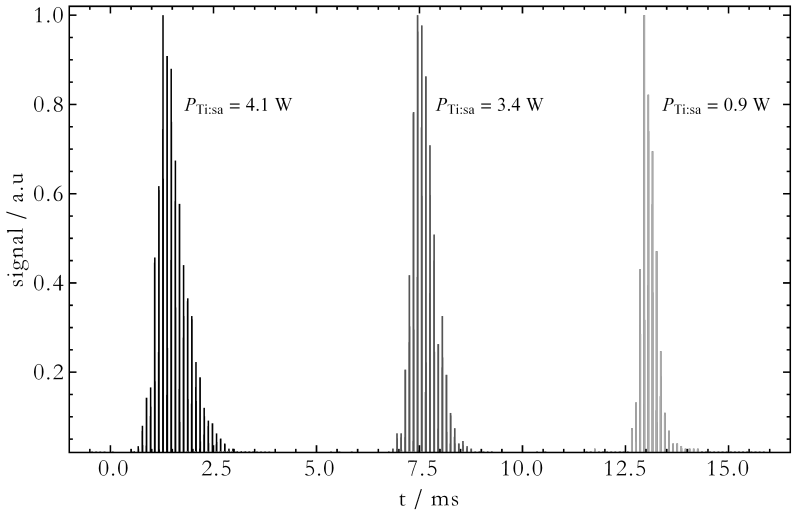

FIGURE 63 FPI spectrum at different Ti:sa power levels showing a single transmission peak for each power setting with an additional offset in time for clarity.

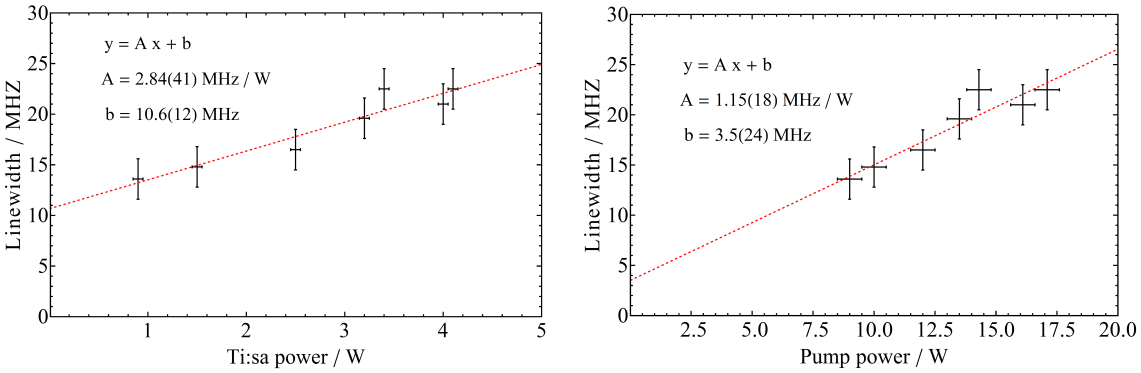

FIGURE 64 Left panel: linewidth dependence on Ti:sa output power. Data points in black, linear fit in red. Right panel: linewidth dependence on pump power.

6.2.5 Seed efficiency and wavelength dependence

The ratio between the output power at the seed wavelength and total output power is the seed efficiency. In the following, this efficiency is not measured directly, it is rather estimated by comparing the output power in the forward (along the seed) direction with and without the seed injected into the cavity. With no injection the cavity will be running freely and will have (nearly) identical output powers going in the forward as well as in the backward output directions since there is no unidirectional element within the cavity. The output power in the forward direction P_{off} will thus be half of the total power. With injection the output P_{on} will be preferred in the forward direction, and if only the injected wave and no other wavelengths are amplified 100% of the radiation will be going in one direction. The seed efficiency is then calculated as

$$\epsilon = \frac{P_{on}}{P_{off}} - 1. \tag{154}$$

This formula represents the actual definition of the seed efficiency relatively well in cases where the free running wavelength and the injected wavelength are close to each other. In cases where the wavelengths considerably differ, the gain in the Ti:sa crystal as well as losses on mirror coatings can lead to significant deviations. A better approach would be to simultaneously measure the power in the forward and backward directions when the seed is on. The measurement of the backward direction could be performed using the rejected light at the optical isolator. This light was however not easily accessible. An even more convenient solution would be using a spectrum analyser if available.

Wavelength tuning with broadband mirror set

The seed efficiency will depend on the injected power of the cw beam as well as on the wavelength due to the wavelength-dependent gain and losses. With the broadband mirror set and a fixed injected power of 15 mW the tuning curve shown in Fig. 65 was measured. In the range from 750-850 nm the seed efficiency stays nearly constant at values close to one. The reason for not reaching the full 100% seed efficiency may be related to pulse timing issues. With injected seed the laser pulse build-up can be much quicker. As the pump pulse is relatively long (120 ns) the inversion has not yet grown to its maximal value, so that the full output power may not be reached.

At wavelengths below 750 nm and above 850 nm the efficiency starts to drop rapidly. The injected power here is likely not high enough to overcome the higher gain of other modes running closer to 800 nm. The seed efficiency drops to 0.5 at 735 nm and 870 nm.

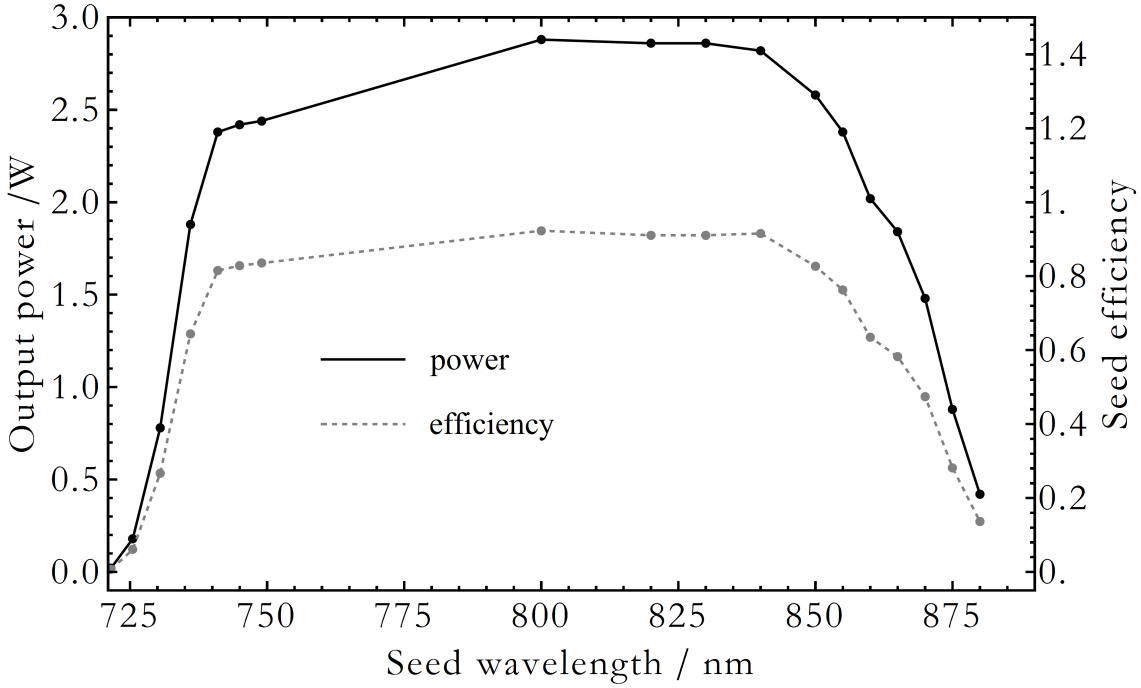

FIGURE 65 Wavelength tuning curve with full broadband mirror set. Shown are the seeded output power (black line) and the seed efficiency (dashed grey line). An injected power of 15 mW was used.

Wavelength tuning with mixed mirror set

The wavelength of 732.71 nm required for a spectroscopic experiment on copper was not reached with good efficiency when using the broadband mirror set. Replacing the two curved broadband mirrors with mirrors coated for the lower wavelength range from 650-740 nm shifted the lowest reachable wavelength to just below 730 nm as can be seen in Fig. 66. The same amount of injected power of 15 mW was used. The seed efficiency is close to one from 735 to 760 nm and drops to 0.5 at about 728 nm. Despite changing two mirrors the lower wavelength limit only improved slightly.

To understand the underlying effects in more detail it is useful to examine the dependence on the injected power for a few different wavelengths. Fig. 67 shows the data for three different wavelengths of 725 nm, 745 nm and 775 nm. At 725 nm the seed efficiency increases as a function of the injected power up to a maximum of 110 mW and reaches close to one for the locked cavity. This behaviour is expected as more injected power is equal to a higher starting photon number at the seed wavelength, leading to fewer round-trips required for amplification as well as a reduced gain for the free-running modes. With a wavelength of 745 nm the seed efficiency is nearly constant when locked and at a high level of 1.06. Even at very low powers the free-running modes are fully suppressed. An efficiency value > 1 suggests that the losses at the seed wavelength are lower than those of the free-running Ti:sa. Furthermore the efficiency even increases at very low injected power (less than 5 mW). This behaviour was reproducible.

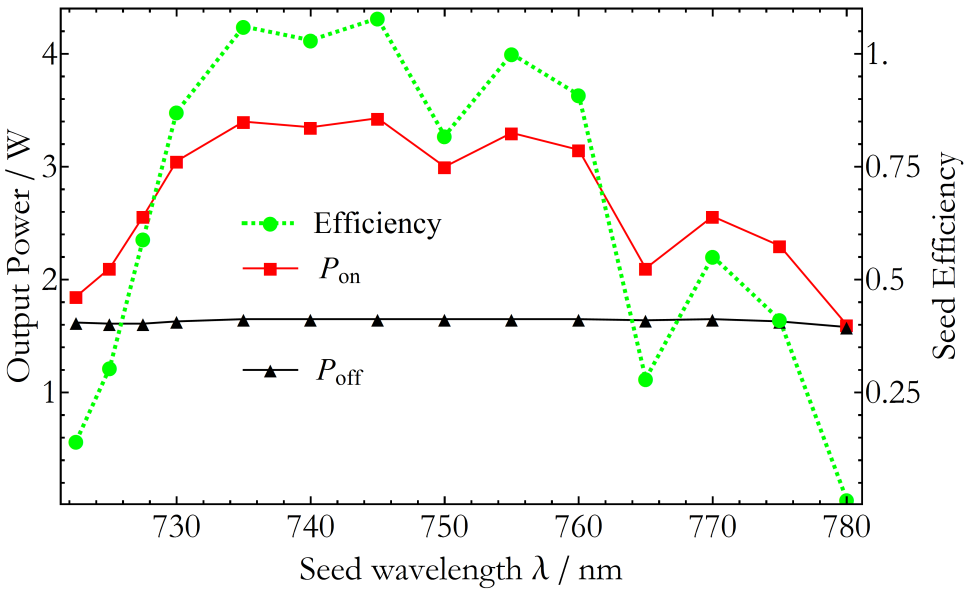

FIGURE 66 Wavelength tuning curve with a mixed mirror set using both broadband output coupler and piezo mirror as well as two curved mirrors coated for 650-740 nm. Shown are the seeded output power P_{on} (red) and the baseline power without seed P_{off} (black) as well as the seed efficiency.

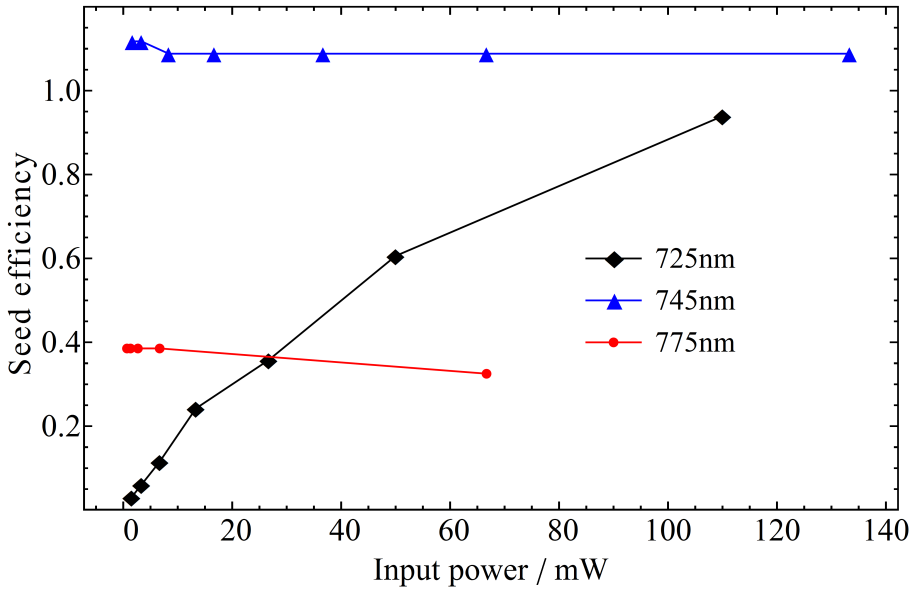

FIGURE 67 Seed efficiency dependence on injected power at 725 nm, 745 nm and 775 nm with mixed mirror set.

One possible explanation may be again changes in pulse timing. With very low injected power the pulse build-up is slightly delayed (but still faster than when free-running). Due to the long pump pulse of the YAG more inversion can be used with delayed pulse build-up. Because of this a later pulse will have slightly more inversion accessible and thus higher output power. A similar trend is seen at 775 nm, the only change here is that the efficiency value of 0.4 is at a lower level. An explanation for this is the two curved mirrors having higher transmission at the seed wavelength leading to large losses, which are unaccounted for.

In summary, the wavelength dependence of the seed efficiency is well understood. The reduced efficiency in the low and high wavelength region can be explained with the large difference in gain between the free-running modes and the mode at the seed wavelength, which will be discussed in more detail in section 6.2.6. Suppression of the free-running modes in the high gain region around 800 nm by change of mirror set had only a limited effect. As the mirror reflectivity of most coatings does not have a sharp cut-off at the boundary of its specified range, a high partial reflectivity can remain in this high-gain region. Better results may be achieved by replacement of all cavity mirrors. The required realignment of the cavity as well as replacement of the piezo-mirror, which is fixed using glue, makes this time consuming.

6.2.6 Single-plate birefringent filter

A change of mirror sets in order to reach certain wavelengths is rather inconvenient. Using more injected power can slightly extend the wavelength range covered with the broadband set. A calculation performed using the multi-mode rate equations, displayed in Fig. 68, shows that for regions far off the gain peak unattainable amounts of input power would be required to reach a seed efficiency of 95%.

For the rate calculations the mode at the seed wavelength was given a number of starting photons N_{seed} that was estimated from the injected power P_{inj} and the cavity round-trip time τ_{cav} as

$$N_{\text{seed}} = \frac{P_{\text{inj}}}{h \cdot \nu_{\text{inj}}} \cdot \tau_{\text{cav}}. \tag{155}$$

While the other modes have no starting boost provided by the injected laser, they may experience a much higher round-trip gain and thus outperform the mode at the seed wavelength. To reduce computing time not every individual mode was calculated, rather they were grouped together in 1-nm intervals with the number of modes per interval estimated from the FSR of the cavity. Compared to the experimental tuning curve in Fig. 65 the calculations would suggest a slightly wider tuning range especially in the higher wavelength region. Reasons for this discrepancy could for example be the assumption of perfect mode-matching in the calculations, wavelength-dependent losses of the coatings or inaccurate estimates of other laser parameters.

To improve the tuning range without the need to change the mirror-set a single birefringent quartz plate was installed. Using the plate to rotate the

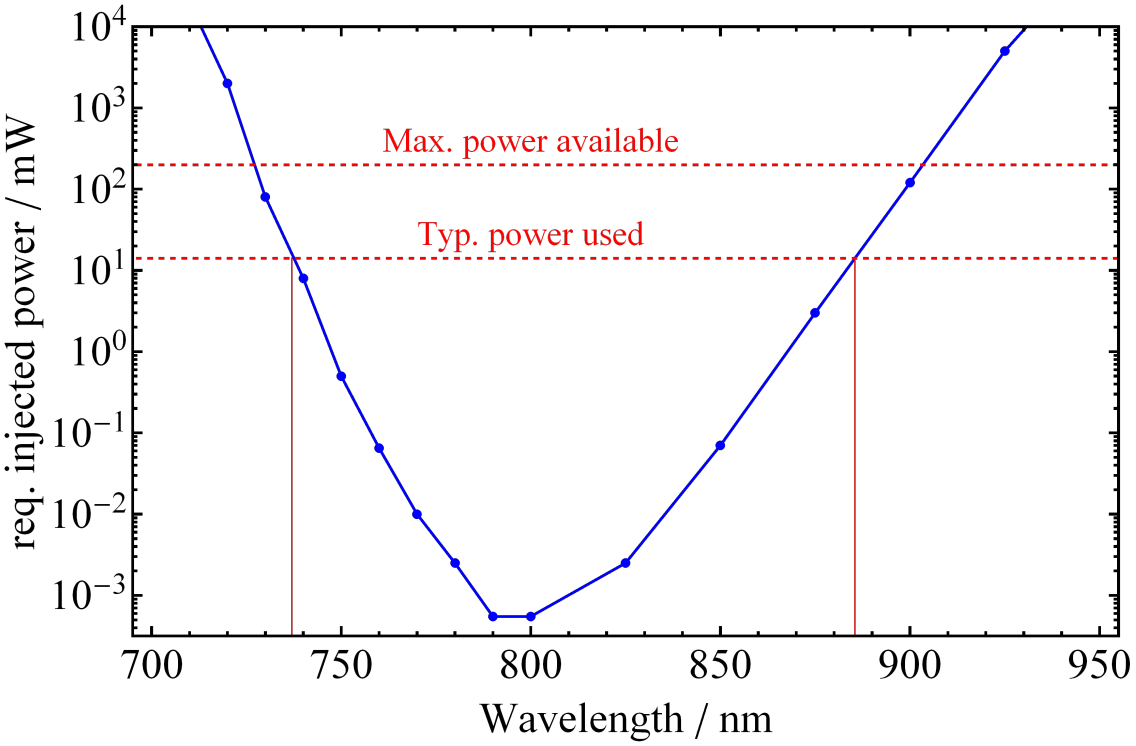

FIGURE 68 Power required to achieve 95% seed efficiency as calculated from rate equations.

polarization causes a wavelength-dependent loss at the Brewster surfaces inside the cavity. A 235 μm plate was acquired with the orientation of the optical axis of the crystal parallel to the surface. The transmission function of this plate was calculated using the Jones-Matrix formalism with the formulation given in section 2.5.2 and is shown in Fig. 69. For the calculation only the plate itself and the two Brewster surfaces of the Ti:sa crystal were assumed. By rotating the angle of the plate the transmission maxima are shifted. The best discrimination against other modes is achieved at a rotation angle of $\phi \approx 40$ degrees which equates to a wavelength of 700 nm at the low wavelength end and just above 1000 nm at the high wavelength end. For rotation angles $\phi > 70°$ or $\phi < 15°$ the filtering action of the plate is very weak. If the discrimination is insufficient further polarizing elements such as Brewster plates could be added to the cavity. A similar setup was used in [102], whereby a commercial three-plate birefringent filter was installed. This however is more expensive and causes a large offset to the laser beam in the resonator.

A comparison of the tuning range with and without the quartz plate is shown in Fig. 70. The lowest reachable wavelength (50% efficiency level) could be reduced from $\approx$ 734 nm to 714 nm for the same injected input power of 15 mW. This limit can likely be lowered further by the addition of Brewster-plates for additional filtering or increased injected power as well as a higher pump power setting. Even though the free-running wavelength is now closer to the injected wavelength due to the birefringent quartz filter, the seed efficiency for some wavelengths again reached values slightly larger than one. The upper wavelength

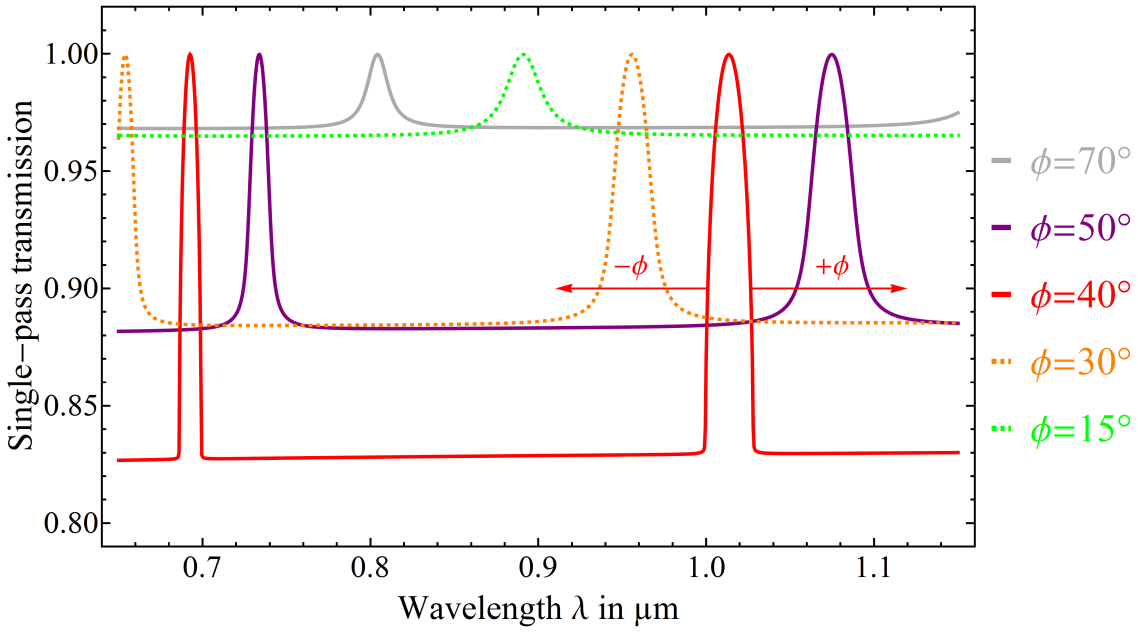

FIGURE 69 Simulated transmission curves of the single plate birefringent filter inserted at Brewster angle.

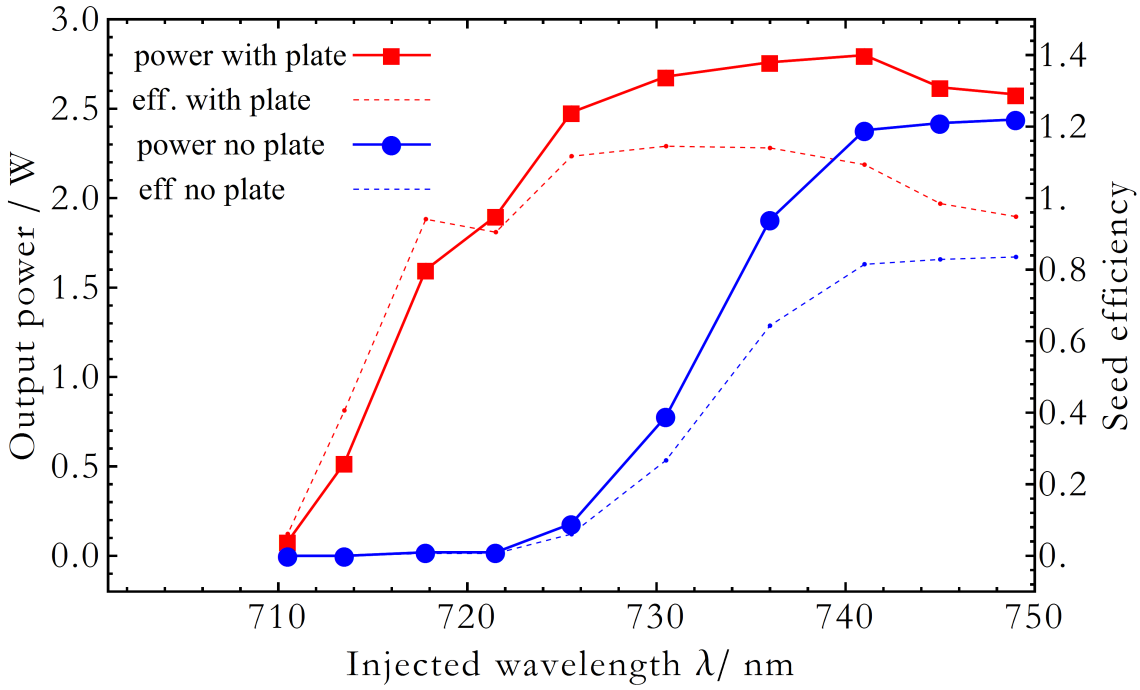

FIGURE 70 Tuning range with and without the birefringent filter plate.

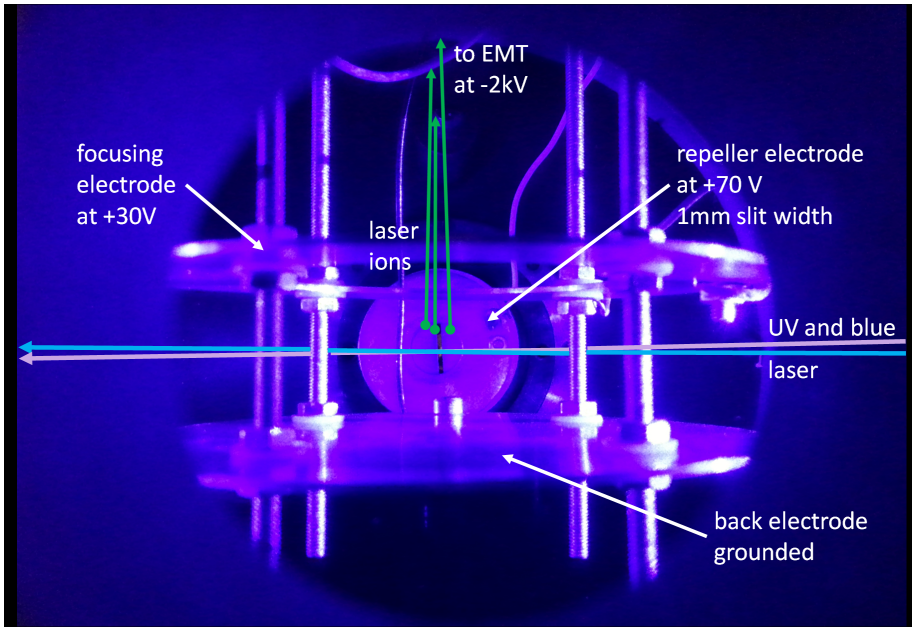

FIGURE 71 View looking down into the atomic beam unit (ABU) showing the collimating slit and ion optics. To visualize the function of the ABU the laser beam path as well as ion trajectories are drawn.

limit still has to be fully characterized. First results suggest insufficient wavelength selection in the wavelength range from 870-890 nm with better performance at wavelengths > 900 nm.

6.3 High resolution resonance ionization spectroscopy of stable copper

To test the capability of the injection-locked Ti:sa laser for high-resolution measurements in combination with the new relative frequency measurement using the scanning FPI (see chapter 5) the hyperfine structure (hfs) of stable copper isotopes was measured using a two-step RIS scheme in the atomic beam unit (ABU). The RIS scheme requires 244 nm for the first excitation step and 441 nm for the second step to an AI as already presented in Article III [88].

6.3.1 Experimental setup for the spectroscopy of copper

The ABU setup has already been introduced in chapter 3.2. To reduce the experimental Doppler broadening, an additional collimating slit was inserted, with a bias voltage simultaneously repelling surface ions created by the oven. Figure 71 shows a view through the top window of the ABU.

To reach the required wavelength for the first step transition at 244.237 nm the injection-locked laser was frequency tripled from a fundamental wavelength of 732.711 nm. High seed efficiency at this low wavelength was obtained using the birefringent plate (see section 6.2.6). The fundamental infra-red (IR) output

power of about 2.8 W resulted in 50 mW of UV light, reduced to 30 mW in front of the ABU due to transport losses. The spot of the UV was slightly elliptical with dimensions of 2x5 mm^2 estimated by eye. This equates to an intensity of 300 mW/cm^2 or 30 $\mu J/cm^2$. The UV power can easily be adjusted by rotating the polarization state of one of the inputs to the frequency tripling crystal. For the second step excitation at 441.679 nm an intra-cavity frequency doubled broadband Ti:sa was employed with an output power of close to 1 W, reduced to 0.8 W after transport. The spot size of the blue laser was $\approx 0.5\,cm^2$ equating to an intensity of 1.6 W/cm^2. In this setup, the two Ti:sa lasers were pumped using two separate Nd:YAG lasers. While allowing for easy temporal synchronization, this results in a slightly larger timing jitter of about 10 ns.

The hyperfine structure is scanned by tuning the master Matisse laser with the injection-locked Ti:sa slave cavity automatically following. Currently the master laser can not be tuned in fixed steps rather the wavelength is tuned continually. The ampere-meter signal measuring the EMT output as well as the FPI signals are recorded.

6.3.2 Copper scans and fitting of data

Several scans at different UV power levels were made. The scan at full power (30 mW) is shown in Fig. 72. Each hyperfine component of the stable ^{63,65}Cu isotopes except for a slight overlap of the last pair at the higher frequency end are well separated. To fit the data a multi-peak Voigt profile is used:

$$Y(\nu) = S \cdot \sum_{i=1}^{N} \psi_i y_i \mathrm{Voigt}(w_G,\, w_L \cdot \gamma_i,\, \nu - \nu_{cog} - \nu_i - \Delta) \tag{156}$$

with the Voigt function explained in section 2.1.3. The equation is given for one isotope only, with overall signal amplitude S and Gaussian and Lorentzian widths w_G and w_L, respectively. The hyperfine coupling constants A and B, which determine the resonance frequencies ν_i (see Eq. 18) of the hyperfine components are fitted. The theoretically calculated signal strength for the hyperfine components are the y_i values (see Eq. 22). Further fit parameters are the center of gravity ν_{cog} of a chosen reference isotope, the isotope shift Δ with respect to that isotope as well as ψ_i and γ_i, which represent modifications to the individual intensities and Lorentzian linewidths for each hyperfine component. The signal ratio between the isotopes $S_{63} : S_{65}$ is fixed to the natural abundance ratio (0.6915 : 0.3085).

Despite the visually good agreement of the fit to the data in the upper panel of Fig. 72, the fit residuals given in the lower panel are still far larger than the assumed errors for the data points, which were estimated by a binning procedure. This suggests that the peak shapes deviate from a normal Voigt profile. One reason for this is likely saturation of the transition. A fit with a more complex ''saturated Voigt'' profile has not yet been attempted. Nevertheless the fit results for the hyperfine parameters should still be reliable as relative peak positions are nearly independent from the exact shape of the peaks.

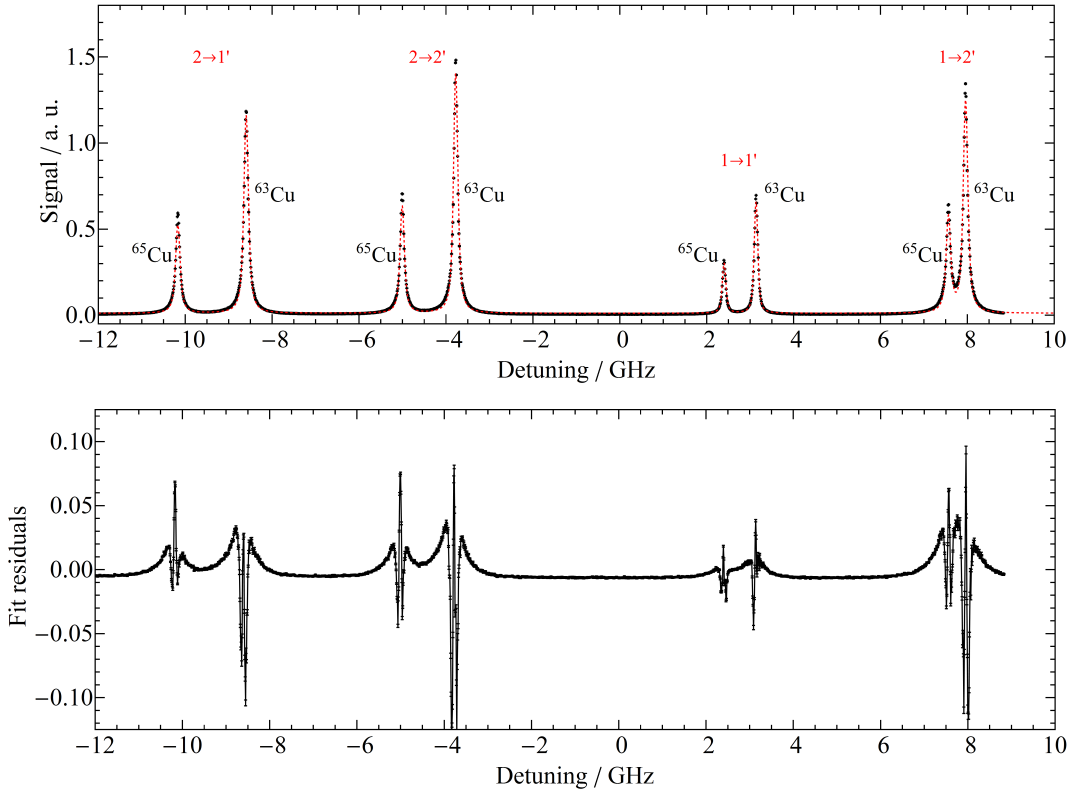

FIGURE 72 Single scan of the 244 nm transition in Cu I illustrating the hyperfine structure. Data points in black, fitted Voigt curve in red. The individual components are marked by their respective isotope and F→F′ transition. The lower panel shows the fit residuals.

A slight asymmetry in the peaks can also be noticed with the left flank residuals generally higher than the right flank. This was more pronounced for the higher resolution spectra. This may either be caused by a non-Gaussian distribution of the seed radiation, or due to non-normal crossing between atomic- and laser beam, which is described in [103].

The fitted Gaussian FWHM of 65(2) MHz was nearly identical for all scans, except for the highest power scan where it was slightly larger at 71(3) MHz. From frequency tripling of a fundamental laser with a linewidth of ≈20 MHz a Gaussian linewidth of $\sqrt{3} \cdot 20 \approx 35$ MHz would be expected. In section 6.2.4 the linewidth of the laser was determined from a short-term measurement. Slower frequency fluctuations could increase the effective linewidth during a scan. Additionally, for a temperature of 1300 K and an opening half-angle of 0.25° the remaining Doppler width should be < 20 MHz. Considering that in a convolution, Gaussian widths add in quadrature, this is only a minor contribution. For the indicated non-normal laser incidence this however may be an underestimation.

6.3.3 Hyperfine parameters and isotope shift

A total of 12 scans were taken, of which six used varying UV power levels and will be discussed in section 6.3.4 and six studied the effect of a delayed ionization pulse, discussed in section 6.3.5.

The mean values of the hyperfine coupling constants for both isotopes and the isotope shift $\Delta IS^{63-65}Cu$ are given in Table 5 as well as comparison with literature values [87, 104]. The errors given in round brackets include only the error estimated from the statistical variation between the scans, while the error value in square brackets includes the uncertainty of the FSR and non-linearity of the FPI (section 5.4.2). The relative FSR uncertainty of 0.015% directly factors into the error as it is proportional to the size of the measured parameter. It is difficult to estimate how much the non-linearity effects the results, since each scan and each peak will be affected differently. For now, the error was assumed to be fixed at $3 \cdot 0.025\%$ of one FSR, equaling to 0.75 MHz, with the factor three due to the frequency tripling process.

The agreement with the literature values for the ground-state parameters is well within the error estimate, possibly even suggesting that the errors due to the FPI are overestimated. For the excited state of ^{63}Cu the literature value is less precise and does not agree within $2.5\,\sigma$. The same is true for the isotope shift value with a deviation of more than $3\,\sigma$. It is likely that the error estimates for the literature values from [104] were underestimated, considering that a much wider spectral width of > 3 GHz and less accurate wavelength determination was used in that work. In [104] a fixed ratio for the excited (ex) and ground state (gs) hyperfine parameters was used for fitting with a value of A_{gs}/A_{ex}=0.415. In our measurement the experimental value is A_{gs}/A_{ex}=0.41101(30) for ^{63}Cu and 0.41095(30) for ^{65}Cu, which agree with each other within the error range.

Hyperfine coupling constants of ^{63}Cu and ^{65}Cu			
	Experiment	Literature	Dual etalon exp.
^{63}Cu A_g/MHz	5866.84(21)[116]	5866.908706(20)*	5887(20)
^{63}Cu A_e/MHz	2411.33(31)[86]	2432(8)†	2416(20)
^{65}Cu A_g/MHz	6284.85(27)[121]	6284.389972(60)*	-
^{65}Cu A_e/MHz	2582.77(28)[87]	2588(15)†	-
ΔIS^{63-65}Cu /MHz	1045.95(21)[79]	977(21)†	1090(100)

TABLE 5 Experimental results for hyperfine parameters and isotope shift of copper as well as comparison with literature values from [104](†) [87](*) and the previous result using the dual-etalon Ti:sa discussed in chapter 5. For the dual-etalon measurement no result is given for ^{65}Cu as a fixed ratio A_{63}/A_{65}=5.867/6.284 was used for the fit.

6.3.4 Saturation and optical pumping effects

Trends for the overall amplitude (as taken from the average of the peak heights) as well as for the Lorentzian linewidth component w_L can be extracted from the data. Based on the transition strength of the first excited state, $\Gamma_1 = 2.03{\cdot}10^6\,s^{-1}$ [72], the FWHM Lorentzian width due to the natural line broadening can be expected to be $\Gamma/2\pi = 0.323\,MHz$. The saturation intensity according to eq. 7 is $18\,mW/cm^2$. This however assumes a monochromatic continuous wave laser source and cannot be directly applied to this experiment.

Results for the saturation of the signal amplitude of the 244 nm transition and for the power broadening of the Lorentzian linewidth are shown in the left and right panels of Fig. 73, respectively. The saturation curve (red line) follows the equation for a simple two-level system reasonably well and yields a saturation intensity of $I_{sat} = 25.6(14)\,mW/cm^2$. The errors of the laser intensity are only due to power fluctuations and do not include the larger uncertainty due to the spot size estimation.

While the Lorentzian linewidth trend may also be plotted using the simple model, the extracted FWHM width at zero power Γ_0 is nearly two orders of magnitude higher than the expected value. This may in part be due to the high peak intensity in the laser pulse, however a second contributing factor which could be verified (see section 6.3.5) is the ionization laser. To account for this second factor, both a fit with the simple model (red line) as well as a model adding an offset term Γ_{off} (blue line) were applied to the data. The two models yield different saturation intensities, both also not agreeing with the saturation curve of the amplitude. The χ^2 value of the simple model is 0.8 as compared to the more complex model with a value of 0.3.

The relative peak heights H_i and linewidths γ_i of the individual hyperfine components change with the excitation step intensity as well. The relative peak heights are the amplitude modifiers ψ_i from Eq. 156 corrected for the linewidth

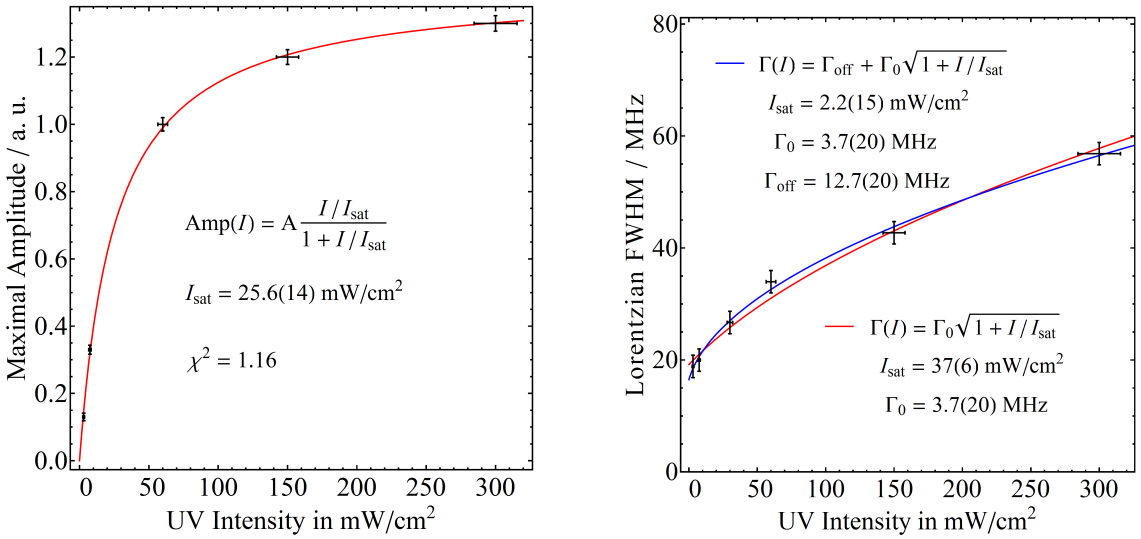

FIGURE 73 Saturation of the 244 nm transition in Cu I. Left panel: saturation curve of the maximal signal amplitude. Data points in black, fit curve in red. Right panel: power broadening of the Lorentzian component of the linewidth of the Voigt profile. Data points in black, fit curves in red and blue using two different models.

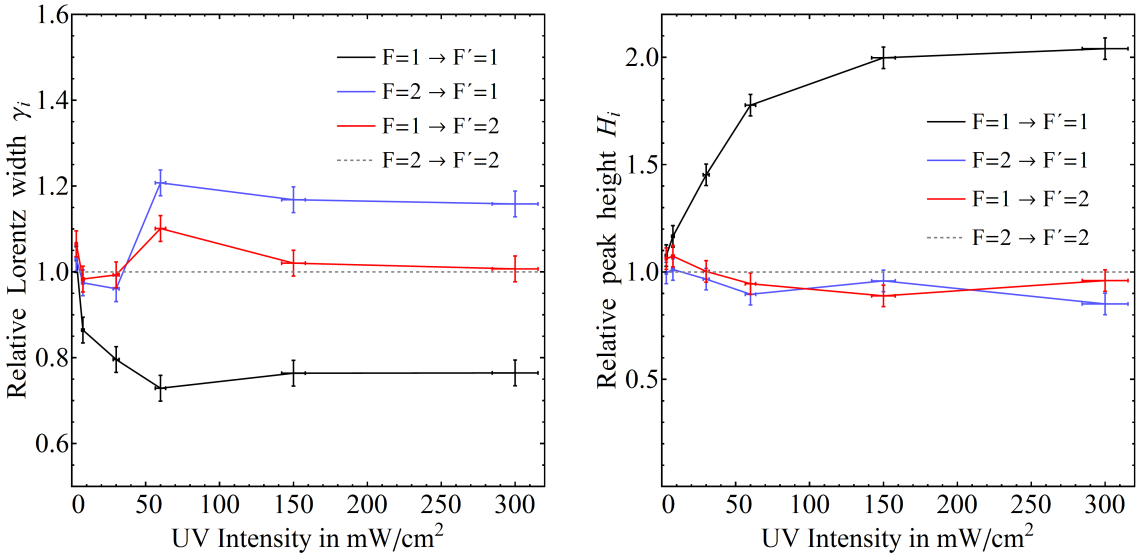

FIGURE 74 Effect of first step intensity on hyperfine component amplitude and width. Left panel: relative Lorentzian widths with the F=2→F′=2 transition as reference. Right panel: relative peak heights with the F=2→F′=2 transition as reference.

contribution to the amplitude with

$$H_i = \psi_i \cdot \frac{\mathrm{Voigt}(w_G, w_L \cdot \gamma_i, 0)}{\mathrm{Voigt}(w_G, w_L, 0)}. \tag{157}$$

For reference the relative linewidth and peak height of the F=2→F´=2 component was kept normalized at 1. The changes in the linewidth of the other three transitions is shown on the left panel of Fig. 74, with the weakest transition from F=1→F´=1 having a nearly 30% narrower width at higher intensities and the F=2→F´=1 transition having a slightly larger width. At the lowest power setting all transitions have similar widths. For the peak heights, shown in the right panel of Fig. 74, only the weakest transition shows a significant deviation from the norm.

6.3.5 Delayed ionization pulse

Recent simulations suggest that the linewidth of a transition is affected by the power broadening caused by the laser driving the ionization process [105]. A delay of the ionization step with respect to the first step excitation is expected to minimize this additional broadening mechanism. In the ionization scheme of Cu two known decay channels of the first excited state exist [72]. One to the ground state ($\Gamma_1 = 2.03 \cdot 10^6/\mathrm{s}$) and another to a level at 13245.423 cm^{-1} ($\Gamma_2 = 3.99 \cdot 10^4/\mathrm{s}$) , resulting in a lifetime of the state $\tau = 1/\sum \Gamma_i = 483$ ns. This is much longer than the duration of the laser pulses with 40(3) ns and 23 ns for the first and second step laser, respectively. The pulse durations are given for the fundamental laser radiation.

The delay between the pulses was adjusted with the trigger of one of the pump lasers. An example of the pulse timing structure for the case of 80 ns delay is shown in Fig. 75, with the delay simply calculated as the time difference of the pulse maxima. The structure represents an averaged signal over many laser pulses, the actual single-shot pulse durations of the lasers are slightly shorter than visible in the figure.

With increasing delay more of the population of the excited state will have spontaneously decayed back to the ground state, reducing the total ionization efficiency as shown in Fig. 76. An exponential function has been fitted to the data, with the exception of the first two data points, as for these significant overlap between the two laser pulses exists. From the fit a lifetime τ of 367(30) ns can be estimated, which is below the literature value. This may be a result of so far unknown decay transitions but remains unclear. It can be noted that the signal strength stays nearly constant up to a delay time of 100 ns.

The Lorentzian linewidth, displayed in Fig. 77, shows a sharp reduction within the first 50 ns delay time (≈ pulse duration) and stays nearly constant at a level of about 3 MHz for longer delays. While this is still a factor of 10 larger than the natural linewidth, the UV intensity was kept at the maximum level of about 300 $\mathrm{mW/cm^2}$ during these tests. Considering that the peak intensity during the pulse is still much higher, this power broadening is not surprising. It should be noted however, that for small values of the Lorentzian width the

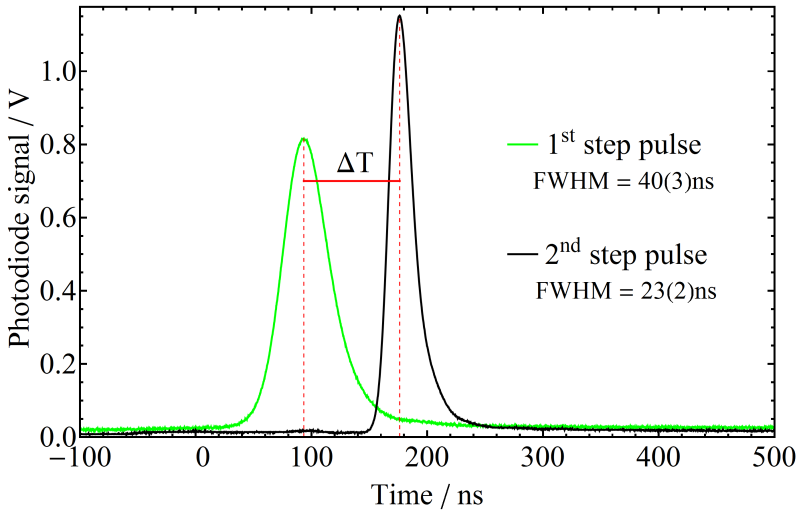

FIGURE 75 Photodiode signals of excitation and ionization laser pulse, showing an example for a measured time delay of $\Delta T = 83$ ns.

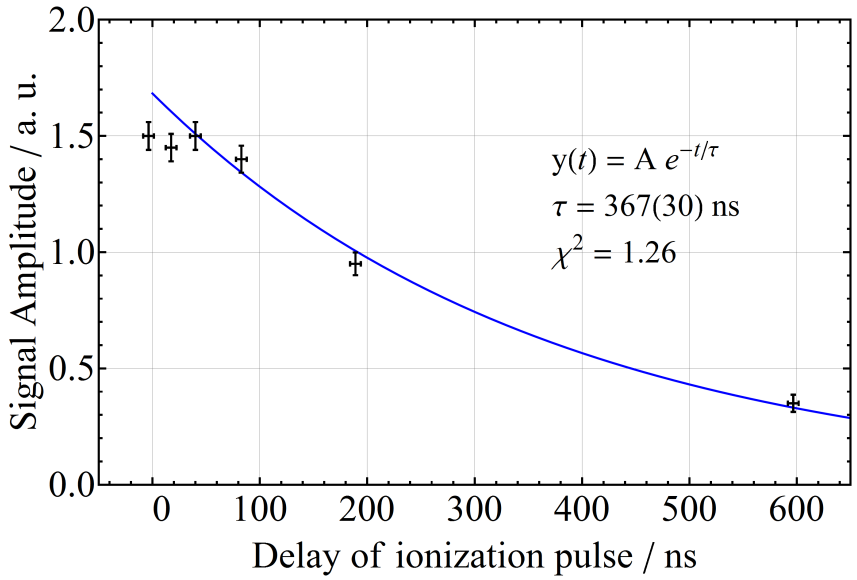

FIGURE 76 Dependence of ion signal on ionization pulse delay time. The fit (blue curve) underestimates the literature value for the life time by about 30%.

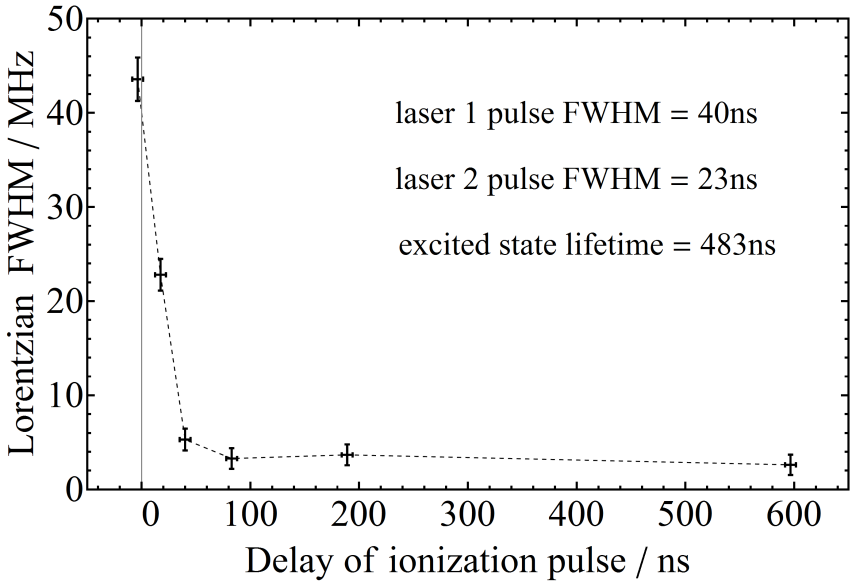

FIGURE 77 Dependence of Lorentzian linewidth on ionization pulse delay.

sensitivity of the fit to this parameter gets weaker and other assumptions about the peak shape may further contribute to a possible error in these measurements. Finally, the dependence of the individual peak heights and Lorentzian widths on the ionization pulse delay with respect to the F=2→F´=2 transition are shown in the left and right panel of Fig. 78, respectively. Little change is noticeable at long delays, but at shorter time-scales within the duration of the laser pulse some fluctuations seem to occur, especially for the peak height of the F=1→F´=1 transition. Similar to the previous result, at high UV power this transition shows a significantly higher signal than expected.

In the future a more sophisticated model using rate equations as discussed in [105, 106] will be applied to this data in order to obtain a better understanding of the effects occurring in pulsed laser RIS.

For completeness the hyperfine parameters for all scans are displayed in Fig. 79 with the settings for each measurement noted in Table 6. The error bars in the plots are showing the FPI non-linearity and statistical error only. The uncertainty of the FSR affects the whole of the dataset in the same way and thus has no impact on the scattering of the values.

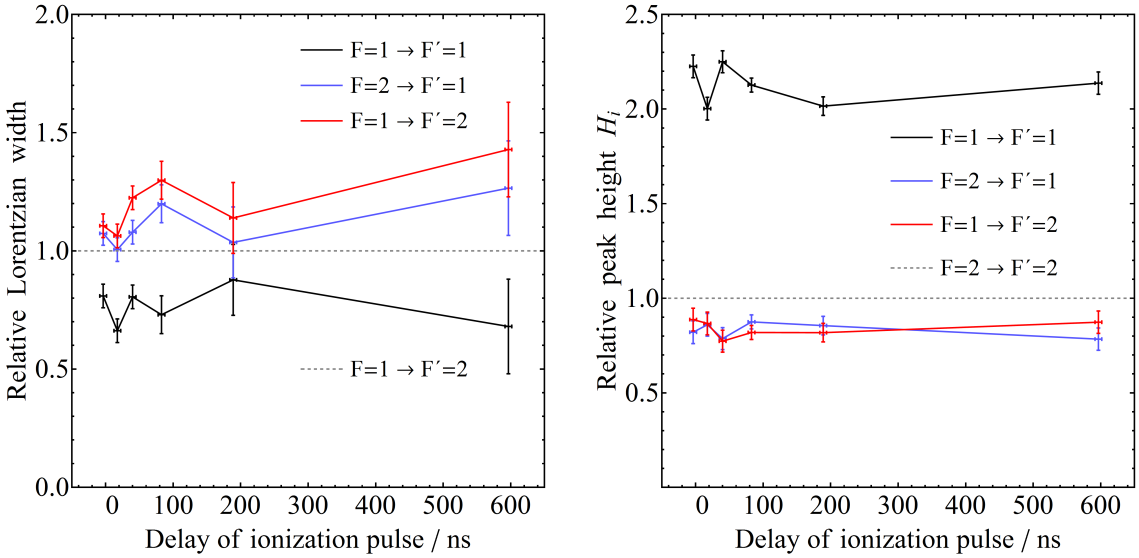

FIGURE 78 Effect of ionization pulse delay on hyperfine component amplitude and width. Left panel: relative Lorentzian widths depending on ionization pulse delay. Right panel: relative peak heights depending on ionization pulse delay.

Exp.#	Intensity / mW·cm^{-2}	Exp.#	Delay / ns
1	3.0(5)	7	-3.6(20)
2	8(1)	8	40.0(20)
3	30(2)	9	82.8(20)
4	60(4)	10	596.6(20)
5	150(8)	11	189.0(20)
6	300(15)	12	17.4(20)

TABLE 6 Settings for the 12 individual hyperfine measurements in Cu. For the first six measurements the delay is constant at 0(10) ns, for the last six measurements the intensity is constant at 300(15) mW/cm^2.

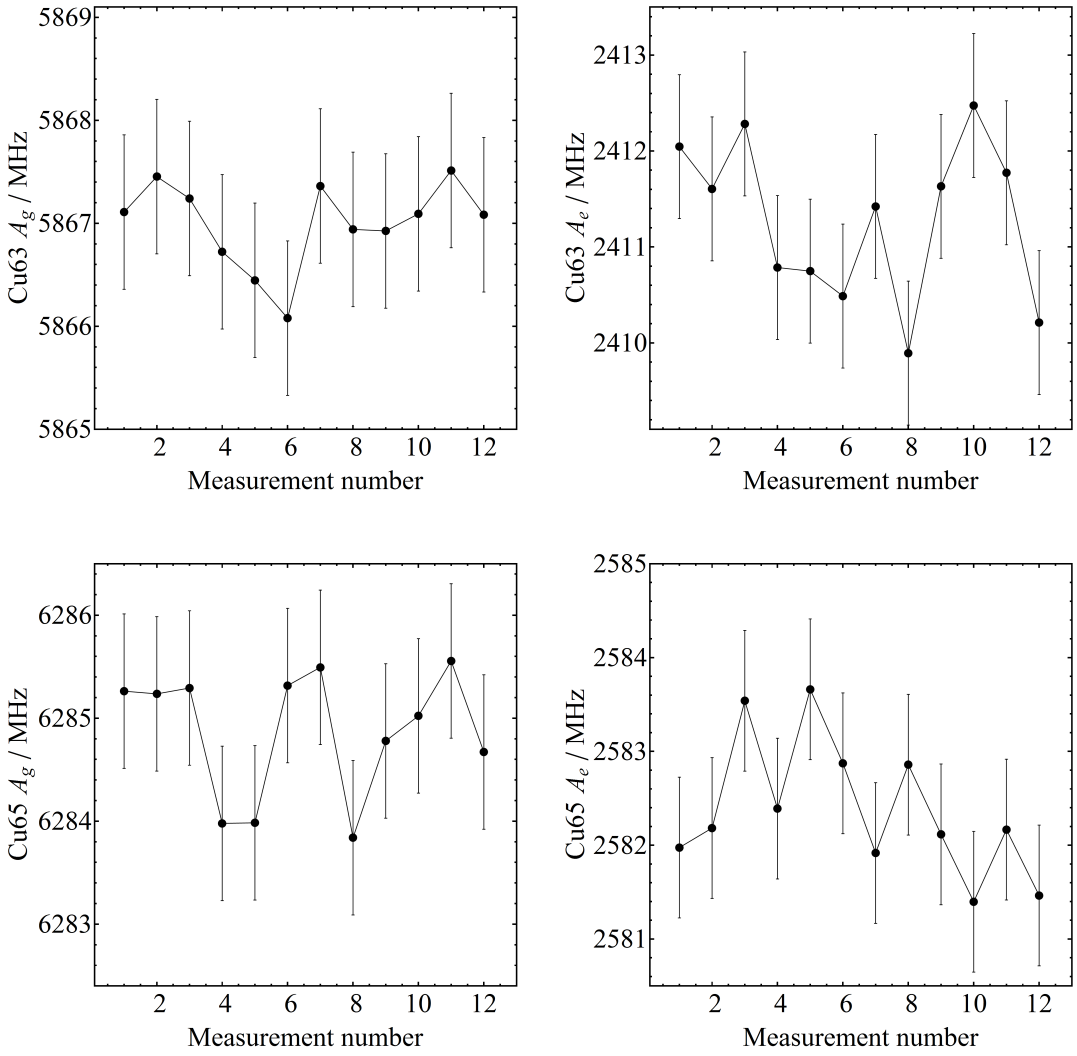

FIGURE 79 Hyperfine parameters for each of the 12 scans of copper. Considering the error margin no obvious systematic trends can be discerned.

6.4 High resolution resonance ionization spectroscopy of ^{227}Ac

For the resonance ionization spectroscopy of actinium and plutonium the injection-locked Ti:sa laser resonator was transported to the laboratory of the Quantum/LARISSA group at the University of Mainz, Germany, with the experiment carried out in further collaboration with the Katholieke Universiteit Leuven, Belgium. The experiment on ^{227}Ac (I=3/2$^-$, $T_{1/2} = 21.772(3)$ years) was performed in preparation for further studies [107] of more exotic isotopes at the on-line RIB facilities LISOL and TRIUMF. For neutral actinium, HFS parameters are not yet documented and the goal was to identify a suitable transition for hyperfine spectroscopy. A high resolution template can furthermore be used to calibrate future lower resolution on-line results.

6.5 Experimental setup for actinium spectroscopy

6.5.1 Narrowband laser system

A photograph of the injection-locked Ti:sa setup is shown in Fig. 80. Pumping of the injection-locked cavity was achieved using an external frequency-doubled 1064 nm YAG laser. Only up to 5 W of 532 nm light was available after doubling in a BBO crystal, however the beam quality of the pump laser was very good, with an M^2 value of close to 1. This allows for a better overlap of the pump beam with the resonator mode in the crystal and as such a lower pump threshold and an increased efficiency. On the other hand the damage threshold is also reduced accordingly.

Instead of the cw Ti:sa available at the IGISOL facility, an external cavity diode laser (ECDL) was used as the master laser which was coupled through a single mode optical fiber. Two 60 dB optical isolators were used after the fiber to prevent optical feedback from the pulsed cavity. After the isolators a typical power of 5-20 mW was available depending on the chosen diode laser and wavelength range. A short telescope on a rail is used for mode-matching. Two master lasers were available: a commercial diode laser system (Toptica Photonics, TA Pro) for the wavelength range from 760-790 nm and a home-built ECDL with a laser-diode from Eagleyard for accessing wavelengths from 830-880 nm. The diode lasers are stabilized using a combination of a quadrature interferometer (iScan, TEM Messtechnik) for fast frequency control and a fringe-offset locking system for precise control. The details of this system can be found in [108, 109]. The fringe-offset locking uses a confocal FPI with a FSR of 298.0856(26) MHz and a stabilized HeNe laser as reference. The data acquisition is based on a set of Arduino [110] micro-controllers. Using this system the precision of the frequency calibration should be better than 1 MHz.

The diode laser systems have a typical frequency jitter of about 5-10 MHz.

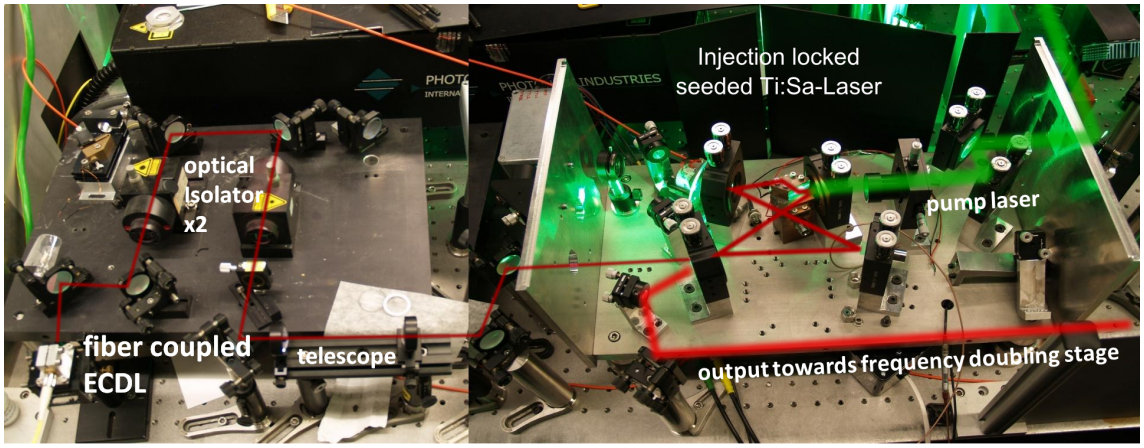

FIGURE 80 Setup of the injection-locked Ti:sa for the actinium and plutonium experiment, see text for details.

With the regulation turned on, the diode laser frequency can be driven towards a set frequency. Data acquisition of the ion signal only takes place whenever the measured laser frequency is within a fixed locking interval (5 MHz) around the set point. A scan is performed by changing the set frequency in steps and recording the ion signal for a short period of time between each step. Due to the fixed locking interval and the frequency jitter of the laser system a small shift of peak positions of ≈ 5 MHz between the two direction of frequency scanning was observed. Due to this, scanning was usually performed in one direction only, or care was taken to compensate for this shift in the evaluation of the data.

The frequency jitter also proved to be slightly detrimental for the performance of the injection-locked cavity. While a stable lock was achieved, the intensity fluctuations on the fast-switched photodiode amplifier signal were significantly stronger when compared to using the cw-Ti:sa as master. Nevertheless, a seed efficiency of close to one and an output power of up to 2 W (at 770 nm) could be reached.

The linewidth of the seeded Ti:sa was measured in order to give a comparison with the conditions at the IGISOL facility. The stabilized HeNe as well as a portion of the seeded output was coupled into a FPI cavity and the spectrum was recorded using an oscilloscope. Without averaging each Ti:sa fringe only consisted of 3-4 pulses as shown in the left panel of Fig. 81. To extract the linewidth a Gaussian envelope was fitted as shown, yielding a FWHM of 9.5(5) MHz. This linewidth is however only representative of very short term fluctuations within a time interval of less than 1 ms. To get a more accurate estimate for the spectroscopic linewidth during a slow scan the oscilloscope was set to record a longer term average shown on the right panel of Fig. 81. A setting of 256 averages was represented a time frame of about 2 s. One immediately notices a dramatically reduced fringe amplitude and strong background fluctuations. Nevertheless, a linewidth of 13.4(8) MHz could be extracted once a quadratic background term was added to the fit. The same procedure was then performed for the output of the master laser, yielding a short-term linewidth of 7.2(3) MHz and a long-term linewidth of 10.1(2) MHz. So despite a significant contribution from the master

laser, the seeded Ti:sa linewidth is still lower than that measured in section 6.2.4. This may be a result of the factor 2-3 lower pump power leading to a reduced frequency chirp.

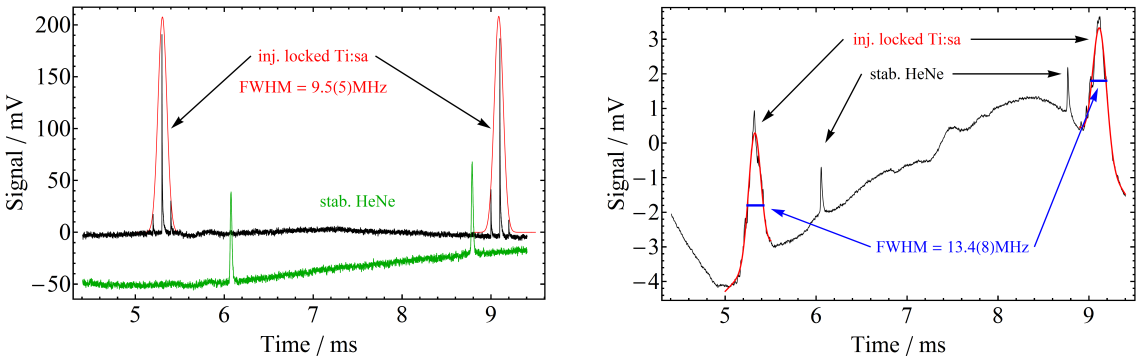

FIGURE 81 Oscillsocope trace of the spectrum of the seeded Ti:sa in the confocal FPI in Mainz. Left panel: recording without averaging. Right panel: recording with 256 averages. See text for details on analysis.

6.5.2 Ionization lasers, ion source and mass spectrometer

The output of the injection-locked cavity was then frequency doubled and transported to the quadrupole mass spectrometer system MABU ("Mainz atomic beam unit"), as shown in Fig. 82, with a simple schematic in Fig. 83. MABU is described in more detail in [111, 112]. Two additional broadband intra-cavity doubled Ti:sa lasers were used for the ionization step, providing up to 1 W in the blue wavelength range. While the seeded Ti:sa beam was sent into the MABU in a perpendicular geometry from a side window, the other two lasers were sent counter-propagating with respect to the atomic beam. As very little power was necessary to saturate the first step transitions the seeded Ti:sa was expanded using a combination of a telescope and a ground glass diffuser to create a uniform intensity distribution in the interaction region. The ionization lasers were focused to a spot size comparable to the oven dimensions with an inner diameter of 2 mm.

Five samples, each with $\approx 10^{11}$ atoms ^{227}Ac were available, supplied by the nuclear chemistry department of the University of Mainz. These were packaged inside zirconium foils of which one was placed into the oven. The current for the ohmic heating of the graphite oven was set between 60-75 A, equivalent to a temperature range of 1400-1700°C. The interaction region of the laser and atomic beam lies between the repeller electrode, used to deflect thermal ions from the oven, and the first extraction electrode. Only a slight collimation of the atomic beam was created by the orifice ($\varnothing$=4 mm) of the repeller electrode, limiting the beam to an opening angle of $\approx 20°$. However, the small diameter of the ionization lasers as well as the high mass number will effectively reduce the possible Doppler broadening. The laser ions arriving at the detector of the MABU after mass filtering had a pulsed time structure with a width of 10 μs. Time-gating was thus successfully employed to minimize background from thermally ionized atoms.

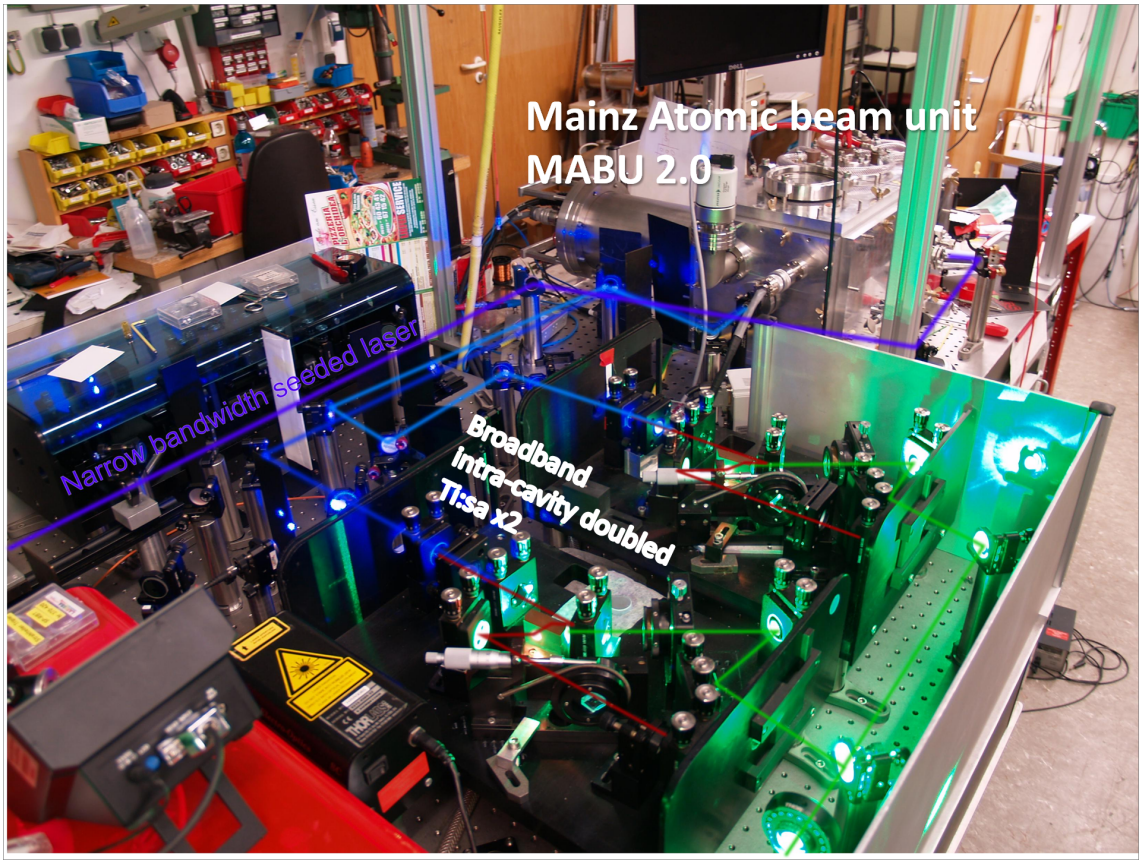

FIGURE 82 Broadband laser systems for the ionization step, optical path and the Mainz Atomic Beam unit (MABU), see text for details.

The mass resolving power (MRP) of the RF quadrupole was $M/\Delta M = 200$.

6.6 Hyperfine structure of actinium

The hyperfine structures of five different transitions were investigated. Figure 84 summarizes the two-step resonance ionization schemes. The value for the ionization potential is taken from [113]. Transitions A, B and C are from the atomic ground state, transitions C and D populate the same excited state and transitions D and E share the same lower level, which is a thermally populated state at 2231.43 cm^{-1} (20% population at 1700 K). The choice of transitions allows a cross-check of the respective hyperfine parameters.

For identification of the second step transitions leading to auto-ionizing (AI) states, laser ionization was applied using in-source spectroscopy. While providing worse resolution, the ion signal was up to a factor of 10^3 higher compared to the cross beam geometry. This allowed a search for AI states at lower temperatures without depleting the atomic sample. Scans were performed by tuning the birefringent filters of the two intra-cavity doubled Ti:sa lasers. As this tuning is very coarse it is unlikely that the optimum transitions have been found. Although still unpublished, extensive AI spectroscopy has been performed for Ac at TRIUMF

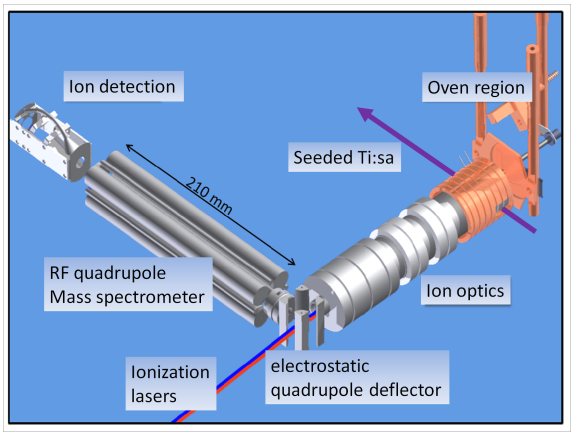

FIGURE 83 3D schematic illustrating the working principle of the MABU system, taken from [112].

and Mainz [114].

The results of all five scans are shown in Fig. 85-89. The data points (black) were calculated as the mean of several independent scans and binned in 20 MHz intervals. The hyperfine structures were fitted with the same formula as given in Eq. 156. To properly account for the Poisson-distributed count-rate signal an iteratively re-weighted fitting procedure was applied. A description of this method is given in [115] and a more general discussion in [116]. The basic idea is as follows: an experimentally measured count rate y is generally distributed with an unknown mean μ and standard deviation σ. Therefore the mean and variance first have to be estimated.For this purpose the data is first fitted without weighting. From the resulting fit the true mean count-rate μ can be estimated and from the relation $\mu = \sigma^2$ the variance as well as the weights $w_i = 1/\sigma_i^2$ may be extracted. Using these new weights and repeating this process iteratively will lead to the maximum likelihood estimate for the fit parameters.

The results for the hyperfine parameters are summarized in Table 7. For each transition both the lower state hyperfine parameters A_L, B_L and the upper or excited state parameters A_U, B_U are given. As expected the ground state parameters agree within errors for transitions A, B and C, for transitions D and E, as well as the excited state parameters for transitions C and D. The error margins for transitions D and E are significantly larger. For transition D this is due to the atomic sample running out, leaving some peaks with very low statistics, while in transition E the parameters are more strongly correlated due to the overlapping resonances and the higher spin states (J=5/2→J=7/2).

For the hyperfine parameters with multiple results the weighted mean was calculated, with the weights w_i assumed as $1/\sigma_i^2$. The results are A = 50.46(48) MHz, B = 595.6(15) MHz for the atomic ground state, A = 255.0(35) MHz, B = 706(19) MHz for the 2231.43 cm^{-1} state and A = 990.7(12) MHz, B = -20.7(36) MHz for the 26066.08 cm^{-1} state. Based on the results, transition B at 438.58 nm is the most promising candidate with the largest total splitting, a clear separation of each hyperfine component as well as having the highest average count-rates. An alternative could be transition A which exhibits a smaller splitting, but has a

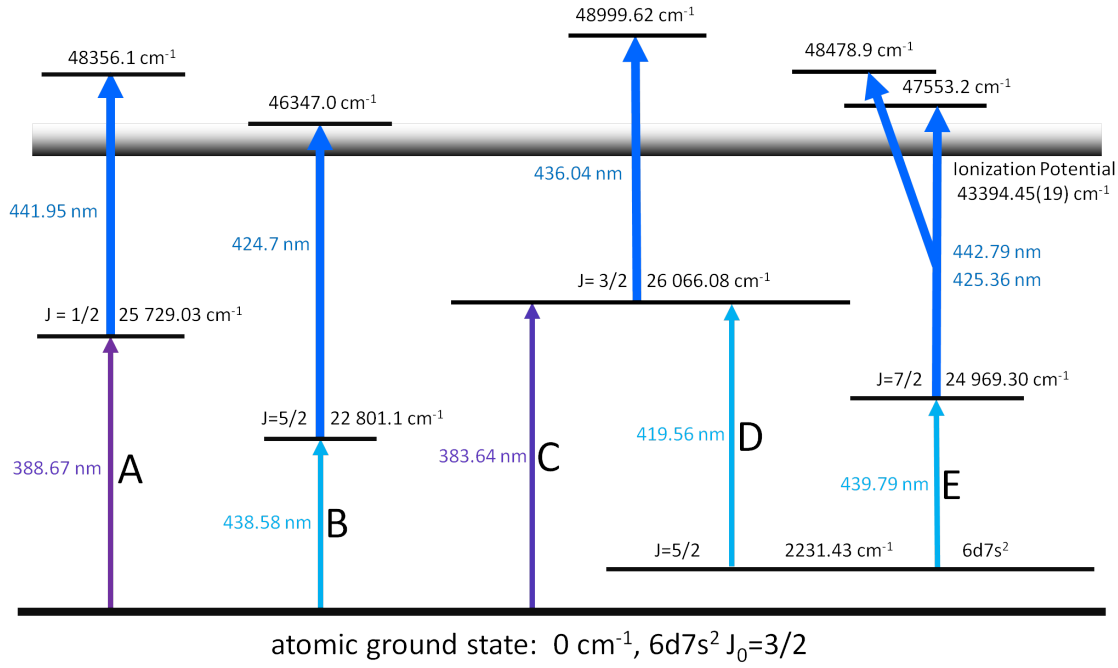

FIGURE 84 Transitions in actinium probed for hyperfine structure with the injection locked Ti:sa system. Energy levels for first excited states taken from [71].

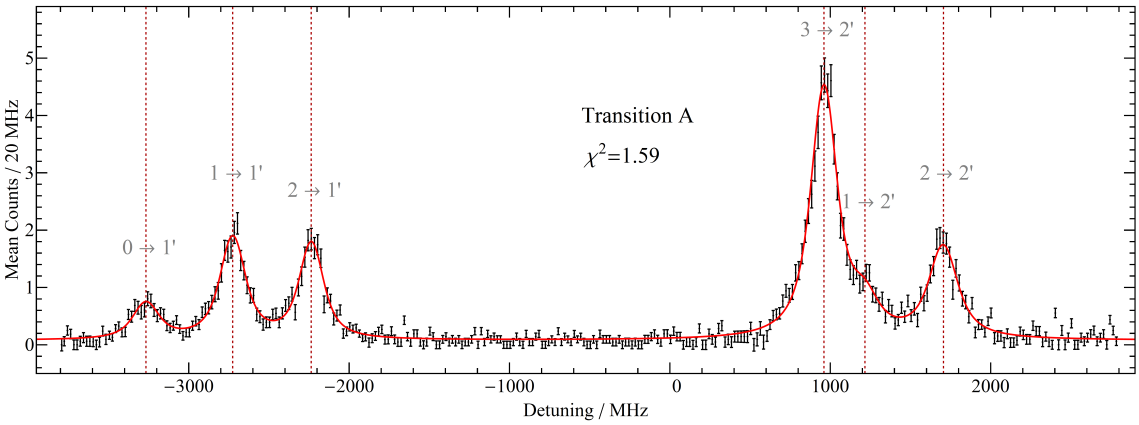

FIGURE 85 Actinium hyperfine structure - transition A (388.67 nm). Data in black, fit curve in red. Dashed lines indicate the position of the HFS components and are labeled with the F→F′ notation.

Transition	A_L/MHz	B_L/MHz	A_U/MHz	B_U/MHz
A	51.1(16)	591.8(41)	1971.5(37)	-
B	50.6(5)	597.0(16)	2104.8(5)	110.1(22)
C	49.5(11)	592.7(30)	-990.6(12)	-20.9(37)
D	253.7(50)	699.2(266)	-1002.0(108)	-8.8(270)
E	256.3(49)	714.9(280)	-280.3(35)	1277.5(305)

TABLE 7 Hyperfine parameters of the five transitions in actinium. Values belonging to the same lower or upper state are indicated in same color. Errors given are statistical only.

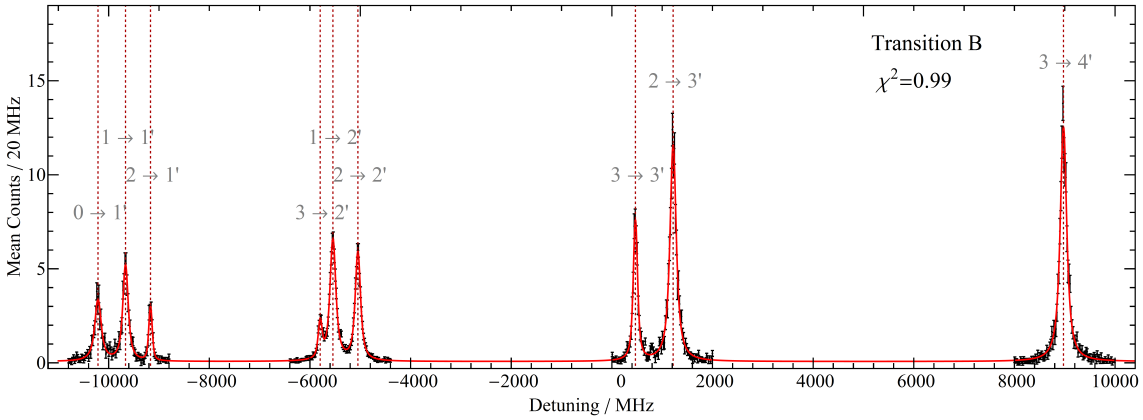

FIGURE 86 Actinium hyperfine structure - transition B (438.58 nm).

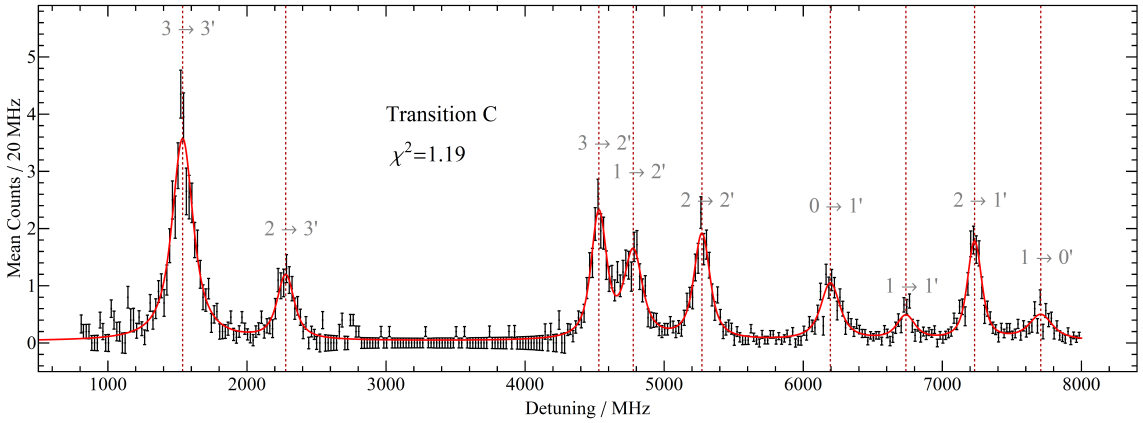

FIGURE 87 Actinium hyperfine structure - transition C (383.64 nm).

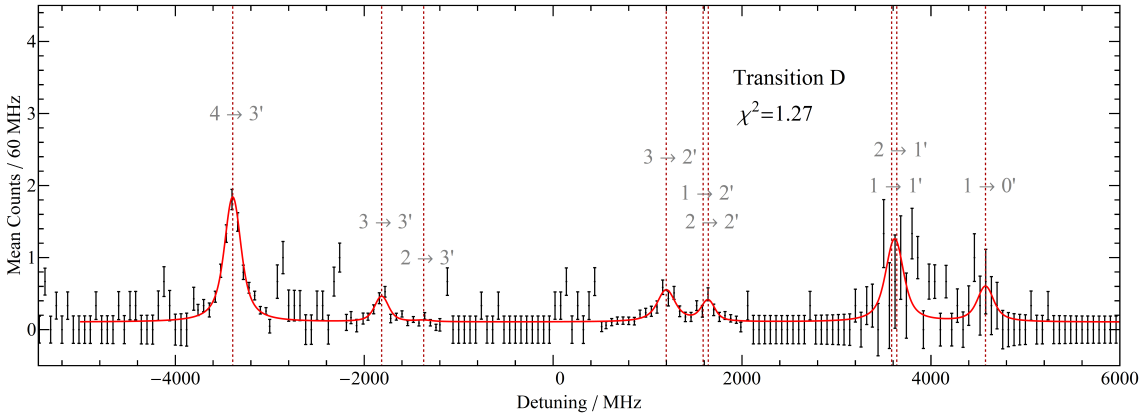

FIGURE 88 Actinium hyperfine structure - transition D (419.56 nm). The very low statistics at the rightmost peaks are due to the atomic sample exhaustion. A larger bin width of 60 MHz was used for this transition.

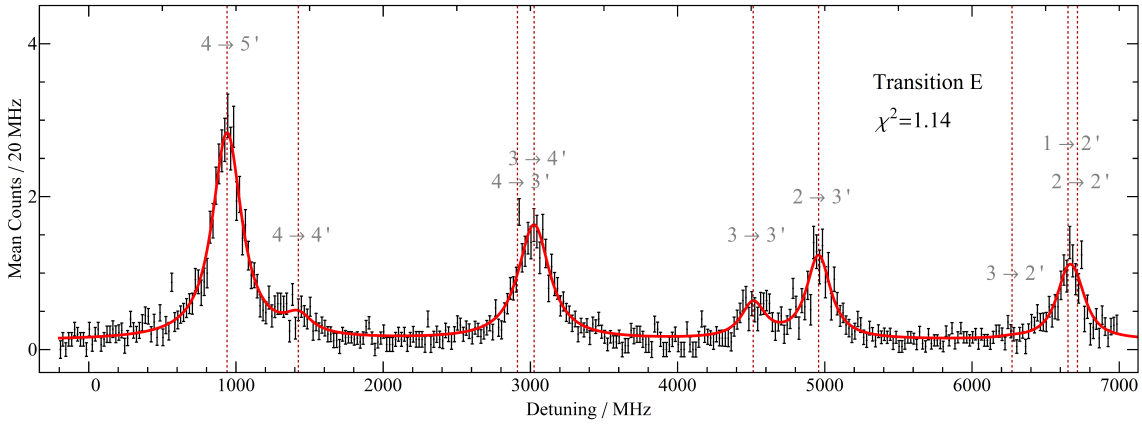

FIGURE 89 Actinium hyperfine structure - transition E (439.79 nm).

$F_L \rightarrow F_U$	Int_{theory}	Int_{exp}	Int_{exp}/Int_{theory}	γ	FWHM/MHz
$0 \rightarrow 1$	0.0625	0.057	0.91(9)	1.05(9)	160(12)
$1 \rightarrow 1$	0.0563	0.089	1.58(11)	0.79(7)	131(9)
$2 \rightarrow 1$	0.00625	0.051	8.13(51)	0.29(7)	82(8)
$1 \rightarrow 2$	0.131	0.11	0.86(4)	0.89(5)	142(6)
$2 \rightarrow 2$	0.0729	0.10	1.39(6)	0.74(4)	126(6)
$3 \rightarrow 2$	0.00417	0.034	8.14(61)	0.42(7)	94(8)
$2 \rightarrow 3$	0.233	0.20	0.87(5)	0.95(5)	149(6)
$3 \rightarrow 3$	0.0583	0.13	2.23(10)	0.54(5)	106(6)
$3 \rightarrow 4$	0.375	0.22	0.59(3)	1.00(3)	154(4)

TABLE 8 Relative theoretical and experimental intensities as well as the total FWHM linewidth of the individual hyperfine components of the hyperfine structure of transition B.

simpler structure with fewer components due to the J=1/2 spin of the excited state.

First laser spectroscopy on more exotic isotopes of actinium ($^{212-215}$Ac and ^{225}Ac) has been performed in-source at LISOL and TRIUMF [107,114]. Considering the limited resolution with this technique, it will be important for fitting constraints to know how well the hyperfine structure is represented by the theoretical intensity distribution. Similar to the analysis for copper the fit parameters for the individual hyperfine components of transition B are given in Table 8. Presented are the theoretical intensities from Eq. 22, the normalized ($\sum_i Int_i = 1$) experimental intensities, the ratios between experimental and theoretical intensities, the relative Lorentzian width γ as well as the FWHM (in MHz) of the Voigt profile of each component.

Most notable are the two weakest transition from $F_L = 2 \rightarrow F_U = 1$ and $F_L = 3 \rightarrow F_U = 2$, where the experimental intensity is more than 8 times higher than the theoretical prediction. Furthermore all transitions ($F_L = X$) $\rightarrow$ ($F_U = X+1$) show a reduced relative intensity ($Int_{exp} < Int_{theory}$). It is therefore important for any future in-source results to accommodate for this in error estimates or to be

Isotope	^{238}Pu	^{239}Pu	^{240}Pu	^{241}Pu	^{242}Pu	^{244}Pu
Spin	0^+	$1/2^+$	0^+	$5/2^+$	0^+	0^+
Half life (years)	87.7	$2.411 \cdot 10^4$	6564	14.35	$3.75 \cdot 10^5$	$8.0 \cdot 10^7$
Magnetic moment (μ_N)		0.203(4)		-0.683(15)		

TABLE 9 Nuclear spin, half-life and magnetic moments of the plutonium isotopes. Data taken from [121].

able to model these effects reliably.

In December 2014 an in-gas jet laser spectroscopy experiment will be performed at LISOL. This milestone experiment will target the isotope ^{215}Ac with the injection-locked Ti:sa laser, in order to obtain the first high resolution results for neutron-deficient actinium [114].

6.7 High resolution resonance ionization spectroscopy of plutonium

Spectroscopy of plutonium (Z=94) was made using the same experimental setup as described in section 6.5. Samples containing a mixture of $^{238-242}$Pu and ^{244}Pu were supplied from the nuclear chemistry department of the University of Mainz, with 10^{15} atoms for the most abundant isotope ^{244}Pu, to a few x 10^9 atoms for ^{238}Pu. Details on spin and half-life of the isotopes is given in Table 9. With the exception of ^{241}Pu, which is a β-emitter, the other isotopes predominantly decay by α-emission.

Absolute charge radii of ^{239,240,242}Pu have been reported from muonic atom measurements [117], which allows the calculation of charge radii for other isotopes by measurement of their respective isotope shifts. The isotope shift for ^{239,240}Pu has been measured with modest resolution in a large number of levels and transition lines [118], whereas the isotope shift for the larger set of isotopes of $^{238-242,244}$Pu was determined with a precision of about 100 MHz in a few levels in neutral Pu [119].

The first high resolution resonance ionization measurements with cw lasers were obtained in [120] with a precision of 15-30 MHz, however not for the isotopes ^{238,241}Pu. In the atomic ground state with angular momentum J=0 ($5f^6 7s^2 7F_0$), no hyperfine splitting is present. In addition, for ^{239}Pu, no electric quadrupole information may be determined due to its nuclear spin I=1/2. Therefore studies of transitions from low-lying thermally populated states (as performed here) or an additional study of the singly-ionized spectrum of plutonium, where hyperfine splittings are larger, are highly desirable. An improvement in precision by a factor of 5-10 could be demonstrated in this work.

Two transitions within the wavelength range of the laser diodes, A and B as indicated in Fig. 90, were investigated for hyperfine structure and isotope shifts. Transition A proceeds from the ground state to a J=1 excited state at 25959.849 cm^{-1}, while transition B goes from a thermally populated state at

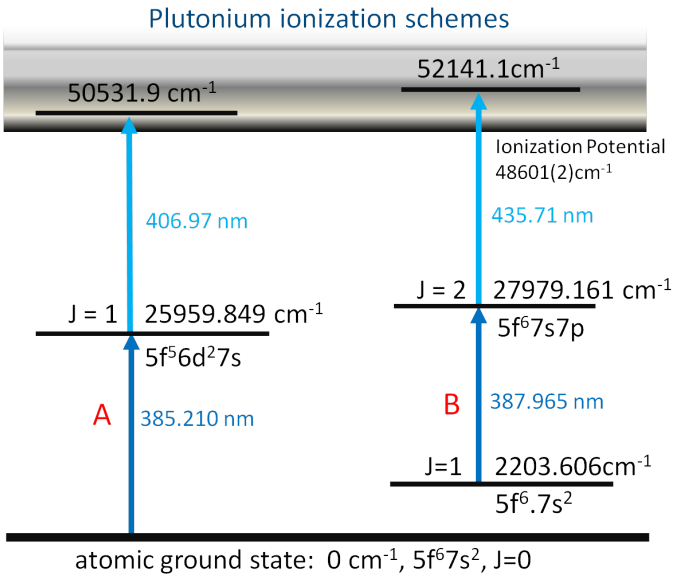

FIGURE 90 Ionization schemes for plutonium used to determine hyperfine structure and isotope shifts. First excited state energies taken from [71], ionization potential from [122] and level configurations from [118].

2203.606 cm^{-1} (J=1, 20 % population at 1300 K) to an excited state with J=2 at 27929.161 cm^{-1}.

The scans of transition A are shown in Fig. 91 for all isotopes. ^{240}Pu was chosen as the reference frequency, for easier comparison with literature data. No clear signal was present for the isotope ^{238}Pu. The overall isotope shifts are relatively small. Complicating the evaluation of the hyperfine structure of ^{241}Pu and determining its isotope shift is the overlap of the leftmost peak with the transition for the much more abundant isotope ^{242}Pu. With the typical mass resolving power of $(M/\Delta M) \approx 200$ the discrimination was not fully sufficient. Additionally, during the evaluation of the data it was noticed that not the whole hyperfine structure was scanned, with a third peak missing on the right.

The situation is clearer for the results of transition B as shown in Fig. 92, as here larger isotope shifts are apparent and a resonance for ^{238}Pu could be found as well, suggesting that the scheme was more efficient despite the lower population of the 2203.6 cm^{-1} level. The scan of ^{239}Pu shows a very narrow collapsed hyperfine structure.

Due to the missing peak in the spectrum of ^{241}Pu of transition A, the structures of transition B were evaluated first. The hyperfine structure of ^{241}Pu is shown in Fig. 93 and for ^{239}Pu in Fig. 94. In the ^{241}Pu structure the peaks for the $F_L = 7/2 \rightarrow F_U = 7/2$ and $F_L = 7/2 \rightarrow F_U = 9/2$ transitions overlap closely. For a reasonable fit the intensity ratio of these two peaks was fixed to the theoretical ratio. From the fit result given in Table 10 the magnetic coupling constant for the lower excited state is close to zero. This result was useful for evaluation of the ^{239}Pu hyperfine structure, which is independent of the electric quadrupole moment. Furthermore, one of the three hyperfine components in ^{239}Pu is very weak compared to the other two, resulting in a very strong correlation between

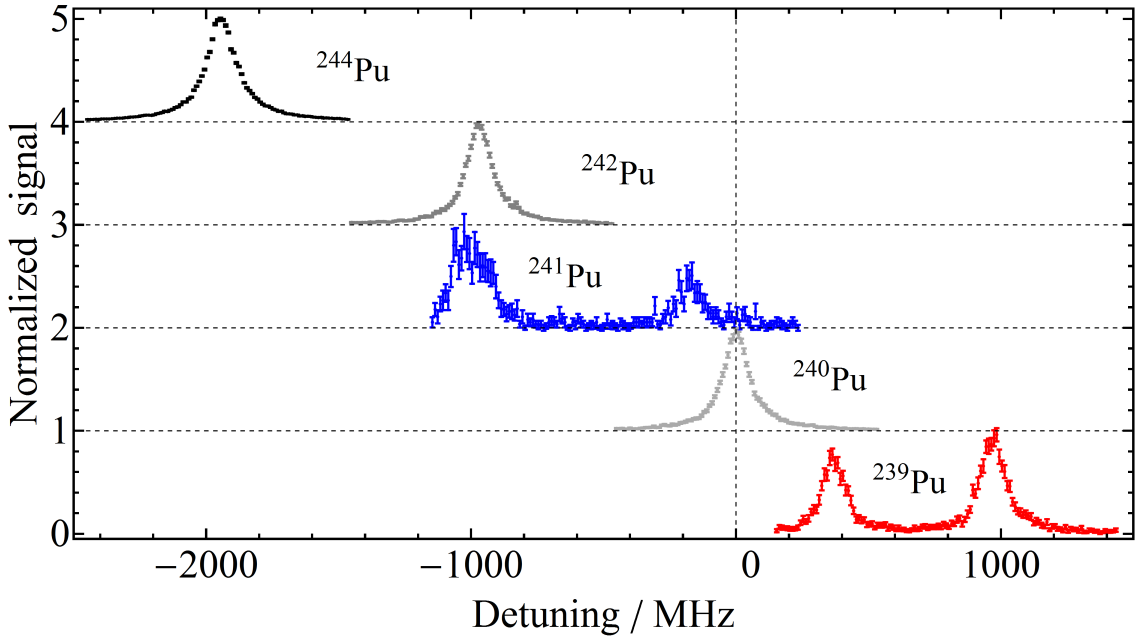

FIGURE 91 Laser scans of the 385.210 nm (A) transition for the plutonium isotopes, with the resonance frequency of ^{240}Pu taken as reference.

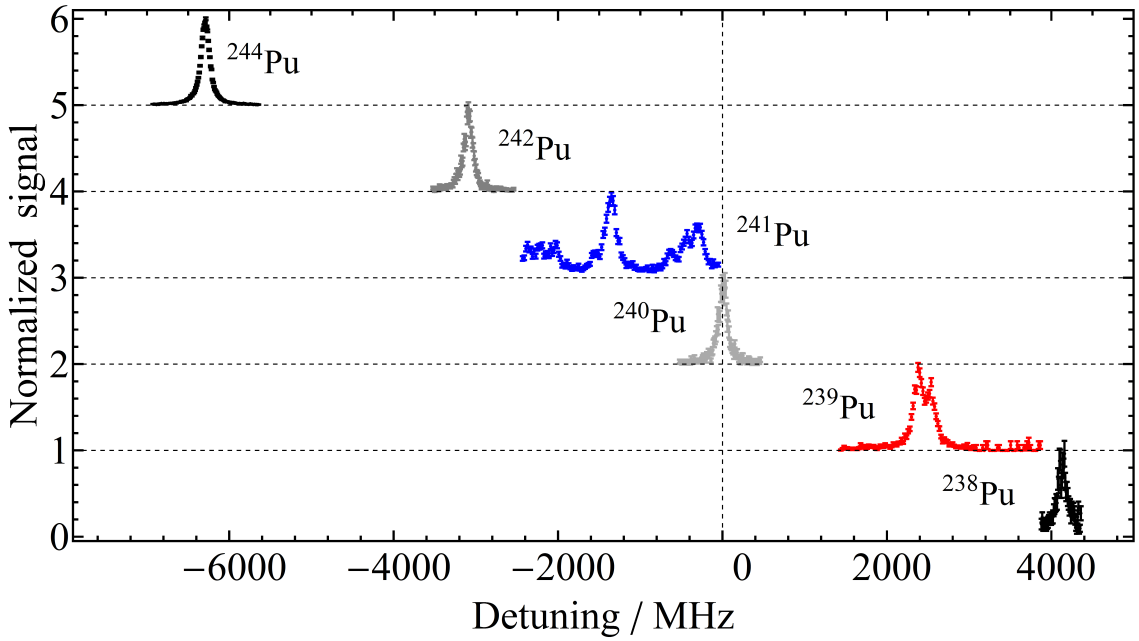

FIGURE 92 Laser scans of the 387.965 nm (B) transition for the plutonium isotopes, with the resonance frequency of ^{240}Pu taken as reference.

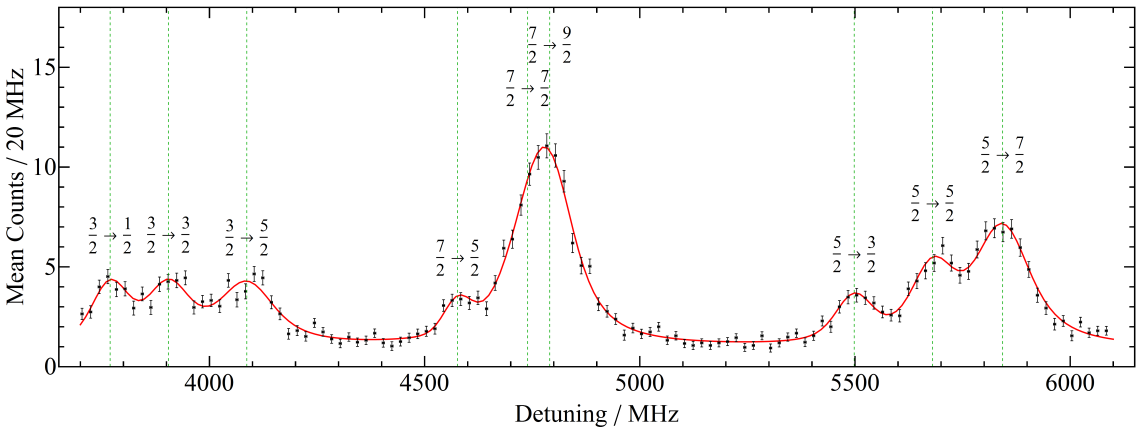

FIGURE 93 Hyperfine structure of transition B for ^{241}Pu.

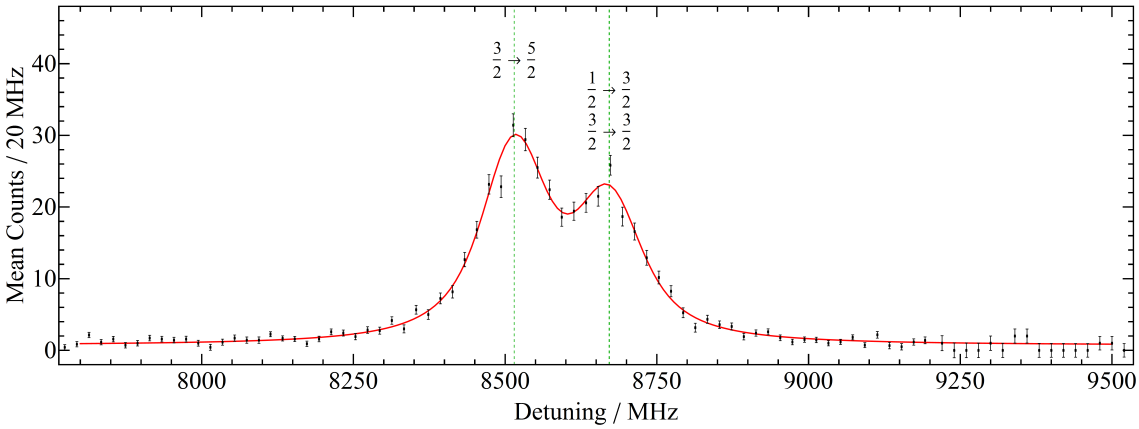

FIGURE 94 Hyperfine structure of transition B for ^{239}Pu.

the lower and upper state magnetic hyperfine coupling constants. A fit with free parameters resulted in extremely large error margins for the coupling constants, which were also not completely independent on the starting values for the fit. For comparison both the unrestrained fit results and the results with the lower state parameter fixed to zero are given.

Using the ratio of isotope shifts between transition A and B for the even isotopes the center of gravity for the hyperfine structure of transition A of ^{241}Pu can be estimated. Both the isotopes ^{242,240}Pu are present in the range of the hyperfine structure of ^{241}Pu as seen in Fig. 95. These were included in the fit using the independently determined centroid positions. Using the calculated center of gravity the fit curve shows the expected position of the missed third hyperfine component. The simplest hyperfine structure is seen in Fig. 96 for ^{239}Pu with only two components and a small remnant of the ^{240}Pu peak. As indicated before the results for the hyperfine structures are summarized in Table 10. The complete set of isotope shifts are listed in Table 11 with respect to the reference isotope ^{240}Pu. No previous high resolution literature data is available for the two transitions.

A King plot of the isotope shift data for both transitions is shown in Fig. 97.

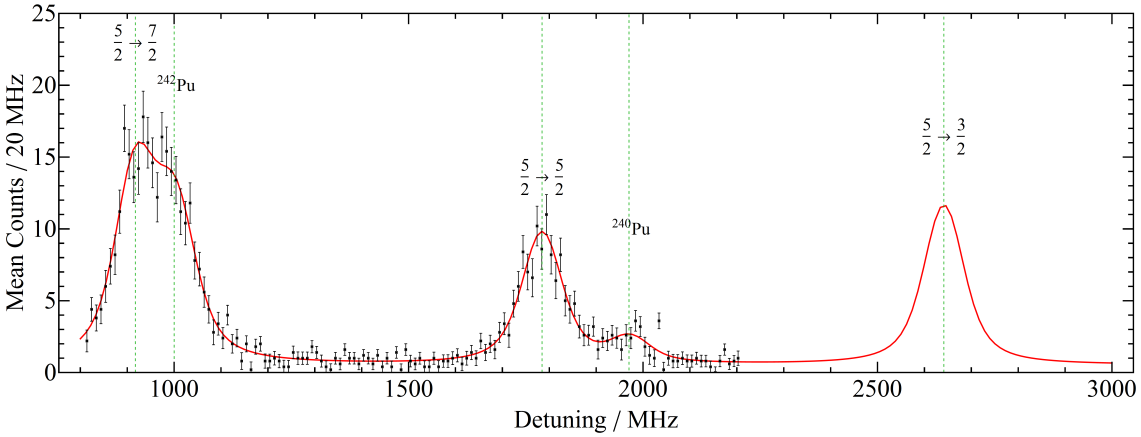

FIGURE 95 Hyperfine structure of transition A for ^{241}Pu.

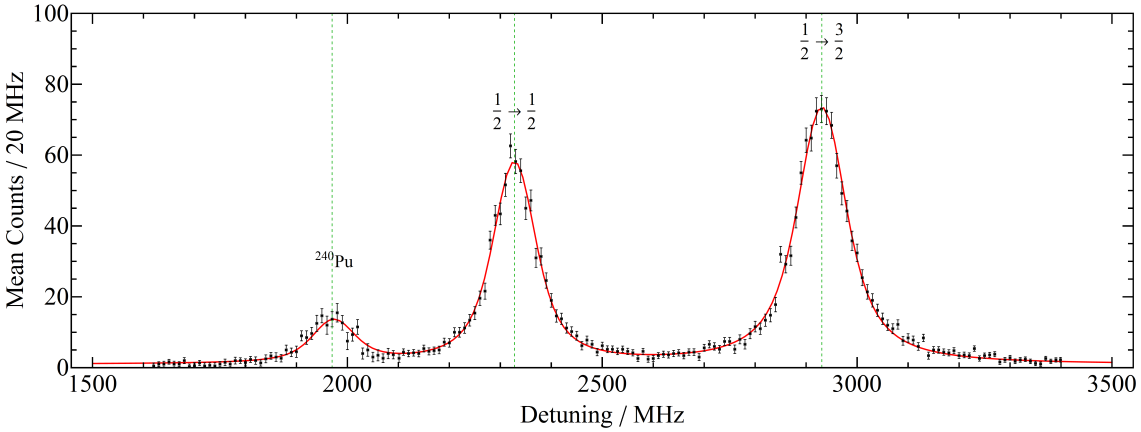

FIGURE 96 Hyperfine structure of transition A for ^{239}Pu.

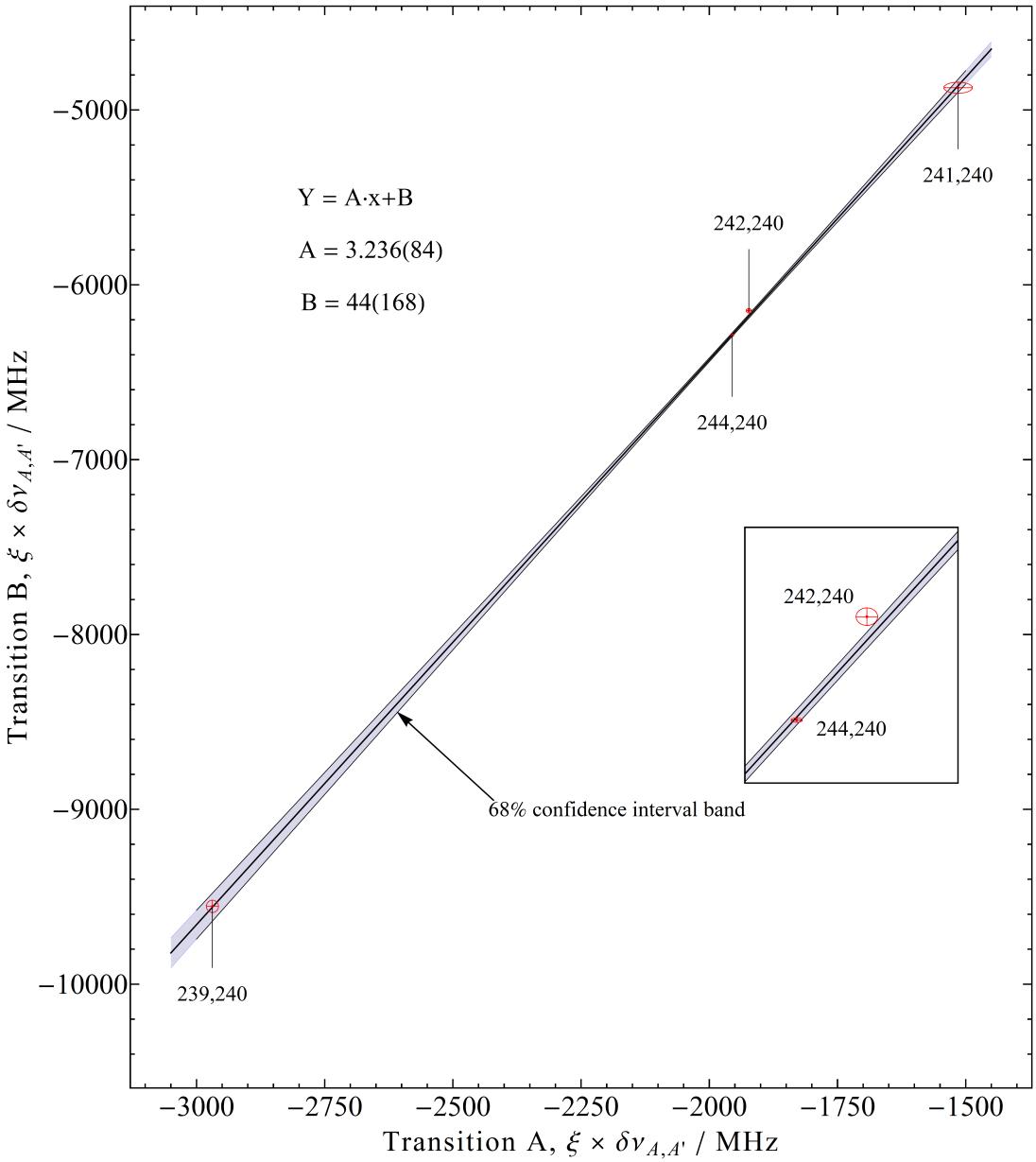

FIGURE 97 King plot of the plutonium isotope shifts for transition A and B. The isotope pair ^{241,240}Pu was not included in the fit as its value is not independent of the other measurements. The inset shows a zoomed portion of the graph.

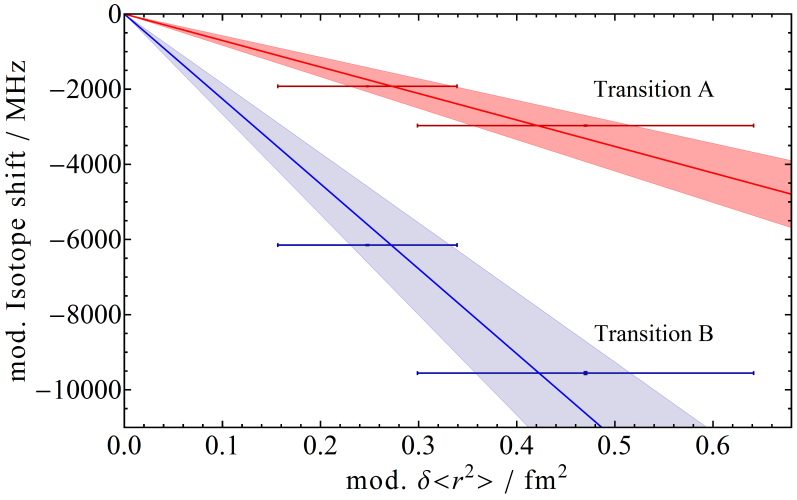

FIGURE 98 King plot of the Pu charge radii against the isotope shifts of transitions A and B. Shown are the data points with error bars and the linear fit lines as well as the 68% confidence interval bands.

This serves as a cross check for the accuracy of the measurements as well as giving access to the ratio of field shift of the two atomic transitions. For calculation of the modification factor ξ (Eq. 38) the isotope pair ^{244,240}Pu was used. The field shift gradient F_B/F_A is 3.236(84). The y-axis intercept is small as expected for heavy elements, with a value of 44(168) MHz and has a large error so that no mass-shift information can be extracted. As the isotope shift of ^{241}Pu for transition A was already calculated from the data of transition B it was not used in the fit for the King plot but is still displayed for completeness. As seen in the inset, the point for the isotope pair ^{242,240}Pu lies just outside of the 68% confidence interval range, however this can be expected considering statistical fluctuations as well as the error estimates.

A King plot of the charge radii from [117] against the isotope shifts of the two transitions is shown in Fig. 98. With ^{240}Pu as the reference isotope only two independent $\delta\langle r^2\rangle$ values can be calculated. As fit curve a linear fit through the origin (assuming negligible mass shift) was used to determine the field shift gradients with F_A = -7.0(7) GHz/fm^2 for transition A and F_B = -22.6(22) GHz/fm^2 for transition B. This negative gradient is expected. As seen in Fig. 90 the transitions remove one electron from the 7s orbital, which has the strongest overlap with the nuclear wavefunction. The correction factor K as mentioned in Eq. 30 has not been included in the analysis. As shown in Fig. 99 the expected correction for $Z = 94$ is of the order of 8%.

In the fall 2014 first success for the laser ionization of plutonium in a gas cell at the IGISOL facility was achieved. This paves the way for high resolution collinear laser spectroscopy of a transition in the Pu^+ ionic species. Plutonium would be so far the heaviest nucleus attempted with collinear laser spectroscopy and upon success would be a milestone on the road towards spectroscopy of the superheavy nuclei.

	^{239}Pu (A)	^{241}Pu (A)	^{239}Pu (B)	^{239}Pu (B)*	^{241}Pu (B)
A_L/MHz	-	-	-2(433)	0 (fixed)	-2.2(37)
B_L/MHz	-	-	-	-	1058.6(76)
A_U/MHz	402.3(10)	-279.4(18)	-63(218)	-62.6(14)	37.7(15)
B_U/MHz	-	105.4(48)	-	-	-175.4(140)

TABLE 10 Hyperfine coupling constants for transitions A and B for both isotopes ^{239}Pu and ^{241}Pu. The star * indicates a restrained fit. Errors in brackets are statistical only.

Transition	$\nu^{238-240}$Pu	$\nu^{239-240}$Pu	^{240}Pu(ref)	$\nu^{241-240}$Pu	$\nu^{242-240}$ Pu	$\nu^{244-240}$Pu
A (385.21 nm)	-	757.8(30)	0	-383.4(70)	-969.4(25)	-1955.2(25)
B (387.96 nm)	4126.7(100)	2438.7(90)	0	-1233.3(80)	-3099.3(60)	-6288.1(30)

TABLE 11 Isotope shifts of plutonium for transitions A and B. The isotope shift of transition A (in grey) for ^{241}Pu is not independent and was calculated using transition B data. All values in MHz. Errors in brackets are statistical only.

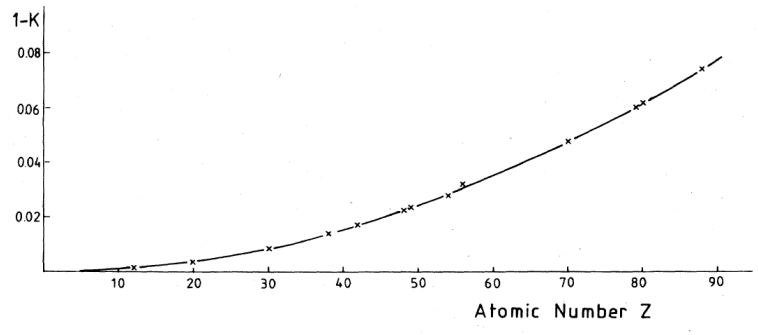

FIGURE 99 Correction factor K for the field shift evaluation. Figure taken from [24].

7 RESONANCE IONIZATION SPECTROSCOPY OF THORIUM

7.1 Motivation

Laser spectroscopy of thorium is an ongoing project dedicated to the search for the low-lying isomeric state in ^{229}Th. The existence of this isomer was first suggested by Kroger and Reich in 1976 [123], the authors inferring an excited state of spin and parity $3/2^+$ within 0.1 keV of the $5/2^+$ ground state. Helmer and Reich later improved the uncertainty of the level energy in 1994 deducing a value of 3.5(10) eV [124]. The most recent estimate of the energy of the isomeric

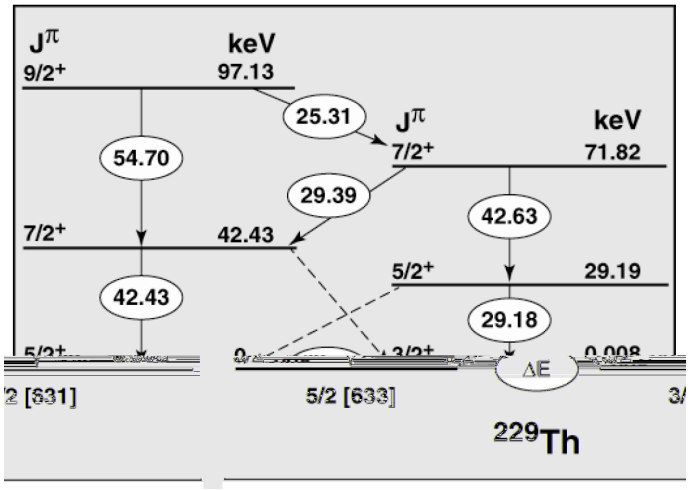

FIGURE 100 Partial nuclear level scheme of ^{229}Th. The ground state and isomeric states belong to different Nilsson bands which are separated for clarity [125].

state is 7.8(5) eV [125], with the nuclear level scheme shown in Fig. 100. This energy was inferred by measuring the γ-ray cascade following the α-decay of ^{233}U, using the NASA electron beam ion trap x-ray microcalorimeter spectrometer. A differencing technique was applied to the γ-ray decay of the $7/2^+$ state at 71.82 keV. The decay populates doublets with γ-ray energies 42.63 keV, 42.43 keV

and 29.39 keV, 29.18 keV, respectively. Despite improvements in technology, the exact energy of the isomer remains elusive and is the subject of heated debate [126]. A measurement with a state-of-the-art magnetic metallic microcalorimeter [127] may clarify outstanding questions.

This extremely low excitation energy compared to typical energy scales in nuclear processes would be accessible to laser excitation with table-top laser systems. This may allow for various applications, most significantly for a ''nuclear clock'' [128--130]. Such a clock transition would not only provide a precision of 10^{-19}, competitive with recent atomic clocks [131], but may also be sensitive to time evolution of fundamental constants such as quark masses [132] or the fine-structure constant α [133].

Direct detection of the $\approx$ 163 nm photons of the isomeric decay has so far been unsuccessful. A recent claim of success [134] has been called into question [135], highlighting the challenge of suppressing background radiation from the decays of daughter and contaminant isotopes. The predicted isomeric excitation energy is of the order of the ionization potential or bound electron states in thorium, resulting in internal conversion (IC) or bound internal conversion (BIC) possibilities. Correspondingly, lifetimes ranging from 10^{-5} s due to IC, and a few minutes (neglecting IC but allowing BIC) to hours (neglecting IC completely, bare nucleus) have been estimated [136, 137].

For a long lifetime of the isomeric state it is thus favourable to keep it in a high charge state. Laser cooling of triply-charged ^{229}Th has been demonstrated [138] and in the solid state nuclear clock approach a 4^+ charge state is assumed [129].

An alternative to the direct detection of the isomeric decay would be the inference through a laser spectroscopy measurement of the atomic hyperfine structure. Due to different spins and magnetic moments of the ground-state and isomeric state, such a measurement will allow the separation of the two states. This may be considered an indirect approach as the energy information is not extracted. However, it has been suggested that a high-precision microwave spectroscopy measurement of the hyperfine structure in Th^{3+} may allow for an indirect determination of the isomer energy [139]. Considering the expected lifetime, laser spectroscopy would be most suitably carried out in the ionized species. If the isomeric energy is different from the current expectation a measurement in the neutral atomic state may prove to be successful as well.

As such the following articles focus both on the efficient laser ionization of thorium, for subsequent collinear spectroscopy on the Th^+ ion, as well as first hyperfine measurements in the neutral state.

7.2 Article IV

Article IV was published in *J. Phys. B. At. Mol. Opt. Phys.* volume 44 (2011), page 165005. It details the development of an efficient laser ionization scheme for thorium. Many new high-lying excited states and hundreds of new autoionizing states have been determined using a grating-based Ti:sa and saturation measurements of the most efficient scheme have been performed. This new scheme will be important for any future spectroscopic experiments on the ionic species. The experiment was carried out in the laboratory of the Quantum/LARISSA group at the University of Mainz. The article is presented in the following 9 pages (print version only).

7.3 Article V

Article V was published in *Eur. Phys. J. A* volume 48 (2012), page 52. It provides an overview of the thorium-related gas-cell developments at the IGISOL facility as well as the first high resolution RIS on ^{228,229,230,232}Th at the University of Mainz. The article presents the ^{233}U α-recoil ion guide for the production of the isomer, discussing extraction efficiency, charge state ratios and molecular impurities. An injection-locked Ti:sa has been used to extract isotope shifts for $^{228-232}$Th and several transitions were investigated for hyperfine structure. The article is presented in the following 16 pages (print version only).

7.4 Article VI

Article VI was published in *J. Phys. B. At. Mol. Opt. Phys.* volume 45 (2012), page 165005. It gives a detailed analysis of the hyperfine structure of ^{229}Th using three different transitions from the atomic ground state. The combined result for the three transitions yields the atomic ground state hyperfine factors and a comparison with the Th^{+} and Th^{3+} ionic charge states is provided. This structure will be used as a template for future online in gas-jet spectroscopy of the isomeric state. The article is presented in the following six pages (print version only).

8 SUMMARY AND FUTURE PROSPECTS

Several experiments have been carried out since the start of this thesis in 2009 using new developments in laser technology made by the author. From 2010-2011 the move of the IGISOL facility to a new accelerator hall limited the possibilities at Jyväskylä, during which time the collaboration with Mainz and LISOL allowed for a continuation of the research work. Highlights of the work both at IGISOL and at other facilities have been presented in the previous chapters.

Intracavity frequency doubling and the related development of difference frequency mixing have significantly extended the possibilities for efficient laser ionization at the IGISOL facility and elsewhere. While not discussed within the scope of this thesis, the technique has already been applied to optical pumping of several elements (Y, Ba) in the radiofrequency quadrupole cooler-buncher for collinear laser spectroscopy.

The grating-based Ti:sa laser is a flexible tool, allowing for continuous wavelength tuning for the search of new laser ionization schemes, but may also be used to quickly compare the efficiency of existing schemes. The laser has been applied to the spectroscopy of samarium, where several new high-lying levels and autoionizing states were found. In a recent experiment on laser ionization of plutonium in a gas cell it was noticed that the three-step ionization schemes determined in hot cavity sources proved less efficient than a simple two step blue-blue scheme. This may be related to quenching of atomic states due to gas collisions. For the search of a more efficient two-step scheme the development of a grating-based Ti:sa laser coupled with intracavity doubling could be an interesting future project.

The aim for higher resolution laser spectroscopy at the IGISOL facility has been hindered by the poor accuracy of the wavelength determination. This has been addressed in this thesis with the introduction of two Fabry-Pérot Interferometers. An immediate application using a new dual-etalon Ti:sa laser, with a reduced linewidth to match the broadening of the atomic transition in a gas cell, has been RIS of ^{63,65}Cu. The HFS analysis using the FPI-calibrated wavelength provided a much closer match with literature data compared to the same analysis using the wavemeter. Work still remains to simplify the data acquisition and

analysis process and to integrate it in a LabVIEW environment. This integration would be of importance for the control of the new cw Ti:sa master laser system.

Since the installation of the injection-locked Ti:sa system at the IGISOL facility in 2013 it has proven itself to be a powerful tool for high-resolution spectroscopy. It combines the high peak intensity expected from pulsed laser systems, with a narrow bandwidth of 20 MHz. For many cases where additional line broadening effects occur this system provides similar resolution as continuous wave systems. The laser has been used for the spectroscopy of actinium and plutonium at the University of Mainz and for spectroscopy on stable copper at IGISOL. In the spectroscopy of copper the impact of a delayed ionization pulse on the experimental linewidth was demonstrated. The laser cavity and locking electronics have been transported to the LISOL facility and will be used for in-gas-jet spectroscopy on ^{215}Ac.

The search for the elusive isomeric state in ^{229}Th will be of continued interest at the IGISOL facility. In a wider context, the laser-IGISOL team has joined a consortium of six leading European research groups providing individual expertise in a variety of fields, encompassing atomic and nuclear physics, quantum optics, metrology, as well as detector- and laser technology. An application called "nuClock" has recently been submitted to a research and innovation action, the Future and Emerging Technologies (FETOPEN) call in Horizon 2020. The nuClock collaboration will focus on two objectives; (i) to find clear evidence of the isomeric transition and to measure its frequency, and (ii) to develop all key components required for the operation of a nuclear clock. The JYFL Accelerator Laboratory is participating as the sole large scale facility, with the role of the IGISOL facility to search for hyperfine structure of the isomer in the neutral atom using in-gas-jet RIS, in the singly-ionized species using laser ionization in-gas-cell followed by high resolution collinear laser spectroscopy, as well as laser spectroscopy of doubly-charged thorium using the new technique of Ion Resonance Ionization Spectroscopy (IRIS).

REFERENCES

[1] V. N. Fedosseev, Yu. Kudryavtsev, and V. I. Mishin. Resonance laser ionization of atoms for nuclear physics. *Physica Scripta*, 85(5):058104, 2012.

[2] B. A. Marsh. Resonance ionization laser ion sources for on-line isotope separators. *Review of Scientific Instruments*, 85(2), 2014.

[3] I.D. Moore, P. Dendooven, and J. Ärje. The IGISOL technique—three decades of developments. *Hyperfine Interactions*, 223(1-3):17--62, 2014.

[4] T. Sonoda, M. Wada, H. Tomita, C. Sakamoto, T. Takatsuka, T. Noto, H. Iimura, Y. Matsuo, T. Kubo, T. Shinozuka, T. Wakui, H. Mita, S. Naimi, T. Furukawa, Y. Itou, P. Schury, H. Miyatake, S. Jeong, H. Ishiyama, Y. Watanabe, and Y. Hirayama. Development of a gas cell-based laser ion source for RIKEN PALIS. *Hyperfine Interactions*, 216(1-3):103--107, 2013.

[5] Yu. Kudryavtsev, T.E. Cocolios, J. Gentens, M. Huyse, O. Ivanov, D. Pauwels, T. Sonoda, P. Van den Bergh, and P. Van Duppen. Dual chamber laser ion source at LISOL . *Nuclear Instruments and Methods in Physics Research Section B: Beam Interactions with Materials and Atoms*, 267(17):2908 -- 2917, 2009.

[6] R. Ferrer, V. T. Sonnenschein, B. Bastin, S. Franchoo, M. Huyse, Yu. Kudryavtsev, T. Kron, N. Lecesne, I.D. Moore, B. Osmond, D. Pauwels, D. Radulov, S. Raeder, L. Rens, M. Reponen, J. Roßnagel, H. Savajols, T. Sonoda, J.C. Thomas, P. Van den Bergh, P. Van Duppen, K. Wendt, and S. Zemlyanoy. Performance of a high repetition pulse rate laser system for in-gas-jet laser ionization studies with the Leuven laser ion source @ LISOL . *NIM B*, 291(0):29 -- 37, 2012.

[7] K. Blaum, C. Geppert, H.-J. Kluge, M. Mukherjee, S. Schwarz, and K. Wendt. A novel scheme for a highly selective laser ion source . *Nuclear Instruments and Methods in Physics Research Section B: Beam Interactions with Materials and Atoms*, 204(0):331 -- 335, 2003. 14th International Conference on Electromagnetic Isotope Separators and Techniques Related to their Applications.

[8] D. A. Fink, S. D. Richter, B. Bastin, K. Blaum, R. Catherall, T. E. Cocolios, D. V. Fedorov, V. N. Fedosseev, K. T. Flanagan, L. Ghys, A. Gottberg, N. Imai, T. Kron, N. Lecesne, K. M. Lynch, B. A. Marsh, T.M. Mendonca, D. Pauwels, E. Rapisarda, J. P. Ramos, R. E. Rossel, S. Rothe, M. D. Seliverstov, M. Sjödin, T. Stora, C. Van Beveren, and K.D.A. Wendt. First application of the Laser Ion Source and Trap (LIST) for on-line experiments at ISOLDE . *Nuclear Instruments and Methods in Physics Research Section B: Beam Interactions with Materials and Atoms*, 317, Part B(0):417 -- 421, 2013. XVIth International Conference on ElectroMagnetic Isotope Separators and Techniques Related to their Applications, December 2–7, 2012 at Matsue, Japan .

[9] T. Sonoda, T.E. Cocolios, J. Gentens, M. Huyse, O. Ivanov, Yu. Kudryavtsev, D. Pauwels, P. Van den Bergh, and P. Van Duppen. The Laser Ion Source Trap (LIST) coupled to a gas cell catcher. *Nuclear Instruments and Methods in Physics Research Section B: Beam Interactions with Materials and Atoms*, 267(17):2918 -- 2926, 2009.

[10] I.D. Moore, T. Eronen, D. Gorelov, J. Hakala, A. Jokinen, A. Kankainen, V.S. Kolhinen, J. Koponen, H. Penttilä, I. Pohjalainen, M. Reponen, J. Rissanen, A. Saastamoinen, S. Rinta-Antila, V. Sonnenschein, and J. Äystö. Towards commissioning the new IGISOL-4 facility. *Nuclear Instruments and Methods in Physics Research Section B: Beam Interactions with Materials and Atoms*, 317, Part B(0):208 -- 213, 2013. {XVIth} International Conference on ElectroMagnetic Isotope Separators and Techniques Related to their Applications, December 2–7, 2012 at Matsue, Japan.

[11] M. Reponen, I.D. Moore, I. Pohjalainen, T. Kessler, P. Karvonen, J. Kurpeta, B. Marsh, S. Piszczek, V. Sonnenschein, and J. Äystö". Gas jet studies towards an optimization of the IGISOL LIST method . *Nuclear Instruments and Methods in Physics Research Section A: Accelerators, Spectrometers, Detectors and Associated Equipment*, 635(1):24 -- 34, 2011.

[12] Yu. Kudryavtsev, R. Ferrer, M. Huyse, P. Van den Bergh, and P. Van Duppen. The in-gas-jet laser ion source: Resonance ionization spectroscopy of radioactive atoms in supersonic gas jets. *Nuclear Instruments and Methods in Physics Research Section B: Beam Interactions with Materials and Atoms*, 297(0):7 -- 22, 2013.

[13] IGLIS-NET. http://kekrnb.kek.jp/iglis-net/.

[14] LA^{3}NET. https://www.liv.ac.uk/la3net/.

[15] H. Haken and H. C. Wolf. *Atom- und Quantenphysik: Eine Einführung in Die Experimentellen und Theoretischen Grundlagen*. Springer London, Limited, 2012.

[16] Wolfgang Demtröder. *Laserspektroskopie 1*. SpringerLink : Bücher. Springer, 2011.

[17] E. T. Jaynes and F. W. Cummings. Comparison of quantum and semiclassical radiation theories with application to the beam maser. *Proceedings of the IEEE*, 51(1):89--109, Jan 1963.

[18] C. Cohen-Tannoudji, J. Dupont-Roc, and G. Grynberg. *Atom—Photon Interactions*. Wiley-VCH Verlag GmbH, 2008.

[19] V. Letokhov. *Laser Photoionization Spectroscopy*. Elsevier Science, 2012.

[20] J. J. Olivero and R. L. Longbothum. Empirical fits to the Voigt line width: A brief review. *Journal of Quantitative Spectroscopy and Radiative Transfer*, 17(2):233 -- 236, 1977.

[21] G. W. F. Drake. *Springer Handbook of Atomic, Molecular, and Optical Physics*. Springer Handbook of Atomic, Molecular, and Optical Physics. Springer, 2006.

[22] E. C. Seltzer. K X-Ray Isotope Shifts. *Phys. Rev.*, 188:1916--1919, Dec 1969.

[23] S. A. Blundell, P. E. G. Baird, C. W. P. Palmer, D. N. Stacey, and G. K. Woodgate. A reformulation of the theory of field isotope shift in atoms. *Journal of Physics B: Atomic and Molecular Physics*, 20(15):3663, 1987.

[24] G. Torbohm, B. Fricke, and A. Rosén. State-dependent volume isotope shifts of low-lying states of group-IIa and -IIb elements. *Phys. Rev. A*, 31:2038--2053, Apr 1985.

[25] W.H. King. *Isotope Shifts in Atomic Spectra*. Physics of Atoms and Molecules. Springer US, 1984.

[26] Siegman, A. E. *Lasers*. University Science Books, 1986.

[27] Norman Hodgson and Horst Weber. *Laser Resonators and Beam Propagation*. Springer Science and Business Media, 2005.

[28] A. E. Siegman. Unstable optical resonators. *Appl. Opt.*, 13(2):353--367, Feb 1974.

[29] S. S. Bulanov, T. Zh. Esirkepov, A. G. R. Thomas, J. K. Koga, and S. V. Bulanov. Schwinger Limit Attainability with Extreme Power Lasers. *Phys. Rev. Lett.*, 105:220407, Nov 2010.

[30] G. D. Boyd and D. A. Kleinman. Parametric Interaction of Focused Gaussian Light Beams. *Journal of Applied Physics*, 39(8):3597--3639, 1968.

[31] Tran-Ba-Chu and M. Broyer. Intracavity cw difference frequency generation by mixing three photons and using Gaussian laser beams. *J. Phys. France*, 46(4):523--533, 1985.

[32] Tran-Ba-Chu, A. J. Bouvier, A. Bouvier, and M. Broyer. Efficient intracavity second harmonic generation (i.s.h.g.) using the optimal pump laser focusing method. *J. Phys. France*, 46(4):551--560, 1985.

[33] A. V. Smith. How to use SNLO nonlinear optics software to select nonlinear crystals and model their performance. *Proc. SPIE*, 4972:50--57, 2003.

[34] P. F. Moulton. Spectroscopic and laser characteristics of Ti:Al2O3. *J. Opt. Soc. Am. B*, 3(1):125--133, Jan 1986.

[35] W. R. Rapoport and C. P. Khattak. Titanium sapphire laser characteristics. *Appl. Opt.*, 27(13):2677--2684, Jul 1988.

[36] J. M. Eggleston, L. G. DeShazer, and K. W. Kangas. Characteristics and kinetics of laser-pumped Ti:sapphire oscillators. *Quantum Electronics, IEEE Journal of*, 24(6):1009--1015, June 1988.

[37] M. Reponen. *Resonance laser ionization developments for IGISOL-4*. PhD thesis, University of Jyväskylä, 2012.

[38] F. X. Zha, J. H. Zhang, and S. D. Xia. Electronic structure of the ion pair model for Ti:Al_2O_3. *Journal of Physics: Condensed Matter*, 6(32):6497, 1994.

[39] J.F. Pinto, L. Esterowitz, G. H. Rosenblatt, M. Kokta, and D. Peressini. Improved Ti:sapphire laser performance with new high figure of merit crystals. *Quantum Electronics, IEEE Journal of*, 30(11):2612--2616, Nov 1994.

[40] P. F. Moulton. Titanium-doped sapphire laser research and design study. technical report, NASA, 1987.

[41] G. Wagner, M. Shiler, and V. Wulfmeyer. Simulations of thermal lensing of a Ti:Sapphire crystal end-pumped with high average power. *Opt. Express*, 13(20):8045--8055, Oct 2005.

[42] I. Matsushima, H. Yashiro, and T. Tomie. 10 kHz 40W Ti:Sapphire regenerative ring amplifier. In *Lasers and Electro-Optics, 2006 and 2006 Quantum Electronics and Laser Science Conference. CLEO/QELS 2006.*, pages 1--2, May 2006.

[43] J. Feng, J. Nasiatka, M. Hertlein, B. Rude, and H. Padmore. Compact cryogenically cooled Ti:Sapphire dual multi-kilohertz amplifiers for synchrotron radiation ultra-fast x-ray applications. *Review of Scientific Instruments*, 84(5), 2013.

[44] H. Kiriyama, T. Shimomura, M. Mori, Y. Nakai, M. Tanoue, S. Kondo, S. Kanazawa, A. S. Pirozhkov, T. Z. Esirkepov, Y. Hayashi, K. Ogura, H. Kotaki, M. Suzuki, I. Daito, H. Okada, A. Kosuge, Y. Fukuda, M. Nishiuchi, M. Kando, S. V. Bulanov, K. Nagashima, M. Yamagiwa, K. Kondo, A. Sugiyama, P. R. Bolton, S. Matsuoka, and H. Kan. Ultra-Intense, High Spatio-Temporal Quality Petawatt-Class Laser System and Applications. *Applied Sciences*, 3(1):214--250, 2013.

[45] R. E. Horn. *Aufbau eines Systems gepulster, abstimmbarer Festkörperlaser zum Einsatz in der Resonanzionisations-Massenspektrometrie*. PhD thesis, University of Mainz, 2003.

[46] W. R. Leeb. Losses introduced by tilting intracavity etalons. *Applied physics*, 6(2):267--272, 1975.

[47] D. C. Hanna and Y-W. J. Koo and D. J. Pratt. A simple technique for improved performance of intracavity Fabry-Perot frequency selectors. *Optics Communications*, 44(3):188 -- 191, 1983.

[48] G. D. Boyd and H. Kogelnik. Generalized Confocal Resonator Theory. *Bell System Technical Journal*, 41(4):1347--1369, 1962.

[49] R. Clark Jones. A new calculus for the treatment of optical systems. *J. Opt. Soc. Am.*, 31(7):488--493, Jul 1941.

[50] B.E.A. Saleh and M.C. Teich. *Fundamentals of Photonics*. Wiley Series in Pure and Applied Optics. Wiley, 2007.

[51] T. Yang, X. Wan, H. Jing, and D. Liu. An improved Jones matrix for a birefringent plate with optical axis parallel to the surface. *Journal of Optics A Pure and Applied Optics*, 9(3):222, 2007.

[52] T.Yang, H. Jing, and D. Liu. An improved description of Jones vectors of the electric fields of incident and refracted rays in a birefringent plate. *Journal of Optics A: Pure and Applied Optics*, 8(3):295, 2006.

[53] Wolfram Research, Inc. Mathematica, 2012.

[54] T. Kessler. *Development and application of laser technologies at radioactive ion beam facilities*. PhD thesis, University of Jyväskylä, 2008.

[55] T. Kessler, T. Eronen, C. Mattolat, I.D. Moore, K. Peräjärvi, P. Ronkanen, P. Thörle, B. Tordoff, N. Trautmann, K. Wendt, K. Wies, and J. Äystö. Upgrade to the IGISOL laser ion source towards spectroscopy on Tc. In Z. Błaszczak, B. Markov, and K. Marinova, editors, *LASER 2006*, pages 121--126. Springer Berlin Heidelberg, 2007.

[56] C. Mattolat. *Spektroskopische Untersuchungen an Technetium und Silizium - Ein Festkörperlasersystem für die Resonanzionisationsspektroskopie*. PhD thesis, University of Mainz, 2010.

[57] S. Rothe, B. A. Marsh, C. Mattolat, V. N. Fedosseev, and K. Wendt. A complementary laser system for ISOLDE RILIS. *Journal of Physics: Conference Series*, 312(5):052020, 2011.

[58] B. Cheal. Private communication, 2014.

[59] S. Fritzsche. On the accuracy of valence–shell computations for heavy and super–heavy elements. *The European Physical Journal D - Atomic, Molecular, Optical and Plasma Physics*, 33(1):15--21, 2005.

[60] A. Borschevsky, E. Eliav, M. J. Vilkas, Y. Ishikawa, and U. Kaldor. Predicted spectrum of atomic nobelium. *Phys. Rev. A*, 75:042514, Apr 2007.

[61] M. Laatiaoui, H. Backe, M. Block, F.-P. Heßberger, P. Kunz, F. Lautenschläger, W. Lauth, M. Swetz, and T. Walther. On laser spectroscopy of the element nobelium (Z = 102). *The European Physical Journal D*, 68(3), 2014.

[62] A. Teigelhöfer, P. Bricault, O. Chachkova, M. Gillner, J. P. Lavoie, R. Li, J. Meißner, W. Neu, and K. D. A. Wendt. Grating tuned Ti:Sa laser for in-source spectroscopy of Rydberg and autoionizing states. *Hyperfine Interactions*, 196:161--168, 2010.

[63] P. Naubereit. Entwicklung eines weitabtimmbaren hochrepetierenden Titan:Saphir-Lasers und Spektroskopie hochliegender Resonanzen an Holmium-165. Master's thesis, University of Mainz, to be published.

[64] Y. Liu. ORNL developments in laser ion sources for radioactive ion beam production. *Hyperfine Interactions*, 227(1-3):85--99, 2014.

[65] R. Bhat, R. Devi, and S. Khosa. Microscopic study of deformation systematics in the samarium mass chain. *Bulg. J. Phys.*, 29:114--127, 2002.

[66] J. Mes, E.J. van Duijn, and W. Hogervorst. High-resolution spectroscopy on ground-state transitions of samarium-i. *Eur. Phys. J. D*, 36:17--22, 2005.

[67] M.-K. Oh, W. Choi, J.-H. Jeon, M. Lee, Y. Choi, S. Park, J.-H. Lee, and K. An. Measurement of hyperfine structures and isotope shifts in $4f^5 5d6s^2$ and $4f^6 6s6p$ of Sm I. *Spectrochimica Acta Part B*, 59:1919--1926, 2004.

[68] J. G. England, I. S. Grant, J. A. R. Griffith, D. E. Evans, D. A. Eastham, G. W. A. Newton, and P. M. Walker. Isotope shifts and hyperfine splitting in 144-154 Sm I. *Journal of Physics G: Nuclear and Particle Physics*, 16(1):105, 1990.

[69] D. A. Eastham, J. G. England, D. E. Evans, M. J. Fawcett, I. S. Grant, J. A. R. Griffith, G. W. A. Newton, and P. M. Walker. Optical isotope shift and hyperfine structure of 153 Sm. *Journal of Physics G: Nuclear Physics*, 10(12):L271, 1984.

[70] V. S. Letokhov, V. I. Mishin, S. K. Sekatsky, V. N. Fedoseyev, G. D. Alkhazov, A. E. Barzakh, V. P. Denisov, and V. E. Starodubsky. Laser spectroscopic studies of nuclei with neutron number N<82 (Eu, Sm and Nd isotopes). *Journal of Physics G: Nuclear and Particle Physics*, 18(7):1177, 1992.

[71] A. Kramida, Yu. Ralchenko, J. Reader, , and NIST ASD Team. 2013.

[72] R.L. Kurucz and B. Bell. Atomic Line Data Kurucz CD-ROM No. 23. 1995.

[73] L. Jia, C. Jing, Z. Zhou, and F. Lin. Studies of high-lying even-parity levels of Sm I: energies and isotope shifts. *J. Opt. Soc. Am. B*, 10:1317--1320, 1993.

[74] T. Jayasekharan, M. A. N. Razvi, and G. L. Bhale. Observation of new even-parity states of Sm I by resonance ionization mass spectrometry. *J. Opt. Soc. Am. B*, 16:641--648, 1996.

[75] A. I. Gomonai and O. I. Plekan. Single-colour resonance three-photon ionization of samarium atoms. *Journal of Physics B: atomic molecular and optical physics*, 36:4155--4174, 2003.

[76] A. K. Pulhani, M. L. Shah, Vas Dev, and B. M. Suri. High-lying even-parity excited levels of atomic samarium. *J. Opt. Soc. Am. B*, 22:1117--1122, 2004.

[77] C.-J. Dai M. Li and J. Xie. Photoionization spectra of even-parity states of sm atom with multistep excitation. *Journal of Quantitative Spectroscopy & Radiative Transfer*, 112:793--799, 2010.

[78] A. Schmitt, B. A. Bushaw, and K. Wendt. Determination of the 154 Sm ionization energy by high-precision laser spectroscopy. *Journal of Physics B: Atomic, Molecular and Optical Physics*, 37(8):1633, 2004.

[79] Annette Schmitt. *Hochauflösende Resonanzionisationspektroskopie an Samarium und Gadolinium*. PhD thesis, University of Mainz, 2004.

[80] Z. Yan-Hong, D. Chang-Jian, and Y. Shi-Wei. Autoionization spectra of Sm atom. *Chinese Physics B*, 22(2):023203, 2013.

[81] S. Hu, S. Mei, S. Zhang, X. Chen, and Y. Xu. Observation and Measurement of the autoionization Spectra of atomic samarium. *Chinese Physics Letters*, 6:64--67, 1989.

[82] S. Hu, S. Zhang, S. Mei, J. Qiu, and X. Chen. Investigation of highly excited states of Sm. *Journal Quant. Spectrosc. Radiat. Transfer*, 43, 1990.

[83] H. Park, H. c. Kim, J. Yi, J. Han, Y. j. Rhee, and J. Lee. The Odd-Parity Autoionization States of Sm Atom Determined by Three-Step Excitation. *Journal of the Korean Physical Society*, 33:288--291, 1998.

[84] T. Jayasekharan, M. A. N. Razvi, and G. L. Bhale. Even-parity bound and autoionizing rydberg series of the samarium atom. *Journal of Physics B: Atomic, Molecular and Optical Physics*, 33(16):3123, 2000.

[85] W. J. Qin and C. J. Dai and Y. Xiaoy. The study of autoionizing states of the samarium atom. *Journal of Quantitative Spectroscopy and Radiative Transfer*, 111(7-8):997 -- 1004, 2010.

[86] J. Mes, E. J. van Duijn, and W. Hogervorst. High-resolution spectroscopy on ground-state transitions of samarium-I. *The European Physical Journal D - Atomic, Molecular, Optical and Plasma Physics*, 36(1):17--22, 2005.

[87] H. Figger, D. Schmitt, and S. Penselin. *Colloq. Int. C.N.R.S*, 164:355, 1967.

[88] V. Sonnenschein, I.D. Moore, H. Khan, I. Pohjalainen, and M. Reponen. Characterization of a dual-etalon Ti:sapphire laser via resonance ionization spectroscopy of stable copper isotopes. *Hyperfine Interactions*, 227(1-3):113--123, 2014.

[89] Y. Liu, J. Shan, U. Gabbert, and N. Qi. Hysteresis and creep modeling and compensation for a piezoelectric actuator using a fractional-order Maxwell resistive capacitor approach. *Smart Materials and Structures*, 22(11):115020, 2013.

[90] S.S. Aphale, B. Bhikkaji, and S.O.R. Moheimani. Minimizing scanning errors in piezoelectric stack-actuated nanopositioning platforms. *Nanotechnology, IEEE Transactions on*, 7(1):79--90, Jan 2008.

[91] J. Akila and S. S. Wadhwa. Correction for nonlinear behavior of piezoelectric tube scanners used in scanning tunneling and atomic force microscopy. *Review of Scientific Instruments*, 66(3):2517--2519, 1995.

[92] A.J. Fleming and K. K. Leang. Charge drives for scanning probe microscope positioning stages. *Ultramicroscopy*, 108(12):1551 -- 1557, 2008.

[93] P. G. Schumann. *Selektiver Nachweis von Uran-236 mittels hochauflösender Resonanzionisations-Massenspektrometrie*. PhD thesis, University of Mainz, 2005.

[94] Daniel A. Steck. Rubidium 85 D Line Data. URL http://steck.us/alkalidata/rubidium85numbers.pdf.

[95] Daniel A. Steck. Rubidium 87 D Line Data. URL http://steck.us/alkalidata/rubidium87numbers.pdf.

[96] D. W. Preston. Doppler-free saturated absorption: Laser spectroscopy. *American Journal of Physics*, 64:1432--1436, November 1996.

[97] W. Z. Zhao, J. E. Simsarian, L. A. Orozco, and G. D. Sprouse. A computer-based digital feedback control of frequency drift of multiple lasers. *Review of Scientific Instruments*, 69(11):3737--3740, 1998.

[98] T. Kessler, H. Tomita, C. Mattolat, S. Raeder, and K. Wendt. An injection-seeded high-repetition rate Ti:Sapphire laser for high-resolution spectroscopy and trace analysis of rare isotopes. *Laser Physics*, 18(7):842--849, 2008.

[99] X. Baillard, A. Gauguet, S. Bize, P. Lemonde, Ph. Laurent, A. Clairon, and P. Rosenbusch. Interference-filter-stabilized external-cavity diode lasers. *Optics Communications*, 266(2):609 -- 613, 2006.

[100] A.D. White. Frequency stabilization of gas lasers. *Quantum Electronics, IEEE Journal of*, 1(8):349--357, Nov 1965.

[101] S. Hannemann, E.-J. van Duijn, and W. Ubachs. A narrow-band injection-seeded pulsed titanium:sapphire oscillator-amplifier system with on-line chirp analysis for high-resolution spectroscopy. *Review of Scientific Instruments*, 78(10), 2007.

[102] H. Tomita, Ch. Mattolat, Th. Kessler, T. Muramatsu, K. Wendt, K. Watanabe, and T. Iguchi. Tunability of injection seeded high repetition rate ti:sapphire laser far off the gain peak. *AIP Conference Proceedings*, 1104(1):195--199, 2009.

[103] P. T. Greenland, M. A. Lauder, and D. J. H. Wort. Atomic beam velocity distributions. *Journal of Physics D: Applied Physics*, 18(7):1223, 1985.

[104] T. E. Cocolios, A. N. Andreyev, B. Bastin, N. Bree, J. Büscher, J. Elseviers, J. Gentens, M. Huyse, Yu. Kudryavtsev, D. Pauwels, T. Sonoda, P. Van den Bergh, and P. Van Duppen. Magnetic dipole moments of ^{57,58,59}Cu. *Phys. Rev. C*, 81:014314, Jan 2010.

[105] R. de Groote. Modeling and Simulation of Two-Step Resonance Ionization Processes using CW and Pulsed Lasers. Master's thesis, KU Leuven, 2013.

[106] S. Gheysen, G. Neyens, and J. Odeurs. Calculated hyperfine spectra for in-source laser spectroscopy and deduced magnetic moments and isomer shifts of ^{68}Cu and ^{70}Cu isomeric states. *Phys. Rev. C*, 69:064310, Jun 2004.

[107] R. Ferrer, B. Bastin, D. Boilley, P. Creemers, P. Delahaye, E. Liénard, X. Fléchard, S. Franchoo, L. Ghys, M. Huyse, Yu. Kudryavtsev, N. Lecesne, H. Lu, F. Lutton, E. Mogilevskiy, D. Pauwels, J. Piot, D. Radulov, L. Rens, H. Savajols, J.C. Thomas, E. Traykov, C. Van Beveren, P. Van den Bergh, and P. Van Duppen. In gas laser ionization and spectroscopy experiments at the Superconducting Separator Spectrometer (S3): Conceptual studies and preliminary design. *Nuclear Instruments and Methods in Physics Research Section B: Beam Interactions with Materials and Atoms*, 317, Part B(0):570 -- 581, 2013. XVIth International Conference on ElectroMagnetic Isotope Separators and Techniques Related to their Applications, December 2–7, 2012 at Matsue, Japan.

[108] A. Hakimi. *Diodenlaserbasierte Resonanzionisations-Massenspektrometrie zu Spektroskopie und Ultrapurenanalyse an Uranisotopen*. PhD thesis, University of Mainz, 2013.

[109] T. Fischbach. Aufbau und Charakterisierung einer interferometrischen Frequenzstabilisierung für Diodenlaser. Master's thesis, University of Mainz, 2012.

[110] Arduino. http://arduino.cc.

[111] J. Rossnagel. Aufbau einer Atomstrahl-Massenspektrometer-Apparatur zur resonanten Laserionisation. Master's thesis, University of Mainz, 2011.

[112] M. Franzmann. Resonanzionisations-Massenspektrometrie an Aktiniden mit der Mainzer Atomstrahlquelle MABU. Master's thesis, University of Mainz, 2013.

[113] J. Roßnagel, S. Raeder, A. Hakimi, R. Ferrer, N. Trautmann, and K. Wendt. Determination of the first ionization potential of actinium. *Phys. Rev. A*, 85:012525, Jan 2012.

[114] S. Raeder. Private communication, 2014.

[115] Leif E. Peterson. Pirls: Poisson iteratively reweighted least squares computer program for additive, multiplicative, power, and non-linear models. *Journal of Statistical Software*, 2(5):1--28, 11 1997.

[116] P. J. Green. Iteratively reweighted least squares for maximum likelihood estimation, and some robust and resistant alternatives. *Journal of the Royal Statistical Society. Series B (Methodological)*, 46(2):pp. 149--192, 1984.

[117] J.D. Zumbro, R.A. Naumann, M.V. Hoehn, W. Reuter, E.B. Shera, C.E. Bemis Jr., and Y. Tanaka. E2 and E4 deformations in ^{232}Th and ^{239,240,242}Pu . *Physics Letters B*, 167(4):383 -- 387, 1986.

[118] J. Blaise and J. F. Wyart. *Energy Levels and Atomic Spectra of Actinides, International Tables of Selected Constants*. Tables Internationes de Constantes, Paris, 1992, 1992.

[119] G. Fricke and K. Heilig. 94-Pu Plutonium. In H. Schopper, editor, *Nuclear Charge Radii*, volume 20 of *Landolt-Börnstein - Group I Elementary Particles, Nuclei and Atoms*, pages 1--5. Springer Berlin Heidelberg, 2004.

[120] P. Kunz. *Resonanzionisations-Massenspektrometrie mit gepulsten und kontinuierlichen Lasern an Plutonium*. PhD thesis, University of Mainz, 2004.

[121] National Nuclear Data Center, Nuclear Science References, version of 25.10.2014, Information extracted from the NSR database. https://www-nds.iaea.org/relnsd/vcharthtml/VChartHTML.html.

[122] S. Köhler, R. Deißenberger, K. Eberhardt, N. Erdmann, G. Herrmann, G. Huber, J.V. Kratz, M. Nunnemann, G. Passler, P.M. Rao, J. Riegel, N. Trautmann, and K. Wendt. Determination of the first ionization potential of actinide elements by resonance ionization mass spectroscopy. *Spectrochimica Acta Part B: Atomic Spectroscopy*, 52(6):717 -- 726, 1997.

[123] L. A. Kroger and C. W. Reich. Features of the low-energy level scheme of ^{229}Th as observed in the α-decay of ^{233}U . *Nuclear Physics A*, 259(1):29 -- 60, 1976.

[124] R. G. Helmer and C. W. Reich. An excited state of ^{229}Th at 3.5 eV. *Phys. Rev. C*, 49:1845--1858, Apr 1994.

[125] B. R. Beck and C.Y. Wu and P. Beiersdorfer and G. V. Brown and J. A. Becker and K. J. Moody and J. B. Wilhelmy and F. S. Porter and C. A. Kilbourne and R. L. Kelley. Improved Value for the Energy Splitting of the Ground-State Doublet in the Nucleus ^{229m}Th. *in proceedings of 12th Int. Conf. on Nucl. Reaction Mechanisms, Varenna, Italy*, 2009. LLNL-PROC-415170.

[126] S. L. Sakharov. On the energy of the 3.5-eV level in ^{229}Th. *Physics of Atomic Nuclei*, 73:1--8, January 2010.

[127] G.A. Kazakov, V. Schauer, J. Schwestka, S.P. Stellmer, J.H. Sterba, A. Fleischmann, L. Gastaldo, A. Pabinger, C. Enss, and T. Schumm. Prospects for measuring the 229Th isomer energy using a metallic magnetic microcalorimeter . *Nuclear Instruments and Methods in Physics Research Section A: Accelerators, Spectrometers, Detectors and Associated Equipment*, 735(0):229 -- 239, 2014.

[128] E. Peik and Chr. Tamm. Nuclear laser spectroscopy of the 3.5 eV transition in Th-229. *EPL (Europhysics Letters)*, 61(2):181, 2003.

[129] G. A. Kazakov, A. N. Litvinov, V. I. Romanenko, L. P. Yatsenko, A. V. Romanenko, M. Schreitl, G. Winkler, and T. Schumm. Performance of a 229 thorium solid-state nuclear clock. *New Journal of Physics*, 14(8):083019, 2012.

[130] C. J. Campbell, A. G. Radnaev, A. Kuzmich, V. A. Dzuba, V. V. Flambaum, and A. Derevianko. Single-Ion Nuclear Clock for Metrology at the 19th Decimal Place. *Phys. Rev. Lett.*, 108:120802, Mar 2012.

[131] N. Hinkley, J. A. Sherman, N. B. Phillips, M. Schioppo, N. D. Lemke, K. Beloy, M. Pizzocaro, C. W. Oates, and A. D. Ludlow. An Atomic Clock with 10^{-18} Instability. *Science*, 341(6151):1215--1218, 2013.

[132] V. V. Flambaum and R. B. Wiringa. Enhanced effect of quark mass variation in ^{229}Th and limits from Oklo data. *Phys. Rev. C*, 79:034302, Mar 2009.

[133] J. C. Berengut, V. A. Dzuba, V. V. Flambaum, and S. G. Porsev. Proposed Experimental Method to Determine α Sensitivity of Splitting between Ground and 7.6 eV Isomeric States in ^{229}Th. *Phys. Rev. Lett.*, 102:210801, May 2009.

[134] X. Zhao, Y. N. Martinez de Escobar, R. Rundberg, E. M. Bond, A. Moody, and D. J. Vieira. Observation of the Deexcitation of the $^{229\mathbf{m}}$Th Nuclear Isomer. *Phys. Rev. Lett.*, 109:160801, Oct 2012.

[135] E. Peik and K. Zimmermann. Comment on ''Observation of the Deexcitation of the ^{229m}Th Nuclear Isomer''. *Phys. Rev. Lett.*, 111:018901, Jul 2013.

[136] F. F. Karpeshin and M. B. Trzhaskovskaya. Impact of the electron environment on the lifetime of the ^{229}Th^{m} low-lying isomer. *Phys. Rev. C*, 76:054313, Nov 2007.

[137] E. Ruchowska, W. A. Płóciennik, J. Żylicz, H. Mach, J. Kvasil, A. Algora, N. Amzal, T. Bäck, M. G. Borge, R. Boutami, P. A. Butler, J. Cederkäll, B. Cederwall, B. Fogelberg, L. M. Fraile, H. O. U. Fynbo, E. Hagebø, P. Hoff, H. Gausemel, A. Jungclaus, R. Kaczarowski, A. Kerek, W. Kurcewicz, K. Lagergren, E. Nacher, B. Rubio, A. Syntfeld, O. Tengblad, A. A. Wasilewski, and L. Weissman. Nuclear structure of ^{229}Th. *Phys. Rev. C*, 73:044326, Apr 2006.

[138] C. J. Campbell, A. G. Radnaev, and A. Kuzmich. Wigner Crystals of ^{229}Th for Optical Excitation of the Nuclear Isomer. *Phys. Rev. Lett.*, 106:223001, Jun 2011.

[139] K. Beloy. Hyperfine Structure in $^{229g}\mathrm{Th}^{3+}$ as a Probe of the $^{229g}\mathrm{Th} \rightarrow {}^{229m}\mathrm{Th}$ Nuclear Excitation Energy. *Phys. Rev. Lett.*, 112:062503, Feb 2014.

APPENDIX 1 HIGH LYING EXCITED STATES IN SAMARIUM

TABLE 12 Energy levels, ion signal intensity and comparison with literature data for second excited states. The bold states have been used as starting points for scans of autoionizing states. The error for the experimental energy levels is $< 0.1\,\mathrm{cm}^{-1}$.

#	exp. value in cm^{-1}	lit. value in cm^{-1}	exp.-lit in cm^{-1}	A + CVL intensity	A intensity	B intensity	J new	J lit.
1	34137.93	-	-	45	-	-	0-2	-
2	34150.25	34150.20	-0.05	161	-	-	2	2
3	**34206.42**	**34206.50**	**0.08**	**208**	-	-	**2**	**2**
4	34212.09	34211.20	-0.89	111	-	-	2	2
5	34222.65	-	-	69	-	-	0-2	-
6	34244.71	-	-	22	-	-	0-2	-
7	**34298.70**	**34298.20**	**-0.50**	**372**	-	-	**2**	**2**
8	34395.28	-	-	279	-	-	0-2	-
9	34398.89	34399.00	0.11	127	-	-	1	1
10	34438.22	34438.00	-0.22	678	-	-	2	2
11	34517.17	-	-	259	-	-	0-2	-
12	34531.17	34531.00	-0.17	143	-	-	2	2
13	34561.88	-	-	188	-	-	0-2	-
14	34590.39	34590.10	-0.29	124	-	-	2	2
15	34630.63	34630.00	-0.63	40	-	-	1	1
16	34648.20	-	-	167	182	-	0-2	-
17	34657.41	34656.80	-0.61	71	9	-	1	1
18	34713.03	34713.10	0.07	209	24	-	1	1
19	34723.34	34723.40	0.06	447	33	-	2	2
20	34796.13	34796.00	-0.13	362	14	-	2	2
21	34842.29	-	-	133	8	-	0-2	-
22	34865.49	34865.60	0.11	139	12	-	2	2
23	34921.52	34921.60	0.08	293	-	-	2	2
24	34930.01	-	-	42	6	-	0-2	-
25	34932.75	34932.80	0.05	369	7	-	1	1
26	35046.80	35046.50	-0.30	472	9	-	1	1
27	35069.81	35069.90	0.09	200	-	-	1	1
28	35072.74	35072.80	0.06	154	23	-	1-2	1-3
29	35116.49	-	-	236	7	-	0-2	-
30	35135.41	35135.40	-0.01	196	8	9	1	1
31	35138.04	35138.10	0.06	196	32	16	2	2-3
32	**35155.15**	**35155.10**	**-0.05**	**1000**	**34**	**14**	**2**	**2-3**
33	35163.72	35163.90	0.18	380	13	-	1	1
34	35222.11	35222.20	0.09	447	23	27	2	2
35	35225.82	35226.00	0.18	227	20	13	1	1
36	35237.10	35237.20	0.10	-	-	73	3	3
37	35242.77	35242.90	0.13	575	12	65	2	2
38	35259.11	35259.50	0.39	535	31	24	2	2
39	35348.68	35348.70	0.02	-	-	30	1-3	1-3
40	35370.82	35371.00	0.18	661	71	49	1	1
41	35414.00	35414.00	0.00	-	-	20	3	3
42	35444.20	35444.40	0.20	486	42	-	1	1
43	35461.09	35461.20	0.11	313	143	27	2	2

TABLE 12 (continued)

#	exp. value in cm^{-1}	lit. value in cm^{-1}	exp.-lit in cm^{-1}	A + CVL int. intensity	A int. intensity	B int. intensity	J new	J lit.
44	35487.36	35487.40	0.04	348	62	-	2	2
45	35491.30	35491.40	0.10	-	-	33	3	3
46	35544.98	35544.90	-0.08	333	90	12	1	1
47	35547.74	35547.60	-0.14	-	-	17	2	2
48	35569.36	35569.40	0.04	735	39	15	2	2
49	35594.10	35594.10	0.00	345	45	80	2	2
50	35605.20	35605.30	0.10	-	-	42	3	3
51	35612.63	35612.70	0.07	124	57	58	1-3	4
52	35651.89	35652.00	0.11	230	83	93	1	1
53	35679.68	35679.70	0.02	-	-	66	3	3
54	35700.05	35700.00	-0.05	294	71	27	1	1
55	35730.54	35730.70	0.16	49	-	31	1-2	3
56	35742.13	35742.20	0.07	139	60	45	1	1
57	35746.92	35747.00	0.08	100	79	84	2	2
58	35748.67	35748.80	0.13	-	-	21	3	3
59	35768.84	35768.90	0.06	-	20	-	2	2
60	35779.17	35779.26	0.09	-	-	24	3	3
61	35785.52	35785.67	0.15	251	225	-	1	1
62	35821.23	35821.30	0.07	44	38	32	2	2
63	35839.00	35839.10	0.10	-	19	30	2	2
64	35899.12	-	-	186	42	59	1-2	-
65	35931.92	35931.90	-0.02	-	19	41	2	2
66	35954.44	-	-	-	-	56	1-3	-
67	35956.57	-	-	-	15	37	1-2	-
68	35959.29	35959.30	0.01	72	77	-	1-2	1-2
69	36007.47	36007.50	0.03	-	-	178	3	3
70	36024.41	36024.50	0.09	257	48	21	1	1
71	36057.63	36057.50	-0.13	167	20	32	2	2
72	36084.74	36084.80	0.06	43	22	-	0-2	3
73	36087.55	36087.50	-0.05	-	-	9	3	3
74	36133.95	36134.00	0.05	-	-	240	3	3
75	36145.89	36145.90	0.01	204	55	35	1	1
76	36162.22	36162.30	0.08	-	-	77	3	3
77	36188.77	36188.80	0.03	122	38	165	2	2
78	36193.81	36193.90	0.09	114	19	21	1	1
79	36201.27	36201.30	0.03	-	42	95	2	2
80	36217.21	36217.20	-0.01	-	-	93	3	3
81	36223.76	36223.60	-0.16	-	-	72	3	3
82	36248.11	36248.15	0.04	92	49	84	2	2
83	36302.68	36302.70	0.02	49	86	99	1-2	3
84	36308.01	36308.20	0.19	65	43	272	1	1
85	36362.28	36362.30	0.02	310	18	106	2	2
86	36377.15	36377.20	0.05	107	174	135	1	1
87	36391.38	36391.40	0.02	-	64	95	2	2
88	36403.92	36404.00	0.08	-	18	73	1	1
89	36409.35	36409.30	-0.05	-	-	24	3	3
90	36474.63	36474.60	-0.03	-	19	153	2	2
91	36515.37	36515.40	0.03	-	10	42	2	2
92	**36536.65**	**36536.70**	**0.05**	-	-	**38**	**1-3**	**1-3**
93	36565.35	36565.50	0.15	-	-	28	1	1

TABLE 12 (continued)

#	exp. value in cm^{-1}	lit. value in cm^{-1}	exp.-lit in cm^{-1}	A + CVL int. intensity	A int. intensity	B int. intensity	J new	J lit.
94	36572.02	36572.00	-0.02	-	-	9	3	3
95	36587.35	36587.40	0.05	-	-	30	3	3
96	36592.80	36592.80	0.00	-	-	26	2	2
97	36628.46	36628.40	-0.06	-	-	91	1	1
98	36644.43	36644.28	-0.15	-	-	216	1	1
99	36682.52	36682.50	-0.02	-	-	17	3	3
100	36701.76	36701.80	0.04	-	-	12	2	2
101	36760.10	36760.10	0.00	-	-	222	2	2
102	36763.19	36763.20	0.01	-	-	36	3	3
103	36776.59	36776.50	-0.09	-	-	28	3	3
104	36778.21	36778.20	-0.01	-	-	13	2	2

APPENDIX 2 AUTOIONIZING STATES IN SAMARIUM

TABLE 13 Energy levels and intensities for some of the strongest AI states detected during scans with schemes A1-3 and B1. Intensities normalized to 1000 for the highest peak. For the narrow resonances with a width $< 1\,\mathrm{cm}^{-1}$ the error for the energy levels is about $0.15\,\mathrm{cm}^{-1}$, but may be larger for the wider resonances.

#	E. in cm^{-1}	lit. E in cm^{-1}	A1 int. in a.u	A2 int. in a.u	A3 int. in a.u	B1 int. in a.u	width in cm^{-1}
1	45425.33	-	-	110	-	-	0.4
2	45524.91	-	-	137	-	-	0.4
3	45544.45	-	-	122	-	-	0.3
4	45544.97	-	-	161	-	-	0.3
5	45546.83	45546.0	-	695	-	-	0.7
6	45650.89	45651.1	-	184	-	-	0.3
7	45651.60	45651.1	-	127	-	-	0.3
8	45692.48	45692.7	-	119	-	-	0.5
9	45715.56	45715.5	-	221	-	-	0.7
10	45847.40	-	-	157	-	-	1.5
11	45860.24	-	-	-	78	-	0.5
12	45864.16	-	-	202	-	-	1.1
13	45875.36	-	-	110	-	-	0.4
14	45883.02	-	-	-	100	-	2.2
15	45907.43	-	-	123	-	-	2.3
16	45908.68	-	-	182	-	-	1.1
17	45931.61	-	-	107	-	-	8.2
18	45934.13	-	-	386	-	-	0.2
19	45938.49	-	-	164	-	-	2.7
20	45959.40	-	-	100	-	-	1.5
21	45987.46	-	-	99	-	-	1.1
22	46045.07	-	-	136	-	-	5.1
23	46132.00	46131.8	-	110	-	-	0.4
24	46382.37	-	-	-	134	-	1.
25	46392.01	-	-	-	108	-	5.4
26	46458.00	46457.2	-	510	-	-	0.5
27	46459.19	-	-	1000	-	-	0.6
28	46546.59	-	-	125	-	-	2.2
29	46547.74	-	-	-	92	-	2.1
30	46834.17	-	-	-	102	-	0.7
31	46835.42	-	139	-	-	-	1.9
32	46859.43	-	262	-	-	-	3.8
33	46864.16	-	318	-	-	-	1.7
34	46883.84	46883.3	134	-	-	-	2.4
35	46897.52	-	159	-	-	-	3.6
36	46947.09	-	128	-	-	-	3.
37	47068.37	-	-	-	96	-	7.5
38	47070.64	-	-	-	154	-	1.9
39	47087.33	-	-	-	128	-	1.
40	47091.19	47091.9	-	-	96	-	2.9
41	47096.45	-	217	-	163	-	0.8
42	47099.68	-	316	-	130	-	1.5
43	47103.69	-	278	-	-	-	2.7

TABLE 13 (continued)

#	E. in cm^{-1}	lit. E in cm^{-1}	A1 int. in a.u	A2 int. in a.u	A3 int. in a.u	B1 int. in a.u	width in cm^{-1}
44	47123.85	-	174	-	104	-	3.7
45	47130.33	-	-	-	94	-	4.4
46	47198.91	-	129	-	87	-	1.3
47	47217.73	-	-	-	129	-	3.9
48	47329.20	-	119	-	-	-	1.2
49	47347.35	-	117	-	-	-	4.2
50	47372.40	-	119	-	-	-	4.5
51	47382.73	-	124	-	-	-	5.9
52	47544.93	-	113	-	-	-	1.6
53	47590.15	-	296	-	-	-	3.5
54	47644.99	-	133	-	-	-	6.4
55	47811.68	47811.6	164	-	-	-	4.
56	47872.62	-	143	-	-	-	5.6
57	48070.92	-	155	-	-	-	2.4
58	48618.31	-	179	-	-	-	0.5
59	48825.48	-	-	-	-	247	5.1
60	48845.04	-	-	-	-	127	17.9
61	48861.31	-	-	-	-	561	6.
62	48868.92	-	-	-	-	430	9.1
63	48886.36	-	-	-	-	131	19.1
64	49032.89	-	-	-	-	86	28.
65	49044.28	-	-	-	-	294	4.9
66	49044.94	-	-	-	-	363	0.5
67	49046.59	-	-	-	-	266	1.4
68	49064.63	-	-	-	-	208	4.4
69	49599.44	-	-	-	-	81	10.1

APPENDIX 3 ANALYSIS OF FPI DATA WITH MATHEMATICA

Analysis of FPI data

Import of all datafiles

```
SetDirectory[NotebookDirectory[]];
Fi = FileNames["*.lvm"];
Fi = Fi[[Ordering@PadRight@StringSplit[Fi, x : NumberString :> ToExpression@x]]];
NN = Length[Fi];
SetSharedVariable[NN];
fpa = ParallelTable[Import[Fi[[i]], "TSV", NumberPoint → ","], {i, 1, NN}];
Table[fp_i = Drop[fpa[[i]], 23], {i, 1, NN}];
```

- Selects data directory and sorts and selects all files with extension *.lvm. Imports all data files and removes Header information. The data is stored in the variables fp_i, each containing a list of timing and signal information for the FPI photodiodes and the current reading.

Binning and export of ion current signal

```
Signal = Flatten[Join[Table[fp_i, {i, 1, NN}]], 1];
Current = Signal^T[[5]];
Time = Signal^T[[1]];
BinIV = 200;
NBin = Round[Length[Time] / BinIV] - 200;
For[p = 1, p < NBin, p++, signal_p = Take[Current, {1 + p * BinIV, BinIV + BinIV * p}]]
For[p = 1, p < NBin, p++, time_p = Take[Time, {1 + p * BinIV, BinIV + BinIV * p}]]
TS = Table[{Mean[signal_i], Mean[time_i]}, {i, 1, NBin}];
Export["Signal.txt", TS, "TSV"];
```

- Selects the timing (Channel 1) and signal (Channel 5) data for all files and uses a binning routine to reduce the amount of data.

Data selection of first FPI scan

```
fpi1 = Take[fp_1, 10 000];
hene = {fpi1^T[[1]], fpi1^T[[4]]}^T;
tisa = {fpi1^T[[1]], (fpi1^T[[2]])}^T;
trigger = {fpi1^T[[1]], fpi1^T[[3]]}^T;
triggerD = {Rest[trigger^T[[1]]], Differences[trigger^T[[2]]]}^T;
tD = Pick[triggerD, triggerD^T[[2]], _?(2 < # &)]^T[[1]];
```

- Selects the HeNe (Channel 4) and Ti:sa (Channel 2) data for the first file. To evaluate the trigger positions the differences of adjacent points in the trigger signal (Channel 3) are taken. Start of the FPI ramp is located where the trigger signal jumps by more than 2 Volts

Finding the peaks of the first ramp

Thresholds for Peak selection

```
YminHene = Max[hene^T[[2]]] / 2;
YminTisa = Max[tisa^T[[2]]] / 2;
Xmin = tD[[1]] + 0.01;
Xmax = tD[[2]] - 0.01;
Distance = 0.005;
```

Module for finding peak positions

```
PeakFind[table_, ymin_, xmin_, xmax_, distance_] :=
 Module[{data1 = table, THE, THE2, Pos1, LPos1},
  data1 = Pick[data1, data1^T[[2]], _?(# > ymin &)];
  data1 = Pick[data1, data1^T[[1]], _?(xmax > # > xmin &)];
  Pos1 = Prepend[Position[Differences[data1^T[[1]]], _?(# > distance &)], {1}];
  LPos1 = Length[Pos1];
  THE = Table[Take[data1, Flatten[{Pos1[[n]] + 1, Pos1[[1 + n]]}]], {n, 1, LPos1 - 1}];
  THE2 = Table[Position[THE[[n]], Max[THE[[n]]^T[[2]]], 2][[1, 1]], {n, 1, LPos1 - 1}];
  PPL = Table[THE[[n, THE2[[n]]]], {n, 1, LPos1 - 1}]^T[[1]];]
```

Apply the module to find peaks of HeNe and Ti:Sa

```
PeakFind[hene, YminHene, Xmin, Xmax, Distance]
PeaksHeNe = PPL
PeakFind[tisa, YminTisa, Xmin, Xmax, Distance]
PeaksTisa = PPL
```

```
{0.047652, 0.06019, 0.072278, 0.083916, 0.095255, 0.106344, 0.117233}
```

```
{0.047452, 0.061938, 0.075774, 0.089111, 0.102098, 0.114735}
```

- To find the peak position of the HeNe and Ti:sa signal a module named PeakFind is used. The module uses thresholds for the y and x positions and selects the signal within these thresholds. A further threshold defines the minimal distance between two peaks, so as not to detect fluctuations within a peak as double-peak.

Compiled functions for faster position finding

```
PPCα := Compile[{{mat, _Real, 2}, {th, _Real}, {di, _Real}, {Ivall, _Real}},
    Position[(Map[Boole[th + di - Ivall < # < th + di + Ivall] &, mat, {2}]), 1],
    Parallelization -> True, RuntimeOptions -> "Speed", RuntimeAttributes -> {Listable}];

PPCβ := Compile[{{mat, _Real, 2}, {th, _Real}, {di, _Real}, {Ivall, _Real},
     {PPint, _Integer}, {FSRReal, _Real}}, Position[
     (Map[Boole[th + di - Ivall - PPint * FSRReal < # < th + di + Ivall - PPint * FSRReal]
        &, mat, {2}]), 1], Parallelization -> True,
    RuntimeOptions -> "Speed", RuntimeAttributes -> {Listable}];
```

- For large lists the in-built *Mathematica* routines are relatively slow. For higher performance the functions for selecting the data within the thresholds are compiled.

Algorithm

- **Start parameters**

```
IV = 0.003;
THe1 = PeaksHeNe;
TTi1 = PeaksTisa;
TT1 = fp1^T[[{1, 3}]]^T;
TTrigger1 = {Rest[TT1^T[[1]]], Differences[TT1^T[[2]]]}^T;
tD1 = Pick[TTrigger1, TTrigger1^T[[2]], _?(2 < # &)]^T[[1]];
Ln1 = Length[tD1];
FSRtisa = PeaksTisa[[3]] - PeaksTisa[[2]]
δ = FSRtisa/2; pp1 = 0; pp2 = 0;
CO = 2;
Tdiff1 = PeaksHeNe[[1]] - tD[[1]]
```

■ **Loop**

```
For[n = 1, n < NN + 1, n++,
 TT_{n+1} = fp_{n+1}^T[[{1, 3}]]^T;
 TTrigger_{n+1} = {Rest[TT_{n+1}^T[[1]]], Differences[TT_{n+1}^T[[2]]]}^T;
tD_{n+1} = Pick[TTrigger_{n+1}, TTrigger_{n+1}^T[[2]], _?(2 < # &)]^T[[1]];
Ln_{n+1} = Length[tD_{n+1}];
 HeNeon = {fp_n^T[[1]], fp_n^T[[4]] - 0}^T;
 TiSa = {fp_n^T[[1]], fp_n^T[[2]]}^T;
 hdiffa_n = THe_n[[1]] - tD_n[[1]];
 TTT = Table[hdiffa_n + tD_n[[kk]] - tD_n[[1]], {kk, 1, Ln_n - CO}];
 haa = PPCα[HeNeon, tD_n[[1]], TTT, IV];
 haa = Replace[haa, x_List :> DeleteCases[x, {}], {0, Infinity}];
 haa = Table[Pick[haa[[kk]], haa[[kk]]^T[[2]], _?(# == 1 &)]^T[[1]], {kk, 1, Length[haa]}];
 haa = Table[HeNeon[[haa[[k]]]], {k, 1, Length[haa]}];
 PP = Table[Last[Ordering[haa[[k]]^T[[2]]]], {k, 1, Length[haa]}];
 peaka_n = Table[(Sum_{j=PP[[k]]-3}^{PP[[k]]+3} haa[[k]]^T[[2]][[j]] * haa[[k]]^T[[1]][[j]])/(Sum_{j=PP[[k]]-3}^{PP[[k]]+3} haa[[k]]^T[[2]][[j]]), {k, 1, Length[haa]}];
 hdiffa_n = THe_n[[2]] - tD_n[[1]];

 tdiffa_n = TTi_n[[1]] - tD_n[[1]];
 TTTi = Table[tdiffa_n + tD_n[[kk]] - tD_n[[1]], {kk, 1, Ln_n - CO}];
 taa = PPCβ[TiSa, tD_n[[1]], TTTi, IV, pp_n, FSRtisa];
 taa = Replace[taa, x_List :> DeleteCases[x, {}], {0, Infinity}];
 taa = Table[Pick[taa[[kk]], taa[[kk]]^T[[2]], _?(# == 1 &)]^T[[1]], {kk, 1, Length[taa]}];
 taa = Table[TiSa[[taa[[k]]]], {k, 1, Length[taa]}];
 PP = Table[Last[Ordering[taa[[k]]^T[[2]]]], {k, 1, Length[taa]}];
 tipeaka_n = Table[(Sum_{j=PP[[k]]-3}^{PP[[k]]+3} taa[[k]]^T[[2]][[j]] * taa[[k]]^T[[1]][[j]])/(Sum_{j=PP[[k]]-3}^{PP[[k]]+3} taa[[k]]^T[[2]][[j]]), {k, 1, Length[taa]}];
 tdiffa_n = TTi_n[[2]] - tD_n[[1]];

 TTi_{n+1} = {tipeaka_n[[1]]} - tD_n[[1]] + tD_{n+1}[[1]] +
    (tipeaka_n[[Ln_n - CO]] - peaka_n[[Ln_n - CO]]) - (tipeaka_n[[1]] - peaka_n[[1]]);
 THe_{n+1} = {peaka_n[[1]]} - tD_n[[1]] + tD_{n+1}[[1]];
 pp_{n+1} = Which[(tipeaka_n[[1]] - tD_n[[1]]) - (tipeaka_1[[1]] - tD1[[1]]) > FSRtisa - δ,
    pp_n + 1, (tipeaka_n[[1]] - tD_n[[1]]) - (tipeaka_1[[1]] - tD1[[1]]) < -FSRtisa + δ, pp_n - 1,
    -FSRtisa + δ < (tipeaka_n[[1]] - tD_n[[1]]) - (tipeaka_1[[1]] - tD1[[1]]) < FSRtisa - δ, 0];
 If[Mod[n, 10] == 0, Print[n];]]
```

- The algorithm uses a loop to identify the peaks for the whole data set. As the laser frequency changes relatively slowly it is possible to estimate the Ti:sa peak positions for the $n + 1^{th}$ file from the n^{th} file. While tracking a Ti:sa peak during a wide scan, the peak may reach the boundaries of the scanning ramp range. To avoid this a jump by one FSR backwards is performed each time the peak moves out of a defined interval. Tracking the number of jumps is the variable pp_n. The algorithm is shown only for the positions of one HeNe peak and one Ti:sa peak. in the full algorithm six peaks each for Ti:sa and HeNe are tracked in order to allow for the linearization procedure as outlined in the thesis. The extracted peak positions are then exported, after which they will be linearized in a separate mathematica file.

APPENDIX 4 SCHEMATIC OF PHOTODIODE AMPLIFIER ELECTRONICS

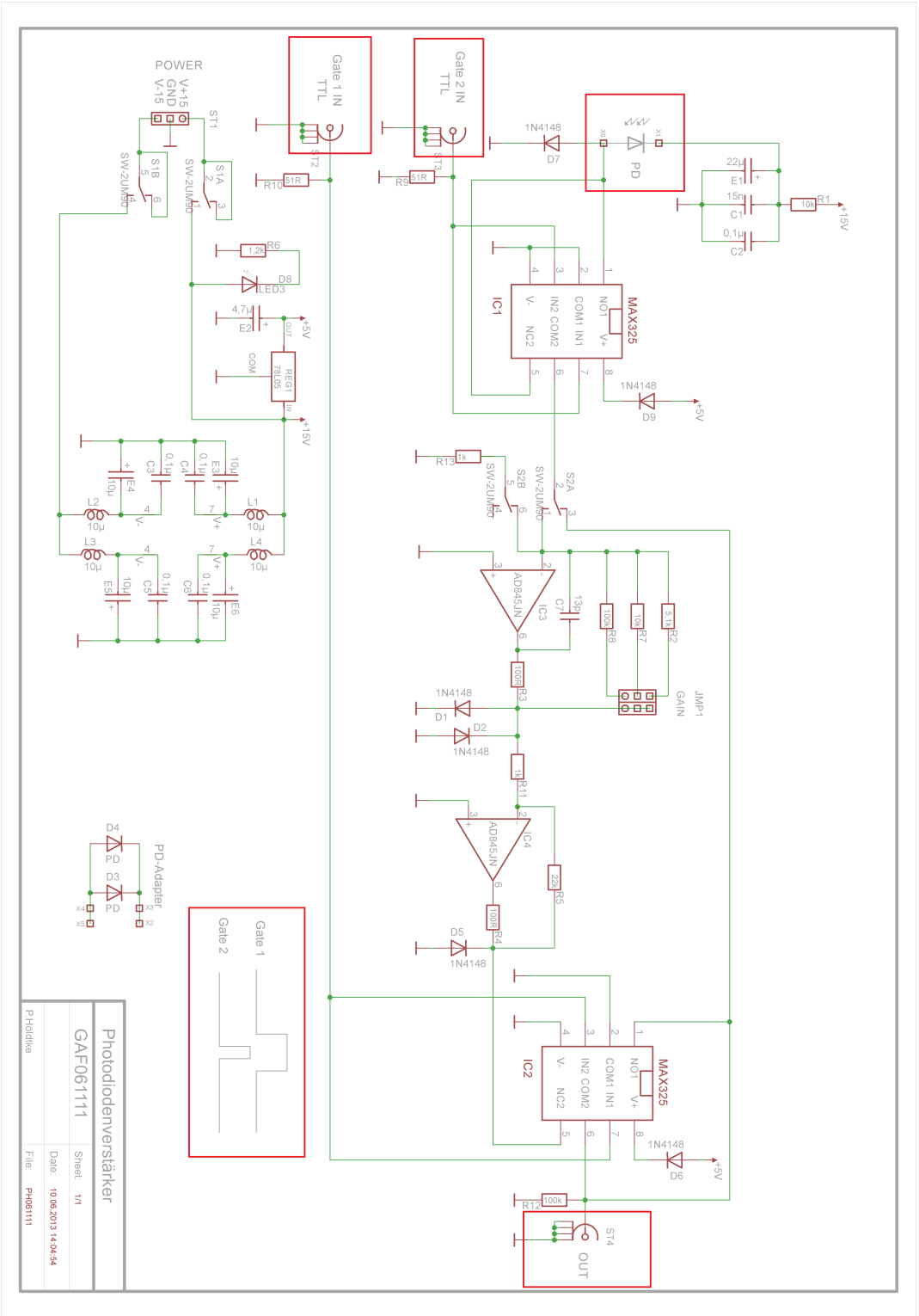

FIGURE A4.1 Fast switchable photodiode amplifier schematic, based on the design from the University of Mainz. The photodiode and the TTL switch inputs as weall as the amplifier output are highlighted in red.